Observing Atmospheric Electricity and Space Weather Effects in Venus' Atmosphere

Blair P. S. McGinness

Department of Meteorology

University of Reading

A thesis presented for the degree of

Doctor of Philosophy

October 2024

Declaration

I confirm that this is my own work and the use of all material from other sources has been properly and fully acknowledged.

Blair McGinness

Acknowledgements

Firstly, I would like to thank my supervisor team - Giles Harrison, Karen Aplin, Martin Airey, and Keri Nicoll. Your support and guidance throughout my PhD has been greatly appreciated. Additionally, thank you to my monitoring committee - Paul Williams and Maarten Ambaum - for keeping me on track, and identifying areas for improvement in my analysis.

I would like to thank the many people in Reading who have made my PhD experience enjoyable. Thank you to all of my 1U09 office mates: Brian, Caleb, Jen, Niamh, Karan, and Andrea. Your presence in the office has kept me motivated throughout my PhD, and kept me going during write up. I would additionally like to thank the other members of my PhD cohort: Alanna, Charlie, Hannah, Harriet, Helen, Isabel, and Natalie. The sense of community that you gave me here was invaluable. There are many more people in the department that I would like to thank, but I hope I can be forgiven for not mentioning everyone by name.

Further, I would like to thank the many other people who have supported me throughout my PhD. Thank you to all my friends for your positive influences. Particular thanks for the support during the first year of my PhD; while covid kept me at home, the various quizzes, online games, and video calls that gave me some level of social interaction were very meaningful to me.

Finally, I would like to thank my family for the support you have given me throughout my PhD. I forgive you for thinking that I have spent the last 4 years studying the weather.

This thesis was funded via an STFC studentship (ST/R000921/1). The various data sources used have been acknowledged in the Data Availability section.

There is great uncertainty respecting the cause of all these things, and they are concealed in the majesty of nature.

Pliny the Elder, *Naturalis Historia* (77 CE).

Abstract

Atmospheric electricity has important impacts across a range of disciplines. On Earth, lightning influences atmospheric chemistry, with related chemical processes considered important to the origins of life. Atmospheric electricity can affect other atmospheric processes, such as the stability, growth, and disintegration of cloud droplets. Previous investigations of atmospheric electricity on Venus have primarily focused on detections of lightning. From comparison with Earth, there are many other aspects of atmospheric electricity which require understanding, such as the effects of cosmic ray ionisation and electric charges on the clouds of Venus.

Through an investigation of a point discharge sensor on Earth, it was discovered that the operation of the sensor depended on both electrostatic and electrodynamic terms - interpreted as both free and displacement currents being detected. Knowledge of these sensors was applied to an investigation of the electrical discharges recorded by the Venera 13 & 14 spacecraft. It was found, via electrical modelling of Venus' atmosphere, that the best reproduction of the Venera data required both low-atmosphere haze layers and a global atmospheric electric circuit. Estimates were made for the strength of such a circuit, with the required conduction currents between -1 and 7 fA/m^2. Finally, space weather effects were investigated at Venus, with both solar energetic particle events and heliospheric current sheet crossings detected at the planet. It was found that space weather events associated with coronal mass ejections had a noticeable impact on the atmosphere of Venus, causing significant increases in the albedo. These are some of the first results demonstrating that there is a space weather effect in Venus' atmosphere.

These results suggest electrical processes have effects in Venus' atmosphere. Future investigations are required to identify any charge separation processes which could produce a global electric circuit, and to identify the mechanisms linking space weather variations to atmospheric processes.

List of Figures

List of Tables

Variables and Notation

Several of the acronyms used throughout this thesis are defined here.

Acronym	Meaning
A	Away
ADC	Analogue to Digital Converter
ACE	Advanced Composition Explorer
CR	Cosmic Ray
CME	Coronal Mass Ejection
DFT	Discrete Fourier Transform
GCR	Galactic Cosmic Ray
HCS	Heliospheric Current Sheet
HMF	Heliospheric Magnetic Field
HZE ions	High atomic number ions
ICME	Interplanetary Coronal Mass Ejection
IMA	Ion Mass Analyser (Venus Express instrument)
KS	Kolmogorov–Smirnov
L_1	Lagrange point 1
LED	Light Emitting Diode
MAG	Magnetometer (Venus Express instrument)
MCP	Multi-Channel Plate
MSL	Mars Science Laboratory
PDC	Point Discharge Current
PSD	Power Spectral Density
RUAO	Reading University Atmospheric Observatory
SEP	Solar Energetic Particle
SIS	Solar Isotope Spectrometer (ACE instrument)
T	Towards
UV	Ultraviolet
VEX	Venus Express
VIRA	Venus International Reference Atmosphere
VSO	Venus Solar Orbit
VMC	Venus Monitoring Camera (Venus Express instrument

A range of notation has been used throughout this thesis. The meaning of individual symbols should be defined in-text, however for reference these meaning of this notation has been stated here. Note that some symbols share several meanings. The relevant meaning of such symbols can be determined from context.

Symbol	Meaning
a, b, c, d	Constants / fit parameters
a, a_1, a_2	Particle radii
A_T, B_T	Constants for Thompson Recombination on Venus
A_B	Constant for Binary Recombination on Venus
a_r	Rayleigh radius
A	Area, fit constant
ADC Bin Size	Size of ADC bins
Bin №	ADC Bin Number
c_D	Drag coefficeint
c_v	Vacuum speed of light
C	Capacitance
C_{xy}	Coherence
$C_{\pm}$	Average thermal velocity of ions
e	Elementary charge
$\mathbf{E}$	Electric field
E	Electric field strength
$E_{breakdown}$	Breakdown field / dielectric strength
E_{Corona}	Corona field
E_{max}	Maximum value of perturbed electric field
$E_{typical}$	Unperturbed electric field
$f(F)$	Electrostatic function
f_{angle}	Fraction of particles traveling in specified direction
f_{nyq}	Nyquist frequency
f_{speed}	Fraction of particles with specified speed
f_x	Approximated Nyquist frequency for irregularly sampled data
$\mathbf{F}$	Force
F	Potential gradient
$F_{Campbell}$, F_{JCI}	Potential gradient recorded by specific sensors
$\mathbf{F_D}$	Drag force
$\mathbf{F_G}$	Force of gravity
G	Gravitational Constant
G_{xx}, G_{yy}	Auto-spectrum
G_{xy}	Cross-spectrum
$g(dF/dt)$	Electrodynamic function
h	Height
i	Imaginary unit

i, j, k	Indices
I	Current, point discharge current
I_D	Displacement/Maxwell current
$\mathbf{J}$	Current density
J_c	Fair weather conduction current density
k_B	Boltzmann Constant
m, c	Linear fit parameters
m	Mass of particle
m_{CO2}	Molecular mass of CO_2
m_{SC}	Spacecraft mass
m_{red}	Reduced mass
m_1, m_2	Masses
M	Minimum PG for point discharge to occur
$M_♀$	Mass of Venus
№	Number
n	Sample size
n_{auto}	Sample size for autocorrelation calculations
n_{CO2}	Number density of CO_2
n_{MC}	Number of Monte-Carlo iterations
n_{50}	Number of segments
$n_{\pm}$	Ion number density
N	Aerosol concentration
N	Number of datapoints in set
N_{i-1}, N_i, N_{i+1}	Count rate on given day
N_j	Concentration of particles with charge j
N_{seg}	Number of datapoints in segment
N_T	Total concentration of particles
N_0	Concentration of neutrally charged particles
p	Momentum
p_n	Number of independent variables
P	Pressure
P_i	Percentage change on day i
q	Ionisation rate
Q	Electric charge
Q_L	Electric charge of lander
r	Radial distance
R_B	Rigidity
R	Resistance
R^2	Coefficient of Determination (R-squared)
$\bar{R}^2$	Adjusted R-squared
R_c	Columnar resistance
$R_♀$	Radius of Venus

S	Area of surface
t	Time
t_{PG}, t_{PDC}	Time of x-axis crossings in given dataset
Δt	Time separation of datapoints
Δt_{xy}	Geometric mean of mean time separations
T	Temperature
T_{planet}	Apparent solar rotation period observed from a planet
T_{Sun}	True solar rotation period
u	Horizontal velocity
v_{ion}	Ion speed
v	Velocity
v_{drift}	Drift velocity
v_w	Lander speed
V	Electric potential
V_a	Atmospheric potential
V_L	Lander potential
V_0	Corona onset potential
W	Wind speed
W_u, W_v	Orthogonal components of the horizontal wind speed
x	Ion asymmetry factor
x_n	Data
y_c	Maximal horizontal offset
Y_{planet}	Orbital period (year) of a planet
$\hat{\mathbf{z}}$	Radial unit vector
z	Altitude
$\mathcal{O}$	Order of magnitude
α	Ion-ion recombination coefficient
α_T	Thompson recombination coefficient
α_B	Binary recombination coefficient
α_{HP}	High pressure recombination coefficient
β, β_+, β_-	Ion-aerosol attachment coefficient (general, positive ions, negative ions)
γ_T	Surface Tension
γ	Electric field enhancement
δ_{95}	95% confidence limit
ϵ	Permittivity
ϵ_0	Permittivity of free space
$\eta_{collision}$	Collision efficiency
η	Breakdown fraction
κ	Polarisability
λ	Energy parameter
$\lambda_{collect}$	Linear number density of collected ions
μ, μ_+, μ_-	Ion mobility (general case, negative ions, positive ions)

μ_0	Permeability of free space
ξ	Attachment coefficient ratio
ρ	Charge density
ρ_M	Mass density
ρ_R	Resistivity
σ	Conductivity
σ_{Total}, σ_+, σ_-	Conductivity (total, positive contribution, negative contribution)
τ	Time difference
τ_{RC}	RC Time Constant
χ	Function
ψ	Electric potential surrounding a particle
ω	Angular frequency
(x,y,z)	Cartesian co-ordinates
(r,ϕ,θ)	Sperical polar co-ordinates
∇	Del operator (Vector derivative)

The value of several constants used in this thesis are presented here.

Constant	**Symbol**	**Value**
Boltzmann Costant	k_B	1.38×10^{-23} JK^{-1}
Elementary Charge	e	1.6×10^{-19} C
Gravitational Constant	G	6.67×10^{-11} Nm^{2}kg^{-2}
Mass of Venus	$M_♀$	4.87×10^{24} kg
Permittivity of free space	ϵ_0	8.85×10^{-12} A^{2}s^{4}m^{-3}kg^{-1}
Radius of Venus	$R_♀$	6051.8 km

Fundamental Physical Formulae

A selection of fundamental formulae from classical physics, relevant to this thesis, have been produced here.

Electromagnetism

Maxwell's equations are given by:

$$\text{Gauss' Law} \qquad \nabla \cdot \mathbf{E} = \frac{\rho}{\epsilon_0} \tag{1}$$

$$\text{Gauss' Law for Magnetism} \qquad \nabla \cdot \mathbf{B} = 0 \tag{2}$$

$$\text{Faraday's Law} \qquad \nabla \times \mathbf{E} = -\frac{\partial \mathbf{B}}{dt} \tag{3}$$

$$\text{Ampere-Maxwell Law} \qquad \nabla \times \mathbf{B} = \mu_0 \mathbf{J} + \frac{1}{c_v^2}\frac{\partial \mathbf{B}}{dt} \tag{4}$$

where $\mathbf{E}, \mathbf{B}$ are the vector electric and magnetic fields respectively, ∇ is the vector differentiation operator, t is time, ρ is the free charge density, $\mathbf{J}$ is the free current density, ϵ_0 is the permitivity of free space, μ_0 is the permeability of free space, and c_v is the vacuum speed of light, given by:

$$c_v = \frac{1}{\sqrt{\epsilon_0 \mu_0}} \tag{5}$$

The Lorentz force on a charge q, with velocity $\mathbf{v}$ is given by:

$$\mathbf{F} = q\big((\mathbf{v} \times \mathbf{B}) + \mathbf{E}\big) \tag{6}$$

The charge continuity equation is given by:

$$\frac{\partial \rho}{\partial t} + \nabla \cdot \mathbf{J} = 0 \tag{7}$$

Ohm's law is given by:

$$\mathbf{J} = \sigma \mathbf{E} \tag{8}$$

for conductivity, σ.

Newtonian and Keplerian Dynamics

Newton's second law of motion is given by:

$$\mathbf{F} = \frac{d\mathbf{p}}{dt} \tag{9}$$

where $\mathbf{F}$ is the force on an object, and $\mathbf{p}$ is the momentum of that object.

In classical physics, the gravitational force between on a given mass, caused by the presence of another mass is given by Newton's universal law of gravitation:

$$\mathbf{F_G} = -\frac{Gm_1m_2}{\mathbf{r}^2}\hat{\mathbf{r}} \tag{10}$$

where m_1, m_2 are the two relevant masses, and $\mathbf{r}$ is the displacement vector between these masses, with $\hat{\mathbf{r}}$ the unit vector in this direction.

Kepler's third law of planetary motion states that the ratio of the orbital periods of two objects in orbit around the Sun is given by:

$$\frac{Y_1}{Y_2} = \left(\frac{a_1}{a_2}\right)^{3/2} \tag{11}$$

where Y_1, Y_2 are the orbital periods of the two objects, and a_1, a_2 are the semi-major axes of these orbits.

Contents

Chapter 1

Introduction

Atmospheric electricity has been explored in detail for Earth, however there are still aspects which are yet to be fully understood. The links that exist between atmospheric electricity and other systems, such as cloud microphysics, are still under investigation. In addition to this, detailed investigations of atmospheric electricity are still yet to be performed for the other planets in our solar system. This thesis follows a series of investigations intended to remedy this research gap for Venus, the sister planet to Earth.

1.1 Motivation

The topic of Atmospheric electricity describes many electrical processes in Earth's atmosphere. Perhaps the most obvious of these processes is lightning. This process is particularly dramatic, releasing acoustic energy as thunder, as well as electromagnetic energy across much of the frequency spectrum. The high energies present during lightning strikes are able to have significant effects on atmospheric chemistry, allowing the production of certain chemical species [122]. It is believed that the chemical processes facilitated by lightning strikes were responsible for the creation of several chemical species which were essential for life to develop on Earth [131, 82].

Lightning is but one aspect of atmospheric electricity. There are many processes involving the collection and separation of electric charge throughout the atmosphere of Earth, and the atmospheres of other planets. The presence of electric charges on cloud droplets is able to increase their stability - inhibiting evaporation - as well as encouraging growth via collisions with other droplets [4]. For particularly large amounts of charge, the opposite can be true, with the electric charge causing droplets to rupture [3]. The extent of the electrification of a planet's atmosphere can have significant implications across a wide range of processes, such as to the chemistry and cloud microphysics present there.

For Venus, little is known about many of the atmospheric processes. From investigations of atmospheric electricity on Earth, suggestions can be made for how similar processes may affect Venus [5]. Many attempts have been made to observe lightning in Venus' atmosphere, with the understanding developed from terrestrial studies of lightning directing these [117]. It is likely that if such a process was present, that it would have significant impacts on the atmosphere. As for Earth's atmosphere, however, lightning is not the only aspect of atmospheric electricity which can affect the planet. Very few investigations of atmospheric electricity in Venus' atmosphere have focused on these other aspects.

Recently, suggestions have been made that the clouds on Venus may be associated with the presence of microbial life [55]. Such a claim has naturally been met with strong resistance, however it has brought to light the limitations of our understanding of the cloud processes on Venus. If microbial life was present in the clouds of Venus, then it follows that the lifetime of these droplets would have significant implications. Based upon the influence that electric charges have on the lifetime of droplets on Earth, we find that atmospheric electricity may be important to the clouds (and maybe life) on Venus.

The fact that little is known of the electrical processes present in Venus' atmosphere is clearly an issue which needs to be solved. The work in this thesis aims to act as a step towards remedying this gap in knowledge.

1.2 Research Aims

One of the few in-situ investigations of atmospheric electricity on Venus, that wasn't attempting to observe lightning, recorded data from a point discharge sensor. To begin our investigation into the electrical processes on Venus we will consider the behaviour of such sensors on Earth. The idea of studying point discharge sensors as part of a greater atmospheric electricity investigation has been well established in the history of atmospheric electricity (as will be discussed in more detail in Chapter 2). Through our investigation, we attempt to identify if any new information on the operation of point discharge sensors could be gleaned, before investigating the data recorded on Venus.

To investigate the operation of such sensors, data from a meteorological field site will be considered. At this site the point discharge is monitored, along with variations in a number of other atmospheric parameters. The aim of this work is to identify how to parameterise the operation of such a sensor, to capture its behaviour most accurately.

Following this investigation, the data collected by the point discharge sensors onboard the Venera 13 & 14 spacecraft will be investigated. To understand the source of the signals recorded by these spacecraft, an electrical model of Venus' atmosphere will be produced. This will then allow calculations of the discharge currents expected for a spacecraft descending through the Venusian atmosphere to be performed. By comparing the recorded data against the model results, the properties of Venus' electrical environment can be constrained.

Finally, Venus' atmosphere will be investigated, by investigating the presence of any space weather effects upon it. A number of previous investigations have considered such effects on the Earth's atmosphere. We will continue the practice of applying methodologies developed for terrestrial atmospheric studies to planetary atmospheric investigations by applying the terrestrial space weather investigations to our investigation of Venus.

The investigation of space weather effects on Venus will be composed of two parts. Firstly, the short term effects of various space weather events will be considered. Impacts to the atmosphere will be identified by considering changes in the planet's albedo. Secondly, longer term periodic variations in the albedo of the planet will be considered. Coherence analysis will be used to identify any atmospheric periodicities which are driven by cosmic ray variations.

In summary, the research aims are as follows:

- Investigate the operation and parameterisations of point discharge sensors
- Investigate the presence and nature of the global atmospheric electric circuit on Venus
- Investigate the effects of space weather events on Venus' atmosphere
- Investigate the effects of cosmic rays on Venus' atmosphere

The links between several of the systems investigated in this thesis have been summarised in the diagram in figure 1.1. This figure shows links between space weather and the electrical environment of a planetary atmosphere, and further how this effects electrical observations.

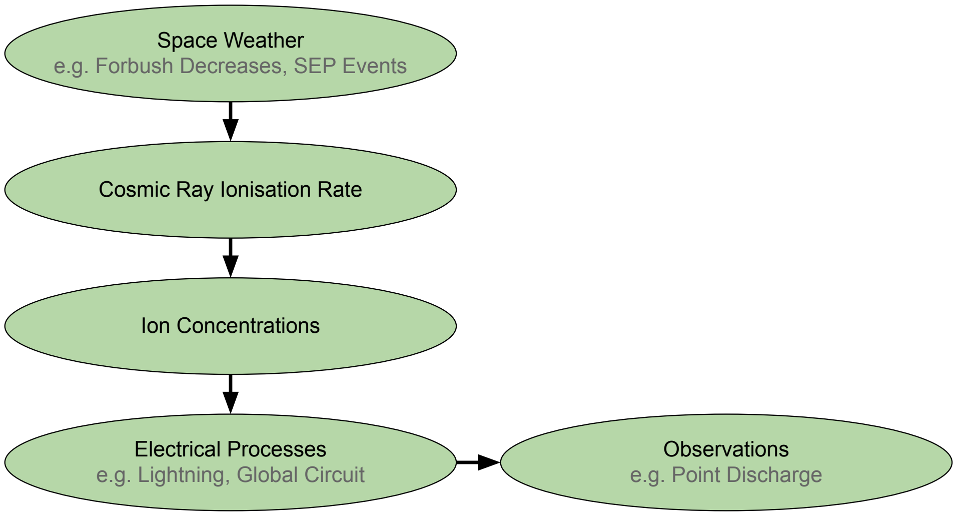

Figure 1.1: Diagram showing the links between several systems investigated in this thesis.

In the remainder of this chapter, some of the core concepts relevant to this thesis are introduced.

1.3 Core Concepts

1.3.1 Global Atmospheric Electric Circuit

The global atmospheric electric circuit of Earth is a conceptual model describing how the conducting ionosphere and surface of the Earth are linked together via the partially conductive atmosphere [158, 9]. A diagram of the global atmospheric electric circuit is shown in figure 1.2.

In disturbed weather "generator" regions, thunderstorm clouds transfer charge from the atmosphere to the surface of the Earth, causing the surface to become negatively charged [158, 5]. There are several charge transfer mechanisms involved in this process, including cloud to ground lightning strikes, charged rain, and point discharge currents [144]. In these disturbed weather regions, charge additionally flows between the atmosphere and the conducting ionosphere. The electrical processes above thunderclouds leads to a variety of transient luminous events (TLEs), including sprites, elves, and blue jets [156, 50]. In disturbed weather regions, the net flow of charge means that the ionosphere acquires a positive charge with respect to the surface [171, 9, 156]. The potential difference between the ionosphere and the surface is an important quantity

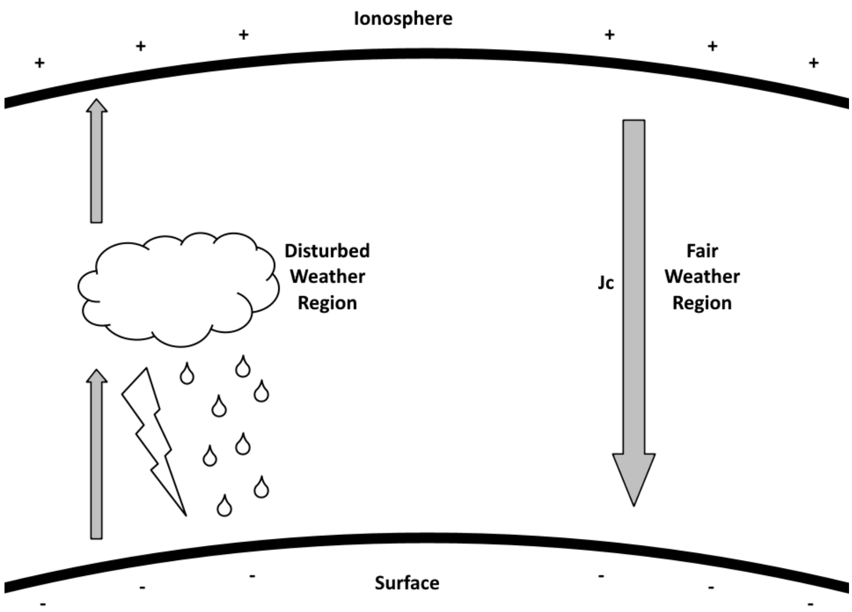

Figure 1.2: Pictorial overview of the Earth's global atmospheric electric circuit.

in atmospheric electrical studies, and is called the ionospheric potential, typically given symbol V_I [9, 66].

Since the ionosphere and the surface of the Earth are both conductive, the charge acquired in disturbed weather regions is distributed globally, meaning that this ionospheric potential is present in fair weather regions also. In these fair weather regions, ions created by cosmic rays or from the Earth's natural radioactivity cause the atmosphere to become slightly conductive [66]. The potential difference between the ionosphere and the Earth's surface causes an ohmic current to flow between the two [66]. This "fair weather conduction current", often given the symbol J_C, flows downwards with approximately constant magnitude across the world, and with approximately constant magnitude with time.

1.3.2 Point/Corona Discharge

Electrical discharges can take a number of forms. For large electric fields, exceeding the dielectric strength of a medium, electrical breakdown can occur - causing a spark discharge [115]. Other discharge processes are able to occur at lower energies, however [115]. When a surface is highly curved, such as at the tip of a sharp point, the electrical field near the point will be enhanced since electrical field lines must be perpendicular when crossing the surface of a conductor [120]. This effect is shown in figure 1.3. This enhancement of the electric field causes the field to be larger near to the point, decreasing away from it. This then allows localised discharge processes to take place near the point, where the field is largest. Commonly, the term "Corona discharge" is used to describe these sub-spark electrical discharges [115].

Corona discharge is a low energy plasma process, driven by the collisional ionisation from electrons (and ions) [115, 94]. As these charges are accelerated by an electric field, they will collide with neutral species. If the particle has been accelerated to a sufficient energy, it will ionise the neutral species, and create additional ions and electrons. This will lead to a cascade

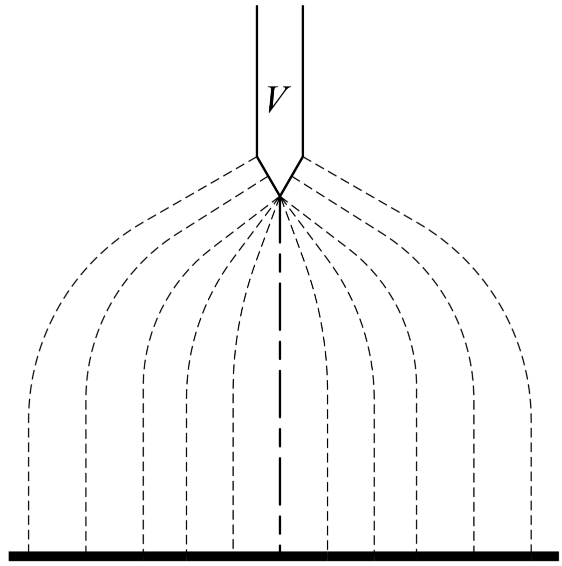

Figure 1.3: Electric field enhancement at the tip of a needle. Dashed lines show electric field lines. Figure taken from [130].

of ionisation, where these particles undergo further collisions, increasing the number of particles able to collide with other neutrals [115].

As the charges are moved by the electric field, a space charge will be built up, which acts to reduce the electric field present [94]. This can cause the ionisation process to be cut off, if the charges are not removed at a sufficient rate [94].

The ionisation cascade also leads to the emission of light [115]. Typically, only a small amount of light will be emitted, causing it to be difficult to observe by the unaided human eye. On occasion though, when the corona discharge is particularly strong, it can cause the tips of objects to glow. In these cases, the process is commonly referred to as “St Elmo’s fire”. Since large electrical potentials will be required for the glow to be visible, typically St Elmo’s fire will occur at the top of tall objects, such as the masts of ships. This relation to ships is responsible for it being named after St Elmo; the patron saint of sailing.

Across the literature, the term point discharge has often been used interchangeably with the term corona discharge. Other authors, instead prefer to use the term “point discharge” to describe corona discharges which occur outside of a laboratory environment, particularly when they have been created by the Earth’s atmospheric electric field. In the proceeding work, the term “point discharge” will be used to emphasise the fact we are dealing with atmospheric electric processes, rather than laboratory conditions.

1.3.3 Electrical Image Charges

The electrical force between two droplets can be influenced greatly by the presence of image charges. These will be discussed here.

The force on a given electrical point charge, Q_1, caused by the electric field of another point charge, Q_2, is given by Coulomb’s law:

$$\mathbf{F} = -\frac{Q_1 Q_2}{4\pi\epsilon_0 r^2}\hat{\mathbf{r}} \tag{1.1}$$

where ϵ_0 is the permittivity of free space, and r is the distance from charge Q_1 to Q_2 in the direction $\hat{\mathbf{r}}$. From Coulomb's law, it can be seen that the force between point charges will be repulsive if the two charges carry the same polarity.

When dealing with the electric field around an isolated spherical conductor, it is possible to consider the conductor to be a point charge. One may naively then consider that when considering the force on a given charge from an electrically charged spherical conductor, that Coulomb's law could again be used. This is in fact not the case, since the spherical conductor is polarisable; the presence of another electrical charge will create "image charges" in the spherical conductor, affecting the magnitude of the force between the two charges [89, 189]. These image charges are illustrated in figure 1.4. At large separations, the effect of these image charges will be negligible, however as the charges are moved closer together, they can cause a significant change to the force between the charges [89]; in the case of like-charges, this can even lead to an attractive force between the two charges, counter to what is expected from Coulombs law [89].

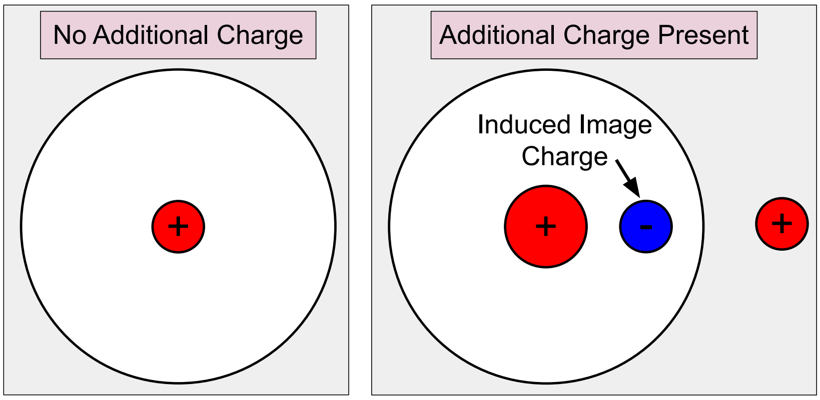

Figure 1.4: Diagram explaining how image charges can form in a polarisabile object, due to the presence of another charge. On the left, a positively charged spherical conductor is shown, with no other electrical charges present. The electric field of this object can be described as that of a point charge. On the right, an additional positive point charge has been introduced. This causes the conductor to become polarised, and introduces image charges; near to the point charge, a negative image charge is induced. Far from the point charge, an additional positive image charge is induced, such that the net charge of the conductor is the same as before the point charge was introduced.

In the case that there are two charged conducting spheres, image charges will again play an important role. In this case, both conducting spheres will be polarised, leading to image charges on both spheres. This complicates calculations of the electrical force between the charges, however the general result is the same as in the case of a single charged sphere: The image charges will affect the magnitude and possibly the polarity of the electrical force between the charges. Since cloud droplets have a non-negligible polarisability, the effects of image charges need to be considered when dealing with the electrical forces between them and other particles.

1.3.4 Cosmic Rays

The term "Cosmic Rays" refers to energetic charged particles originating from outside of the Earth [13]. These particles are primarily composed of atomic nuclei, of which the majority component is protons (Hydrogen nuclei) with alpha particles (Helium nuclei) forming a smaller component, and finally HZE ions (nuclei of atoms heavier than helium) forming an even smaller portion [14, 13]. Cosmic Rays which originate from the Sun are referred to as Solar Energetic Particles (SEPs), while particles originating outwith the solar system are referred to as Galactic Cosmic Rays (GCRs) [14, 138]. The term "cosmic rays" can be ambiguous as it refers both to GCR on their own, and to GCR & SEPs collectively. For clarity, the full term of "galactic cosmic rays" will be used whenever we are referring specifically to particles produced outwith the solar system, and the term "cosmic rays" will describe the general case of both GCR and SEPs.

1.3.5 Heliospheric Magnetic Field

The shape of the Sun's magnetic field is strongly affected by the solar wind. The outflow of material in the solar wind acts to stretch magnetic field lines away from the Sun, according to the "frozen-in flux theorem". Additionally, the rotation of the Sun twists the shape of these magnetic field lines into an Archimedean spiral. Such a shape is shown in figure 1.5a. Away from the Sun, this magnetic field is referred to as the Heliospheric Magnetic Field (HMF). The field lines in the HMF are directed either away from or towards the Sun. At the boundary between regions where the HMF is pointed towards and away from the Sun, there is a current sheet, referred to as the Heliospheric Current Sheet (HCS). A diagram showing the orientation of this current sheet boundary is shown in figure 1.5b.

The Sun's magnetic poles switch polarity in a periodic cycle, taking $\sim$11 years for each change. This 11 year cycle is also associated with a change in the frequency of sunspots and space weather events. Solar maximum is described as the time with the largest number of sunspots, and also features an increase in space weather event rates. This occurs shortly before the change in polarity of the magnetic poles. Solar minimum describes the time with fewest sunspots/space weather events, and occurs at the opposing point of phase as solar maximum. There is a larger periodicity of 22 years also associated with this reversal in the sun's magnetic poles, since the poles need to flip polarity twice in order for the starting polarity to be recovered. The 22 year cycle can be seen in time series of sunspot numbers, since the peaks in consecutive solar cycles are visibly differently shaped.

1.4 Structure of Subsequent Chapters

Following this introduction of several core concepts, the next chapter, Chapter 2, is a review of literature relevant to the investigations in this thesis. Next, in Chapter 3, the investigation into several terrestrial point discharge sensors is discussed. Following this, in Chapter 4, the investigation into the Venera 13 & 14 point discharge data via the construction of an electrical model of Venus' atmosphere is described. In Chapter 5, the investigations into the effects of space weather events and cosmic ray variations on Venus' atmosphere are described. Finally, in

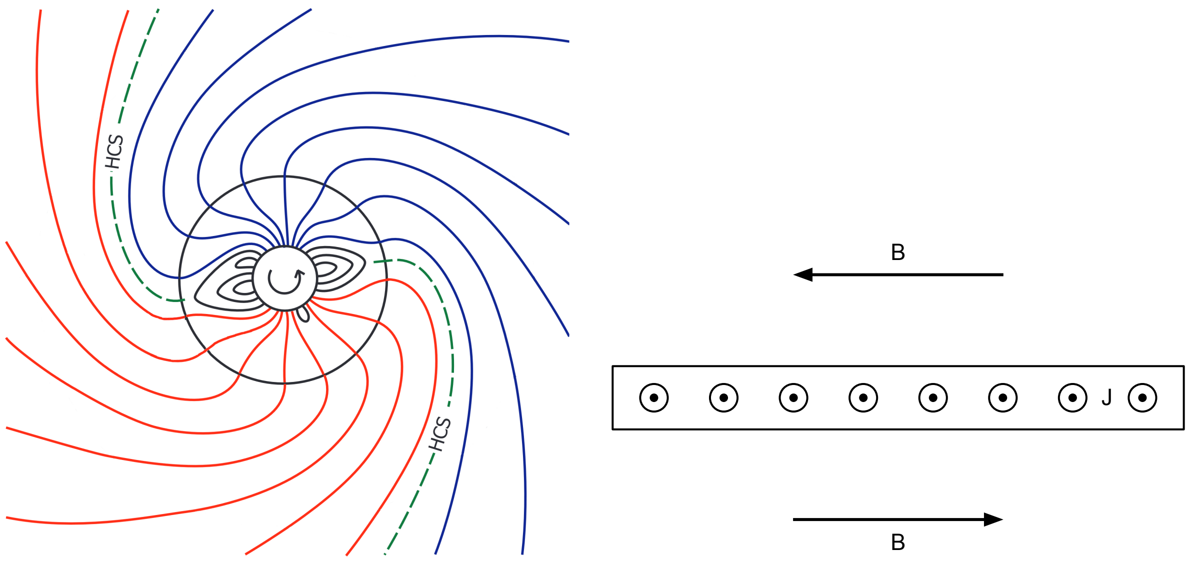

(a) HMF Archimedean Spiral

(b) Current Sheet

Figure 1.5: Diagrams showcasing the strucutre of the Heliospheric Magnetic Field. (a) shows the Archimedean spiral which the HMF field lines follow. Red and blue solid lines show magnetic field lines pointed towards/away from the Sun (innermost black circle). Figure altered from [141]. (b) shows how a current sheet forms between magnetic field lines of opposing polarity. Such a current sheet separates the regions of opposing HMF polarity.

Chapter 6, the results from these investigations are discussed, with the conclusions and possible future work discussed in Chapter 7.

There are two appendices included in this thesis. Appendix A reproduces the derivation performed by Chalmers [32] to obtain a theoretical parameterisation for the operation of a point discharge sensor. Appendix B describes the logarithmic electrometer circuit used in one of the two point discharge sensors at the Reading University Atmospheric Observatory.

Chapter 2

Literature Review

This chapter is a review of the relevant literature to this thesis. First, the field of terrestrial atmospheric electricity will be considered. In particular, attention will be brought to the topic of point discharge sensors, their role in the history of atmospheric electricity, and how understanding of their operation has evolved. In addition to this, attention will be brought to the effects of atmospheric electricity on the Earth's atmosphere. Next, atmospheric electricity on other planets in our solar system will be considered. Following this is a discussion of several aspects of Venus. An overview of several aspects of the planet is given, with comparisons made to Earth. Additionally, investigations of lightning and other atmospheric electricity investigations are discussed. Finally, space weather and its effects on planetary atmospheres will be considered. Attention will be brought to the nature of cosmic rays and their impacts on planetary atmospheres, in addition to the nature of a number of space weather events, and their impacts.

2.1 Terrestrial Atmospheric Electricity

The field of Atmospheric electricity describes a range of electrical processes occurring naturally within Earth's atmosphere. Through dramatic processes, such as lightning strikes, it can be said that atmospheric electricity has been observed for all of human existence. The understanding of these processes took place more recently, however, with the links between several of these processes in the global atmospheric electric circuit being developed in the early 20th Century.

Details of the Global Atmospheric Electric Circuit have been discussed in Chapter 1. In the investigations leading to the discovery of this system, the process of point discharge has appeared in several forms. A summary of how point discharge has factored into several of these investigations has been discussed here.

2.1.1 The role of PDCs in Atmospheric Electricity History

Point discharge has been observed for a great many years, primarily through the phenomenon of St Elmo's fire. In the 1st Century BCE, De Bello Africo - attributed to Julius Caesar - described several occurrences of the phenomenon, and in the 1st Century CE, Pliny the Elder describes his understanding of the nature of it [28, 143]. As is also the case for early lightning observations, however, these reports do not consider the electrical nature of the point discharge process, instead attributing it to the work of the gods. The 18th century work of Benjamin Franklin helped to relate the process of lightning to that of electricity, and was a fundamental step towards our current understanding of atmospheric electricity [49]. We will consider later investigations, from the 20th and 21st centuries, where it was well accepted that both point discharge and lightning were electrical processes.

Throughout the early 20th Century, there was disagreement in theories of the charge structure of thunderclouds, championed by two scientists: G.C. Simpson, and C.T.R. Wilson [204]. Simpson believed that the base of thunderclouds carried a net positive charge, with negative charge situated above this, i.e a negative dipole. This argument was driven by observations of charged rain, where a net positive charge was observed to be brought down from the clouds [165]. Wilson on the other hand, believed that the positive charge in thunderclouds was situated towards the top, with negative charge beneath, i.e. a positive dipole. Throughout this dispute, investigations involving point discharge currents played a pivotal role. Several investigations relevant to this topic, featuring both naturally occuring PDC processes and the analysis of PDC sensors will be discussed here.

The observations by Simpson on charged rain found that at the surface, the predominant charge of rain drops from thunderclouds was positive [165]. This suggests that the lower regions of these thunderclouds carry a net positive charge.

In 1921, Wilson reported his findings of an investigation into the electric field during lightning strikes [205]. Wilson found that the electric field changes observed during the majority of lightning strikes were consistent with negative charge being brought from the cloud to the Earth, which he named a "positive discharge" [205]. Wilson made arguments in favour of thunderclouds following a positive dipole structure, based on the relative frequency of these positive discharges. In this report, Wilson addressed Simpson's evidence towards a negative dipole structure from the observations of charged rain, arguing that the arrival of positively charged rain at the Earth's surface did not provide evidence that the rain was positively charged as it left the cloud [205]. Wilson argued that it was possible that some of the positive ions emitted from point discharge processes on the ground caused a reversal of the charge of the rain droplets, causing them to be observed to be positive at the surface, despite being negatively charged at the cloud base [**wilson20**]. Wilson described the leaves of trees and blades of grass as possible sources for these point discharge currents [**wilson20**]. The general upwards flow of positive ions from point discharge processes, along with the negative charges carried downwards from the cloud by the rain would together lead to a negative charge being brought to Earth by the thundercloud. This, along with the positive charge brought to the upper atmosphere, would then be able to maintain the charge separation between the surface and ionosphere, which is lost via the fair weather conduction current. These mechanisms formed the basis of Wilson's model of the global atmospheric electric circuit.

In 1936, Whipple and Scrase reported their results of an investigation into the point discharge data recorded at Kew Observatory [201]. The PDC data used in this investigation was measured using a galvonometer connected to an sharp point on the tip of a tall mast. Whipple and Scrase analysed both the PDC response of the sensor to atmospheric conditions, as will be discussed in section 2.1.2, and several trends recorded by the PDC sensor in a period of continuous observation, which will be discussed here.

Whipple and Scrase observed that there was a diurnal variation in the net outflow of positive discharge currents from the PDC sensor. These diurnal variations were then compared against the diurnal variation of global thunderstorm frequency. It was seen that there was a close relationship between these two variations, which led to the conclusion that there was a physical link between the transfer of charge to the Earth in disturbed weather and the fair weather conduction current. The figure Whipple and Scrase used to compare these diurnal variations has been shown in figure 2.1.

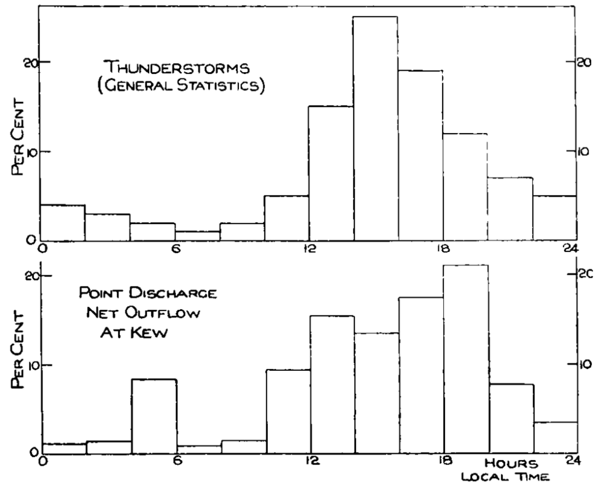

Figure 2.1: Comparison of the diurnal variation in thunderstorm occurrence with the net outflow of point discharge from Kew Observatory. Figure taken from [201].

Whipple and Scrase further went on to compare the diurnal variation in thunderstorm area with the PG data recorded by the ship Carnegie. This data, oft referred to as the "Carnegie curve", showed a diurnal variation in PG dependent on Universal Time, not the local time [68, 70]. Whipple and Scrase found that there was a good agreement between the Carnegie curve and the global thunderstorm area, suggesting that the two were related [201]. This result helped to confirm that disturbed weather regions on Earth were in fact linked to fair weather regions, and has been considered an important milestone in the history of atmospheric electricity: offering confirmation to Wilson's theory of a global atmospheric electric circuit [68].

In order to resolve the dispute over the thundercloud charge structure, it was desired to observe the charge structure in-situ. To obtain this data, Simpson and Scrase [167] developed an instrument able to determine the polarity of the potential gradient as it rose through the atmosphere attached to a balloon. This instrument was named the alti-electrograph, with the mixed Latin and Greek roots of this word being excused as the authors wished to convey the meaning of "height" readily in its name [167]. The device additionally took measurements of pressure and humidity [167].

The alti-electrograph recorded the polarity of the potential gradient of the atmosphere via observations of the PDC occurring at electrodes extending above and below the instrument [167]. It was known that for a long conductor in an electrical field, point discharge will occur such that a conventional current will flow into the conductor at the end where the potential is positive, relative to the conductor, and flow out from the conductor at the end where the potential is negative. As such, the alti-electrograph was constructed such that the electrodes formed a tall vertical conductor and measurements were taken of the polarity of current flowing through the two electrodes. These measurements could then be used to infer the polarity of PG in the atmosphere. The polarity of current was determined by connecting both electrodes to a piece of pole finding paper. As the current flowed between the electrodes, a deposit of prussian blue would be built up at the anode, with no such marking at the cathode. The polarity was able to be determined as a function of time by moving the two electrodes across the paper. Finally, by recovering the alti-electrograph after its sounding, it was possible to compare the polarity data against the pressure data, providing a profile of the polarity with height. Since it was required to recover the instrumentation in order to access the data collected, a system was designed to release the alti-electrograph instrumentation from the balloon, and have it descend to Earth using a parachute [167]. Typically, this separation was set to occur at an altitude of 8-9km, however in some cases this separation did not occur, and measurements were taken even higher than expected. A photograph of the alti-electrograph as shown in the report by Simpson and Scrase has been included in figure 2.2.

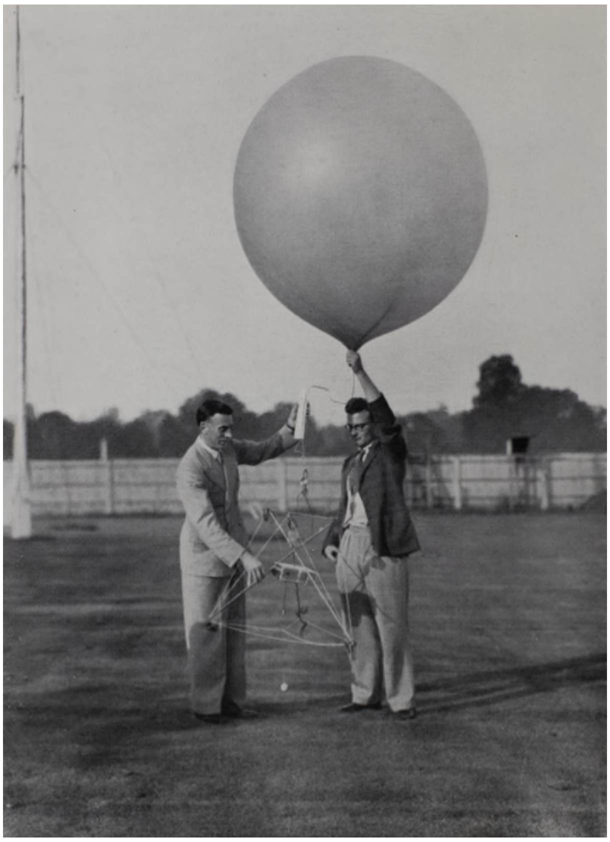

Figure 2.2: Photograph of the alti-electrograph being launched. Figure taken from [167].

The alti-electrograph apparatus described here was used in a number of atmospheric soundings; from July 1934 to October 1936 70 of these soundings were performed, in a range of weather conditions. Through analysis of the typical trends in the data, it was found that the main body of thunderclouds were negatively charged, with the upper region being positively charged. In addition, it was found that frequently there were smaller positively charged regions below the negative region. These findings are in agreement with our modern understanding of thunderstorm charge distributions, where there are two regions of net positive charge, a smaller one at the base and larger one in the upper cloud, with a region of negative charge in between [203]. The experimental evidence that the bulk positive charge in a thundercloud lies above the negative charge provided confirmation of Wilson's model of the global atmospheric electric circuit, supplying a mechanism for the charge separation between the Earth's surface and Ionosphere to continually be regenerated.

Simpson and Scrase showed that there was a smaller region of positive charge at the base of thunderclouds. The findings of the positive dipole above this were well accepted, however the discovery of this lower charge region were initially met with difficulty. In a subsequent paper, Simpson and Robinson [166] discuss the complaints against this finding by re-analysing the data from the original soundings, again finding evidence for this charge region. In addition to this re-analysis, multiple additional soundings using the alti-electrograph were performed. In all of these soundings, the lower positive charge was identified, providing strong evidence for its existence. In these additional soundings, Simpson and Robinson additionally attempted to determine the nature of the charge separation process creating the positive dipole, by comparing the estimated temperature with the charge structure. Through this analysis, it was determined that the centers of the main charge regions were both below 0°C, suggesting that processes involving ice crystals were important to this charge separation [166].

The region of positive charge at the base of thunderclouds is responsible for the production of the positively charged rains which were observed underneath these clouds [165]. In order to explain the presence of positively charged rains, Wilson had made the assertion that the ions emitted by PDC at the surface could cause a reversal of negative charges carried by the rain drops. Given that it is now accepted that these charged rains are positive when leaving the clouds, it is important to note that although these point discharge currents are not required to explain the observed polarity of charged rains, the effects of naturally occurring PDCs are still considered to be important to the flow of charge in the Global Atmospheric Electric Circuit. A number of studies published following the discovery of the tripolar structure of thunder clouds have drawn importance to the effects of these PDCs, with them identified as an important method by which a net negative charge is brought to the Earth's surface from the atmosphere [33, 120, 88].

In addition to these investigations early in the history of the global atmospheric electric circuit, point discharge sensors have been used in a range of other investigations, some of which will be described here.

Following the alti-electrograph soundings of Simpson and Scrase [167], point discharge sensors have been used in a number of further investigations of the electrical structure of thunderclouds. As mentioned previously, the alti-electrograph designed by Simpson and Scrase required the recovery of the instrumentation in order to retrieve the collected data. A subsequent investigation by Belin [16] managed to remove this limitation by modifying a radio-sonde to take point discharge measurements. The radio-sonde would then transmit the data to a reciever on the surface, removing the need to recover the instrumentation.

Later, Chapman [35] used a similar (radio-sonde based) method in order to investigate the electrical structure of thunderclouds further. Chapman used this radio-sonde instrumentation to investigate how the electrical structure of thunderclouds aligns to the temperature profile inside these clouds, since virtually all previous investigations had not measured the temperature and the electric field directly. Additionally, Chapman used these modified radiosondes to investigate the PGs inside blizzards [36]. Through this investigation, Chapman was able to show that the electrification in these snowstorms was not limited to the ground [36].

Recognising the value of these previous studies, Weber and Few developed a similar instrument in 1978 [199]. The authors described such an instrument, using a radio-sonde modified to take point-discharge measurements, as a "corona-sonde". The coronasonde was described as inexpensive, easy to use, and was able to provide quantitative information on the PG inside electrical clouds [199]. Later, in order to ensure the accuracy of this quantitative information, laboratory experiments were performed to understand the influence of several atmospheric parameters - such as temperature, pressure, water vapor content, and wind speed - on the recorded point discharge currents [26]. The utility of the coronasonde instrument meant that it was used in a number of investigations [199, 200, 27]. These investigations helped to further the understanding of the charge structure inside thunderclouds, as well as provide more evidence for the presence of an electrical tripole [199, 200, 27, 203].

Atmospheric soundings using point discharge sensors are not limited to balloon based measurements. On Earth, a point discharge sensor package has been used to take measurements via rocket soundings [153]. Additionally, these sensors can be used onboard spacecraft. The Venera 13 & 14 missions utilised point discharge sensors on board their "groza-2" instrumentation package, taking electrical measurements in the atmosphere of Venus [103]. Little information is available on the specifics of these sensors, however the principal investigator of the instrumentation package, Leonid Ksanformality, confirmed during a personal communication with Lorenz [116] that it contained a point discharge electrode. Additionally, some recent work has been performed to attempt to infer details on the sensor design by logical considerations [173].

Point discharge sensors have some appeal as modern atmospheric electricity sensors. These devices are typically robust and very cheap to produce since they are mechanically simple, with no moving parts. Since these sensors are so robust, they are suitable to be used in conditions which would normally prohibit other atmospheric electricity sensors, such as electric field mills. This advantage is what led to the use of such a sensor onboard a rocket [153]. Another example of this utility is given in a 2016 investigation of the electrical properties of dust devils by Lorenz [119]. In this investigation, an instrument package was deployed in the Chihuahuan desert, and left to collect data for over a month without maintenance [119]. It was found that the point discharge sensors operated well over this period, allowing electrical measurements of dust devils as they passed overhead [119].

Finally, there is an advantage to monitoring when the process of point discharge is present. At the Reading University Atmospheric Observatory (RUAO) in 2016, some anomalous wind speed recordings were made by several anemometers [25]. The source of these anomalies was able to be identified when the data was compared against point discharge readings, also made at the field site. During the times of the anomalous readings, large amounts of point discharge were being observed. This led to the conclusion that the anomalous readings were actually caused by point discharge currents interacting with the data logger system, rather than corresponding to actual data.

In order to utilise PDC sensors effectively as atmospheric electricity instruments, it is important to understand the dependence of the measured current on the atmospheric conditions. Several attempts in the literature to parameterise these sensors will be discussed in the subsequent section.

2.1.2 Parameterising PDC Sensors

It has long been desired to have a relation between the current recorded by a PDC sensor, and the properties of the electrical environment of the sensor. Several attempts have been made throughout the literature to parameterise these sensors in such a way. Oftentimes, both the potential of the PDC sensor, V, and the PG of the atmosphere, F, are used in these parameterisations. Assuming that the PG is constant with height between the point and ground, it is expected that these two quantities should be related to the height of the sensor above the ground, h, via:

$$F = V/h \tag{2.1}$$

For consistency, we will only use the PG in our reproductions of these parameterisations, with terms dependent on the potential converted into PG.

It was also found that many parameterisations were dependent on the minimum PG requried for the point discharge process to occur. In the equations reproduced here, this quantity will be given by the symbol M.

An early attempt to parameterise a PDC sensor was performed by Whipple and Scrase [201]. This investigation involved analysis of PDC data recorded at Kew Observatory, against PG data. Figure 6 from Whipple and Scrase's paper has been reproduced here in figure 2.3, showing the PDC data against the PG data.

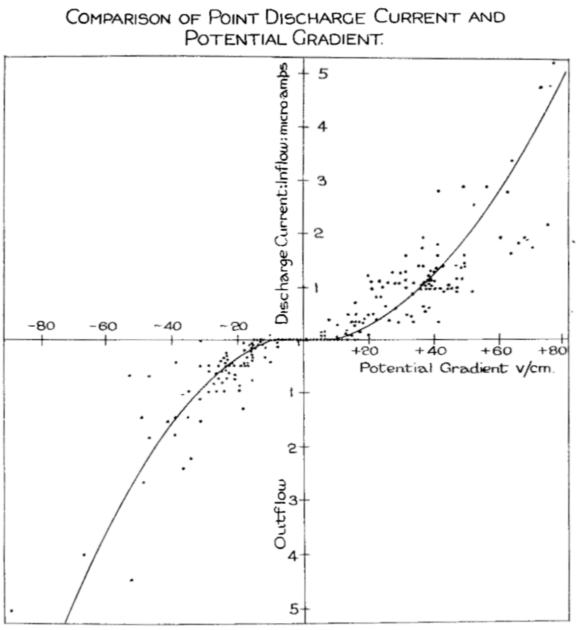

Figure 2.3: PDC vs PG data recorded at Kew Observatory. Figure taken from [201].

From this empirical investigation, a power law relationship between the PG and PDC was identified. This took the form:

$$I = a(F^2 - M^2) \tag{2.2}$$

where a is some constant [201].

Later, Chalmers [30] derived this relationship from theoretical considerations. For this derivation, it was assumed that the point discharge process was limited by the build up of space charges, and that these charges were removed from the vicinity of the sharp point by electrical forces alone.

Chalmers' 1952 derivation made the assumption that wind had a negligible effect on the point discharge process. Note that the literature makes the point that this assumption is not the same as the assumption that the wind speed itself is negligible; the effects of the wind speed on the space charge could also be assumed to be negligible if we are dealing with several PDC sources close together [30, 94]. In this case, as the ions forming the space charge are removed from the vicinity of a given point, the ions from another point's space charge move to replace them. As such, the wind speed does not act to greatly reduce the space charge around a given point.

In the cases where the wind speed is not able to be neglected, the dependence of this parameter on the PDC process is uncertain. Several studies have investigated this relationship, and arrived at various parameterisations for PDC sensors:

In 1955, via theoretical considerations, Chalmers and Mapleton [34] derived an equation for the parameterisation of PDC from an isolated point. This was given by:

$$I = a(hF)^b W^c \tag{2.3}$$

where h is the height of the point above ground, and a, b, c are constants (with theory providing $b + c = 2$). Note that it was identified at the time that since there is no term dependent on M, the minimum PG for PDC to occur, as there is in equation 2.2, then this equation will only be approximately accurate, and will diverge from observations at low PGs. To verify the theoretical equation, Chalmers and Mapleton investigated the PDC detected by a a captive balloon. The data found from this investigation reinforced that the form of equation derived was a valid one.

Several subsequent reports, by a number of authors, cite a report by Chapman [35], crediting it with the form of an additional PDC parameterisation. The present author has been unable to find any extant copy of this report, so is limited in what can be discussed on the report. It would be remiss, however, to skip over it completely, due to the the important role that this parameterisation appears to have played in the development of others. The parameteristation given by Chapman is of the form:

$$I = a(F - M)v_{ion} \tag{2.4}$$

where v_{ion} is the velocity of ions away from the point, either from wind or electric field, depending on the atmospheric conditions.

In 1957 Large and Pierce [108], and Kirkman and Chalmers [94] reported the results from 2 investigations into these sensors. Kirkman and Chalmers' experimental approach involved measuring the PDC at the top of a tall mast, along with the PG and wind speed. The data collected was divided into bins according to wind speed, allowing the effects of wind speed and PG to be investigated separately. It was found that the PDC was dependent on the PG according to:

$$I = a(F - M) \tag{2.5}$$

with the constant a changing across wind speed bins. It was found that there was a linear relationship between the wind speed and the value of a, such that the overall behaviour of the PDC sensor could be described by:

$$I = b(W + c)(F - M) \tag{2.6}$$

The investigation by Large and Pierce [108] took a different approach, with the PDC deployed in the free atmosphere, able to be affected by varying wind speeds, but with an artifical electric field present. This allowed the potential of the point to be regulated, allowing a range of PGs to be investigated during otherwise fair weather.

During low wind conditions, Large and Pierce found that the PDC was given by:

$$I = a(F - M)F \tag{2.7}$$

i.e., it was independent of the wind speed. At larger wind speeds, it was found that there was a linear relationship between the wind speed and the PDC, as was found by Kirkman and Chalmers [94].

Large and Pierce compared the data collected from their investigation against equation 2.4. From a suggestion from J.A. Chalmers, it was assumed that the ion velocity was given by a vector addition of the horizontal wind speed, and some vertical term proportional to the PG - describing the ion drift velocity. So, the term v_{ion} in equation 2.4 is given by:

$$v_{ion} \propto (W^2 + bF^2)^{1/2} \tag{2.8}$$

for some constant b.

Equation 2.4 would then be given by:

$$I = a(F - M)(W^2 + bF^2)^{1/2} \tag{2.9}$$

Large and Pierce found that this equation represented the data well.

Following the investigation by Large and Pierce [108], Chalmers [31] investigated the data from several of these previous investigations, attempting to see if an equation of the form of that in equation 2.4 would fit the data. Data from the investigations of Chalmers and Mapleton [34], Kirkman and Chalmers [94], Large and Pierce [108], and Chapman [35] were investigated. It was found that for each of these datasets, it was required to adjust the parameters a, b, and M, however in all cases, a good fit to equation 2.9 was found. As such, it was accepted that equation 2.9 provided a good parameterisation of PDC sensors, but theory was required in order to understand the meaning of the parameters a, and b.

Chalmers later derived the form of equation 2.9 from theoretical considerations [32]. To derive this equation, two limiting cases were considered, depending on the wind speed relative to the drift velocity of ions in the atmospheric PG. The results from these two limiting cases were then combined, to provide equation 2.9. Since this equation was arrived at via theoretical considerations, it was possible to provide meaning to the constants a, b. According to theory, these should be given by:

$$a = 2\pi\epsilon h \tag{2.10}$$

where ϵ is the permittivity of air and h is the height of the point above ground, and:

$$b = \mu^2 \tag{2.11}$$

where μ is the ion mobility. This derivation allows two of the parameters in equation 2.4 to be predicted by theory. These values are not in exact agreement with those found from other investigations, however.

There are a number of assumptions made in the parameterisations discussed throughout this section. Lab based investigations of the corona discharge process have shown that it is dependent on properties such as the temperature, gas pressure, and atmospheric composition [63, 19]. Typically, at the surface of Earth, there is not a severe change in these properties, however care has to be taken when applying these results in general.

2.1.3 Electrical Effects on the Atmosphere

There are a number of mechanisms by which electric charges and electrical processes can affect the Earth's atmosphere. Several of these mechanisms will be discussed here, in turn.

Lightning is perhaps the most drastic and obvious natural electrical process in Earth's atmosphere. This phenomenon has impacts across a wide range of fields. An obvious impact is the threat to human life caused by lightning strikes [210]. The injury and fatality rates in the caused by lightning strikes in the USA are recorded by NOAA; a report of these rates between 1959 and 1994 showed over 3,000 fatalities and almost 10,000 injuries in this time period [39]. This report described lightning as "the most constant and widespread threat to people and property during the thunderstorm season" [39]. The frequency of lightning strikes in the future is likely to be influenced by the effects of climate change. Currently there is research suggesting that increased temperatures could cause either an increase or a decrease in the global lightning rate [144, 66, 46, 90]. If the rate of lightning strikes does increase, then it follows that the rate of injuries caused by the hazard of lightning will become more frequent as time goes on.

Lightning strikes can additionally have impacts on atmospheric chemistry [122]. The conditions inside the plasma channel of a lightning strike are very high energy, allowing a range of chemical processes to occur [122]. These processes can lead to the creation of a several important chemical species, such as nitrogen oxides and ozone [122]. Additionally, it has been considered that lightning chemistry may have been important to the production of important chemical species in the early Earth, and as such the process of lightning is considered to be a key process in the origin of life on Earth [131, 82]. The enabling of additional chemical processes from atmospheric electricity is not restricted to lightning phenomena; point discharge currents are additionally able to allow other chemical processes to occur. This is often noted in the production of ozone, however it can also allow nitrogen oxides to be produced [10, 151].

Point discharge may also affect populations of airborne particulate matter: The atmospheric ions produced from the point discharge process can reduce the concentration of particulate matter in the atmosphere [92].

Particles, aerosols, and droplets in Earth's atmosphere will be affected by the presence of electric charge. These charges can originate from a number of processes. As mentioned previously, point discharge can be a source for atmospheric ions. Additionally, ionisation throughout the atmosphere can occur from cosmic ray interactions which produce a large number of positive and negative ions [158, 190]. Atmospheric ions can also be produced from radioactive decay [158]. This is typically more prevalent near the surface, where radon concentrations are larger [158]. Atmospheric ions can become attached to aerosols in the atmosphere through processes of ion-aerosol attachment [190].

The charge separation in thunderstorms is described to occur via a two step process [149, 121]: First individual particles become charged. Next, there is a spatial separation of the particles charged to different polarities. The method of charging for the individual particles has previously been unclear, however there is now a growing consensus that it occurs due to collisions between graupel and ice crystals [149]. These collisions lead to an exchange of charge between the graupel and ice crystals, which then become separated spatially due to their differing sizes.

An additional charging mechanism for particles in Earth's atmosphere is tribocharging [78]. This is a collisional process between particles, where differences in composition or particle size will lead to an exchange of charge. The process of tribocharging is important to the electrical charging of dust clouds [119, 78].

Finally, the presence of a global atmospheric electric circuit can also lead to droplets at cloud edges acquiring an increased amount of charge [135, 74, 212, 186]. This effect is driven by the fact that the conductivity inside clouds is significantly lower than the conductivity outside a cloud [135, 212, 186]. The reason for this change in conductivity is the attachment of highly mobile ions to cloud droplets, reducing the mobility of the ions [135, 212, 74]. This reduction in mobility leads to a reduction in atmospheric conductivity. As discussed in chapter 1, in fair weather conditions there is a vertical current flow between the ionosphere and surface of Earth, referred to as the fair weather conduction current. Naturally, if electrically active clouds are present then the conditions are not considered to be fair weather, however stratus clouds can be present in fair weather conditions [135, 74]. If there is broken cloud cover, then the vertical conduction current will flow along the path of least resistance, around the low conductivity clouds [135]. In the case where there is continuous cloud coverage, however, the current is forced to flow through the cloud [135]. This has been shown via analysis of the magnitude of the fair weather current density in different cloud conditions, and during fog [135, 18]. These investigations have shown that although the conductivity of the atmosphere varies in these conditions, the conduction current remains approximately constant. The flow of current through resistive clouds leads to space charge effects at the edges of the cloud.

The space charge at the cloud edges can be described via considerations of Gauss' law and Ohm's Law [212, 74]. Gauss' law provides:

$$\nabla \cdot \mathbf{E} = \frac{\rho}{\epsilon_0} \tag{2.12}$$

for electric field, $\mathbf{E}$, charge density, ρ, and permittivity of free space, ϵ_0. Ohm's law allows the electric field to related to the current density, $\mathbf{J}$, via:

$$\mathbf{J} = \sigma \mathbf{E} \tag{2.13}$$

We consider the current density as that of the fair weather conduction current, i.e.:

$$\mathbf{J} = -J_c \hat{\mathbf{z}} \tag{2.14}$$

where $\hat{\mathbf{z}}$ is a radial unit vector pointed outward from the Earth. Combining equations 2.12, 2.13, and 2.14, we can obtain an equation for the charge density in the atmosphere:

$$\rho = -\epsilon_0 J_c \frac{d}{dz}\left(\frac{1}{\sigma}\right) \tag{2.15}$$

where z is the distance from the surface of the Earth, in the direction of $\hat{\mathbf{z}}$, i.e. the altitude. At the lower edge of the clouds, the resistivity - given by $1/\sigma$ - increases with altitude, z. Thus, from equation 2.15, it can be seen that a negative space charge should be present. Similarly, at the upper edge of the clouds, the resistivity decreases with increasing altitude. Again, considering equation 2.15, it can be seen that a positive space charge should be present. These space charges are illustrated in figure 2.15.

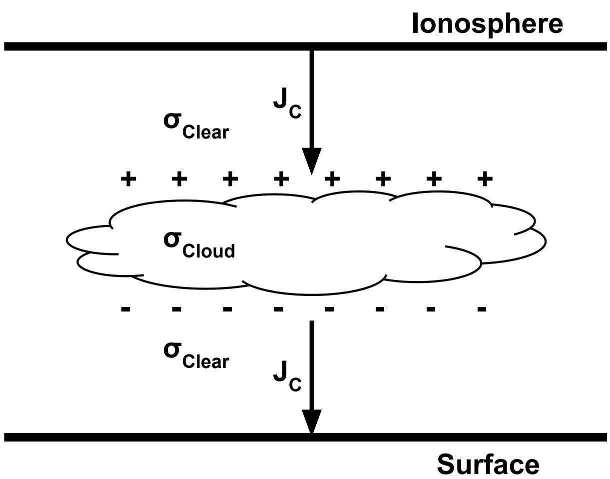

Figure 2.4: Schematic diagram of how the fair weather conduction current leads to cloud edge charging. Figure reproduced from [71].

Several studies have compared the space charges described by equation 2.15 against observations at the cloud edges. Zhou and Tinsley [212] constructed an ionisation model to investigate this, finding average droplet charges of 50-100 elementary charges; these results were shown to be in agreement with previous observations [212, 15]. Nicoll and Harrison [137] investigated the charge densities at cloud edges using a balloon based charge sensor. This investigation found a general agreement between the observations and the theoretical predictions, however some local variability was also observed [137]. It was thus concluded that dynamical processes, such as turbulence and updraughts, play an important role in mixing the space charges within the clouds [137].

The presence of electric charges can affect the stability and growth of cloud particles. The growth of cloud droplets is affected by the evaporation/condensation of vapor, and collisions with other droplets, both of which are affected by the presence of electric charges. The effects of charge on these processes will be discussed here.

As a cloud droplet moves through the atmosphere, it will collide with a number of particles. The collisional efficiency of the cloud droplet is determined by the fraction of particles in the cylinder swept out by this droplet which collide with the droplet [187]. This collisional efficiency is given by the equation:

$$\eta_{Collision} = \frac{y_c^2}{(a_1 + a_2)^2} \tag{2.16}$$

where a_1, a_2 are the radii of the droplet and particle, and y_c is the maximum initial horizontal offset of the particle from the droplet which will lead to a collision [145, 189]. These parameters are shown in figure 2.5. The collision efficiency of a droplet will typically be less than 1, since the flow of air around the droplet will carry particles around it, without resulting in collisions [145]; this effect is also shown in figure 2.5.

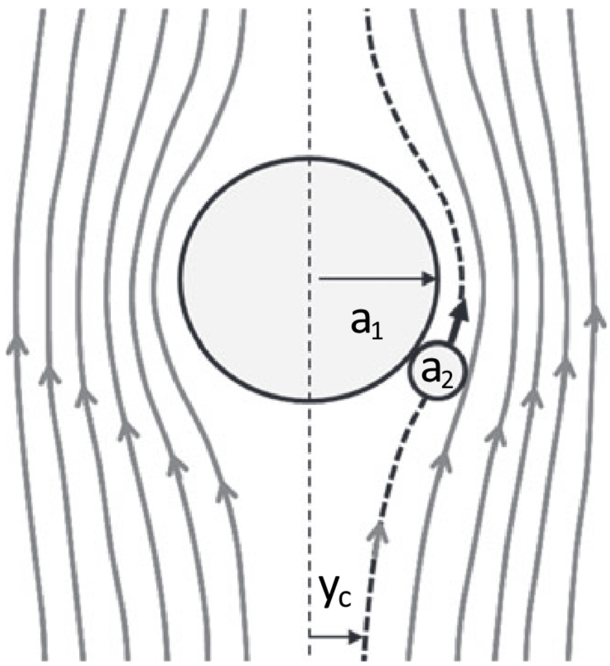

Figure 2.5: Schematic diagram of a collision between a particle and droplet. Grey arrows show the streamlines of air flowing past the droplet. The radius of the droplet and particle are given by a_1, a_2 respectively, while the initial horizontal offset of the droplet from the particle is given by y_c. Figure modified from [74].

Several investigations have modelled the effect that that electrical forces can have on the collision efficiency of droplets. In this modelling, two scenarios are often used: the case where a charged sphere is interacting with a point charge, and where two charged spheres are interacting. In a study by Semonin and Plumlee [162], the collection efficiencies of the collisions between a droplet and particle were calculated, for differing charges on the droplet and particle, and for varying background electric fields. This investigation did not consider the effect of image charges in determinations of the electric forces, and as such found that when there was no background electric field, the collection efficiency was decreased when the droplet and particle were charged with the same polarity.

Later, Grover and Beard [57] investigated the effects on collision efficiency in two regimes; firstly, the charges on the droplet and particle were considered to be point charges in the centre of the objects, and next they were considered to be conducting spheres, with the effects of image charges included. This was performed to investigate under what conditions the assumption of point charges would be valid. It was found that as the Reynolds number decreases, the effects of electric forces will become more important than the fluid flow, and cause the differences between the "point charges" and "conducting spheres" descriptions to be larger. Grover and Beard found that the collision efficiency was significantly improved for droplets and particles with opposing charges.

Many further investigations have studied the collision efficiencies including the effects of image charges. An investigation by Tinsley et al. [187], calculated the collection efficiency of a droplet collecting aerosol particles, with varying charge on the two particles. This investigation found that the collection efficiency was able to be greatly increased by the presence of charge. This increase in efficiency was named "electroscavenging" by the authors. Importantly, Tinsley et al. found that this increase in collection efficiency occurred even if the charges on the droplet and aerosol were the same polarity; showing the importance of these image charges. A subsequent investigation by Tripathi and Harrison [189], found similar evidence of this electroscavenging. This study additionally showed that the charge on the droplet was unimportant, since the attractive force between the droplet and aerosol was due to the image charges induced in the droplet [189].

The process of electroscavenging can have important implications for weather modification [93]. Rain enhancement has been used in certain situations, where there is a need for greater rainfall. Additionally, in many situations, the presence of fog can be a hazard, so it is desired to have a method to clear this fog from particular locations. Electroscavenging can be used to achieve both of these goals. At larger droplet sizes, the main growth mechanism is via collisions. As such, if electrical charges can be introduced to these droplets, their growth rate would be increased. This would result in an increase in the number of rain droplets which are produced, leading to an increased rainfall rate. In fog, the low visibility is caused by a large concentration of small droplets. By encouraging collisions with these droplets, the concentration of small droplets would decrease - leading to an increased visibility.

The viability of using electroscavenging to achieve these goals has been investigated. Khain et al. [93] produced a numerical model to determine if charging some of the droplets in fog/clouds would have beneficial results. This modelling approach found that the collision rate was greatly increased in these conditions, and showed that electroscavenging could be beneficial for these purposes [93].

In addition to the enhancement of collision rates, the presence of electrical charges can affect the microphysics of individual droplets. We will discuss two methods which increase and decrease the stability of these droplets.

The condensation of vapor onto a droplet (or the evaporation of vapor from a droplet) is described by Köhler theory [4]. Köhler theory allows the critical supersaturation of vapor which would cause a droplet to become activated to be calculated [4]. This critical value is important, since it defines the supersaturation which will lead to the onset of droplet growth. For charged droplets, the repulsive electrostatic force between like charges leads to a decrease in the pressure of the droplet [4]. The net result of this is that the critical supersaturation of the droplet is decreased, meaning that droplet activation can occur at lower vapor supersaturations, and that evaporation of vapor from the droplet is inhibited [4, 145]. This is named the Rayleigh effect [4]. Several investigations have investigated the Rayleigh effect on Earth's clouds, concluding that it is able to have a significant impact on the cloud microphysics, particularly when the dissolved salt concentration of the droplet is low [71, 74].

Although the repulsive electrostatic force acts to increase the stability of droplets, if a critical charge is reached then these electrostatic forces may rip the droplet apart. This process has often been referred to as "Rayleigh explosions", following Lord Rayleigh's 1982 investigation [150]. In this work, Rayleigh derived a critical minimum radius for a droplet carrying a charge, Q; under this radius, the droplet would be ripped apart by the electrostatic forces. The critical radius was given by:

$$a_r^3 = \frac{Q^2}{64\pi\epsilon_0\gamma_T} \tag{2.17}$$

where ϵ_0 is the permitivity of free space, and γ_T is the surface tension.

A number of investigations have been performed to investigate this Rayleigh explosion process. Attempts have been made to to capture images of the droplet fission [2]. Additionally, the charge of droplets undergoing Rayligh explosions has been investigated. Investigations performed by Gomez and Tang [54] and Davis and Bridges [40] found that the break up of droplets frequently occured at droplet charges smaller than the Rayleigh limit.

The effects of electric charge on droplet lifetime were investigated by Airey et al [3]. This investigation compared the enhancement of a droplet's lifetime by the Rayleigh effect inhibiting evaporation to the reduction of its lifetime from these Rayleigh explosions. Overall, Airey et al. concluded that the presence of large amounts of charge acted to reduce the droplet lifetimes, through these Rayleigh explosions [3].

The effects of atmospheric electricity on the atmosphere are clearly varied. It should be clear from these effects that understanding the nature of electrification in a planet's atmosphere is of significant importance. Particularly, atmospheric electricity can have varied effects on the microphysics of droplets both in clouds, and in other regions, such as fogs.

2.2 Planetary Atmospheric Electricity

So far, we have only considered studies of atmospheric electricity on Earth. Electrical effects are present in the atmospheres of other planets in our solar system. The field of "planetary atmospheric electricity" describes such effects.

More is known about some of these electrical processes than others. The ubiquitous nature of cosmic rays means that for all planetary atmospheres there will be ionisation to some extent. The amount of ionisation will vary, however, with the magnetic field strength, atmospheric density, and presence or absence of radioisotopes being important factors.

Lightning observations have been made on other planets in our solar systems for many years now [6]. The Voyager missions led to observations of lightning on all of the Jovian planets, via a number of instruments [154]. The observations of lightning here ranged from optical detections, to radio detections, and to the observation of whistler waves [154, 6]. These initial observations of lightning have been confirmed by subsequent investigations, with the Gallileo spacecraft observing lightning on Jupiter and the Cassini spacecraft observing lightning on Saturn [111, 47, 6].

As of yet, lightning has not been observed in Mars' atmosphere, however it is believed to be likely that this process is present there [6, 5]. On Earth, dust devils produce large electric fields, however these fields do not exceed the breakdown field required for lightning [6, 5]. On Mars, the low atmospheric pressure causes a reduction in this breakdown field, and so it is believed that the electric fields created by these dust devils would be sufficient to allow lightning to occur [6, 5, 44].

There have been a number of investigations of lightning on Venus, however there has been no conclusive evidence either for or against the presence of lightning on the planet. Several of these investigations into Venusian lightning are discussed in section 2.3.2.

2.2.1 Extra-Terrestrial Global Atmospheric Electric Circuits

It has been proposed that the concept of a global atmospheric electric circuit may not be unique to Earth, and these systems may also be present on other planets [5, 44]. Several considerations have been made for the requirements of such a system to exist. It has been stated that the minimum requirements would include a conductive ionosphere and surface, a charge generation region, and mobile charge carriers in the atmosphere [5, 44].

The presence of such a system has been investigated for the atmosphere of Mars [45, 41]. It is believed that such a system would be analogous but different to the global atmospheric electric circuit on Earth [45, 41]. Dust storms would create a potential difference between the ionosphere and surface of Mars, much like thunderclouds do on Earth [45]. Again, fair weather regions would complete this circuit, with a vertical conduction current between the ionosphere and surface [45].

The difference between the charging mechanism on Mars versus Earth leads to several differences between the two systems [45]. On Mars, the dust storms believed to be charge generation regions have a strong seasonal dependence [45]. Global dust storms only exist for part of the Martian year, meaning that at other times, the charge generation will occur as a result of smaller dust devil systems [45]. These dust devils would result in a lower amount of charge separation than the global storms, and so a lower potential difference between the ionosphere and surface, and a weaker fair weather conduction current [45].

Additionally, the polarity of the Martian global atmospheric electric circuit is believed to differ from Earth's circuit. As has been discussed previously, thunderstorms on Earth predominantly have a positive dipole; meaning that there is a large positive charge towards the cloud top, with negative charge towards the base [167]. The polarity of this dipole leads to the surface of Earth gaining a net negative charge with respect to the ionosphere. Based on terrestrial understanding, it is believed that the charge generation in Martian dust storms is driven by the process of tribocharging [5, 69]. This process occurs where the collisions of particles with different properties (e.g. size and material) causes an exchange of charge between them [69]. Laboratory studies of the triboelectrification of dust have shown that typically heavier dust grains will acquire a positive charge, while smaller grains acquire a negative charge [45, 69]. It is additionally believed that the convective nature of the dust storms will lead to a vertical separation between particles of different mass; lighter, negatively charged particles will be lofted higher than heavier, positively charged particles [45, 69]. The combined effects of the charging process and separation of particle sizes leads to a separation of charge in the dust storms, which is expected to produce a negative dipole in these storms [45]. Note that this dipole is of the opposite polarity to the dipole on Earth, and as such it is expected that the charge separation between surface and ionosphere will also be opposite to that on Earth [45]. So, the polarity of the vertical electric field and the fair weather conduction current are expected to be inverted in the proposed Martian global atmospheric electric circuit, when compared to the Terrestrial circuit.

Venus has been considered as another planet which may house an extra-terrestrial global atmospheric electric circuit [5]. The following section discusses various comparisons between Venus and the Earth, including a discussion of the atmospheric electric environment of Venus.

2.3 Venus

Venus has oft been described as a "sister" or 'twin" planet to Earth [86]. In this section, we describe several aspects of the planet and atmosphere, and draw comparisons between these properties and those of Earth. Additionally, several attempts to observe lightning in Venus' atmosphere are discussed in section 2.3.2, and an overview of further atmospheric electricity investigations in Venus' atmosphere is given in section 2.3.3.

2.3.1 Overview and Comparison with Earth

Global Properties

The mean distance between the Earth and the Sun is ~150Gm, often stated simply as 1AU [86]. Venus is located closer to the Sun than Earth, at a mean distance of ~0.72AU [86]. This close proximity to the Sun has a number of impacts, such as a different charged particle environment (discussed in section 2.4.2), and a greater incident solar energy flux. As is described by Kepler's third law of planetary motion, Venus' closer orbit to the Sun leads to a shorter orbital period than on Earth, with a Venusian year taking only 224.7 Earth days [86]. Conversely a sidereal day on Venus takes significantly longer than on Earth, at ~243 days [86]. In addition, this is a retrograde rotation, meaning that it is in the opposing direction to that of Earth. Venus is the only planet in our solar system to rotate in such a way. The mass of Venus is comparable to that of Earth, with Venus having a mass of 4.87×10^{24}kg compared to Earth's 5.98×10^{24}kg.

It is also important to note that unlike the Earth, Venus has no intrinsic magnetic field [86]. The impacts of this difference on incident charged particles will be discussed in the section 2.4.2.

Images of the Earth and Venus taken from space have been shown in figure 2.6.

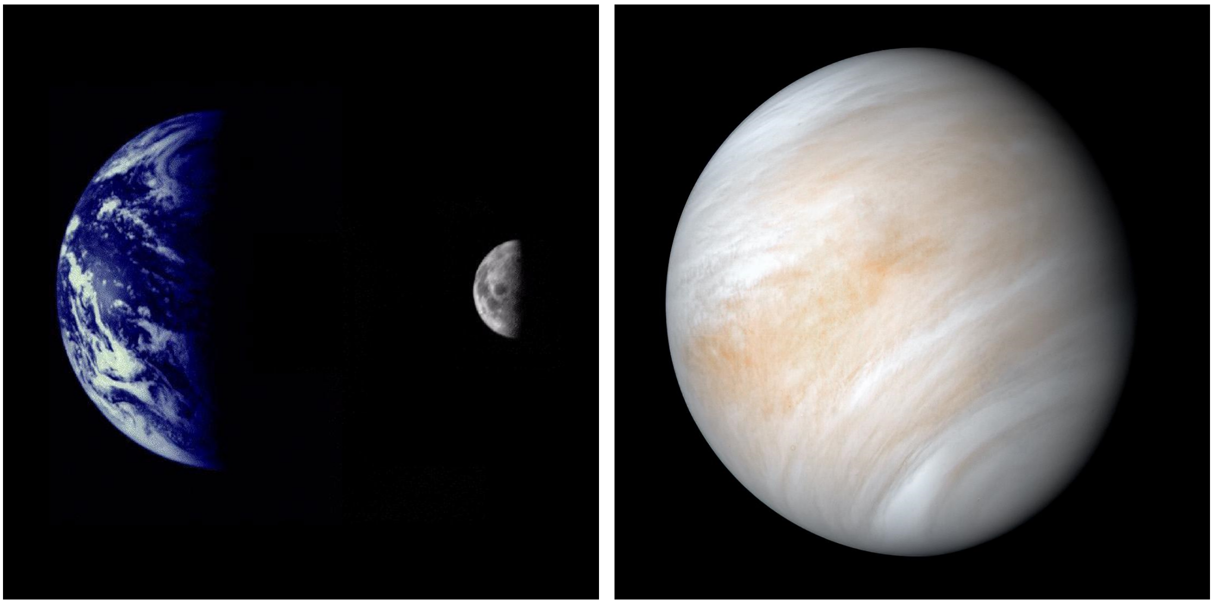

(a) Earth-Moon System

(b) Venus

Figure 2.6: Images of the Earth-Moon system (a) and Venus (b) taken by the Mariner 10 spacecraft. Note that the two images do not show the same scale. Images taken from [126].

Atmospheric Properties

The temperatures at the surface of the Earth vary greatly with factors such as the latitude, season, and local solar time, in addition to the current weather conditions. From reanalysis data, the global mean temperature at surface of the Earth is calculated to be 287-289K, however these temperatures can range greatly across the surface at any given time [164]. The surface pressure on Earth additionally varies with the weather conditions, however the mean sea level pressure is stated to be 101.3 kPa [128].

Relative to the surface temperatures on Earth, the surface of Venus is extremely hot, with an average temperature of 760K. Latitudinal variations in the temperature of the surface are not well constrained by in-situ observations [86, 24]. From the in-situ data available, and from infrared observations made by the Akatsuki spacecraft, it is believed that the latitudinal variation is of the order of magnitude of 1K [86, 24, 170]. Additionally, there is virtually no diurnal variation in temperature at the surface, with any longitudinal variations driven primarily by lithospheric mechanisms [86, 170]. The pressure at the surface of Venus is also significantly greater than on Earth, with pressures reaching 9 MPa [24, 179]. These high pressures, along with the runaway greenhouse effect in Venus' atmosphere, are responsible for the Very high surface temperatures [179].

The atmosphere of Earth is divided into a number of layers according to the temperature [11]. These include the troposphere, stratosphere, mesosphere, and thermosphere [11]. In the troposphere and mesosphere, atmospheric temperature decreases with increasing height, while in the mesosphere and thermosphere the temperature increases.

On Venus, the atmosphere is typically considered in three layers; the lower atmosphere (extending from the surface to the cloud tops), the middle atmosphere (extending from the cloud tops to ∼100km) and the upper atmosphere (extending upwards of ∼100km) [86]. By analogy with Earth, these layers are often named the troposphere, mesosphere, and thermosphere respectively, however they do not share the same temperature characteristics as on Earth [179].

Direct comparisons can be made between the temperature/pressure profiles of Earth and Venus. In figure 2.7, atmospheric profiles of temperature with varying pressure have been shown for both planets.

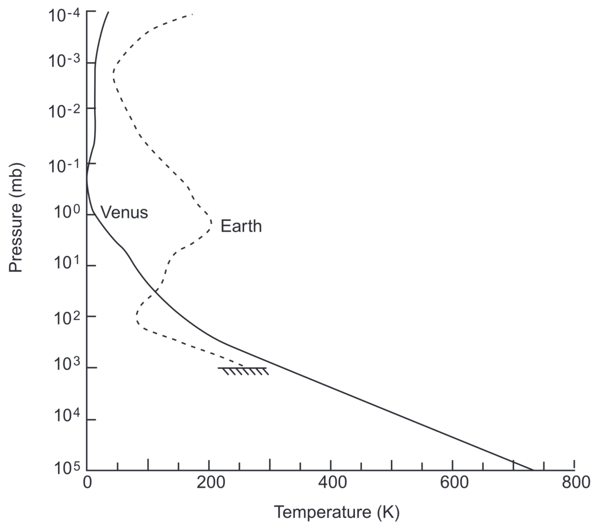

Figure 2.7: Profiles of temperature with pressure for the atmospheres of the Earth and Venus. The surface of the Earth is indicated on the figure. Figure taken from [178]

From figure 2.7 the extreme conditions on the Surface of Venus can be seen, as the profile reaches far greater temperatures and pressures than for Earth. During the overlapping pressure range of the profiles, however, there is a reasonable agreement between the two temperature profiles [178, 179]. The higher temperatures on Earth near to the 1mb level are due to the absorption of UV sunlight in the Earth's ozone layer, which does not have a Venusian analogue [178, 179].

The atmosphere on Earth is primarily composed of a mixture of Nitrogen (∼78%) and oxygen (∼21%) with trace amounts of other gases [11]. On Venus, the atmosphere is primarily carbon dioxide (∼96%) with a small amount of nitrogen (∼3%) and trace amounts of other gases [179]. It is interesting to note that the total abundance of nitrogen in both planets atmospheres' is broadly similar, however the very high amount of CO_2 in Venus' causes the relative abundance to be significantly lesser [179].

Finally, we note that the atmosphere of Venus undergoes "super-rotation"; i.e. the atmosphere rotates faster than the surface of the planet [86, 179]. At an altitude of 10km, typical wind speeds are $\sim$ 10m/s [86]. These speeds increase with altitude, with speeds at the cloud tops reaching over 100 m/s [86, 179]. This corresponds to a rotation period of $\sim$4 Earth days (compare with the 243 days for the surface to rotate) [86, 179]. Above the cloud layer, the wind speeds gradually decrease with altitude.

Clouds

Clouds on Earth are formed of droplets of water. These clouds can be highly variable with time, forming and dissipating readily [128]. In addition, the vertical extent of clouds can be highly variable, varying from tens of metres to the entire height of the troposphere [128]. The clouds on Earth take a number of forms; ranging from highly electrically active cumulonimbus, to high altitude altostratus clouds, and to wispy cirrus clouds [11].

In contrast, Venus is perpetually shrouded by a thick layer of clouds [188]. These clouds are most easily compared with the stratiform clouds on Earth, however differ in the size of particles present [86]. The size distribution of the cloud particles on Venus is considered to be multimodal, with either two or three size modes [86, 188]. These particle sizes are significantly smaller than those of terrestrial clouds, and are more often compared with the aerosols/hazes present on Earth [86, 188]. The clouds on Venus are very tenuous compared to Earth's, which, combined with the low particle size, means that the optical density of Venus' clouds is relatively low [86]. The clouds have a very high optical depth, however, obscuring the surface from outside observation, due to the very large physical extent of the clouds [86]. The main cloud layer on Venus spans between $\sim$45 and $\sim$70km, and is often divided into an upper, middle, and lower cloud layer [86, 188]. The exact composition of the cloud droplets is unknown, however it has been observed that sulphuric acid droplets form a major component [86, 188]. In addition to this main cloud deck, haze layers have been observed above and below the cloud layers. Since they are located above the optically thick cloud layer, the upper hazes are able to be observed ex-situ [86]. The upper haze region spans from the cloud tops at 70km to $\sim$ 90km [86, 188]. Since the lower haze lies beneath the optically thick cloud layer, they have only been able to be observed by a limited number of in-situ investigations [86]. From spectrophotometric observations, it has been identified that there is a haze layer spanning from the lower clouds at $\sim$45km to $\sim$ 30km [86]. The limited observations of this lower haze appear to suggest that this haze is variable, with some evidence found for aerosols down to an altitude of 10km [86, 148]. Spectrophotometric observations from Venera 13 and 14 additionally found a structure at $\sim$ 2km which was interpreted to be a further haze layer [56]. The nephelometer instruments onboard the four Pioneer Venus probes were used to investigate the clouds of Venus [147]. These nephelometer instruments have made some observations of the sub-cloud haze. A prominent feature was present in the data from two of these probes, at an altitude of $\sim$6km [147]. The cloud particle size spectrometer onboard the Pioneer Venus "sounder" probe has also been used to search for sub-cloud haze [98]. This instrument found evidence for a haze layer spanning down to 30km [98].

On Earth, lightning has commonly been observed from the clouds [125]. Additionally, lightning has been observed during volcanic eruptions [125]. On Venus, there is great debate surrounding the presence of lightning of any form in the atmosphere [117]. This topic is further discussed in section 2.3.2.

Recently, interest has been brought to Venus' clouds, through suggestions that they may harbour life [55]. This is a controversial claim, however it does show that further understanding of the clouds on Venus is required.

Surface and Subsurface

The optically thick clouds of Venus conceal the surface from view by ex-situ optical measurements [86, 24, 179]. As such, the conditions on the surface of the planet have been obscured for a great many years, and even now still pose a challenge to investigate [86, 179]. For a great many years, the conditions on the surface of Venus were a complete mystery, however it is known now that the surface of Venus is very hot, dry, and rocky [86, 179]. The most obvious difference between the surface of Venus and that of Earth is the lack of liquid oceans. On Earth, approximately ∼70% of the surface is covered in liquid water, with no analagous feature on Venus [179].

Very few images of the Venusian surface have been taken from in-situ spacecraft. The only spacecraft missions to have achieved such a feat are Venera 9, 10, 13, and 14. Several of the images taken from Venus' surface are shown in figure 2.8. Following a reprocessing of the Venera images, Ksanformality [104] reported the presence of several objects appearing in the images. These objects were initially interpreted to potentially be Venusian flora and fauna, with names such as "scorpion" and "mushroom" given to them [104, 106]. Later investigation has found alternate explanations for these objects, with many explained as being image artefacts [133].

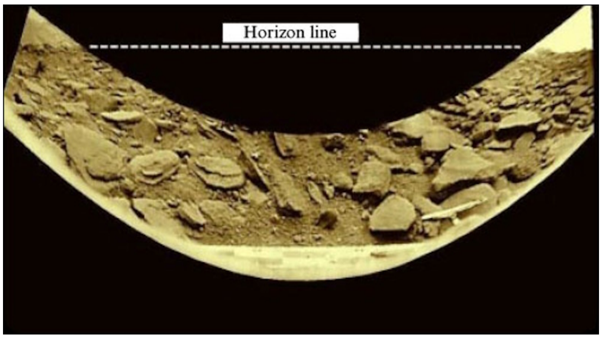

(a) Venera 9

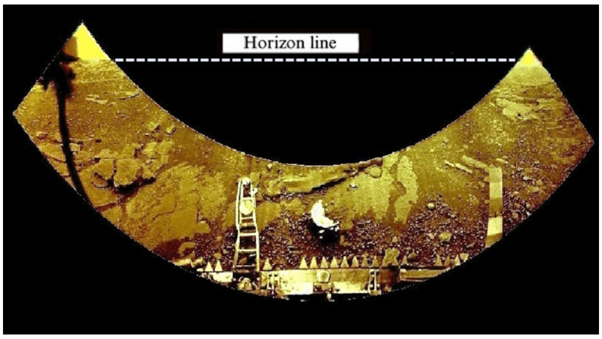

(b) Venera 13

Figure 2.8: Images of Venus' surface taken by the Venera 9 (a) and Venera 13 (b) spacecraft. Images taken from [106].

As on Earth, there is evidence of volcanism on Venus [24, 179]. It is estimated that over one million such volcanoes exist across Venus' surface [179]. Unlike for Earth, however, these volcanoes are not organised into linear chains along tectonic plate boundaries [24, 179]. This difference in volcano clustering is interpreted as being evidence that plate tectonic processes do not currently occur on Venus [24].

The "rock cycle" of a planet is commonly investigated in planetary geology [86]. This cycle considers the balance between fresh rocks being supplied to the surface by volcanic and tectonic processes, and the destruction of these rocks via processes such as erosion and transportation

[86]. It has been reported that the rock cycles of the Earth and Venus vary substantially [86]; the processes driving chemical weathering of these rocks on Venus are significantly different than those on Earth due to the high temperatures and lack of surface water [86, 53]. Meanwhile, the low surface winds and lack of freeze-thaw effects mean that the effects of mechanical weathering also differ greatly on Venus.

The surface of Earth is conductive relative to the atmosphere. Note that this conductive surface with respect to the atmosphere is essential for the global atmospheric electric circuit (described in section 1.3.1) to be formed [158]. On Venus, there is uncertainly in the composition of the surface, however radar studies have made estimates of this [5, 86]. Based on these investigations, it would appear that the surface of Venus is more conductive than its atmosphere, as is the case for Earth [5]. In addition, it is believed that there may be deposits of heavy metals on the surface, which would increase the conductivity further [5].

2.3.2 Venus Lightning

The presence or absence of lightning on Venus has been a very contentious subject [117]. There are a number of investigations which claim to have detected lightning, however none of these have been widely accepted as proof of lightning in the planet's atmosphere. Additionally, several investigations which attempted to observe lightning on Venus have been unable to detect any evidence of it. A number of investigations into observations of lightning on Venus are considered here.

The first optical detections of lightning on Venus occurred via the Venera 9 mission [24]. This spacecraft, along with its twin craft Venera 10, carried spectrometers with a wide field of view [99]. While observing the nightside of Venus, the instrument onboard Venera 9 appeared to detect optical signals of lightning [117]. Krasnopolsky [100] reports that the optical spectrum detected was not significantly affected by Rayleigh extinction, so it could not have been emitted from the lowest 20km of the atmosphere. This rules out volcanism as the lightning source of these detections [100]. The detections of lightning from Venera 9 have been disputed; the Venera 10 spacecraft was unable to detect lightning emission as Venera 9 did, however a similar observation was made "off-disk" [117]. This observation was interpreted to be of the dust trail of a comet, however Lorenz [117] suggests that both this observation, and the Venera 9 lightning observation, may be caused by some spacecraft effect.

To refine the search for optical signatures of lightning, predictions have been made for the emission spectrum of such a process in Venus' atmosphere [21]. In 1983, Borucki et al. [21] published their findings on the spectrum of a laboratory simulation of Venusian lightning strikes. This investigation used a spark-gap to simulate the effects of lightning [21]. It was later reported that this experimental method caused a contamination of the recorded spectrum, as emission from the spark gap electrodes affected the recorded radiation [22]. A further study by Borucki et al. [22] in 1985 considered the spectra from laser induced plasmas in several gas mixtures, allowing the lightning spectra in different planetary atmospheres to be investigated. It was found that this experimental method was able to describe the terrestrial lightning spectrum well, and predictions were made for the lightning spectrum on Venus [22].

Attempts have been made to observe Venusian lightning from the surface of Earth [117]. In particular, we draw attention to an investigation by Hansell et al. [64]. This investigation made use of the 153 cm telescope on Mt. Bigelow, Arizona, which is often referred to as the "61-inch" [64, 117, 184]. This telescope is shown in figure 2.9. To attempt to observe the optical signatures of lightning above the reflected light from the Sun, it was necessary to observe Venus only when the night side dominated observations [64]. In addition, in order to receive the maximal amount of energy from these lightning strikes, it was desired that the distance between Earth and Venus was minimised [64]. These criteria led to a restriction of possible observing times to those near to inferior conjunction (i.e. when Venus passes between the Earth and Sun) [64]. Coronograph optics were utilised to block the light from the dayside portion of Venus [64]. Given knowledge on the expected lightning spectrum from the investigation by Borucki et al. [22], a primary filter was selected at 777.4 nm since this was expected to correspond to a strong lightning emission line for Venus [64].

(a) Observatory Dome (b) Telescope

Figure 2.9: The "61-inch" telescope located on Mt. Bigalow. Images taken from [184]

Observations were taken of the night side of Venus from the 24th of February to the 15th of March 1993 [64]. These observations consisted of 30 pixel × 30 pixel images, with approximate exposure times of 50 ms [64]. Following this, the data was processed to remove effects such as the CCD sensitivity and bias [64]. Further, the images were filtered via a computer program to select images which may show lightning strikes [64]. These images were analysed manually to identify lightning flashes, with a requirement that lightning events had to be detected across more than one pixel [64]. The selection criteria for what was considered a detection has been congratulated by subsequent reviews as being highly rigorous [117, 24]. Across the observation time of this investigation, several events passed the required criteria to be considered an observation of a lightning strike [64].

The Venera 11 & 12 landers included an instrumentation package, "Groza" (translated as "Thunderstorm") [101, 117, 102]. This package featured several instruments designed to observe both lightning and thunder in Venus' atmosphere during the descent of the craft, and from the surface [87, 101]. To measure lightning, the Groza instrument featured a loop antenna, designed to measure radio bursts caused by lightning strikes [87, 24, 103, 102]. During the descents of the spacecraft, both Venera 11 & 12 detected radio signals similar to those detected on Earth from distant thunderstorms [101, 102]. The signals recorded by the Venera 11 lander were suggestive of stronger thunderstorm activity than those recorded by Venera 12 [101, 102]. The two landers had similar trajectories through Venus' atmosphere, at a similar location, but landed several days apart [101, 102]. It was thus concluded that the difference between the data from the two spacecraft was suggestive of a local nature of the electrical activity on Venus [102]. The analysis of this data was performed before the detections of lightning from Venera 9 were analysed, so it is considered that the Venera 11 & 12 instruments were the first detections of lightning on Venus [117].

The instrumentation used on the Venera missions, including the Groza package, was improved upon between the Venera 11 & 12, and 13 & 14 missions [87]. The Venera 13 & 14 landers carried an updated sensor package, "Groza-2", featuring several new instruments including a seismometer and a point discharge sensor [87, 103]. As Venera 13 & 14 descended through Venus' atmosphere, similar results to their predecessors were found [103]. It was reported that the Venera 13 signal showed an electrical storm intensity between those of Venera 11 & 12 [103]. Additionally, it was noted that of the four landers, only Venera 12 recorded a signal while on the surface of Venus [103].

Following the electrical observations of Venera 11, data from the Pioneer Venus orbiter was analysed to search for evidence of lightning [183, 160]. Several impulsive signals were identified from the electric field detector onboard this craft [183]. The impulsive nature of these signals being similar to that of terrestrial lightning signals, and the consistency of the signal propagation with that of whistler waves led to the interpretation of these signals as being evidence of lightning events [183]. Further analysis of this dataset appeared to be consistent with this interpretation, however other authors suggested that other plasma phenomena may be responsible for the observations [160, 159, 182, 181, 180]. As Lorenz [117] describes, this disagreement led to an "extensive debate in the literature".

Further electromagnetic signals were detected from near-Venus space by the Galileo and Venus express missions [62]. The plasma wave instrument onboard the Galileo craft was able to take electric field measurements at a high frequency [62]. During a flyby of Venus, several impulsive events were detected, which were interpreted as "strong evidence" of lightning in Venus' atmosphere [62]. Later, however, in a personal communication with Lorenz [117], the lead investigator of this report stated that they no longer believe that lightning was responsible for this detection, and offered a number of possible origins for the signals. The Venus Express mission was inserted into a high inclination orbit of Venus, where it took measurements with a suite of sensors. It was reported by Russell et al. [155] that the magnetometer onboard Venus Express observed the presence of whistler waves, which was considered by the authors to "resolve" the controversy of the presence of such signals originating from lightning processes. It was noted by Lorenz [117], however, that as for other electromagnetic observations of Venusian lightning, there is an ambiguity in the origin of the detected signals.

The observations of whistler waves in Venus' atmosphere are suggestive of a high flash rate of lightning strikes [52]. This high flash rate does not appear to be in agreement with the relatively uncommon optical observations of lightning strikes [52]. As such, it has been considered if some non-lightning source could be responsible for the generation of these whistler waves. A study by George et al. [52] considered data from the FIELDS instrument on board the parker solar probe (PSP) during a flyby of Venus. The data from this instrument allowed the Poynting vector of a burst of whistler waves to be determined, showing the direction of propagation of these waves [52]. These waves were observed to be travelling planetward, meaning that they could not have originated in the atmosphere of Venus, and so are not generated by lightning [52]. This observation of non-lightning whistler waves in near-Venus space suggests that the high lightning flash rate suggested by previous whistler observations may be an overestimate, as non-lightning whisters will also be included in the detections [52].

In addition to these positive detections of lightning, there have been a number of investigations which attempted to observe lightning on Venus and were unsuccessful. Several such investigations are described here.

As part of the instrumentation in the Groza and Groza-2 packages onboard Venera 11-14, microphones were included in an attempt to observe thunder in the Venusian atmosphere [117, 87]. Unfortunately, no such observations were able to be performed due to the high level of noise [117]. The data from these sensors was able to be used, however, with estimates of the wind speed in Venus' atmosphere made from the ambient noise levels [105, 117].

During the spacecraft Cassini's journey to the Saturnian system, two Venus flybys were performed [61]. These flybys allowed for observations of both the night and dayside of the planet, where a search for lightning was performed [61]. This search used the Radio and Plasma Wave Science instrument onboard Cassini to search for impulsive radio signals caused by lightning strikes [61]. Following these Venus flybys, the Cassini spacecraft additionally performed a flyby of Earth, where a similar investigation was performed [61]. During this Earth flyby, many radio observations were made at a high statistical significance. During the Venus flybys, however, no such observations occurred. As this method had been demonstrated to be an effective search for lightning signals on Earth, the non-detection for Venus carries a high significance. Following this null result, the investigators, Gurnett et al. [61], arrive at the conclusion that "if lightning exists on Venus it is either extremely rare, or very different from terrestrial lightning". This result does not remove the possibility of lightning processes in Venus' atmosphere, only that a process similar to terrestrial lightning did not occur during the period of observation by the Cassini spacecraft [117].

Further, during the Galileo flyby of Venus, several images of Venus' nightside were taken, with no evidence of lightning obtained [17]. This non-detection is significantly less strong than the Cassini non-detections, however, since the observation time was significantly lower [117]. Another investigation with a relatively short observation time was performed using the star scanner instrument onboard Venus express [23]. This investigation was limited in its observation time since the star scanner was often not pointed at Venus, as it was typically used for navigation of the craft [23]. Lightning was not able to be detected above the false alarm rate during this observational period [23].

Following the controversial history of lightning detections on Venus, the Akatsuki spacecraft carried a dedicated optical lightning detection instrument, the “Lightning and Airglow Camera” [118]. This instrument is designed to observe brief flashes at the nightside of Venus, at a wavelength of 777 nm [118]. As of 2019 it was reported that no lightning flashes had been observed in the previous 3 years of deployment, allowing an upper limit on the flash rate to be determined [118]. It was noted that this flash rate was not inconsistent with the observations previously made in the ground based experiments of Hansell et al. [64, 118]. Following this, a single lightning flash may have been observed by Akatsuki, with a publication of these results in pre-print at the time of writing [177].

According to a personal communication reported by Lorenz [117], following the successful optical detections of lightning by Hansell et al. at Mt. Bigelow, an additional attempt was made to observe lightning the following year. This experiment did not result in an observation of lightning, and the null result was not published [117]. Lorenz [117] raises the point that it is likely that many such null-results from optical surveys exist, however there is a tendency to not publish such results.

2.3.3 Venus Atmospheric Electricity

A large number of studies on atmospheric activity on Venus have been focused on investigations of the lightning which may be present there. Despite this, there have been a small number of investigations into other aspects of the electrical environment.

As discussed earlier, it has been proposed that there may be a global atmospheric electric circuit in Venus’ atmosphere [5]. There are several issues with such a proposal, however. Firstly, there is the lack of conclusive evidence for lightning on the planet [5]. Secondly, the dense atmosphere near to the surface of Venus causes the breakdown voltage to be particularly large, inhibiting cloud-ground lightning strikes if lightning did occur on the planet [5]. This removes a mechanism for the surface of Venus to become charged with respect to its ionosphere. As was mentioned in section 2.1, however, it is believed by many that point discharge, not lightning, is the dominant method by which negative charge is brought to Earth’s surface in the terrestrial global atmospheric electric circuit [33, 120]. As such, it is not necessary to have cloud-ground lightning strikes in order to sustain this charge separation. Additionally, there are other possible methods which may be of greater importance on Venus, such as charged rain (or some analogous process). So, we conclude that the presence or absence of lightning does not fully govern the presence of a global atmospheric electric circuit on the planet.

Several attempts have been made to model the electrical environment of Venus. Borucki et al. [20] constructed a model of Venus’ atmosphere, numerically solving a set of ion and electron-aerosol balance equations. From this model, estimates were able to be made of the concentrations of positive ions, negative ions, and electrons, and a conductivity profile of Venus’ atmosphere was produced [20]. Michael et al. [129] produced a similar model, solving the ion and electron-aerosol balance equations via a different method [129]. This model additionally allowed polydisperse aerosol distributions to be used, as opposed to the model by Borucki et al.

which was only able to consider a small number of monodisperse distributions [129, 20]. Both these models broadly agree in their findings, in particular that the concentration of electrons is negligible at low altitudes [129, 20]. No direct observations have been made on the conductivity of Venus' atmosphere, so the modelled conductivities found from these investigations are useful for investigations which require some knowledge of the magnitude of conductivity present.

The presence of nitrogen oxides in the lower atmosphere of Venus has been investigated. A study by Krasnopolsky [100] combined observations with a photochemical model of Venus' atmosphere. The observations revealed the presence of NO in the lower atmosphere of Venus, while the model allowed an estimate for the mixing ratio of this to be obtained [100]. As mentioned previously, on Earth, lightning is a major source of nitrogen oxides in the atmosphere. Further, on Venus, it is the only known source of NO in the lower atmosphere [100]. As such, this investigation provides some indirect investigation of the presence of atmospheric electricity processes in Venus' atmosphere [100].

As mentioned previously, the Groza-2 instrument package on board Venera 13 & 14 featured a point discharge sensor [103]. This sensor was used to measure electrical discharges from the landers in order to ensure that the electrical signals recorded by other instruments were not anomalous readings caused by the electrical discharges [103]. The point discharge readings taken served this purpose, ruling out electrical discharges as the root of these signals [103]. The data recorded by these sensors was not used in any other investigations at the time. Only recently has attention been brought back to the data recorded by these point discharge sensors [116]. In 2018, Lorenz [116] discussed the shape of the point discharge profile recorded by the two spacecraft; for both spacecraft profiles, the discharge currents increase with the spacecraft descent between ∼35km and 15-20km before becoming approximately constant with height until the surface, where the signal reduced to zero. The point discharge profiles that were reproduced by Lorenz are shown in figure 2.10.

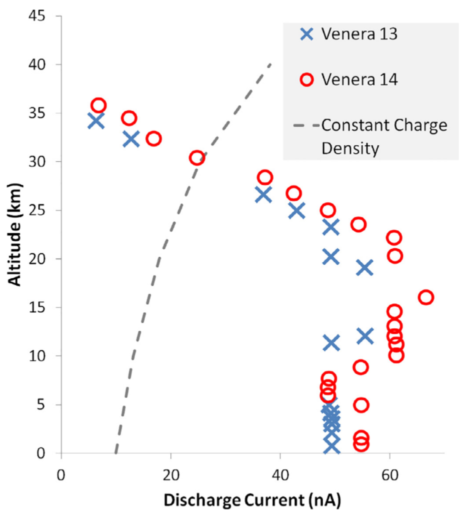

Figure 2.10: Point discharge profiles from Venera 13 & 14 reproduced from [103] by [116]. The point discharge profile predicted by Lorenz [116] for a spacecraft encountering a constant charge density in the atmosphere has been included as a dashed line.

It was noted by Lorenz that the point discharge profiles recorded by the Venera 13 & 14 landers were “essentially the same”, and as such their shape would be controlled by the atmosphere of Venus [116]. Thus, Lorenz considered what factors would control their behaviour, proposing several scenarios. One such scenario was that the spacecraft was collecting charge via collisions with a charged haze layer in the lower atmosphere. Lorenz’ interpretation of the point discharge profile that would be caused by a profile of constant charge density is additionally shown in figure 2.10. Lorenz additionally considered that the point discharge data could be driven by a vertical electric field, caused by a global atmospheric electric circuit on Venus [116]. No firm conclusions on the source of the Venera PDC observations were made by Lorenz, however this paper did bring into consideration this mostly abandoned dataset from the Venera missions.

2.4 Space Weather Effects on Atmospheres

Space weather describes variations to near-Earth (or near-Planet) space. These variations are driven by changes to the Heliospheric Magnetic Field (HMF) and to the cosmic ray environment. Several of these space weather events are driven by coronal mass ejections. These will be discussed first, followed by a discussion of cosmic rays and their effects, and then the impacts of a number of types of space weather event.

2.4.1 Coronal Mass Ejections

Coronal mass ejections (CMEs) are large eruptions of plasma from the Sun [85]. These events have often been observed to occur at the same time as solar flares, however the two phenomena are different and able to occur separately [96, 65]. CMEs can occur from anywhere on the Sun, however are most common at lower latitudes [85]. Once moved away from the sun into the heliosphere, the collection of plasma and magentic field is referred to as an Interplanetary Coronal Mass Ejection (ICME) [85]. These ICMEs are often supersonic with reference to the surrounding solar wind, and so can cause shocks [85].

The majority of these ICMEs emitted are not directed at Earth [85]. ICMEs which do collide with Earth’s atmosphere, however can have notable effects on the Earth’s space weather environment. The magnetic field of the ICME can compress the magnetic field lines, causing an expansion of Earth’s auroral ovals [85]. Additionally, the ICME can lead to an increase in the rate of magnetic reconnection, allowing the Earth to be more exposed to solar wind plasma [85]. These two effects lead to the occurrence of geomagnetic storms [85, 208]. CMEs and ICMEs additionally can affect the count rates of both solar and galactic cosmic rays; These effects will be discussed in several of the subsequent sections.

2.4.2 Observation of Cosmic Rays

The energy distribution differs between solar energetic particles and galactic cosmic rays. GCR tend to have energies between 10^7 eV and 10^{21} eV, while SEPs have energies up to 10^9eV [132]. The energy of cosmic ray particles will affect how they interact with a planet’s atmosphere. At low particle energies, an incident cosmic ray will cause an atmospheric particle to become ionised as it is absorbed by the atmosphere [193, 138]. At higher energies, however, it is possible for the primary cosmic ray to produce a large number of secondary particles in an ionisation cascade

[193, 138]. Additionally, the momenta of incident cosmic rays will affect their interactions with Earth's magnetic field.

The Lorenz force is able to curve the trajectory of a charged particle in the presence of a magnetic field. For charged particles in Earth's magnetic field, this force will act to deflect particles away from the equator. The amount of deflection is related to the rigidity of the particles, defined by:

$$R_B \equiv \frac{p}{|Q|} \tag{2.18}$$

where p is the particle momentum, and Q is the particle charge. Particles with a lower rigidity will be deflected to higher latitudes than high rigidity particles [13, 14]. This leads to an "energy screening" effect, where particles of all energies can reach the poles, but only high energy particles can reach the equator [13].

For surface based observations of cosmic rays, it is possible to observe cosmic rays through the particles produced from their collisions with atmospheric species. A report by Simpson et al. [169] showed that the charged particle component of the secondary particles produced by cosmic ray collisions were typically only dependent on the higher energy particles, with the effects of low energy particles neglected. Simpson et al. argued that in order to monitor variations in the lower energy primary particles, secondary particles which are able to travel to low altitudes should be considered. Additionally, a study by Simpson [168] had shown that observations of the secondary neutrons produced by cosmic ray collisions had a strong latitudinal dependence, compared to charged particles. Since the minimum energy of incident cosmic rays is related to the latitude, it can be seen that the observations of neutrons are sensitive to the particle energies at the rigidity cut-off, rather than just higher energy particles. Following this investigation, a worldwide network of neutron monitors has been produced, to observe variations in the cosmic ray count rate at different rigidity cut-offs [13, 79, 193].

The latitudinal rigidity cut-off of cosmic rays on Earth is dependent on the Earth's intrinsic magnetic field. On planets lacking such a magnetic field, such as Venus, there is no such rigidity cut off, and as such no energy-screening of cosmic ray particles occurs [138]; particles of all energies are able to impinge on the atmosphere of Venus at all latitudes. Additionally, the proximity of Venus to the Sun means that it is exposed to larger SEP fluxes than Earth [138]. These effects, combined with the dense atmosphere of Venus, mean that cosmic rays are able to affect the ionisation in Venus' atmosphere greatly [138]. As such, it is important to consider how this ionisation rate varies, and the consequences of the variances in it.

As has been discussed previously, the ionisation caused by cosmic rays is important to the conductivity of the atmosphere. This conductivity facilitates the fair weather conduction current in Earth's global atmospheric electric circuit. In addition to this, the role that ions play in droplet nucleation has also been studied. Ion induced nucleation is a process where vapor directly condenses onto an ion - i.e. the ion acts as a condensation nucleus [5]. This process could mean that cosmic ray count rates would have a direct impact on cloud formation rates. It has been shown that the process of ion induced nucleation requires a very large supersaturation of vapour to be present, and as such it is not possible naturally in Earth's atmosphere [5]. In the atmospheres of other planets, in particular Uranus, Neptune, and Venus, it is believed that sufficient supersaturations of vapor would exist to allow this process to occur [5]. As such, the variations in cosmic ray count rates are of particular importance to the understanding of the cloud processes in these planets' atmospheres.

Along with their different energies, the different sources of GCRs and SEPs lead to a difference in their arrival rates. SEPs have a very variable emission rate, with solar flares and coronal mass ejections from the Sun causing bursts of particles to be emitted [193]. GCRs, however, arrive at the solar system continuously, and have their arrival rate at the Earth (or Venus) modulated by the heliospheric magnetic field (HMF) and the solar wind [193]. There are several different periodic variations exhibited by the GCR count rate, which will be considered here.

Firstly, the solar cycle affects the cosmic ray count rate. This causes a periodic variation in observed GCR count rate, with ∼11 year period [197, 13]. This periodic variation is anticorrelated to the sunspot number; i.e. the GCR count rate is highest at solar minimum, and lowest at solar maximum. In addition to the ∼11 year periodicity, the full ∼22 year cycle of the Sun's magnetic field can affect the GCR count rate [197, 13]. This causes the peaks of the count rate to differ between subsequent ∼11 year cycles [197, 13].

The GCR count rate additionally varies as a result of Solar rotation [13]. Variations with a period of ∼27 days have been observed in the cosmic ray data recorded at Earth [13]. Any given point on the equator of the Sun will appear to complete a rotation of the Sun every 27 days, as viewed from Earth, meaning that regions of fast solar wind will have a periodicity of ∼27 days from the Earth's observational frame. This periodic variation has been shown to be correlated to the ∼27 day periodic variation occasionally visible in the cosmic ray data [13, 197]. These effects are occasionally described as "Forbush decreases", a term which is also used for a type of space weather event with different origin. This other type of Forbush decrease will be discussed in section 2.4.5. For clarity, the periodic variation caused by the rotation of the Sun will not be referred to as a Forbush decrease in this work.

Finally, it has been observed that there is a ∼1.68 year periodicity present in cosmic ray count rates [194, 152]. It has been shown that this cosmic ray variation shows a close relationship to variations to coronal holes and active regions on the Sun [194]. Intriguingly, unlike the 11 year periodicity, this 1.68 year variation does not exist in the radiative emission from the Sun [67].

2.4.3 Effects of Cosmic Rays

The impacts of cosmic rays on planetary atmospheres has been investigated. As discussed earlier, the ionisation caused by cosmic ray collisions is important to the conductivity of the atmosphere. This conductivity directly affects the magnitude of the fair weather conduction current [76]. As such, this ionisation provides a mechanism for solar effects (impacting cosmic ray count rates) to affect the lower atmosphere (from atmospheric electricity effects) [76].

The connection between the cosmic ray count rate and fair weather conduction current has been investigated. A series of measurements of the conduction currents made at the Lerwick Observatory have been analysed along with cosmic ray data [76]. This analysis showed that there was a statistically significant difference in the conduction current at the cosmic ray minimum (associated with solar maximum) and cosmic ray maximum (associated with solar minimum) [76]. It was observed that at the cosmic ray maximum the conduction current was greater than at the cosmic ray minimum. This is to be expected, since the increased cosmic ray count rate will cause an increase in the ionisation rate, and so an increase in the atmospheric conductivity.

Additionally, investigations have been made on the effects that cosmic rays have on the Earth's clouds. A number of such investigations have identified a correlation between cosmic ray count rates and the global cloud cover, following the 11 year solar cycle [175, 124]. Links have also been made between this variation to cloud cover and variations in the Earth's climate [175, 124, 191]. These results are somewhat controversial, however, with other investigations either not observing the correlation between these variations, or observing that the variations to cloud cover are driven by a different source [107, 91, 43, 113]. As such, care must be taken when considering these effects.

One issue with using the 11 year variation in cosmic ray count rates to investigate the effects of cosmic rays on the atmosphere is that this 11 year variation is also present in other datasets, such as the solar irradiance [67]. This leads to an ambiguity in the cause of any observed variations [67]. To avoid this issue, other variations in the cosmic ray count rate can be investigated. As discussed before, the 1.68 year periodicity in GCRs is not present in the solar irradiance, and so provides an ideal candidate for investigating cosmic ray effects. Additionally, the 27 day periodicities caused by the rotation of the Sun can provide clear variations in the cosmic ray data which can be searched for in other datasets. These two periodicities have been identified in cloud data recorded at Lerwick Observatory in addition to the cosmic ray data, showing some relationship between the cosmic ray variations and Earth's clouds [73, 67].

The effects of cosmic rays have been investigated for other planetary atmospheres. On Uranus and Neptune, the impact of periodicities in the cosmic ray count rate have been investigated [7, 8]. Initially, an 11 year periodic variation in Neptune's brightness was found [7]. Since there is a well known 11 year cycle in charged particle count rates, it was proposed that a source of this periodicity could be from GCR interactions with Neptune [7]. As for the terrestrial investigations, there was an ambiguity in the source of this variation, since the variation was also present in the optical emissions from the Sun. As for Earth, the effects of the $\sim$1.68 year cosmic ray periodicity were investigated. It was found that this periodicity was also present in the brightness data of Neptune, suggesting that there is some cosmic ray effect on the planet's atmosphere present [7].

In addition to this, the brightness data of Neptune was investigated using multiple regression methods for a number of scenarios [7]. These scenarios considered which terms were important in describing Neptune's brightness variations [7]. It was found that the brightness variations of Neptune are best described if both the optical and GCR variations are considered together, with the GCR interacting with Neptune's atmosphere via the process of ion induced nucleation [7]. A similar investigation was performed for Uranus' atmosphere [8]. Again, this investigation found that the variations in Uranus' brightness were best described by an optical effect, along with a GCR effect, driven by ion-induced nucleation [8].

The importance of cosmic rays on Venus have been considered in terms of the ionisation rate. This rate has been modelled by Nordheim et al. [138]. This study considered the ionisation from SEPs and GCR, as well as from ground radioactivity and EUV/Xrays. The ionisation rate profiles found showed that there would be strong amounts of ionisation in the main cloud deck of Venus, with the peak ionisation rate at around 60km. Nordheim et al. considered that there was a high ionisation rate at the altitudes where ion-induced nucleation would be likely, however also mentioned that the ionisation rate was not particularly variable at this altitude, and so the rate of this process is unlikely to fluctuate drastically [138].

2.4.4 SEP Events

Solar energetic particles are charged particles accelerated by energetic energy releases from the Sun [132]. These can include solar flares, coronal mass ejections, and the shocks caused by ICMEs [132, 146]. Bursts of emission of these SEPs are referred to as SEP events. The majority of SEPs are of low energies, and as such do not penetrate far into the atmosphere. As such, satellite based measurements of SEP fluxes are important in determining the number of particles which impinge on the Earth's atmosphere [132].

As for the periodic variations in GCRs, the change of cosmic ray count rate caused by these SEP events can affect the Earth's atmosphere [132]. These effects can take a range of different forms. A number of investigations have noticed chemical changes to the atmosphere caused by these events. Several studies have shown that following SEP events, the concentrations of ozone and nitrogen oxides are significantly impacted [80, 163, 211]. Additionally, an investigation has shown that following a SEP event, the abundance of odd-hydrogen was enhanced [37].

It has additionally been observed that SEP events can impact the fair weather conduction current on Earth [136, 42]. Potential impacts of perturbations to the conduction current have been discussed in the context of cosmic ray variations already.

2.4.5 Forbush Decreases

The movement of an ICME past an observer can impact the observed GCR count rate. Interactions between the ICME and any shocks generated by the ICME are able to cause a reduction in GCR counts lasting for several days [29]. This effect was first observed by Scott E. Forbush, leading to the events being named "Forbush Decreases" [48]. Forbush decreases are typically characterised as a rapid decrease in GCR count rate, followed by a slow exponential recovery [29]. Since CMEs can occur at any time throughout the solar cycle, so can Forbush decreases. These events occur most often at solar maximum, however, with the largest decreases only occurring near to this time [29].

As discussed in section 2.4.3, it can often be difficult to differentiate atmospheric effects caused by cosmic rays from effects caused by other sources such as the radiative emission from the Sun [75]. For Forbush events, however, we observe a rapid change in GCR counts which is not associated with a change in radiative emission [75]. As such, these events can be useful case studies for investigating the atmospheric effects of cosmic ray variations [72, 75]. A number of investigations have used these Forbush events to identify any cosmic ray effects on the Earth's atmosphere.

In an investigation by Harrison and Stephenson [75], the diffuse fraction (related to local cloud cover) was investigated at the times of Forbush events. This analysis was performed by compositing the cosmic ray and diffuse fraction data across all events. This allowed the general trend of cosmic ray data during these events to be observed, along with the trend of the perturbations to the diffuse fraction caused by these events. This method was additionally used later by Harrison and Ambaum [72] in an investigation of the diffuse fraction recorded at Lerwick Observatory. An advantage of this methodology was that it allowed the statistical significance of the perturbation caused by these events to be calculated. In both investigations it was found that the there was a statistically significant (above the 95% confidence limit) decrease in the diffuse fraction, coincident with the Forbush decrease [75, 72].

Although typically detected using neutron detectors on Earth, it is possible to detect Forbush decreases using spacecraft, both near Earth and in other areas of the solar system [112]. A number of observations of Forbush events located away from Earth will be highlighted here. In 1992, Van Allen and Fillius [195] reported observations of Forbush decreases detected by the pioneer 10 and 11 spacecraft, located 53 and 34 AU from the Sun respectively. It was believed that these Forbush decreases were caused by the same ICME, which was also detected by Voyager 1. In 2017, Witasse et al. [207] reported observations of Forbush decreases observed by a number of spacecraft, including MAVEN (at Mars), Rosetta (3.1 AU from the Sun) and Cassini (at Saturn). Again, it was believed that the same ICME was responsible for these decreases, and data from these spacecraft were compared to investigate how these events changed as the ICME propagated away from the Sun. In 2018, Winslow [206] observed Forbush events at Mercury, Earth and Mars, using a range of spacecraft. Again, the changes to the Forbush decrease as it propagated away from the Sun was investigated.

These Forbush events have additionally been observed within the atmosphere of Mars, via the Mars Science Laboratory (MSL) [59]. A number of these Forbush events have been investigated, comparing the data from MSL to that from the MAVEN spacecraft [59]. Additionally, these forbush events have been used to evaluate any risks to human exploration of Mars, from radiation hazards [60].

2.4.6 Heliospheric Current Sheet Crossings

As discussed in Chapter 1, the heliospheric magnetic field typically comprises two regions of field lines - those directed towards the Sun and those directed away - with a current sheet separating these regions. This current sheet is referred to as the Heliospheric Current Sheet (HCS). At solar minimum this current sheet lies predominantly in the ecliptic plane, however its shape becomes more warped towards solar maximum [185, 97]. The shape of the current sheet is not constant with time, instead it fluctuates; passing above and below the ecliptic [142].

As the Sun rotates, the twisted shape of HCS the will sweep past observers in the ecliptic plane. At Earth, a given point passes by approximately every 27 days. At any given time, an observer in the ecliptic plane will typically observe the HMF to point either towards or away from the Sun [139]. As the ripples in the HCS pass by an observer, however, they may pass from one side of the current sheet to the other [97]. This would be observed as a change in polarity of the HMF. These HCS crossings typically happen to Earth every 7-14 days [97, 139]. The polarity of the HMF has important implications for the interactions between the HMF and the magnetosphere of planets, so these HCS crossings will be associated with different behaviours.

In addition to the polarity of the HMF being important, changes caused by the passage of the HCS have also been investigated. It has been documented that as the HCS passes over Earth, changes occur in the cosmic ray environment [185, 209]. Through consideration of neutron monitor data during several of these events, the typical form of this variation has been identified; as a HCS passes, the neutron count rate will increase briefly before decaying to a level lower than before the event [185, 209]. This behaviour has been observed for crossings of either polarity - where the HMF polarity changes from pointing away from the sun to towards the sun, or vice versa. It has been noted, however, that there appears to be a greater impact to the cosmic ray environment for events where the magnetic field changes direction from away from the Sun to towards the Sun [185].

Investigations have been made into the impact that these current sheet crossings have on the atmosphere of Earth. In 2004, Kniveton and Tinsley [97] reported tentative results from their investigation of a number of HCS crossings. This investigation showed that under certain conditions they observed perturbations to the cloud cover of Earth following these crossings [97]. Additionally, investigations have been made on impacts to atmospheric electricity processes. Owens et al. [139] investigated the lightning rates for different HMF polarities. This investigation found that the lightning rate was significantly greater when the HMF was in the towards direction, rather than the away direction [139]. In a subsequent investigation, Owens et al. [140] found that the lightning rate was enhanced at the time of HCS crossings, as well as at the time one solar rotation before and after these crossings.

2.5 Summary

The effects of atmospheric electricity and space weather on a planet's atmosphere are varied, and can be of importance to other atmospheric processes. It is clear that many investigations of Venus' electrical environment have been fixated on the lightning phenomenon, and this has stalled progress into furthering the understanding of other electrical processes on the planet. Following the many successful investigations of Earth's electrical environment using point discharge sensors, it is hoped that analysis of data from several of these sensors will help to further our electrical knowledge of Venus.

Chapter 3

Terrestrial Point Discharge Investigations

Point discharge current (PDC) sensors have been used as atmospheric electricity instruments for many years. These sensors measure the magnitude and polarity of point discharge currents (discussed in chapter 1), produced due to ambient atmospheric conditions. Several key atmospheric electricity investigations utilising such sensors have been discussed in chapter 2. Recently, attention has been brought to the point discharge data recorded in-situ in Venus' atmosphere from the Venera 13 & 14 spacecraft. This dataset is of great interest due to the limited amount of in-situ electrical data which exists for Venus. To understand the physical meaning of this point discharge data, the operation of terrestrial sensors was investigated.

Despite the long history of point discharge sensors as atmospheric electricity instruments, the response of these instruments to atmospheric conditions has not been well understood [120]. Early investigations found that the current recorded by a PDC sensor was strongly dependent on the Potential Gradient (PG) - i.e. the negative of the electric field. These investigations found a power law relationship between the PDC and the PG, of the form:

$$I = a(F^2 - M^2) \tag{3.1}$$

where I is the PDC, F is the PG, and a, M are constants, with M corresponding to the minimum PG required for PDCs to be produced [201, 30].

Later parameterisations have identified the wind speed as an important term in the description of the PDC process. Chalmers [32] derived an equation including the effects of both the PG and wind speed, given by:

$$I = a(F - M)(W^2 - bF^2)^{1/2} \tag{3.2}$$

where W is the wind speed, and b is an additional constant.

In this chapter we will investigate the response of a PDC sensor to atmospheric conditions, using the parameterisations given by equations 3.1 and 3.2 to inform our initial expectations. Additionally, the quality of several parameterisations, including the two provided here, will be investigated.

In section 3.1 the apparatus used for this investigation, along with the required calibration analysis will be described. In section 3.3 the data from a logarithmic PDC sensor will be used to compare variations in the PDC process against variations to the potential gradient. In section 3.4, the data from a linear PDC sensor will be used to investigate several parameterisations of PDC sensors. In section 3.5 the results from sections 3.3 and 3.4 will be discussed, and finally, the conclusions of this work will be described in section 3.6.

3.1 Apparatus

For this investigation, the data collected from several instruments deployed at the Reading University Atmospheric Observatory (RUAO) was used. This field site is in a semi-rural location, at a latitude of 51.44 ° N and longitude of 0.94 ° W. The RUAO site houses a large number of meteorological instruments, with measurements logged at a frequency of 1 Hz. This data is available on the RUAO website at `https://research.reading.ac.uk/meteorology/atmospheric-observatory`. The data from two electrical field mills, two PDC sensors, and a set of three anemometers was used. Images of these instruments in their deployment at the RUAO are shown in figure 3.1.

(a) Electric Field Mills, and PDC sensors

(b) Anemometers

Figure 3.1: Photographs of instruments at the RUAO. (a) shows the electric field mills and PDC sensors which are used in this investigation. From left to right is the Chubb JCI 131 electric field mill, logarithmic PDC sensor, linear PDC sensor, and Campbell Scientific CS110 field mill. (b) shows the set of 3 anemometers which are used in this investigation.

The operation of these sensors, along with preliminary analysis performed on their data, is discussed in the following section.

3.1.1 Electric Field Mills

The Potential Gradient (PG) has been observed at the RUAO since 2004 using a Chubb JCI 131 electric field mill mounted on a 3m mast. This instrument has been set-up to record the PGs typical to fair weather conditions with a high resolution. As such, the sensor has a limited operational range, meaning that it is only able to detect PGs up to a certain magnitude. Often during disturbed weather events, the PG of the atmosphere will be out of range of this sensor, so a reading cannot be taken.

To make up for this shortfall, in March 2024 an additional electric field mill was deployed at the RUAO site. This instrument was a Campbell Scientific CS110 field mill. This is an auto-ranging instrument, able to record PGs across a wide range of values. As such, it is able to record the large PG signals present during disturbed weather events, while also measuring lower magnitudes of PG with a reasonable accuracy. Due to the nature of electric field mills, an additional geometric calibration is often required after deployment, to account for the disruption of the local electric field. Such a calibration was not performed for the deployment of the CS110 field mill, so a similar calibration has been performed as part of the analysis described here.

PG Calibrations

The Chubb JCI 131 instrument has been well calibrated in its deployment at the field site, via comparison against a passive wire electrode. As such, we assume that the PG values recorded are accurate within its operational range. In order to calibrate the Campbell instrument, the recorded data will be compared against that from the JCI instrument. Since the JCI field mill has a relatively small operational range, care must be taken to identify datapoints which lie outside of its range. The data recorded by the two instruments in a several hour, disturbed weather, period is shown in figure 3.2:

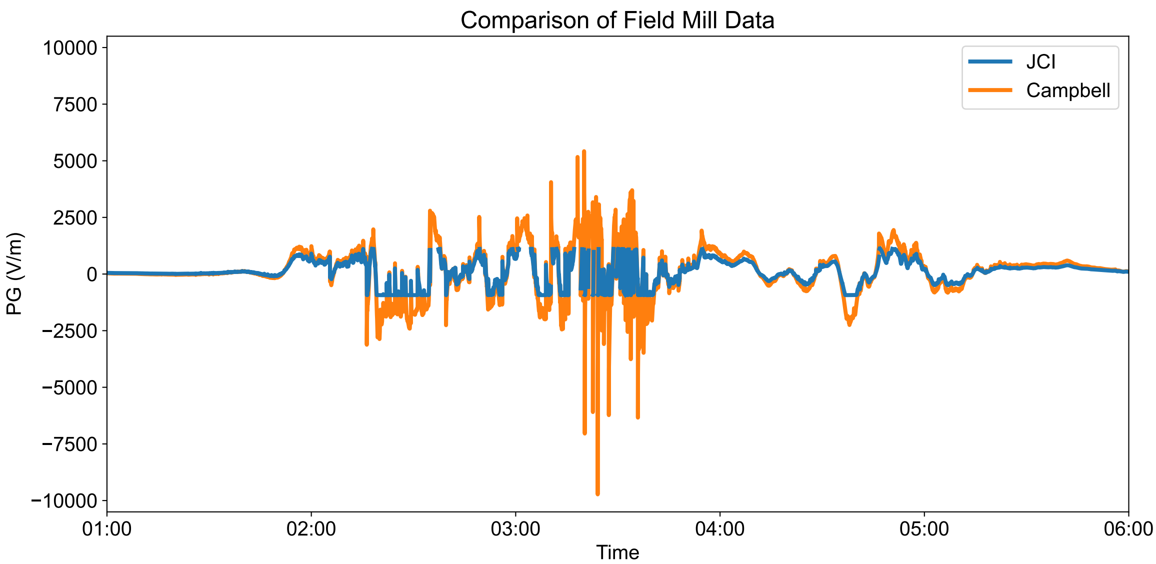

Figure 3.2: Time Series of PG data from two electric field mills in a several hour period. The data from the Chubb JCI 131 field mill is shown in blue, with data from the Campbell CS110 mill is shown in orange.

In figure 3.2, the data from the JCI instrument appears to follow the Campbell instrument within a certain range, but is “clipped” outwith this range. In order to understand the nature of this clipping, a subset of the data will be investigated. Figure 3.3 shows the PG data from the two instruments over a half hour period, along with points showing the NaN (not-a-number) values recorded by the JCI instrument.

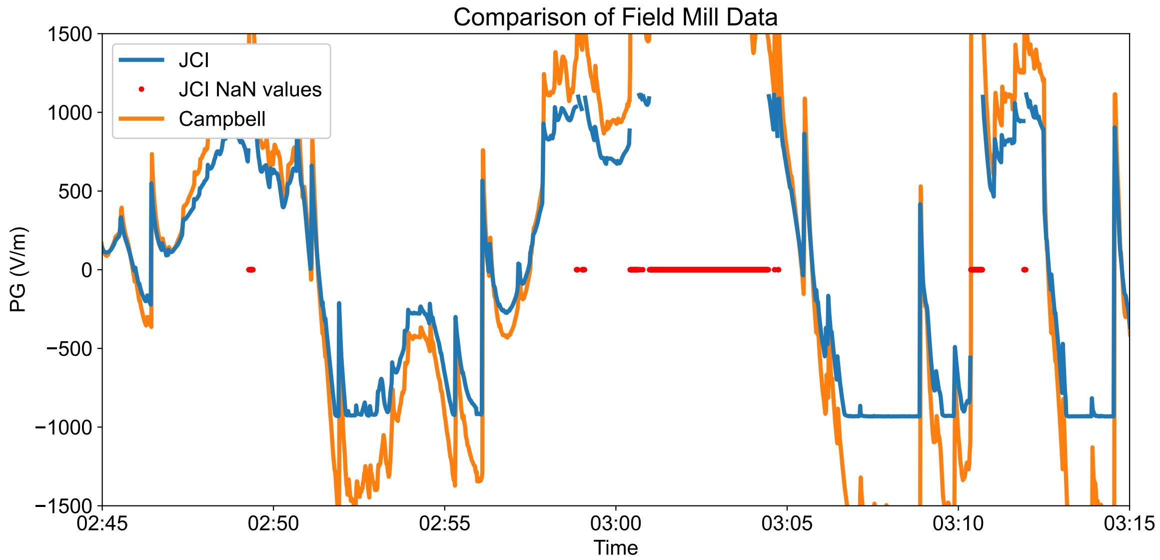

Figure 3.3: Time Series of PG data from two electric field mills in a half hour period. The data from the Chubb JCI 131 field mill is shown in blue, with data from the Campbell CS110 mill shown in orange. Additionally, for each datapoint recorded as a NaN by the JCI instrument, a red dot has been plotted at the time of the datapoint.

From inspection of figure 3.3, it can be inferred that the clipping behaviour is different for different polarities of PG. For positive PGs, it can be seen that the JCI instrument will record a NaN for any datapoints which are outwith its range. this can be clearly seen between 03:00 and 03:05 in figure 3.3. For negative PGs, however, it appears that the JCI instrument instead records some saturation value when the signal becomes clipped. This can be seen in figure 3.3 between 03:05 and 03:10. It should also be noted in figure 3.3 that the time-series of data from the Campbell instrument appears to follow the same shape as the JCI instrument, but is scaled by some factor. This relationship will be investigated, once the range of the JCI sensor has been identified. The value of the maximum PG recordable by the JCI instrument, and the saturation value for minimum PGs will be investigated first.

The data recorded by both instruments over the course of 1 day has been investigated. For demonstration here, the data from the 2nd of May 2024 has been used, as the data from this day is considered further in this investigation. The PG values recorded by the Campbell instrument have been compared against the values recorded by the JCI instrument at the same time, in figure 3.4a.

As can be seen, the majority of the points in figure 3.4a lie along a straight line. Note that the points which lie away from this line are likely due to short timescale perturbations which have been detected by the two sensors at slightly different times. In order to calibrate the sensors, these perturbations will be removed via re-sampling of the data. In the left hand side

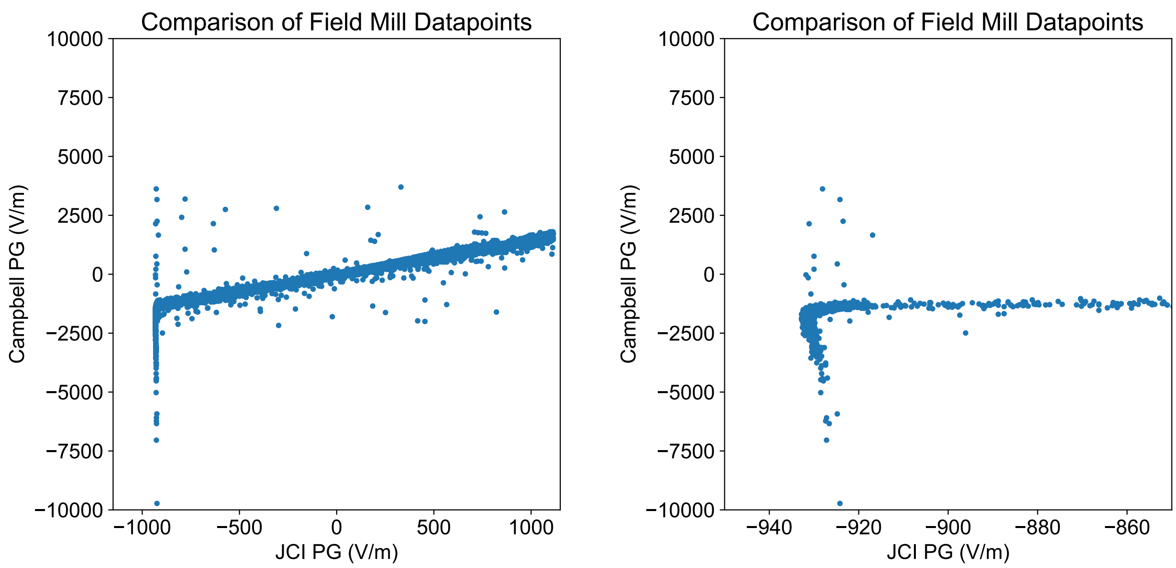

(a) Full x-axis Range

(b) Reduced x-axis Range

Figure 3.4: Comparison of data collected by the JCI field mill to the CS110 field mill. In both figures, results from each field mill have been plotted against each other, with the JCI data on the x-axis and the CS110 data on the y-axis. In (a), the x-axis range was set such that all datapoints are visible. In (b), a reduced x-axis range was used, focusing on the lower end of the JCI data.

of figure 3.4a, there are several datapoints spread across a range of y values, which all appear to have the same x value. From our considerations so far, we would expect this x value to be our saturation value. To investigate this saturation value we focus on a subset of the data, with x values near to this minimum. The PG data in this subset is shown in figure 3.4b.

From figure 3.4b it can be seen that there is not only one saturation value; instead, as the PG exceeds the range of the JCI sensor, the PG recorded by the sensor begins to increase again. As such, we find that there are some values recorded by the JCI instrument which are not uniquely mapped to a single PG input - i.e. it is possible that two different potential gradient values would cause the same reading to be taken by the JCI instrument. Since there is an ambiguity in the PG at these values, we are unable to use these datapoints in our calibration of the two sensors. To remedy this, a lower bound was set for the JCI data, such that datapoints which correspond ambiguously to an input PG are neglected from the dataset. From inspection of figure 3.4b, this lower limit was set at -910 V/m.

Following this, the JCI field mill data was used to calibrate the Campbell data. To remove the short timescale perturbations in the data, the data from both sensors was re-sampled, finding the average PG detected in a 1 minute period. This time averaging was only performed for times where the PG was within the range of the JCI instrument, to ensure that the resulting average was not affected by data points which were not recorded properly. The time averaged data from both sensors has been compared in figure 3.5.

As can be seen in figure 3.5, there appears to be a linear relationship between the data from the two sensors, as should be expected. This relationship is of the form:

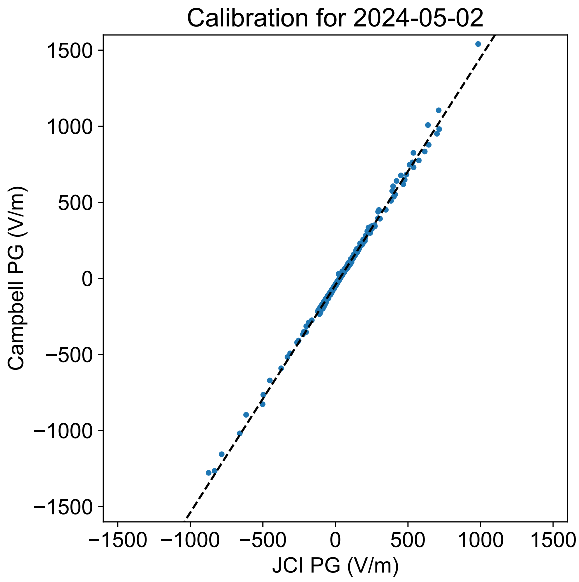

Figure 3.5: Calibration line for the JCI and CS110 field mills on a selected day (2nd May 2024). The PG data,time averaged in 1 minute periods, from both sensors has been compared. Error bars for these time-averages have been neglected for visibility, due to their small size. A linear fit has been performed on this data, indicated by a black dashed line.

$$F_{Campbell} = m \times F_{JCI} + c \tag{3.3}$$

where m and c are some constants. Through least squares fitting, these constants were determined to be 1.51 $\pm$ 0.01 and -47.5 $\pm$ 0.5 V/m for m and c respectively for the data from 02/05/24.

Following this calibration procedure, the data from the Campbell instrument was used when available due to its large operational range being advantageous. Data from the JCI instrument was used when data from the Campbell instrument was not available.

3.1.2 Logarithmic PDC Sensor

A logarithmic PDC sensor was deployed at the observatory, also on a 3m mast. A brief evaluation of this sensor has previously been reported by Marlton et al [123]. Such a sensor has a voltage response which is proportional to the logarithm of the point discharge current. This response is advantageous, since it allows a wide range of currents to be observed, spanning across several orders of magnitude.

The logarithmic point discharge sensor used in this investigation consisted of a logarithmic electrometer attached to an upwards pointing tapestry needle, used to enhance the atmospheric electric field. A close up image of this sensor is shown in figure 3.6, in which this needle is visible. The logarithmic electrometer utilised an operational amplifier (op-amp) in an inverting-amplifier configuration, with an arrangement of LEDs used as a feedback resistor. The nature of these feedback LEDs was such that the output voltage from the amplifier was proportional to the logarithm of the input current. The electrometer circuit additionally included a temperature

Figure 3.6: Close up image of the logarithmic PDC sensor deployed at the RUAO.

compensation circuit, to account for changes in the ambient temperature, and a polarity switching circuit, which allowed both polarities of input current to be recorded. Since this electrometer converted the input point discharge current into a voltage proportional to the logarithm of this current, it allowed point discharge currents to be measured across several orders of magnitude.

The logarithmic PDC sensor has been deployed at the RUAO site since 2012, however the sensor has been adjusted and re-calibrated several times in that period. The dates of the initial deployment and recalibrations have been summarised in table 3.1:

Sensor Status	Date
Initial deployment/calibration	14/01/2012
Re-calibration	$\sim$ 2015
Sensor removed from deployment	17/04/18
Sensor re-calibrated and returned to site	11/02/20

Table 3.1: Summary of the operation of the logarithmic PDC sensor operating at the RUAO. The dates of each known calibration of the sensor have been listed.

For this investigation, we have investigated the data from the most recent calibration of the sensor, in 2020. Since this calibration, the relationship between the logged voltage and the input current was given by:

$$I = -10^{(-8.023 \times V - 4.831)} \tag{3.4}$$

for positive currents/voltages, and

$$I = 10^{(8.282 \times V - 4.632)} \tag{3.5}$$

for negative currents/voltages, where I, V are in Amps and Volts respectively.

The convention that we will use in this chapter is that a positive current corresponds to a positive conventional current flowing into the sensor.

3.1.3 Linear PDC Sensor

Recently, an additional PDC sensor has been deployed at the RUAO site. This sensor was of a simpler design to the logarithmic sensor, providing a linear response between the input current and the logged voltage. Due to the linear response, a polarity switching circuit was not required for both polarities of current to be logged. As for the logarithmic sensor, a upwards pointing tapestry needle (of the same approximate size) was used in order to enhance the atmospheric electric field. Again, this sensor was mounted on a 3m mast, nearby to the other atmospheric electricity sensors.

As for the logarithmic sensor, we use the convention that a positive current corresponds to a positive conventional current flowing into the sensor.

3.1.4 Anemometers

Several anemometers are deployed at the RUAO site, providing a range of information on the wind speed. For this investigation, the data collected by a set of 3 orthogonal propeller anemometers was used. Two of these sensors measured the horizontal wind speed in orthogonal directions, with the third measuring the vertical wind speed. These anemometers were positioned 3m off of the ground, allowing for the wind speed at the height of the PDC sensors to be measured directly.

The PDC parameterisations investigated in this study are dependent on the magnitude of the horizontal wind speed. This was calculated from the recorded wind speed from the two horizontal sensors, using equation 3.6:

$$W = \sqrt{W_u^2 + W_v^2} \tag{3.6}$$

where W is the horizontal wind speed, and W_u and W_v are the wind speeds in two orthogonal horizontal directions.

3.2 Methodology

The data from the two point discharge sensors deployed at the RUAO site will be analysed in different ways.

An advantage of the logarithmic sensor was that it was able to measure discharge currents over a wide range of magnitudes. As such, the sensor is able to detect the faint currents present at low PGs. We will use this property to investigate a time series of the PDC, and how it compares to the time series of the PG at the same time. This allows us to compare the timing of variations between the two sensors. This investigation is described in section 3.3. The work described here has been published as a peer reviewed conference paper [127].

The large operational range of this logarithmic sensor allows various point discharge processes, occurring at different magnitudes, to be observed. It has previously been reported that the behaviour of point discharge will be varied for different magnitudes of current [115]. As such, we find that this sensor, which is able to observe a wide range of magnitudes, is not ideally suited to an investigation into parameterising the PDC process.

To develop a parameterisation of the PDC process, the data from the linear PDC sensor will instead be considered. In this investigation, we will compare the PDCs recorded by the sensor against the atmospheric conditions, namely the PG and Wind speed. Through doing this, we will evaluate the quality of several different parameterisations for the sensor.

3.3 Logarithmic PDC Investigation

The parameterisations of PDC sensors given by equations 3.1 and 3.2 both show that the PDC should be proportional to the PG. As such, we would expect that any variations in the PG would be coincident with changes to the PDC recorded. We will investigate the timings of these variations, for a subset of the PDC data. For this investigation a 15 minute period on the 1st of March 2020 was used.

3.3.1 PDC Timeseries

The PDC data has been shown as a timeseries in figure 3.7. Since the PDC is varying over several orders of magnitude, a log y axis was desired. However, both positive and negative currents were being considered, so this would require separate plots for these different polarities. Instead, a symmetric log y axis was used, with linear scale between -10^{-15} and 10^{-15} A. This allowed a wide range of magnitudes of current to be visible, while also allowing both polarities to be shown on the same figure.

It was observed that the PDC data varied at a high frequency, often changing polarity between one datapoint and the next. This high frequency variation made it difficult to identify features in the PDC timeseries. To remedy this, the data was resampled at a frequency of 0.2 Hz by finding the mean PDC value across a range of 5s bins. This allowed the high frequency variation to be removed.

3.3.2 PG Timeseries

Next, the timeseries of the PDC data was compared against a time series of the PG data. The time series of the two datasets are shown on the same axes in figure 3.8. Symmetric log axes have been used for both datasets, with linear range between -1×10^{-12} and 1×10^{-12} A for the PDC data, and -10 and 10 V/m for the PG.

From inspection of figure 3.8, it can be seen that the time series for the PDC and PG do not appear perfectly aligned in time; at several points, changes to the PDC time series appear to precede changes to the PG. To investigate this apparent misalignment in time, key features were compared between the two time series. The times when each time series crossed the x-axis

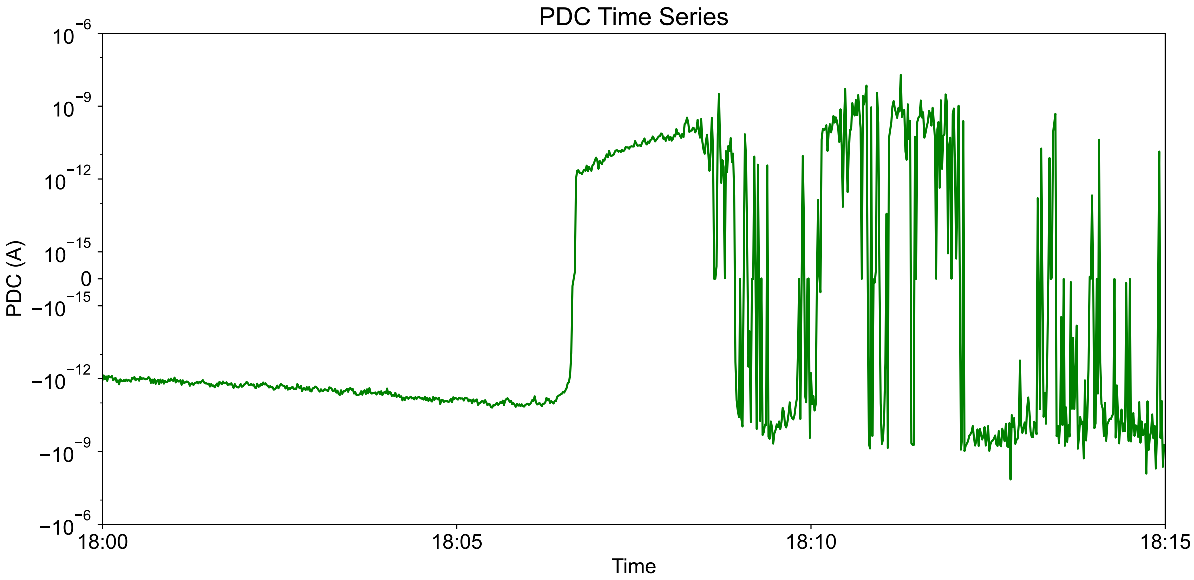

Figure 3.7: Time series of the PDC data recorded by the logarithmic PDC sensor in a 15 minute period. A symmetric logarithmic y-axis was used, with a linear range between $\pm$ 1fA.

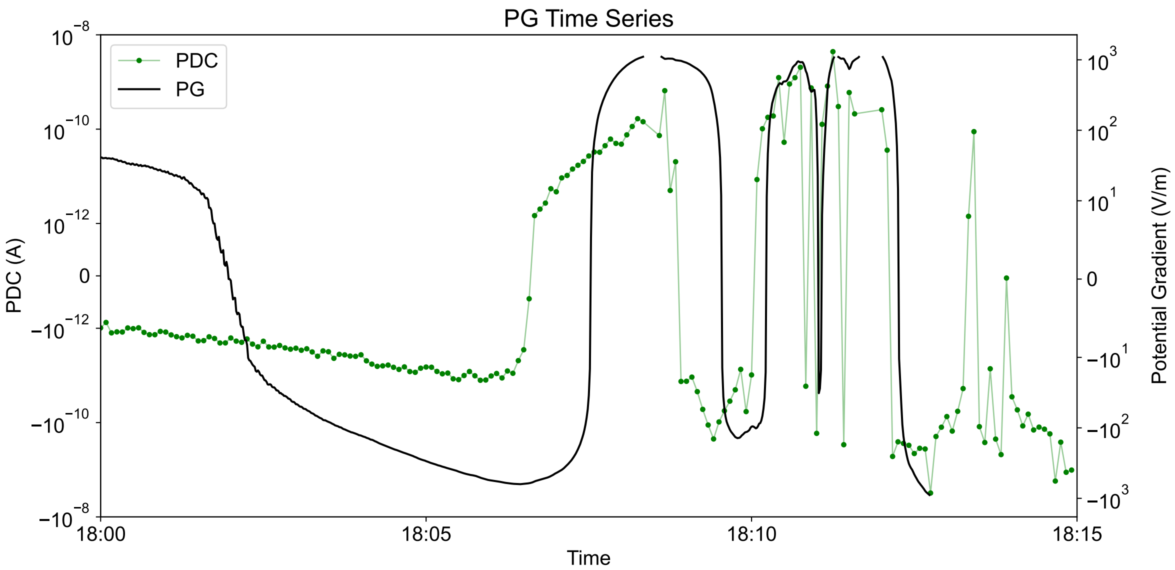

Figure 3.8: Time series of PDC data (green) and PG data (black) on the same x-axis. For both time series, symmetric y axes were used, with a linear range between $\pm$1pA for the PDC, and $\pm$10 V/m for the PG.

were selected as the features to compare, since these should occur at the same time according to both of the parameterisations given by equations 3.1 and 3.2.

To compare the timing of the x-axis crossings between these two datasets, first the axis crossings for the PDC time series were found. This was performed by locating any datapoints which had a different polarity to the previous datapoint, and finding the midpoint between the two datapoints. Note that due to the 0.2 Hz sampling rate being used, the exact time of the axis crossing is uncertain within $\pm$2.5s of this identified time. In order to ensure that we are considering easily identifiable features, we have considered a subset of these axis crossings, where the polarity of the PDC data is constant for 15s on either side of the axis crossing. For the dataset considered here, 4 such axis crossings were selected. These will be used for the analysis in this section.

Next, we wish to compare these axis crossings with the corresponding features from the PG time series. As for the PDC data, axis crossings were identified by finding the times where the polarity of the PG signal changes sign. As for the PDC crossings, the time of these axis crossings will carry some uncertainty, however since the PG data is sampled at 1 Hz, this uncertainty range will be $\pm$ 0.5s.

Next, for each axis crossing in the PDC dataset, the nearest axis crossing in the PG dataset was identified. The time difference between each of these crossings, and the corresponding crossing for the PDC data was calculated via equation 3.7

$$\tau = t_{PG} - t_{PDC} \tag{3.7}$$

where t_{PG} and t_{PDC} are the times of the x-axis crossings for the PG and PDC profiles respectively. The time offsets calculated from equation 3.7 are shown in table 3.2.

PDC & PG

Axis Crossing №	1	2	3	4
Time Offset (s)	54 $\pm$ 3	40 $\pm$ 3	11 $\pm$ 3	8 $\pm$ 3

Table 3.2: Time differences between several x-axis crossings in the PDC data and the corresponding axis crossings in the PG data. Positive values represent the axis crossing occurring in the PDC data before occurring in the PG data, with negative values representing the axis crossing occurring in the PG data before the PDC data. The uncertainty in each time difference has been quoted.

Note that due to the sampling uncertainties of the two datasets, an uncertainty of $\pm$ 3s is assumed on these values. This uncertainty is given by the sum of the uncertainties from the two datasets, rather than performing traditional error propagation, since these uncertainties are not Gaussian in nature.

The results shown in table 3.2 agree with the observations found from inspection of the two time series; the x-axis crossings of the PG trace lag behind the crossings for the PDC trace by a considerable time. The Root Mean Squared Error (RMSE) for these offsets has also been calculated, giving a value of 34s.

3.3.3 Timeseries of Rate of Change of PG

To understand why there is a time offset between the two time series in figure 3.8, the theoretical assumptions behind previous parameterisations of PDC sensors were considered. These parameterisations only described electrostatic dependencies, neglecting any electrodynamical effects which influence the recorded discharge current. As such, we consider if these electrodynamic effects could be important.

One well known electrodynamical effect is the electric displacement current (also known as Maxwell current). The Maxwell current, I_D, crossing a surface S is given by equation 3.8:

$$I_D = \iint_S \epsilon \frac{\partial \mathbf{E}}{\partial t} \cdot dS \tag{3.8}$$

where ϵ is the permittivity, S is the area of the surface, and $\partial E/\partial t$ is the rate of change of electric field with respect to time. To be consistent with our sign convention for the discharge currents, discussed in section 3.1, the Maxwell current flowing into the PDC sensor will be given by:

$$I_D = A\epsilon \frac{dF}{dt} \tag{3.9}$$

where A is a constant, dependent on the geometry of the sensor.

To explore if an electrodynamical effect, such as the Maxwell current may be important, the rate of change of PG was compared against the PDC, as shown in figure 3.9. Symmetric log y-axes were once again used, with a linear region between -10 and 10 V/sm for the rate of change of PG.

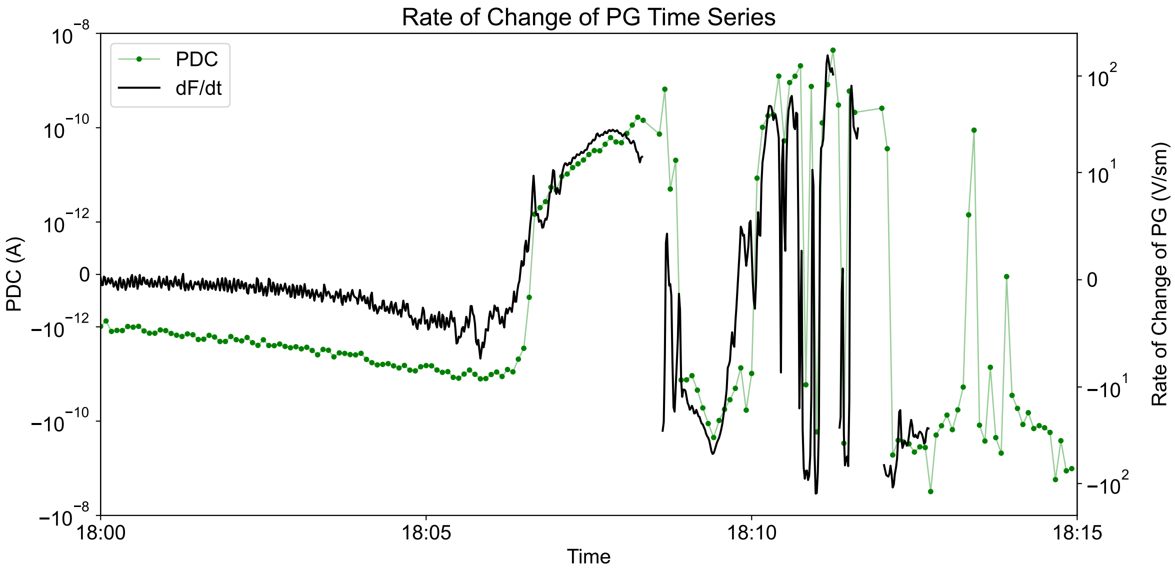

Figure 3.9: Time series of PDC data (green) and the rate of change of the PG (black) on the same x-axis. For both time series, symmetric y axes were used, with a linear range between $\pm$1pA for the PDC, and $\pm$10 V/sm for the PG.

From inspection of figure 3.9, the shape of the two time series appear significantly closer than for figure 3.8. It now appears, however, that changes to the PDC data are succeeding changes to the rate of change of PG. As before, in order to investigate this effect, the locations of axis crossings were investigated.

As was done previously, the location of the x-axis crossings in the rate of change of PG profile which are closest to the crossings for the PDC profile were identified. The time difference between these crossings and the PDC crossings are shown in table 3.3:

Note that the large error in the offset for axis crossing 4 is due to a lack of data in the relevant time period, caused by the PG being out of the range of the electric field mill.

It can be seen that for all of these axis crossings, the time offset is negative, showing that

PDC & dF/dt

Axis Crossing №	1	2	3	4
Time Offset (s)	-11 ± 3	-9 ± 3	-2 ± 3	-17.5 ± 14.5

Table 3.3: Time differences between several x-axis crossings in the PDC data and the corresponding axis crossings in the rate of change of the PG. Positive values represent the axis crossing occurring in the PDC data before occurring in the rate of change of PG data, with negative values representing the axis crossing occurring in the rate of change of PG data before the PDC data. The uncertainty in each time difference has been quoted.

the PDC axis crossings are occurring after the rate of change of PG. The RMSE calculated for these crossings was 11s, however, which was a marked improvement over the result for the PG timeseries.

3.3.4 Combined Fit

It was found that the axis crossings from the electrostatic PG data were preceding those in the PDC data, while the crossings from the electrodynamic rate of change of PG were succeeding them. As such, it was proposed that the best description of the PDC data may arise from a combination of both electrostatic and electrodynamic terms. To investigate this, a fit to the PDC data was considered of the form:

$$I = f(F) + g\left(\frac{\partial F}{\partial t}\right) \tag{3.10}$$

where I is the point discharge current, F is the potential gradient, $\partial F/\partial t$ is the rate of change of PG with respect to time, and f and g are functions describing electrostatic and electrodynamic behaviours respectively.

Simple functions for f and g were selected for this investigation, according to equations 3.11 and 3.12:

$$f(F) = aF \tag{3.11}$$

$$g\left(\frac{\partial F}{\partial t}\right) = b\frac{\partial F}{\partial t} \tag{3.12}$$

where a and b are some constants. It should be noted that the effects of wind speed have been neglected from the electrostatic term in equation 3.11. It is likely that including the wind speed could allow a better fit to the data, however, this would necessitate multiple terms being included in the fit, increasing its complexity.

The optimal parameters for the parameters a, b in equations 3.11 & 3.12 were determined using least squares minimisation. Initially, the value of the ratio a/b was fit for by considering the x-axis crossings, as has been done for the PG and rate of change of PG in this section. The value of a/b which minimised the RMSE between the axis crossings for the PDC data and the fit from equation 3.10 was determined. Next, the optimal value of a (and therefore b) was determined by minimising the RMSE between the value of the PDC and the fitted PDC across the entire dataset. This process yielded optimal values for a and b as 1.19 $\times 10^{-14}$ Am/V and

1.15×10^{-12} Asm/V respectively. The time series of the modelled PDC using these parameters has been compared against the time series for the PDC data in figure 3.10.

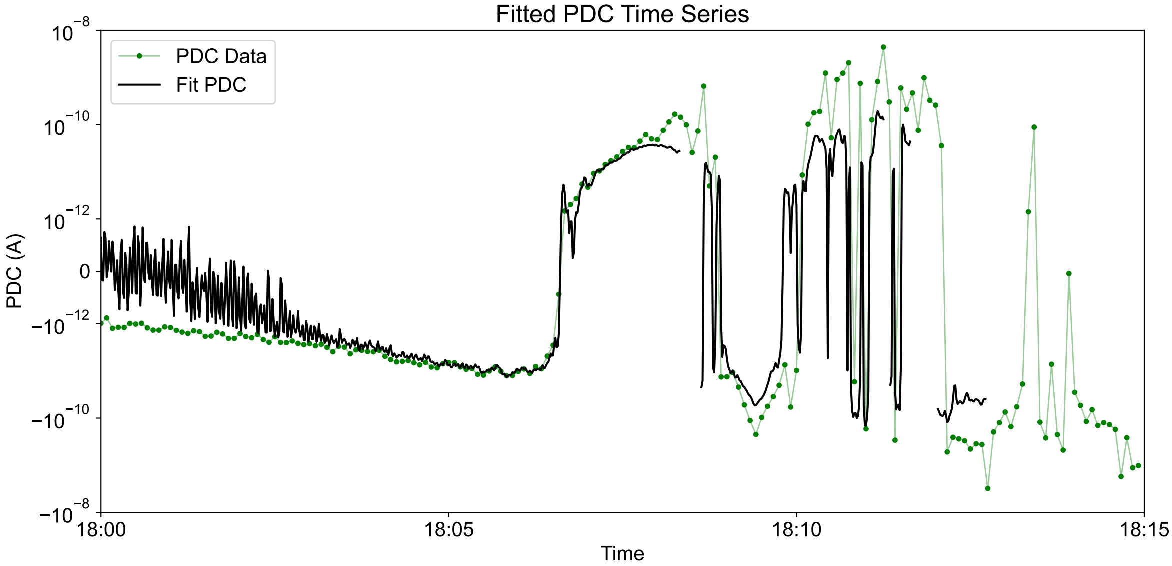

Figure 3.10: Time series of PDC data (green) and the PDC fit described by equation 3.10 (black) on the same x-axis. A symmetric y axes was used, with a linear range between ±1pA.

The time offsets for the axis crossings between the fitted PDC and the PDC data are shown in table 3.4.

PDC data & PDC fit

Axis Crossing №	1	2	3	4
Time Offset (s)	0 ± 3	-2 ± 3	-2 ± 3	-17.5 ± 14.5

Table 3.4: Time differences between several x-axis crossings in the PDC data and the corresponding axis crossings in the PDC fit described by equation 3.10. Positive values represent the axis crossing occurring in the PDC data before occurring in PDC fit, with negative values representing the axis crossing occurring in the PDC fit before the PDC data. The uncertainty in each time difference has been quoted.

The RMSE of these offsets was calculated to be 9s. Since this is lower than the previous two RMSEs found, we can conclude that the shape of the PDC profile is best reproduced when both electrostatic and electrodynamic terms are included in our fit.

3.4 Linear PDC Sensor Investigation

Following the investigation into the logarithmic PDC sensor using the JCI field mill, a new linear PDC sensor and wide range CS110 field mill were deployed at the RUAO. We will investigate the data collected by these sensors in this section. Since these sensors were deployed at the field site only recently, a limited amount of data was available. Following the deployment of both sensors, a day featuring a large amount of disturbed weather was identified on the 2nd of May 2024. We have investigated the PDC data collected on this day.

First in our analysis of the PDC dataset, we identified two classes of datapoints: those corresponding to the point discharge process, and those which were background readings. This was done by examining time series of the data from the PDC sensor. An example of these time series is shown in figure 3.11. The PG during the same period was plotted on the same x axis.

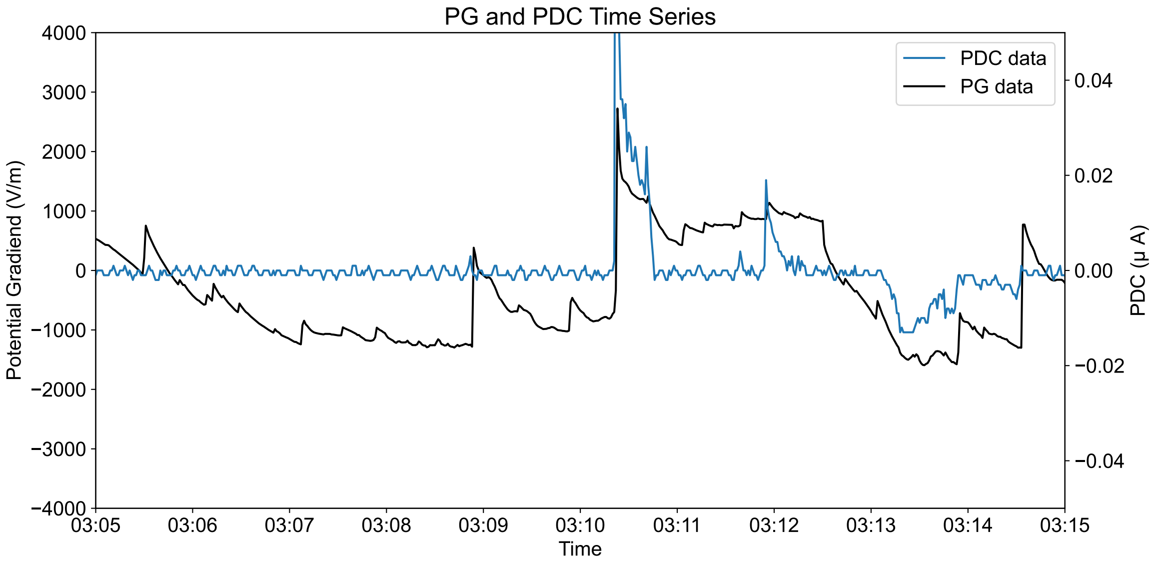

Figure 3.11: Time series of the linear PDC data (blue) and the PG recorded by the CS110 field mill (black), shown on the same x-axis. These time series have been shown for a 10 minute period.

As can be seen in figure 3.11, for some of this data (e.g. near 03:10, 03:12, and 03:13) a change in PG is coincident with a change in PDC. This data can be interpreted as actual measurements of PDC. At other times, however, we find that the PG will vary while the PDC is largely unaffected: sitting at values between -0.01 and 0.01 µA. This can be seen in figure 3.11 between 03:05 and 03:10. These readings were interpreted to be background values, not corresponding to PDC. For our investigation, we will only consider data greater than 0.02 µA, to ensure that these background values are removed from our dataset.

It is known that the positive and negative PDC processes behave slightly differently [115]. Because of this, we have separated the positive and negative PDC data, to deal with them individually. In doing this, it was found that the subset of positive datapoints was appreciably larger than the subset of negative data, so the investigation has only focused on this positive data. The PDC data used in this analysis is shown in figures 3.12a and 3.12b, where it has been compared against the PG and wind speed respectively.

We will analyse this PDC data to evaluate several parameterisations of PDC sensors. From inspection of figure 3.12b it can be seen that our dataset corresponds to relatively low wind speeds only, with the maximum wind speed in the dataset as 3.6 m/s. This factor is important to consider in the conclusions from this work.

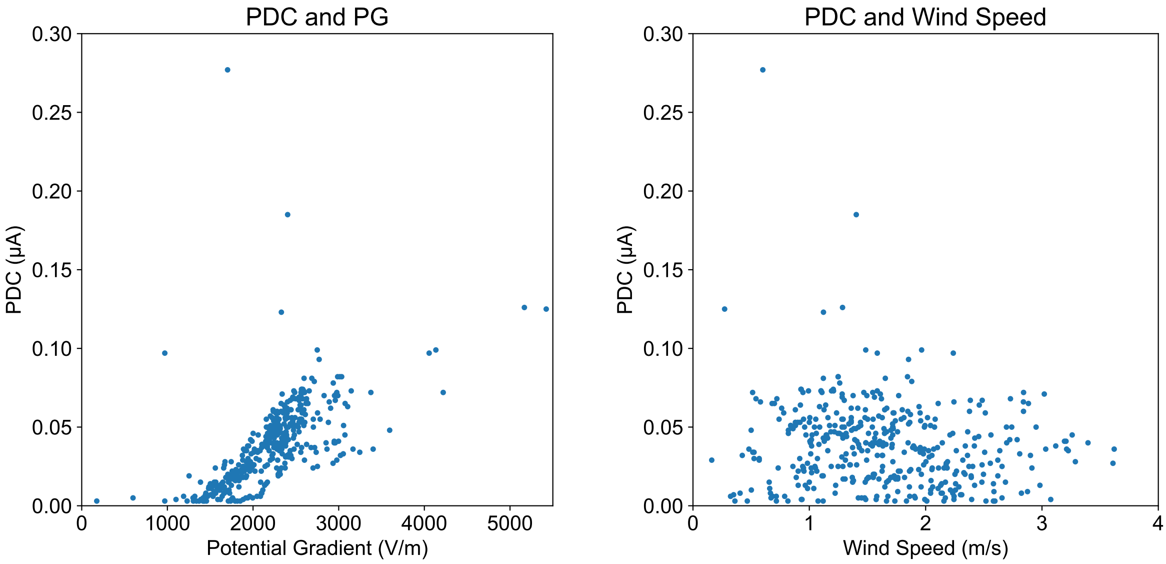

(a) PDC vs PG

(b) PDC vs Wind Speed

Figure 3.12: Scatter plots showing how the PDC data varies with potential gradient in (a), and with wind speed in (b). Note "wind speed" refers to the horizontal wind speed.

3.4.1 Simple Power Law Fits

The first parameterisation of PDC sensors to be considered was the "Power Law" fit, with the PG as the only independent variable. We will test how well a fit based on this relationship is able to explain the PDC data recorded. The fit considered was given by:

$$I = \begin{cases} a(F^2 - M^2) & \text{if } |F| > |M| \\ 0 & \text{otherwise} \end{cases} \tag{3.13}$$

Since only one independent variable was being considered, we can find the expected shape of the relationship between the PG and PDC by considering a lowess fit to the data. The shape of this fit will then be compared against the shape of the fit given by equation 3.13. This lowess fit is compared against the PDC and PG data in figure 3.13.

Next, the power law was fit to this data. The optimal values for the parameters a and M were determined from non-linear regression. Initially, the square of the residuals was used as the cost function for this regression (i.e. least squares regression was used). The parameters a and M were determined to be 1.6×10^{-8} μAm^2/V^2 and 3.2×10^{-6} V/m via this method. The power law fit using these parameters is compared against the PDC data in figure 3.14a. Note that the lowess fit has been included in this figure, in order to showcase the expected shape of fit.

From figure 3.14a, it can be seen that the least squares fit deviates significantly from the lowess fit. Additionally, the fit does not appear to pass through the bulk of the points. In order to explore the the quality of this fit, a goodness of fit metric was developed. For each data point, the recorded PDC value was compared against the expected value from the fit. This comparison is shown in figure 3.14b. Next, the coefficient of determination (i.e. R^2) was determined for

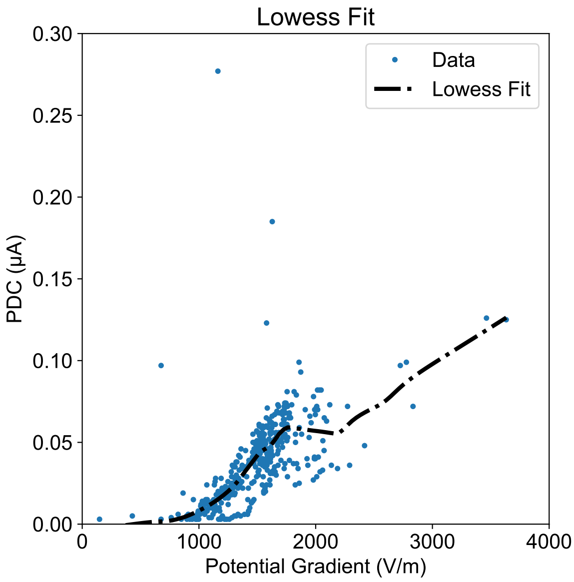

Figure 3.13: Scatter plot of the PDC data against the PG data, with a lowess fit to the data shown as a black dot-dashed line.

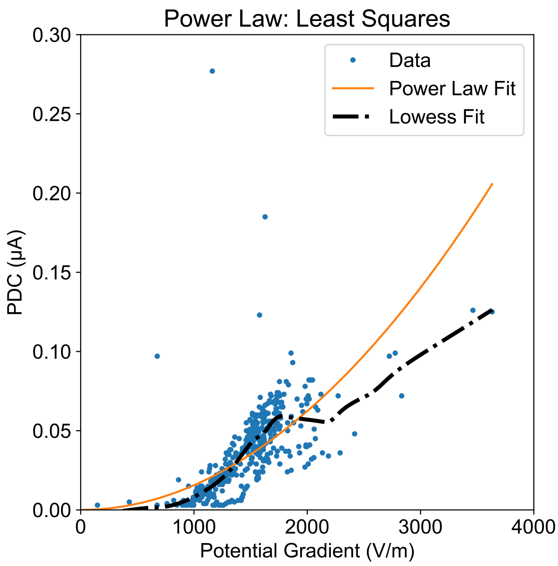

(a) Power law fit to data

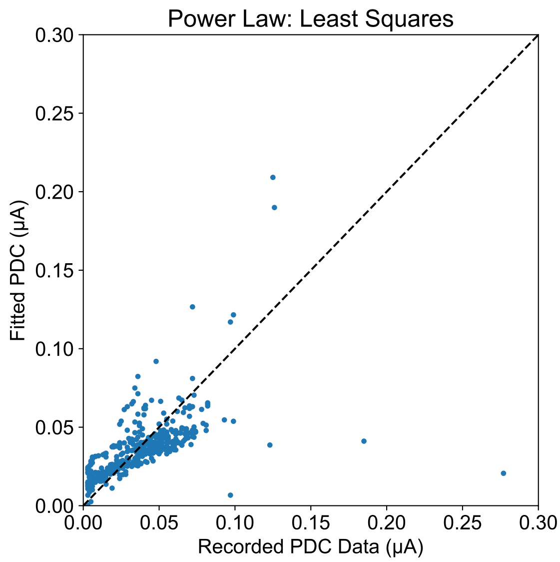

(b) Evaluation of fit

Figure 3.14: Power law fit to the PDC data using a least squares method, and an evaluation of this fit. (a) shows a scatter plot of the PDC data against the PG. The lowess fit from figure 3.13 has been shown as a black dot-dashed line. The power law fit to the data has been shown as an orange line. (b) shows the expected value of the PDC from this power law fit line compared against the value from the PDC data, for each PDC datapoint. The 1:1 line has been indicated on this figure using a black dashed line.

this data, for the 1:1 line passing through it. We will later wish to compare the goodness of fit for fits with a differing number of independent variables. In these cases, the adjusted R^2 ($\bar{R}^2$) should be used, to account for the increase in R^2 caused by these additional variables. The adjusted R^2 is given by:

$$\bar{R}^2 = 1 - (1 - R^2)\frac{n-1}{n-p_n-1} \tag{3.14}$$

where n is the sample size of the dataset and p_n is the number of independent variables used. For consistency with later analysis, we will use $\bar{R}^2$ as our goodness of fit metric here.

For the least squares method shown in figure 3.14, the $\bar{R}^2$ was found to be -0.30. Since this value is less than 0, it suggests that this is a particularly bad fit to the data. To investigate why this fit was so poor, we have tested the same shape of fit with different parameters. The fit to the data with the parameters a & M set as 2.8×10^{-8} Am^2/V^2 and 900 V/m respectively is shown in figure 3.15.

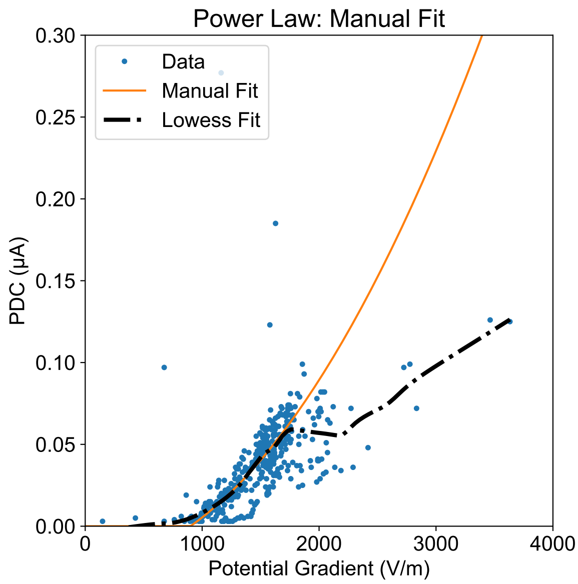

Figure 3.15: Power law fit to the PDC data, with manually specified fit parameters. The PDC and PG data have been shown as a scatter plot, and the lowess fit from figure 3.13 has been shown as a black dot-dashed line. The power law fit has been shown as an orange line.

By inspection, this fit appears to fit the data better than the fit determined via least squares regression. The fit line agrees more closely to the lowess curve, and notably, the fit line passes through the bulk of the datapoints. In order to identify why this fit was not selected by this regression, distributions of the residuals for the two fits were compared. These are shown as histograms of the absolute value of the residuals, in figure 3.16. The root mean squared, and root median squared of the residuals have been indicated as solid and dashed lines respectively.

From inspection of the two histograms in figure 3.16, it can be seen that the distributions of residuals are very different shapes for the two fits. In the least squares case, the distribution is rather wide, with a modal value significantly distanced from zero. There are also relatively few "outlier" points in the tail of the distribution. In the manual fit case, the distribution appears to be narrower, with a modal value close to zero, however there is a large tail to this distribution. This leads to many "outlier" values being present. The result of these outliers in the distribution tail is that the root mean squared value is significantly larger than for the least squares case. Since the least squares cost function is based on the root mean squared value, this cost function is strongly affected by these outlier points. As such, we conclude that a different

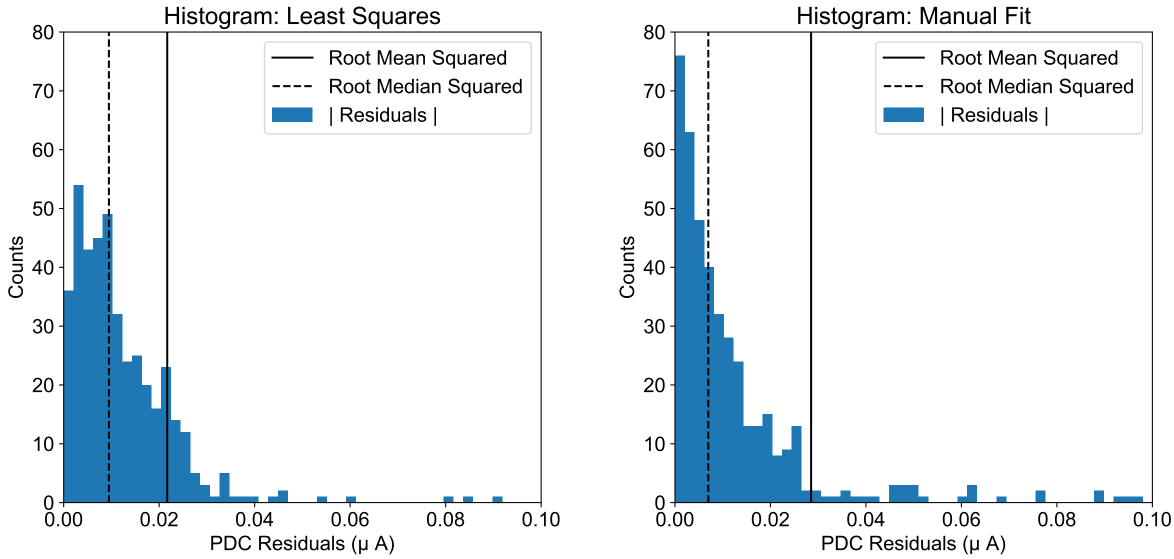

(a) Least squares method

(b) Manually specified parameters

Figure 3.16: Histograms of the absolute value of residuals of two power law fits, using different fit parameters. In (a), the residuals are for the fit in figure 3.14a, where the fit parameters have been determined using a least squares method. In (b), the residuals are for the fit in figure 3.15, where the fit parameters were specified manually. The values of the root mean squared, and root median squared of the residuals have been indicated on both figures by solid and dashed vertical lines respectively.

cost function will need to be used, in order to diminish the effect of the outlier points.

Two solutions have been proposed for this. Firstly, it is possible to identify the outlier points, and remove them from the mean squared calculation. This “outlier removed root mean squared” can then be minimised in order to find the best fit. The other proposed solution is to use the root median squared. As can be seen in the histograms in figure 3.16, the root median squared value appears to represent the distributions well, being largely unaffected by the outliers in the long tail. The fits achieved using these two cost functions will be evaluated.

Firstly, the outlier-removed least squares method was utilized. The outlier points were identified by considering the distribution of the squared residuals between the fit and the data. The values which were greater than 1.5 $\times$ the interquartile range + the third quartile were specified as outliers. The mean of the remaining datapoints was then minimised. Through this process, the parameters a and M were determined to be 2.9×10^{-8} Am^2/V^2 and 878 V/m respectively. As for the least squares regression, the fit and evaluation of the fit have been shown in figure 3.17. It was found that the $\bar{R}^2$ for this fit was 0.27.

Next, the same analysis was performed for the root median squared cost function. In this case, the parameters a, M were found to be 3.1×10^{-8} Am^2/V^2 and 922 V/m respectively. The fit and evaluation were shown in figure 3.18. The $\bar{R}^2$ for this fit was 0.28.

From inspection of the the fits to the PDC data in figures 3.14a, 3.17a, and 3.18a, it can be seen that both the outlier-removed least squares and median of squares methods provide better fits to the data than the least squares methods. In these two cases, the fit lines broadly agree with the lowess curve. This conclusion is also reinforced by the $\bar{R}^2$ values for the three fits;

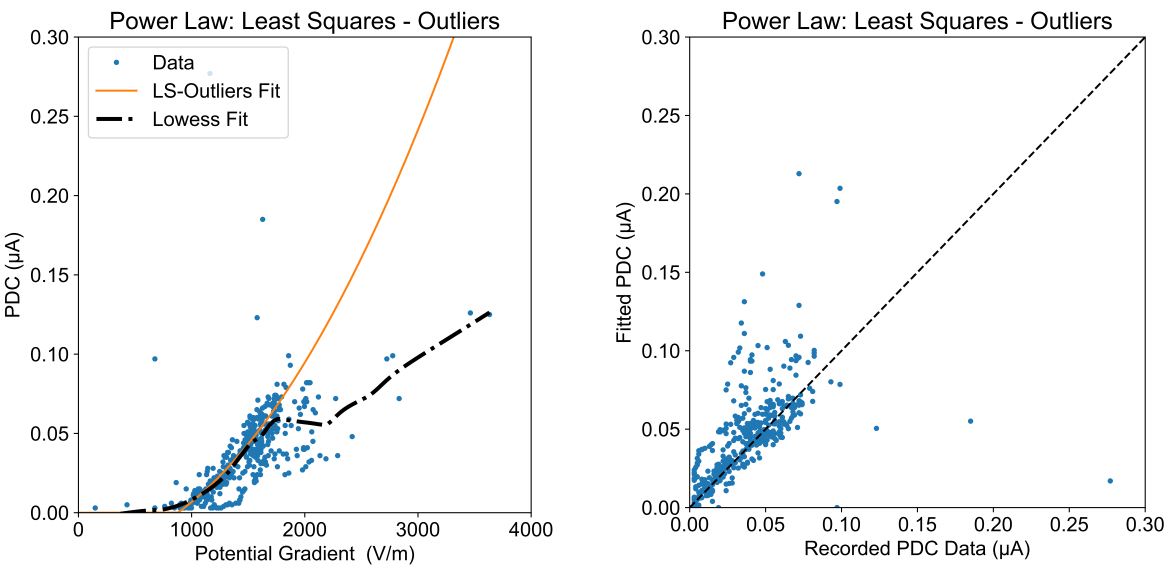

(a) Power Law Fit to Data

(b) Evaluation of Fit

Figure 3.17: Power law fit to the PDC data using an outlier-removed least squares method, and an evaluation of this fit. (a) shows a scatter plot of the PDC data against the PG. The lowess fit from figure 3.13 has been shown as a black dot-dashed line. The power law fit to the data has been shown as an orange line. (b) shows the expected value of the PDC from this power law fit line compared against the value from the PDC data, for each PDC datapoint. The 1:1 line has been indicated on this figure using a black dashed line.

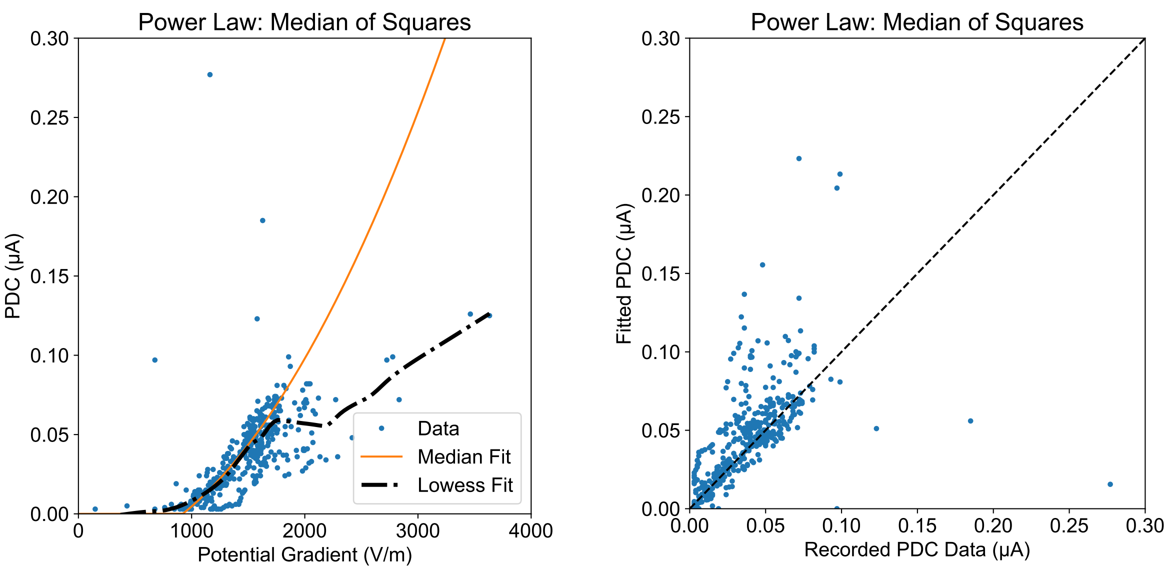

(a) Power Law fit to Data

(b) Evaluation of Fit

Figure 3.18: Power law fit to the PDC data using a median of squares method, and an evaluation of this fit. (a) shows a scatter plot of the PDC data against the PG. The lowess fit from figure 3.13 has been shown as a black dot-dashed line. The power law fit to the data has been shown as an orange line. (b) shows the expected value of the PDC from this power law fit line compared against the value from the PDC data, for each PDC datapoint. The 1:1 line has been indicated on this figure using a black dashed line.

the $\bar{R}^2$ value for the median of squares fit is the largest, followed by the outlier removed least squares value, with the least squares value being very poor. As such, these two methods will be used for the subsequent analysis.

We next wish to investigate other fits to the PDC data. The two cost functions for non-linear regression which returned good fits to the data will be now be applied to these other fits.

3.4.2 Chalmers' Fit

The parameterisation developed by Chalmers [32], incorporating both wind speed and PG into the fit for the PDC will now be investigated. This fit is given by:

$$I = \begin{cases} a(F-M)(W^2+bF^2)^{1/2} & \text{if } |F| > |M| \\ 0 & \text{otherwise} \end{cases} \tag{3.15}$$

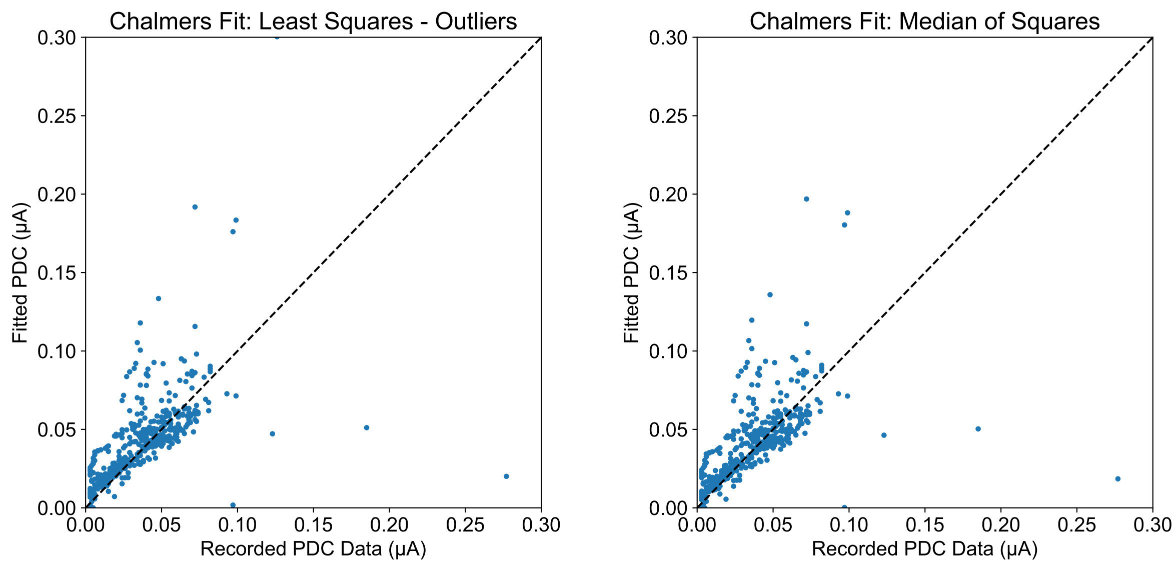

(a) Outlier-Removed Least Squares Method

(b) Median of Squares Method

Figure 3.19: Evaluation of two fits to the PDC data using Chalmers' derived fit, with fit parameters found via different methods. In both figures, the expected value of the PDC from the fit has been compared against the value of the PDC data. The 1:1 line has been shown on each figure as a black dashed line. The fit parameters used for the fit in (a) were found using an outlier-removed least squares method. The fit parameters used for (b) were found using a median of squares method.

As for the power law fit, the parameters a, b, and M will be determined via non-linear regression. Again, the expected PDC values from the fit were compared with the recorded PDC data, and an $\bar{R}^2$ was determined for the 1:1 line. The comparisons found for the outlier removed least squares, and median of squares methods are shown in figures 3.19a and 3.19b.

The fit parameters a, M, b found via both of these methods have been reported in table 3.5. The $\bar{R}^2$ values found for the outlier removed least squares and median of squares methods were found to be 0.22 and 0.22 respectively.

Note that both of these $\bar{R}^2$ values are worse than those for the power law fits. We thus conclude that for the dataset considered here, we do not gain an improvement in the parameterisation of the sensor if we include the wind speed, rather than just considering the PG. This is surprising, since many previous investigations have reported that the inclusion of wind speed is important for describing the point discharge process. It is important to note that for the entire dataset considered, the wind speed was relatively low. We can investigate the low wind speed limit of equation 3.15; in the case that $W^2 \ll bF^2$, and $|F| > |M|$ we find:

$$I \approx ab^{1/2}(F - M)F \tag{3.16}$$

Comparing this against the power law fit in equation 3.13, we find that these equations have sightly different forms. At large wind speeds, the Chalmers' fit may include the effects of wind, however at low wind speeds it alters the relationship between PG and PDC from the power law parameterisation. We can conclude that at these low wind speeds, the power law parameterisation given by 3.13 is a better fit to the data than Chalmers' parameterisation.

3.4.3 Addition of Maxwell Terms

Next, the inclusion of Maxwell currents on the operation of PDC sensors was investigated. Based on our investigation in section 3.3, the PDC signal matches up to a PG signal better if there is an additional term proportional to the rate of change of the PG added. We will investigate if including these terms in the parameterisations will provide a better fit to the PDC data than neglecting them.

We first consider this additional term in the power law fit. The resulting fit will be of the form:

$$I = \begin{cases} a(F^2 - M^2) + c\frac{dF}{dt} & \text{if } |F| > |M| \\ c\frac{dF}{dt} & \text{otherwise} \end{cases} \tag{3.17}$$

Again, the same analysis as before was performed for this fit. The comparison of the expected PDCs against the recorded PDCs is shown for the two cost functions in figure 3.20.

The $\bar{R}^2$ values found for the outlier removed least squares and median of squares methods were found to be 0.32 and 0.36 respectively.

From comparison to the $\bar{R}^2$ values found from the power law fit, it can be seen that the inclusion of the Maxwell term has a significant improvement on the paramerisation of the sensor. This reinforces the conclusion found from section 3.3; it is important to consider Maxwell currents in the considerations of the response of a PDC sensor.

Finally, the inclusion of this maxwell term on Chalmers' fit was investigated. The fit took the form:

$$I = \begin{cases} a(F - M)(W^2 + bF^2)^{1/2} + c\frac{dF}{dt} & \text{if } |F| > |M| \\ c\frac{dF}{dt} & \text{otherwise} \end{cases} \tag{3.18}$$

The comparison of the expected PDCs from this fit against the recorded PDCs is shown for the two cost functions in figure 3.21.

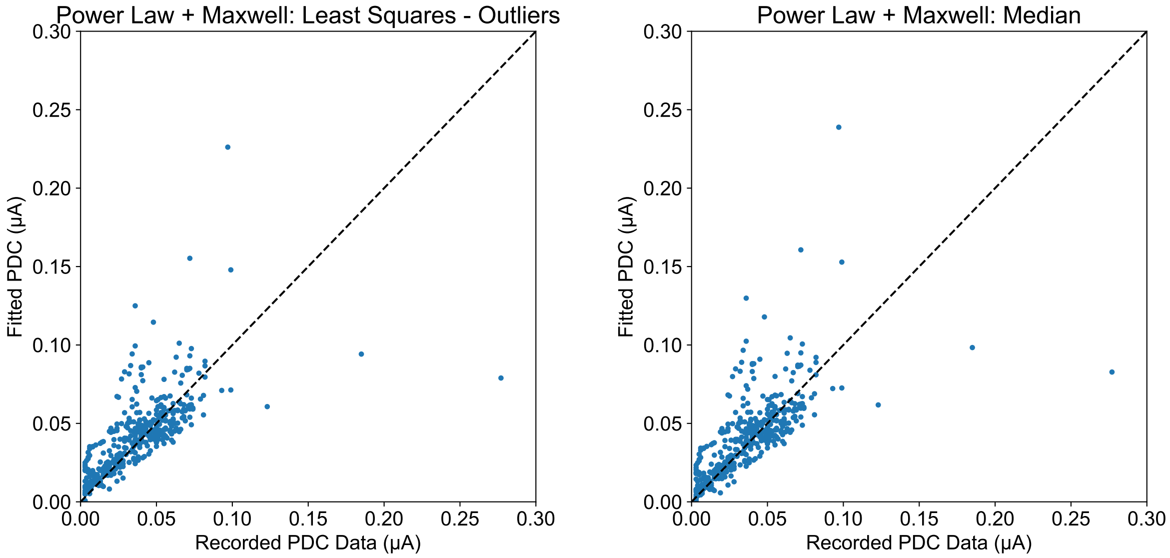

(a) Outlier-Removed Least Squares Method

(b) Median of Squares Method

Figure 3.20: Evaluation of two fits to the PDC data using a Power law with an additional Maxwell current term, with fit parameters found via different methods. In both figures, the expected value of the PDC from the fit has been compared against the value of the PDC data. The 1:1 line has been shown on each figure as a black dashed line. The fit parameters used for the fit in (a) were found using an outlier-removed least squares method. The fit parameters used for (b) were found using a median of squares method.

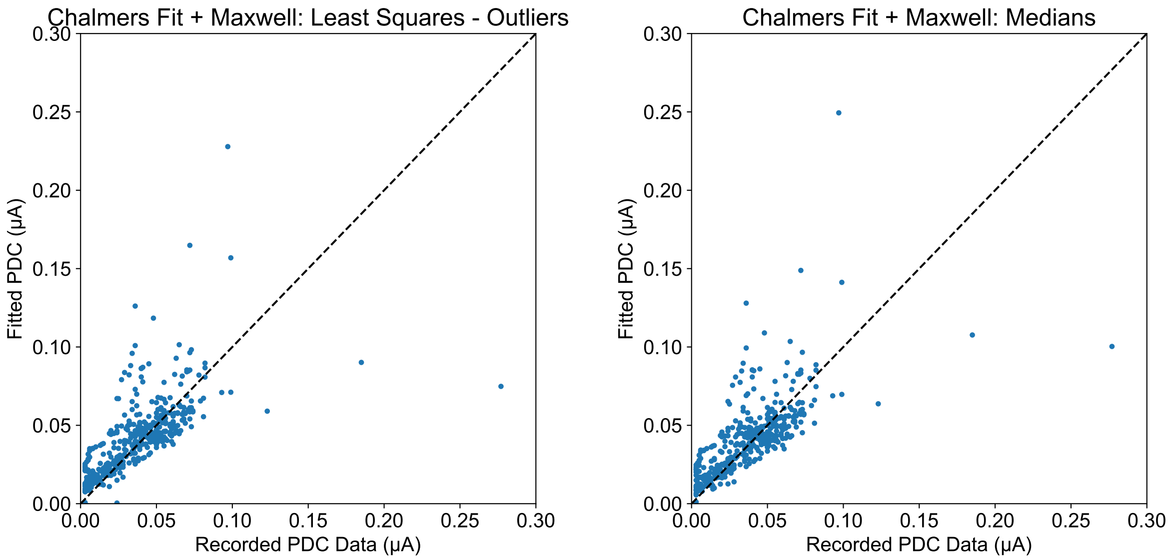

(a) Outlier-Removed Least Squares Method

(b) Median of Squares Method

Figure 3.21: Evaluation of two fits to the PDC data using Chalmers' derived fit with an additional Maxwell current term. (a) and (b) show the evaluations of fits using fit parameters found from different methods. In both figures, the expected value of the PDC from the fit has been compared against the value of the PDC data. The 1:1 line has been shown on each figure as a black dashed line. The fit parameters used for the fit in (a) were found using an outlier-removed least squares method. The fit parameters used for (b) were found using a median of squares method.

The $\bar{R}^2$ values found for the outlier removed least squares and median of squares methods were found to be 0.31 and 0.31 respectively.

As for the power law fit, it can be seen that the inclusion of these terms provides a considerable increase in the $\bar{R}^2$ value for the fit. However, we find again that the $\bar{R}^2$ values for the Chalmers' fit including the Maxwell term are worse than for the power law including the Maxwell term.

The four fits considered in this investigation, along with the value of the parameters determined for them have been summarised in table 3.5:

Fit Name	Fit Equation	Fitted Parameters	
		Outlier-Removed	Median
Power Law	$I = a(F^2 - M^2)$	a = 2.9×10^{-8} µAm^2/V^2 M = 878 V/m	a = 3.1×10^{-8} µAm^2/V^2 M = 922 V/m
Chalmers'	$I = a(F - M)$ $\times (W^2 + bF^2)^{1/2}$	a = 3×10^{-6} µA/Vs M = 609 V/m b = 1.0×10^{-4} m^4/V^{2}s^2	a = 3.1×10^{-6} µA/Vs M = 631 V/m b = 9.0×10^{-5} m^4/V^{2}s^2
Power Law + Maxwell	$I = a(F^2 - M^2)$ $+ c\frac{dF}{dt}$	a = 2.5×10^{-8} µAm^2/V^2 M = 779 V/m c = 3.7×10^{-5} µAsm/V	a = 3.1×10^{-8} µAm^2/V^2 M = 920 V/m c = 6.5×10^{-5} µAsm/V
Chalmers' + Maxwell	$I = a(F - M)$ $\times (W^2 + bF^2)^{1/2}$ $+ c\frac{dF}{dt}$	a = 3×10^{-6} µA/Vs M = 635 V/m b = 1.1×10^{-4} m^4/V^{2}s^2 c = 4.4×10^{-5} µAsm/V	a = 2.9×10^{-6} µA/Vs M = 604 V/m b = 1.0×10^{-4} m^4/V^{2}s^2 c = 4.9×10^{-5} µAsm/V

Table 3.5: Fit parameters found for the 4 PDC paramerisations considered in this investigation, for the two fitting methods considered. The form of each parameterisation has been shown, along with the fit parameters found for both the outlier-removed least squares cost function, and the median of squares cost function for each parameterisation.

The $\bar{R}^2$ values found for each of the fits in table 3.5 have been summarised in table 3.6

Fit Name	$\bar{R}^2$ Value	
	Outlier Removed	Median
Power Law	0.27	0.28
Chalmers'	0.22	0.22
Power Law + Maxwell	0.32	0.36
Chalmers' + Maxwell	0.31	0.31

Table 3.6: $\bar{R}^2$ values found for each of the 4 parameterisations considered in this investigation, for the two utilised fitting methods: Outlier-removed least squares, and median of squares.

3.5 Discussion

From investigation into the time series of PDC data, it was found that including terms based on both the PG and the rate of change of PG provided an improved description of the recorded PDC than just considering one of these terms. The dependence on PG is not unexpected since many previous parameterisations have included electrostatic terms dependent on some power of the potential gradient. The dependence on the rate of change of PG was unexpected, however, since it implies that some electrodynamic effect is important, which has been neglected from these previous parameterisations.

The candidate suggested for this electrodynamic effect is the electric displacement current. If this was the case, then it would mean that the sensor is responsive to both "free currents", caused by the movement of charges in the discharge current, and displacement currents, caused by the changing atmospheric electric field. It is unclear, however, why previous attempts to parameterise these sensors have not encountered effects caused by displacement currents. Among other factors, it is possible that some geometric aspect of this particular sensor is enhancing the currents, the high sampling frequency of the sensor makes it particularly sensitive to these variations, or that the large observational range of this sensor means it is well suited to detecting these effects.

Following this investigation, several parameterisations of a linear PDC sensor were evaluated. To perform this evaluation, a selection of PDCs recorded under low wind speed conditions were used. Two discoveries were found; firstly, it was discovered that in these low wind conditions, the parameterisation derived by Chalmers [32] is unable to describe the PDC data better than a simpler power law description. There have been many studies showing that in high wind speed conditions, the effects of wind speed are very important to descriptions of the point discharge process. As such, we arrive at the conclusion that the inclusion of these wind speed terms could offer an improvement on the power law description at high wind speeds, however our dataset lies in the low wind speed limit of the parameterisation, and that the low wind speed limit of Chalmers' parameterisation is a worse description of the PDC process than a simple power law.

Additionally, it was shown that the inclusion of a Maxwell current term in the parameterisations of the PDC sensor led to an improvement of the quality of the parameterisation, This was true for both the power law fit and the fit derived by Chalmers. This conclusion reinforces the previous work in investigating the timing of variations in the PDC time series, showing that we require both electrostatic and electrodynamic terms in order to fully describe the PDC process.

As was mentioned before, these Maxwell currents have not been identified by previous PDC sensor investigations. To investigate if these currents have a universal importance, rather than just affecting the sensors in our field site, it is important to carry out future investigations on other datasets. For such an investigation, we would require data with a high temporal resolution, from co-located electric field mills and PDC sensors (and ideally anemometers also). The availability of such a dataset has not been currently identified (outside of the data from the RUAO which was used in this investigation). It is hoped that such datasets are produced by further investigations into atmospheric electricity.

The inclusion of both electrodynamic and electrostatic terms in a parameterisation of the PDC sensor is problematic if this sensor is to be used alone as an atmospheric electrical instrument. Since the output signal is dependent on both the electric field and its derivative, it would be difficult to recover the electric field from just a point discharge measurement. The issues caused by the inclusion of electrodynamic effects would likely be worse for sensors moving vertically in the atmosphere, such as Coronasondes (radiosondes carrying a point discharge sensor) and spacecraft with point discharge instrumentation (e.g. Venera 13 & 14) [26, 103]. The potential difference between the sensor and the atmosphere for these instruments is fundamentally dependent on electrodynamic processes, which would add additional complexity to any attempt to recover the atmospheric electric field signal. The presence of both electrostatic and electrodynamic effects can have an advantage in these deployments however. If it is unclear if there is any electric signal to look for, then the inclusion of both electrostatic and electrodynamic terms means that a detector has a higher chance of detecting the presence of electric effects, even if their precise nature cannot be obtained.

3.6 Conclusions

The operation of two point discharge sensors were investigated via different means.

First, the time response of a logarithmic point discharge sensor was investigated. The logarithmic nature of this sensor allowed observations to be taken across many orders of magnitude of current. From inspection of the timing of several features in the point discharge time series, it was found that the point discharge data was best described by both a an electrostatic term, dependent on the PG, and an electrodynamic term, dependent on the rate of change of PG.

Next, several parameterisations of a linear point discharge sensor were evaluated. These evaluations were performed by considering the goodness of fit for parameterisations with different forms. It was found that for data at low wind speeds, a power law parameterisation describes the operation of the sensor better than the parameterisation developed by Chalmers [32]. Additionally, these parameterisations were evaluated with additional electrodynamic terms dependent on the Maxwell current included. As for the previous investigation, it was found that the inclusion of these electrodynamic terms, alongside electrostatic terms, provided the best description of the operation of the point discharge sensor.

Chapter 4

Venera 13 & 14 Point Discharge Reanalysis

The Venera 11-14 spacecraft have taken the only in-situ measurements of atmospheric electricity from Venus' atmosphere, using the "Groza" (thunderstorm) and "Groza-2" instrumentation packages. These observations have been introduced in chapter 2. Following the impulsive electrical signals detected by Venera 11 & 12, a concern was raised that electrical discharges from the spacecraft themselves could be responsible. To address this concern, the Groza instrument was updated before the subsequent Venera 13 & 14 missions. As part of this updated "Groza-2" instrument, point discharge current (PDC) sensors were included, allowing electrical charges from the spacecraft to be measured during the descent through Venus' atmosphere. Terrestrial

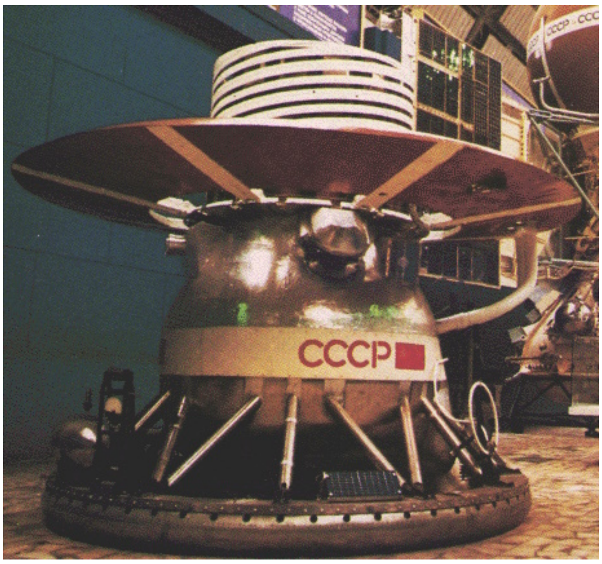

(a) Venera 13 Lander

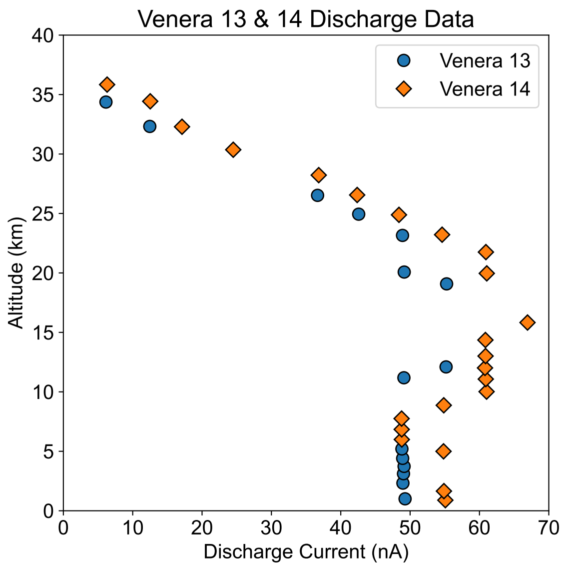

(b) Discharge Current Data

Figure 4.1: (a) Image of the Venera 13 Lander. Image taken from [202]. (b) Discharge current data from the Venera 13 & 14 landers, reproduced from [103]. The Venera 13 data is shown as blue circles, with the Venera 14 data as orange diamonds. Both datasets show an increase in discharge current as the lander descends, with a peak being reached at around 25km, with the data becoming more consistent with height between 25km and the surface.

versions of these PDC sensors have been introduced in chapter 2, and investigated in chapter 3. The Venera 13 lander is shown in figure 4.1a, in which the Groza-2 instrument can be identified from the loop antena in the bottom right of the image. The electrical discharges recorded by the Venera 13 & 14 spacecraft during their descents through the Venusian atmosphere are shown in figure 4.1b.

The Venera 13 & 14 landers reached Venus 4 days apart, and landed on the surface 950km apart [87]. Despite these differences in time and position, the discharge currents recorded by both landers had remarkably similar shapes. These similar shapes, at different times and positions suggest that there may be some structure present in the lower atmosphere of Venus which is responsible for the shape of the discharge current profiles [116].

To understand the electrical discharges from the Venera 13 & 14 landers more fully, and to identify any implications for Venus' electrical environment, an electrical model of Venus' atmosphere has been produced. This modelling approach compared modeled point discharge currents against the observed currents with the intention of determining the electrical structure of Venus' atmosphere.

The steps involved in this modelling approach have been described in section 4.1. Following this, the Venera PDC data is discussed further in section 4.2. In sections 4.4 and 4.5 the calculations involved in the electrical modelling of Venus, and of a spacecraft descending through the atmosphere are described. In section 4.6, the results from the electrical modelling are compared against the observed data, to investigate features which must be present in the Venusian atmosphere. Finally, in section 4.7, the implications of this investigation are discussed.

4.1 Modelling Approach - Venus Aerosol Ion Model

In this investigation, the point discharge data recorded by the Venera 13 & 14 landers will be used to probe the electrical environment of Venus. To pursue this, an electrical model of Venus' atmosphere was constructed to determine the point discharge signals which would be expected. An overview of this modelling approach will be provided here.

The model of Venus' atmosphere was named VAIL (Venus Aerosol Ion modeL). This model determined the local ion concentrations of Venus' atmosphere, by calculating the equilibrium solution to a set of ion-aerosol balance equations analytically. These ion concentrations were further used to determine the conductivity and columnar resistance of Venus' atmosphere. Additionally, as a model input the presence of a global atmospheric electric circuit could be specified. This would allow the atmospheric potential, and electric field as a function of altitude to be determined. The calculations involved in finding these electrical parameters are described in section 4.4.

Using the electrical parameters found for Venus' atmosphere, the effects on a spacecraft descending through Venus' atmosphere (as the Venera 13 & 14 landers did) were determined. The electric potential of such a spacecraft was determined, by considering several charging and discharging mechanisms. Additionally, by applying knowledge of terrestrial point discharge sensors, the point discharge current which would be emitted by the spacecraft were determined. These charging/discharging considerations are described in section 4.5.

Finally, these results from the electrical modelling were compared against the point discharge signals recorded in-situ by Venera 13 & 14. Through this comparison, the model inputs are able to be adjusted in order to determine the atmospheric conditions which reproduce the Venera results best.

4.2 Venera 13 & 14 Point Discharge Data

There exists very little information on the Venera instrumentation. In particular, there is very little known of the design of the discharge electrode. Additionally, the original data has been destroyed, with the only extant data in a figure in a paper discussing the Venera electrical measurements. Through correspondence with the now late Leonid Ksanformality - principal investigator of the Groza-2 instrument - Lorenz [116] was able to glean some more information on how the sensor operated. From this correspondence, it was determined that the discharge electrode was likely similar in design to the point discharge sensors used for atmospheric electricity measurements on Earth. Specific information on the size or location of this sensor are still unknown, however.

From inspection of the datapoints in figure 4.1b, it can clearly be seen that the recorded PDC takes one of several discrete values. This was believed to be due to the nature of the analogue to digital conversion (ADC) that occurred as part of data collection onboard the lander. In order to investigate the nature of this ADC, we have considered the magnitude of these discrete values. In figure 4.2a, we have plotted all the Venera 13 & 14 PDC values normalised by the smallest PDC value, against themselves. From this figure, it can be seen that all of the datapoints lie very close to integer values, which have been indicated by grid lines. The ADC bin number can then be found for each of these datapoints, as it is the gridline which is closest to the point. The number of datapoints associated with each ADC bin number is shown by the histogram in figure 4.2b.

Next, the size of each ADC bin was determined. This was found by finding the average value of each datapoint divided by its bin number, i.e:

$$\text{ADC Bin Size} = \frac{1}{n}\sum^{n} \frac{I_{PDC}}{\text{Bin №}} \tag{4.1}$$

for n datapoints. This allowed a bin size of 6.11 ± 0.01 nA to be identified, with the uncertainty calculated as one standard error on the mean. In figure 4.2, we can see that we have datapoints in 10 of the ADC bins. We would expect however, that every integer multiple of the bin size (up to the max value) would correspond to an ADC bin, including 0. As such, we would expect 2 further bins to be counted, which had no datapoints observed in them (bins 0 and 5). Additionally, it is expected that the number of ADC bins will be some power of 2. The nearest power of 2 which is greater than 12 (the number of bins we require) is 16. As such, we make the logical assumption that a 4-bit ADC was used, which would provide 16 possible bins.

The largest datapoint that was recorded by either Venera lander was in bin 11. Since we would expect the largest possible recording to be bin 15, we can draw the conclusion that the discharge currents recorded were not saturation values, since it would have been possible for

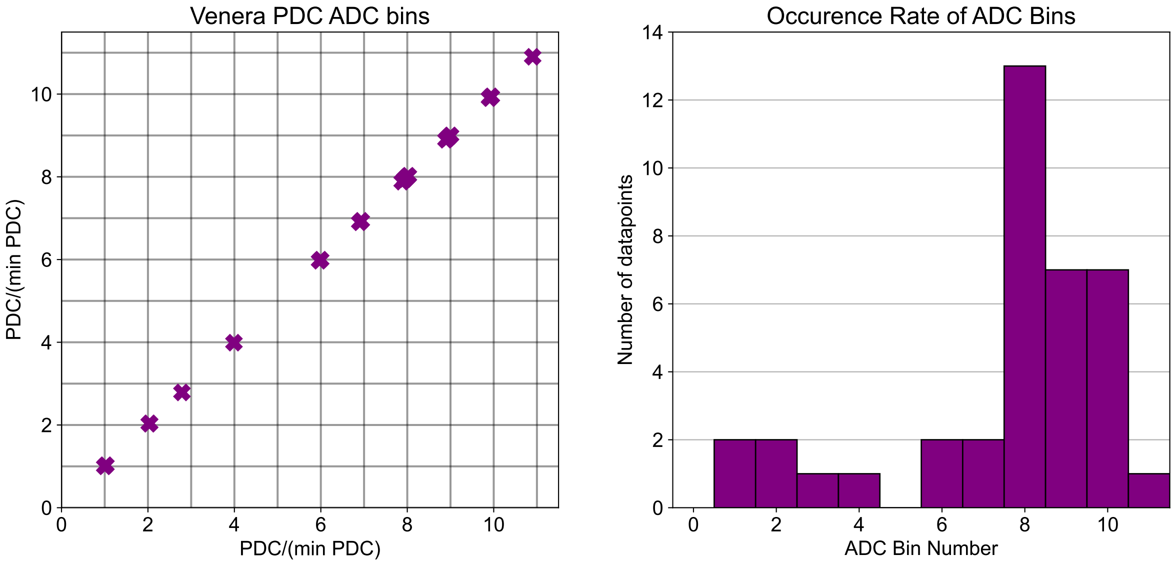

(a) Assignment of ADC bin number

(b) ADC Occurrence Rates

Figure 4.2: Analysis of the magnitudes of the Venera 13 & discharge current datapoints. (a) shows each datapoint as a multiple of the smallest datapoint recorded. From this plot it can be seen that every datapoint is approximately an integer multiple of this smallest value. This allows ADC bin number of each datapoint to be determined. (b) shows the number of datapoints recorded in each ADC bin.

larger currents to be recorded than were actually recorded.

Additionally, we consider that the size of these ADC bins leads to a reading error in the PDC data. From our analysis we have determined that the ADC bins likely have a size of 6.11 nA, so we find that the PDC data has a reading error of ± 3.06 nA.

Unfortunately, no polarity information has been recorded for the Venera 13 & 14 discharge currents. From the profiles shown in figure 4.1b, it can be seen that the PDC varies smoothly with height. As such, we would expect that the recorded PDC signals are all of the same polarity, as the signal does not appear to cross 0. So, although it is unknown what polarity of signal is present, we can make the reasonable assumption that all recorded PDCs were of the same polarity.

Through personal communication with Galina Bazilevskaya [12] from the Russian Academy of Sciences, it was discovered that the electronics on the Venera 13 & 14 spacecraft utilised semiconductor devices, rather than vacuum tubes. Based on this information, it may be possible to make some assumptions on the polarity of signal which was observed, however these assumptions would not be rigorous.

4.3 Model Input Data

There are a number of datasets used for our analysis of the Venera PDC data. These datasets are summarised in the following section, along with the calculations which were performed to provide inputs to the model. In many cases interpolation was required in order to have data at the desired altitude. For the majority of this work, the results will be shown using a Piecewise Cubic Hermite Interpolating Polynomial (PCHIP) function. To verify that the choice of interpolator did not impact the model results, several interpolators were considered in this analysis, with the results from the different interpolators compared in section 4.4.6. The PCHIP interpolator was chosen since it had a number of desirable properties; this interpolation function preserves the monotonicity of the data input, meaning that it does not suffer from “overshoot” in the same way that typical cubic interpolation does, instead acting more similar to a linear interpolation. In contrast to a linear interpolation, however, PCHIP interpolation will be smoothly varying and differentiable, in a similar fashion to a cubic interpolation. These properties have been demonstrated in figure 4.3:

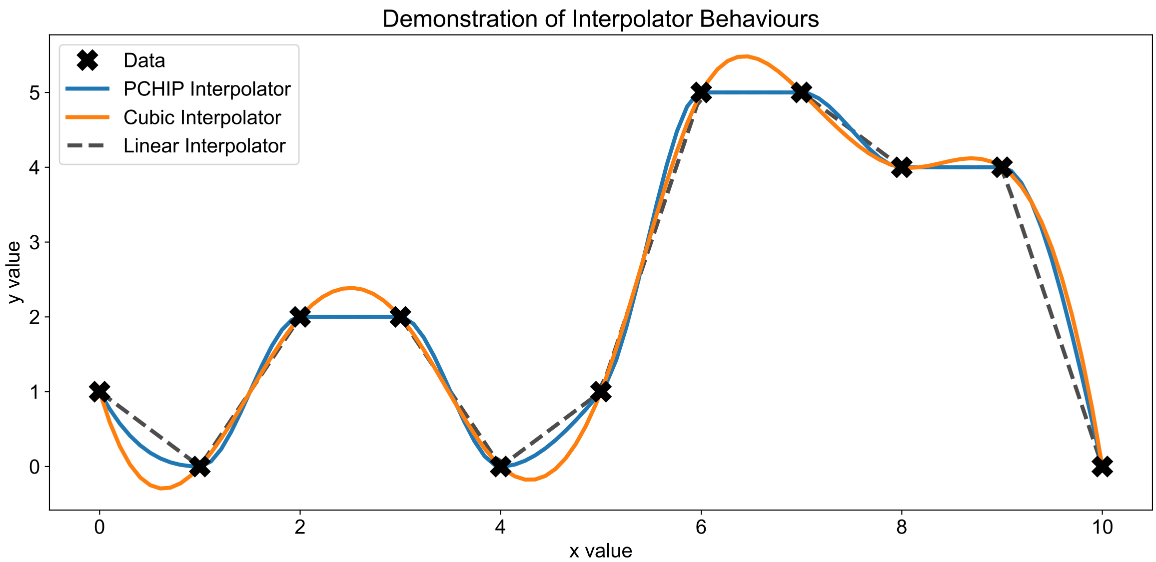

Figure 4.3: Demonstration of the behaviour of different interpolation methods on example data. The PCHIP interpolator (blue) passes through each datapoint smoothly without overshooting. The Cubic Interpolator (orange) passes through the data smoothly but has several overshoots. The linear interpolator (grey dashed) passes through the datapoints without overshooting, however the line does not change direction smoothly, meaning that there are discontinuities in its derivative.

4.3.1 Venera PDC

The Venera 13 & 14 PDC data discussed previously will be used for our analysis. For this analysis we wish to draw comparisons to the general atmosphere of Venus, rather than a specific case for one or other of the landers. As such, we wish to consider the average discharge current from the two landers at a particular altitude. Since the altitude of the datapoints differs between the two datasets, in order to find the average discharge current we first fit an interpolation through each of the datasets. The average PDC profile was then identified by finding the mean of the two interpolations, at the desired altitudes. The interpolations created, as well as the mean profile are shown in figure 4.4:

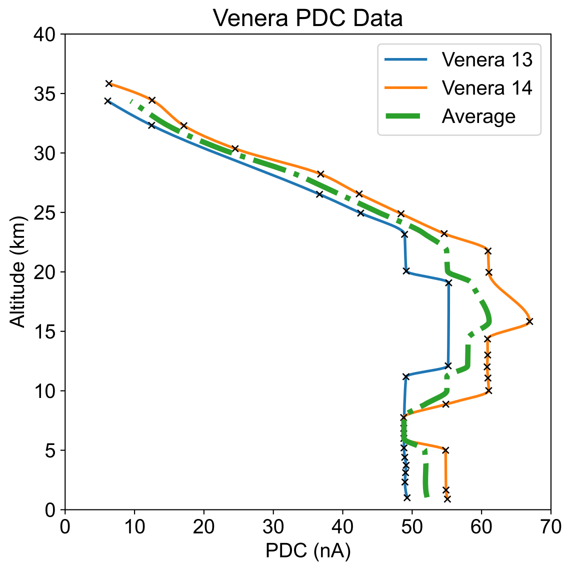

Figure 4.4: Interpolations of the Venera 13 & 14 discharge current data (blue and orange respectively), along with the mean of the two interpolations (green dot-dashed line). The original discharge data for both Venera 13 & 14 has been shown using black crosses.

4.3.2 Standard Atmospheric Properties

Firstly, some atmospheric parameters for Venus' atmosphere were required. For our purposes we assumed that the atmosphere of Venus was 100% CO_2. This is a reasonable assumption to have made, since in actuality the concentration of CO_2 is ~96% [179].

To obtain information on atmospheric profiles, the Venus International Reference Atmosphere [95] (VIRA) was used. This is a model of Venus' atmosphere, and provides data for parameters such as the temperature, pressure, and atmospheric density at several altitudes, for a range of latitudes. For our work, data for the latitudes 0-30° were used. The profiles for temperature, pressure, and density are shown in figure 4.5.

As well as the mass density of the atmosphere, we also require the number density of molecules in the atmosphere. Since we have assumed a 100% CO_2 atmosphere, this is trivial to obtain. The concentration of CO_2 can be obtained by dividing the mass density by the molecular mass of CO_2, i.e.:

$$n_{CO_2} = \frac{\rho_M}{m_{CO_2}} \tag{4.2}$$

where n_{CO_2} is the number density of CO_2 molecules, ρ_M is the mass density of the atmosphere, and m_{CO_2} is the molecular mass of CO_2, i.e 44 amu.

4.3.3 Cloud Data

There is a limited amount of in-situ data on the clouds of Venus. The Pioneer Venus probes carried instrumentation to detect the size and concentration of particles in the Venusian atmosphere. From the pioneer data, it was discovered that there was likely a trimodal size distribution of particles in the atmosphere, however this claim has been contested with claims that one of

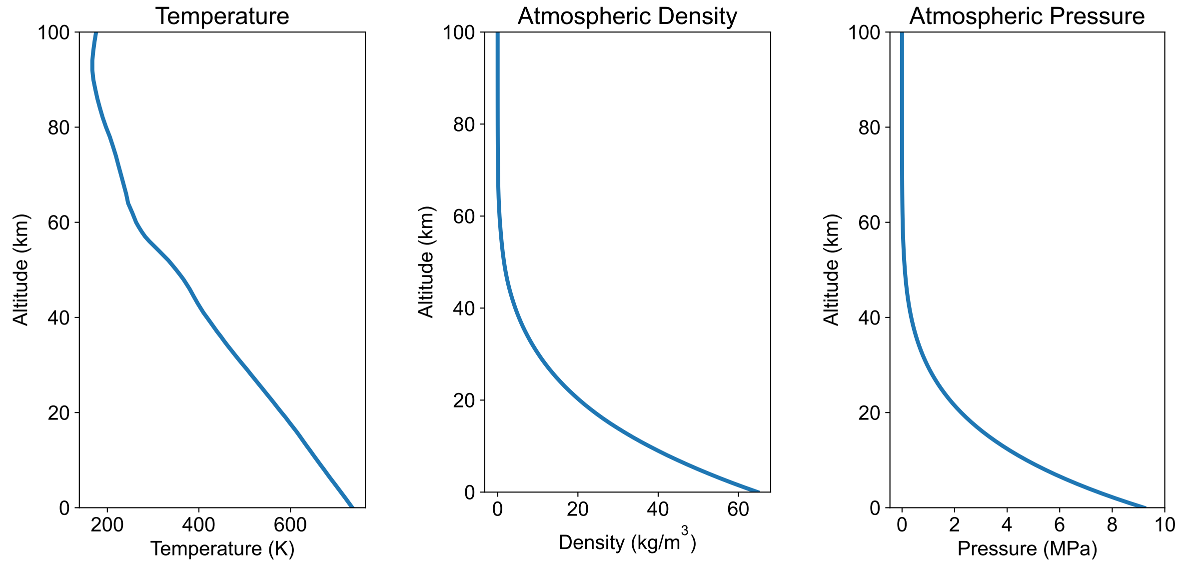

(a) Temperature (b) Density (c) Pressure

Figure 4.5: Figures showing the temperature (a), density (b) and pressure (c) of the Venusian atmosphere, as given by the Venus International Reference Atmosphere [95].

the three modes is just the tail of the distribution. In our analysis we will use the dataset of particle sizes and concentrations produced by Knollenberg and Hunten [98], which assumes that there is indeed a trimodal distribution. This dataset provided details of the size distributions for each of these three modes, with the largest and smallest modes corresponding to log-normal distributions, and the central mode corresponding to a normal distribution.

Through much of our analysis, we will consider these size distributions to be monodisperse; i.e. we assume that each aerosol mode can be well described by considering all the particles in that mode having the same size. The mean size and total number density of particles in each of these three modes has been shown in figure 4.6.

In section 4.4, the impact of the assumption of monodisperse size distributions on the model results is investigated.

4.3.4 Ionisation Rate

The ionisation rate in Venus' atmosphere has previously been determined by Nordheim [138], using a numerical model of a cosmic ray cascade. Nordheim produced several profiles for the ionisation rate, for different times in the solar cycle. Since the Venera 13 & 14 landers reached Venus near to the solar maximum, for our purposes the ionisation rate calculated at solar maximum was used. The profile of this ionisation rate is shown in figure 4.7:

4.3.5 Ion Properties

For our work, several assumptions needed to be made about the properties of ions in Venus' atmosphere.

Following Borucki et al's work [20], it was assumed that only two species of ion were present: One describing the average positive ion, and one describing the average negative ion. The mass

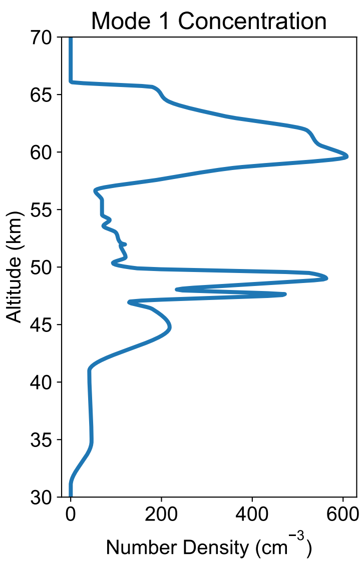

(a) Mode 1 Concentration

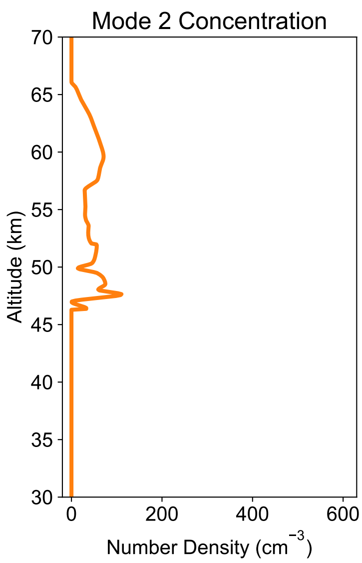

(b) Mode 2 Concentration

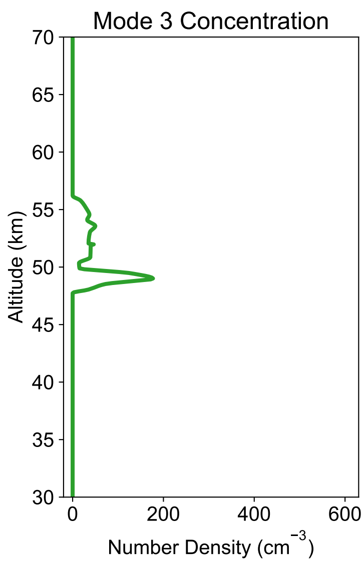

(c) Mode 3 Concentration

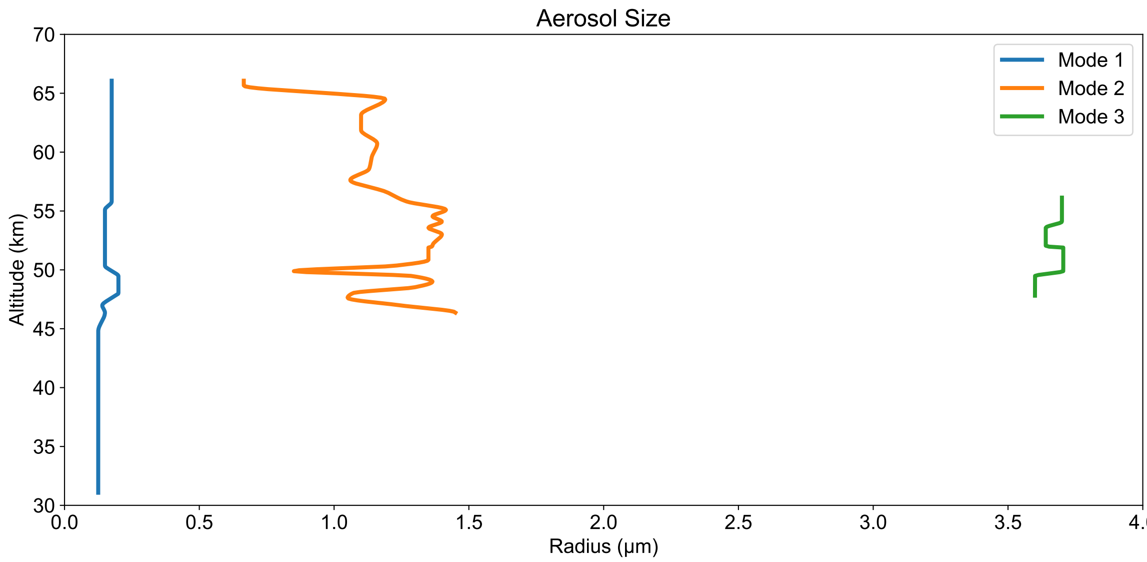

(d) Aerosol Mode Sizes

Figure 4.6: Figures showing the total number density of aerosols in Mode 1 (a), Mode 2 (b) and Mode 3 (c). The mean radius of particles in each of these modes have been shown in (d), with blue, orange, and green lines describing modes 1, 2, and 3 respectively.

of each positive ion was assumed to be 80amu, and the mass of each negative ion was assumed to be 125amu.

Borucki et al's work found that electrons exist in very low concentrations in Venus' upper atmosphere. This concentration of free electrons dropped off rapidly with decreasing height. Due to their high mobility, these electrons provided an important contribution to the atmospheric conductivity at altitudes above ∼65 km, however at lower altitudes, their effect was negligible. For our work, we are mainly concerned with the lower atmosphere, since this is the location where the Venera PDC data was recorded, so we have neglected electrons from our model. Instead it was assumed that the electrons produced from ionisation will rapidly form negative

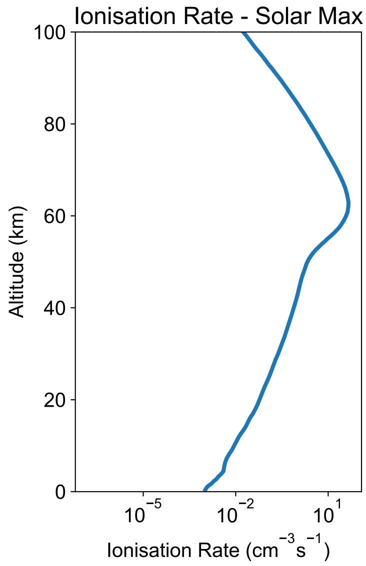

Figure 4.7: Ionisation rate at solar maximum, as a function of altitude, as calculated by [138].

ions.

As well as the mass of ions, we are also required to obtain the mobility of these ions in the atmosphere. The ion mobility is defined as the proportionality factor between an electric field and the the drift velocity of the ion in that electric field. This relation is described in equation 4.3:

$$E = \mu \, v_{drift} \tag{4.3}$$

where E is the electric field strength, v_{drift} is the drift velocity of an ion in that electric field, and μ is the mobility of the ion. To calculate the mobility of ions, the same method as outlined by Borucki et al. has been used [20]. The ion mobility for positive/negative ions is given by:

$$\mu_{\pm} = 3.74 \times 10^{16} (m_{red,\pm} \cdot \kappa)^{-1/2} \, n_{CO_2} \tag{4.4}$$

where κ is the polarisability of CO_2, n_{CO_2} is the number density of CO_2 in the atmosphere, and m_{red} is the reduced mass of the ion and a CO_2 molecule. Note, that the reduced mass of two masses, m_1 and m_2 is given by equation 4.5:

$$m_{red} = \frac{m_1 m_2}{m_1 + m_2} \tag{4.5}$$

A profile of the mobilities of positive and negative ions is shown in figure 4.8.

4.3.6 Spacecraft Descent Speed

To model the electrical charging of a spacecraft descending through Venus' atmosphere, we require information on the descent speed of such a craft. Unfortunately, the descent speed of the Venera spacecraft as a function of altitude is unknown. It was reported, however, that the spacecraft landed at a speed of 7.5 m/s [87]. Additionally, it is known that for the final 47km of

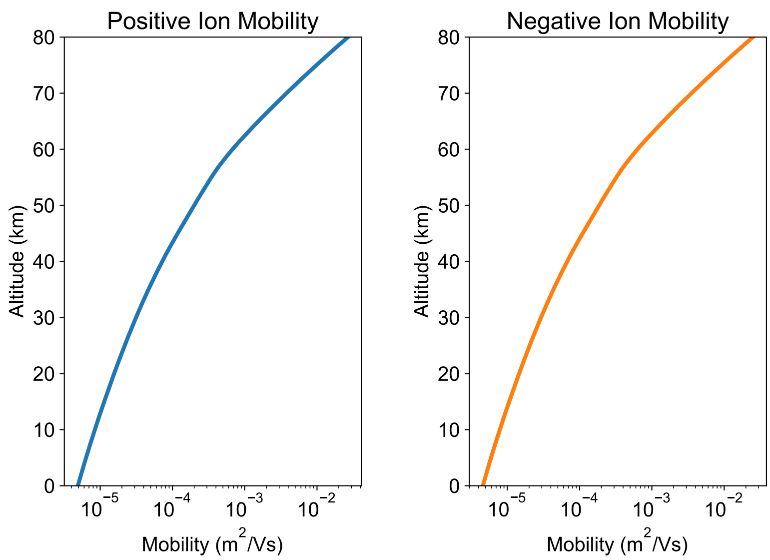

(a) Positive Mobility (b) Negative Mobility

Figure 4.8: Profiles of the ion mobilities used in the VAIL model. (a) shows the positive ion mobility profile, and (b) the negative.

descent, the spacecraft were in the "post-parachute phase" of their descent [87]. At this point, the parachutes which had been slowing the spacecraft since an altitude of 62 km were jettisoned, with the spacecraft using Venus' thick atmosphere to aerobrake [87]. As such, we can estimate the descent speed of the spacecraft, by assuming they were travelling at terminal velocity from 47 km down to the surface.

While at terminal velocity, the forces of weight and drag on the spacecraft will be balanced. Considering the mass of the atmosphere as negligible compared to the mass of the planet, the force of gravity is given by:

$$\mathbf{F_G}(z) = -\frac{GM_{♀}m_{sc}}{(R_{♀}+z)^2}\hat{\mathbf{z}} \tag{4.6}$$

where G is the constant of gravitation, $M_{♀}$ is the mass of Venus, m_{sc} is the mass of the spacecraft, $R_{♀}$ is the radius of Venus, and z is the distance from the surface of the planet, i.e. the altitude. Assuming the spacecraft is travelling vertically downwards, the force of drag will act upwards on the spacecraft. Generally, the force of drag is given by:

$$\mathbf{F_D}(z) = \frac{1}{2}\rho_M v^2 A\, C_D \hat{\mathbf{r}} \tag{4.7}$$

where ρ_M is the mass density of the atmosphere, v is the speed of the spacecraft, A is the cross sectional area of the spacecraft perpendicular to the spacecraft velocity, and C_D is the drag co-efficient.

At terminal velocity, the downwards force of gravity and the upwards drag are balanced, so we obtain:

$$0 = \mathbf{F_G} + \mathbf{F_D} = -\frac{GM_{♀}m_{sc}}{(R_{♀}+z)^2} + \frac{1}{2}\rho_M v^2 A C_D \tag{4.8}$$

Rearranging equation 4.8, the descent speed of the spacecraft can be written:

$$v^2 = \frac{1}{(R_♀ + z)^2\, \rho_M(z)} \left(\frac{2GM_♀ m_{sc}}{A\, C_D} \right) = \frac{1}{(R_♀ + z)^2\, \rho_M(z)} k \tag{4.9}$$

Where k is a collection of constants. We can find the value of k using the landing speed of the spacecraft, $v_{land} \approx 7.5$ km as a boundary condition. At the surface of Venus, we find $z = 0$, so:

$$k = (R_♀\, v_{land})^2\, \rho_M(0) \tag{4.10}$$

This value for k, can then be used in equation 4.9 in order to calculate the terminal velocity at any altitude, using the atmospheric density as provided in section 4.3. The spacecraft speed calculated for the final 50km of descent is shown in figure 4.9. Note that since $R_♀ \gg z$, this profile is approximately proportional to the inverse of the density profile in figure 4.5b.

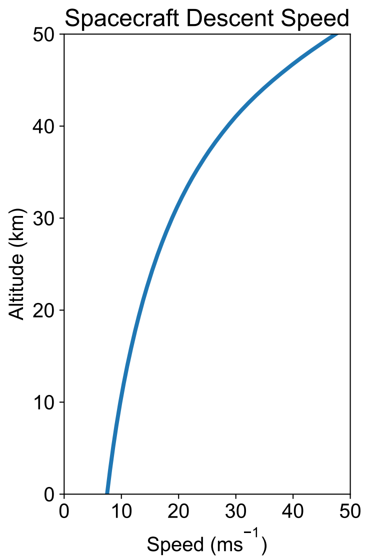

Figure 4.9: Descent speed of the Venera spacecraft, as calculated using equations 4.9 & 4.10.

Note that equations 4.9 & 4.10 will only be valid for the lowest 47km of the atmosphere, as this is where the spacecraft were in their "post parachute" phase. Above this altitude the drag coefficients of the spacecraft will be different due to the presence of parachutes. We have not uncovered any data on the descent speed of the spacecraft at these altitudes, however, so for our purposes we will extend these equations up to the top of our model space. In doing this, processes which are dependent on the spacecraft speed (such as the charging rate, and emitted PDC) will be affected, so we will not consider these properties to be modeled well at altitudes above 47 km.

4.3.7 Corona Onset

The corona onset potential describes the minimum electrical potential required for an object to undergo point discharge. This quantity is dependent on the geometry of the object, as well as the atmospheric medium surrounding it. As mentioned previously, the geometry of the groza-2 discharge electrode was unknown. Additionally, even if details such as the length and sharpness of the electrode were known, it is still non-trivial to determine what the corona onset potential would be. We will develop equations to determine the corona onset potential for the Venera 13 & 14 discharge electrodes, making several approximations.

The breakdown field or dielectric strength of a medium is the maximum electric field which can be present before electrical breakdown occurs. We estimate the size of this breakdown field on Venus via extrapolations from Earth's atmosphere. On Earth, at a pressure of 1 atm (101325 Pa), the dielectric strength of air is 3 MV/m. The dielectric strength of CO_2 is reported to be 0.95 × the dielectric strength of air. Additionally, We can assume that the dielectric strength of a gas is directly proportional to its pressure. This assumption is motivated by Paschen's Law - an empirical relationship which how the pressure and size of the gap between two electrodes affects the potential difference required for breakdown between them [115].

Based on these properties, We can determine the breakdown field for Venus' atmosphere via:

$$E_{breakdown}(z) = 0.95 \times (E_{breakdown})|_{(air,1atm)} \frac{P(z)}{P(1atm)} \tag{4.11}$$

$$E_{breakdown}(z) = \frac{0.95 \times 3 \times 10^6}{101325} P(z) \tag{4.12}$$

for $P(z)$ in Pascals. A profile of the calculated breakdown field has been shown in figure 4.10

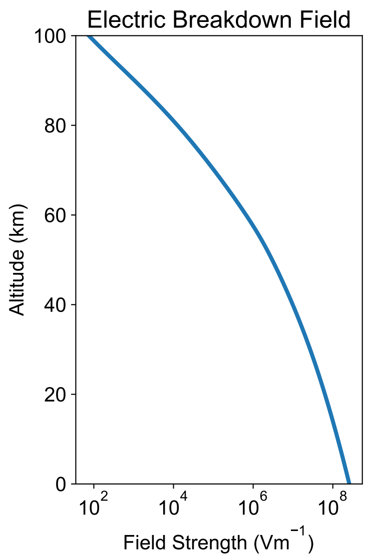

Figure 4.10: Profile of the electrical breakdown field calculated for Venus' atmosphere.

The onset of corona discharge is expected to occur when the electric field is below this dielectric strength. For our purposes, we assume that when the maximum electric field is some fraction of the dielectric strength, point discharge will occur. We express this required electric field as:

$$E_{Corona} = \eta E_{breakdown} \tag{4.13}$$

where η is some constant, referred to as the "breakdown fraction" in this work. The importance of the value of the breakdown fraction is investigated in section 4.6, however a value of 0.001 will typically be used, based on considerations from terrestrial investigations.

The magnitude of the maximum electric field is dependent on both the electric potential of the spacecraft and the geometry of the point discharge electrode. From electrostatic modelling, estimates have previously been made of the electric field enhancement of the Venera discharge electrodes [173, 176]. The electric field enhancement is a quantity given by the ratio of the maximum electric field surrounding an object to the typical electric field that would be expected if not for the perturbation to the field, i,e:

$$E_{max} = \gamma E_{typical} \tag{4.14}$$

where γ is the electric field enhancement, E_{max} is the maximum electric field, and $E_{typical}$ is the electric field that would be present if not for the perturbation. The electrostatic modelling of the Venera spacecraft yielded an electric field enhancement ≈ 10 at the tip of the discharge electrode.

If we model the spacecraft as being approximately spherical, then we can find the undisturbed electric field surrounding the spacecraft in terms of the spacecraft potential, V:

$$E_{typical} = \frac{V}{r} \tag{4.15}$$

where r is the distance from the center of the spacecraft. Combining equations 4.14 and 4.15, we can find the maximum electric field (at the tip of the discharge electrode) in terms of this potential:

$$E_{max} = \gamma \frac{V}{r} \tag{4.16}$$

where r is the distance to the tip of the discharge electrode.

Finally, we would expect point discharge to occur when the electric field at this electrode is equal to the electric field required for point discharge. This can be shown by equating the maximum electric field from equation 4.16 to the corona field from 4.13 to give:

$$\eta E_{breakdown} = \gamma \frac{V}{r} \tag{4.17}$$

Re-arranging, we find the minimum spacecraft potential required for point discharge to occur is given by:

$$V_{corona}(z) = \frac{r\eta}{\gamma} E_{breakdown}(z) \tag{4.18}$$

where the corona onset potential, V_{corona}, is a function of altitude, z, due to the pressure dependence of the breakdown field.

4.4 VAIL - Electrical Environment Calculations

As a first step in our modelling approach, the electrical properties of Venus' atmosphere were determined. This involved first determining the concentration of positive and negative ions in the atmosphere, before considering properties such as the conductivity and electric field. The calculations involved to determine these parameters are outlined in the following section.

The production of ions in the atmosphere occurs as a result of ionisation processes producing positive ions and free electrons. For our work, we assume that all free electrons will readily form negative ions, so this ionisation process produces positive and negative ions in equal amounts. The production rate is thus given by:

$$\left(\frac{dn_{\pm}}{dt}\right)_P = q \tag{4.19}$$

where $n_{\pm}$ is the concentration of positive/negative ions, and q is the ionisation rate. This ionisation rate has previously been calculated for Venus, as was discussed in section 4.3. This profile of ionisation rate with height will be used for our analysis.

Ion-ion recombination occurs when positive and negative ions combine, and neutralise each other's electric charge. The rate of this process is dependent on the number of ions of each polarity present in the atmosphere, given by:

$$\left(\frac{dn_{\pm}}{dt}\right)_R = -\alpha n_+ n_- \tag{4.20}$$

where α is the ion-ion recombination coefficient. The evaluation of this coefficient is discussed in section 4.4.1.

Finally, ion-aerosol attachment occurs when an atmospheric ion is collected by a relatively massive aerosol particle, reducing the mobility of the ion significantly. This process does not reduce the space charge caused by the presence of the ion, however the reduction in mobility means the ion no longer has a significant effect on the atmospheric conductivity. The rate of this process is given by:

$$\left(\frac{dn_{\pm}}{dt}\right)_A = -n_{\pm}\beta_{\pm}N \tag{4.21}$$

where N is the concentration of aerosol particles, and β is the ion-aerosol attachment coefficient. The evaluation of this coefficient is discussed in section 4.4.2.

The total rate of change of ion concentration can be determined by combining equations 4.19, 4.20, & 4.21. We find the total rate of change is given by:

$$\frac{dn_{\pm}}{dt} = \left(\frac{dn_{\pm}}{dt}\right)_P + \left(\frac{dn_{\pm}}{dt}\right)_R + \left(\frac{dn_{\pm}}{dt}\right)_A \tag{4.22}$$

$$\frac{dn_{\pm}}{dt} = q - \alpha n_+ n_- - n_{\pm}\beta_{\pm}N \tag{4.23}$$

The equilibrium ion concentration is derived from this equation in section 4.4.3.

4.4.1 Ion-Ion Recombination Coefficient

Ion-ion recombination proceeds via a number of processes. Each of these processes has a different recombination rate. For Venus's atmosphere, the important terms are the 3-body Thomson term, $\alpha_T \, n_{CO_2}$, the binary term, α_B, and the high pressure diffusion controlled term, α_{HP} [20]. The total ion-ion recombination coefficient is found by taking the reciprocal sum of these individual terms [20]:

$$\frac{1}{\alpha} = \frac{1}{\alpha_T \, n_{CO_2}} + \frac{1}{\alpha_B} + \frac{1}{\alpha_{HP}} \tag{4.24}$$

Thomson Recombination

The 3-body Thomson term describes ions recombining with the assistance of an atmospheric molecule. For Venus, this would typically be a CO_2 molecule. The rate of ion-ion recombination will depend on how readily available these CO_2 molecules are, hence the inclusion of the CO_2 number density in the recombination rate term. The recombination coefficient for the 3-body Thomson process on Venus is given by equation 4.25 [20].

$$\alpha_T = A_T \times \left(\frac{B_T}{T}\right)^{2.5} \tag{4.25}$$

where T is the atmospheric temperature, $A_T = 2{\times}10^{-37}$ m^{6}s^{-1}, and $B_T = 300$ K.

Binary Recombination

The Binary recombination term describes a complex process where two ions will neutralise one another, without the influence of an atmospheric molecule. This term is given by equation 4.26 for Venus [20]:

$$\alpha_B = A_B \times T^{\frac{1}{2}} \tag{4.26}$$

where T is again temperature, and $A_B = 9{\times}\ 10^{-13}$ m^{3}s^{-1}.

High Pressure Recombination

The High Pressure diffusion controlled term describes ions of opposite polarity drifting towards one another via the Coulomb force. This mechanism was the first process proposed to explain ion-ion recombination on Earth [114]. It was found, however, that the process requires very low temperatures or a very dense gas for it to occur, and thus the mechanism is not important for recombination at Earth [114]. It is believed, however, that this term would be important for ions in the deep atmosphere of Venus, where the pressures greatly exceed those on Earth. The high pressure term is given by equation 4.27 [20]:

$$\alpha_{HP} = \frac{e}{\epsilon_0}(\mu_+ + \mu_-) \tag{4.27}$$

where ϵ_0 is the permittivity of free space, e is the elementary charge, and μ_+, μ_- are the mobilities of positive and negative ions respectively.

Overall Considerations

The profiles of the three recombination terms, with height, are shown in figure 4.11.

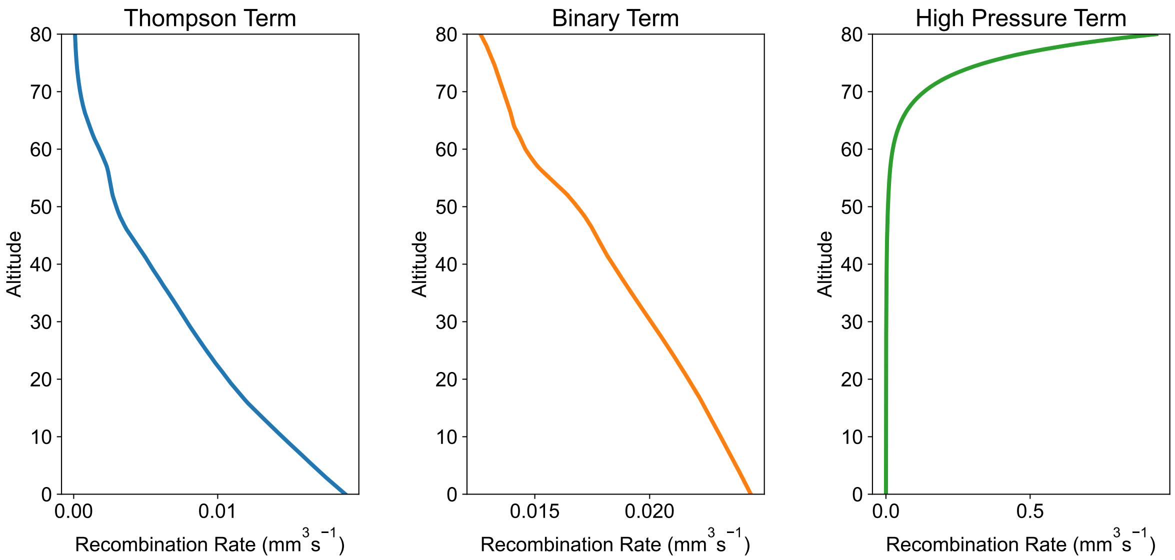

(a) Thomson Term (b) Binary Term (c) High Pressure Term

Figure 4.11: Profiles of the three ion-ion recombination rates as calculated by VAIL. (a) shows the Thomson recombination rate, (b) the Binary recombination rate, and (c) the High Pressure recombination rate.

The total ion-ion recombination rate as calculated in equation 4.24 has been shown in figure 4.12. In order to see the relative importance of each of the terms in calculating this result, the profiles of each recombination rate have been overlaid on the same axes. At all altitudes considered, the binary term is significantly larger than the other terms, thus it is never dominant in the reciprocal sum. It can be clearly seen in figure 4.12 that the total recombination rate is strongly dependent on the high pressure term at low altitudes, and on the three body term at high altitudes.

4.4.2 Ion-Aerosol Attachment

The ion-aerosol attachment term in equation 4.23 is largely simplified. In reality, the coefficient β will vary depending on the charge and size of an aerosol, and we will often need to calculate this term when considering aerosol distributions where there are a range of charges and sizes present. In order to capture this complexity, the ion-aerosol attachment can be written as:

$$\beta_{\pm}N = \sum_i \sum_j (\beta_{\pm}^{i,j} N^{i,j}) \tag{4.28}$$

where i,j are indices corresponding to the radius and electric charge of the aerosol particle.

We will need to determine both the ion-aerosol attachment coefficient and the aerosol number density as functions of aerosol size and charge. These will both be discussed in this section.

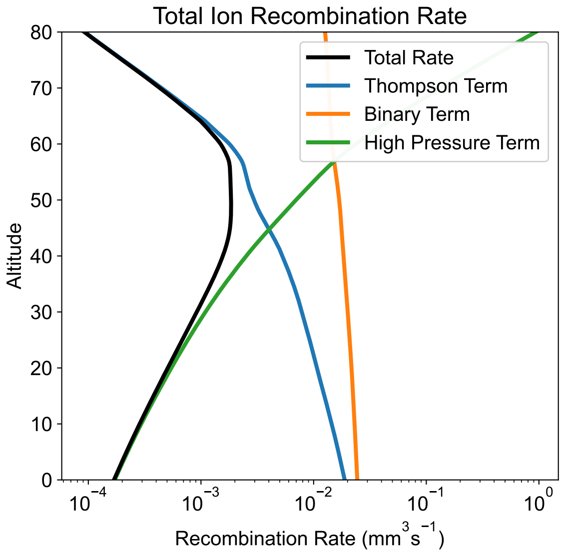

Figure 4.12: Height profiles of the total recombination rate, and the three component terms on the same axes.

Attachment Coefficient

Previously, several methods for calculating the ion-aerosol attachment coefficient have been developed. Some of these equations incorporate effects such as image charges and the ambient electric field [83]. For simplicity, and the ability to be calculated via the analytical approach used here, the simpler equations, developed by Gunn [58] will be used. The approach used by Gunn to derive these equations will be discussed here.

Gunn noted that the ion-aerosol attachment coefficient can be determined by considering the "current" of ions flowing onto the surface of an aerosol. This current is related to the ion-aerosol attachment coefficient via equation 4.29:

$$nN\beta = \frac{IN}{e} \tag{4.29}$$

where n, N, β and e are as before, and I is the ion current.

Gunn determined the value of this current by first considering the effects of ion diffusion and drift velocity. The current transported to an aerosol (in units of esu/s) is given by equations 4.30 and 4.31 for positive and negative ions respectively.

$$I_+ = \frac{\pi a^2 eC_+ n_+ exp\left[\frac{-e}{k_B T}(\psi_b - \psi_0)\right]}{1 + \frac{a^2 C_+}{4Q\mu_+}\left\{1 - exp\left[\frac{-e}{k_B T}(\psi_b - \psi_0)\right]\right\}} \tag{4.30}$$

$$I_- = \frac{\pi a^2 eC_- n_- exp\left[\frac{-e}{k_B T}(\psi_b - \psi_0)\right]}{1 + \frac{a^2 C_-}{4Q\mu_-}\left\{exp\left[\frac{-e}{k_B T}(\psi_b - \psi_0)\right] - 1\right\}} \tag{4.31}$$

where a is the aerosol radius, Q is the aerosol charge, and n, C, and µ are the number density, average thermal velocity, and mobility of the ions respectively, with the subscript differentiating between positive and negative ions. ψ_b and ψ_0 describe the electrical potential at one free path above the surface of the aerosol, and at a far field distance of R_0 from the aerosol.

Gunn went on to make the assumptions that the molecular diffusion was large compared to eddy diffusion, and that the spacing of aerosols was large compared to the radius of these aerosols. These assumptions allow the currents to be written in simpler forms, as:

$$I_+ = \frac{4\pi Q e N_+ \mu_+}{exp\left[\frac{eQ}{ak_BT}\right] - 1} \tag{4.32}$$

$$I_- = \frac{4\pi Q e N_- \mu_-}{1 - exp\left[\frac{eQ}{ak_BT}\right]} \tag{4.33}$$

Finally, by using equation 4.29 and equations 4.32 and 4.33, and by converting the current from esu/s to amps, we can find equations for the ion-aerosol attachment coefficient [190]:

$$\beta_+ = \frac{1}{\epsilon_0} \frac{Q\mu_+}{exp\left[\frac{Qe}{4\pi\epsilon_0 a}\frac{1}{k_BT}\right] - 1} \tag{4.34}$$

$$\beta_- = \frac{1}{\epsilon_0} \frac{Q\mu_-}{1 - exp\left[\frac{-Qe}{4\pi\epsilon_0 a}\frac{1}{k_BT}\right]} \tag{4.35}$$

Note that these equations are undefined for zero aerosol charge (Q=0). In order to find an equation for the ion-aerosol attachment in this case, we can expand the Taylor series of the denominator to give equation 4.36 for positive ions.

$$\beta_+\big|_{Q=0} = \frac{4\pi a k_B T \mu_+}{e} \tag{4.36}$$

An equivalent equation is found for negative ions, but with μ_- in place of μ_+.

Aerosol Size Distributions

As mentioned in section 4.3, instead of considering a full distribution of all aerosol sizes, several modal values were identified. The ion-aerosol attachment coefficient was then determined for each of these modal values, and used to find the full ion-aerosol attachment term.

Aerosol Charge Distributions

In order to calculate the ion-aerosol attachment term, we require some information on the charge distribution of aerosols. Since positive ions are more mobile than negative ions in Venus' atmosphere, it is expected that they will more readily become attached to aerosols, and as such, the average charge of aerosols will become offset from zero. The equilibrium aerosol distribution which would be obtained in this way has been studied previously by Clement and Harrison [38]. This investigation led to an equation for the ratio of the concentration of particles carrying a given charge j, N_j to the concentration of uncharged particles, N_0:

$$\frac{N_j}{N_0} = \frac{x^j}{j^\lambda} \, sinh(\lambda j) \, exp(-j^2\lambda) \tag{4.37}$$

where x is the ion asymmetry ratio given by:

$$x = \frac{n_+\mu_+}{n_-\mu_-} \tag{4.38}$$

for positive (negative) ion number density n_+ (n_-), and mobility μ_+ (μ_-), and λ is given by:

$$\lambda = \frac{e^2}{8\pi\epsilon_0 k_B T}\frac{1}{a} \tag{4.39}$$

where T is the temperature, a is the radius of the particle, and e, ϵ_0, k_B are the elementary charge, permittivity of free space, and Boltzmann constant respectively.

The form of equation 4.37 means that to determine the number density of particles with a certain charge, we need to know the number density of uncharged particles. To get around this, we can instead find the ratio of N_j to the number density of particles of all charges, N_T:

$$\frac{N_j}{N_T} = \left(\frac{N_T}{N_0}\right)^{-1}\frac{N_j}{N_0} = \left(\sum_{i=-\infty}^{i=\infty}\frac{N_i}{N_0}\right)^{-1}\frac{N_j}{N_0} \tag{4.40}$$

where N_i/N_0 is determined using equation 4.37. We can then find the number density of particles of a particular charge, j, from equation 4.40 if we are given the total particle concentration. In reality, we are not able to calculate N_i/N_0 across an infinite range of is, in order to calculate N_T/N_0. As such, care has to be taken to ensure that a sufficient range of is are used, such that the limit is being approximated correctly.

To calculate the charge distribution in this way we require knowledge of the equilibrium ion asymmetry ratio. This is determined via calculations of the positive and negative ion concentrations, which in turn depend on the aerosol distribution. As such, we are unable to analytically determine the aerosol distribution.

For the remainder of this work, we will instead consider the net charge on aerosols to be neutral when considering the attachment rate of ions, and so set the ion asymmetry ratio to 1. Note that when we consider the effects of space charge in the atmosphere, then we do not make this assumption of neutral aerosol charge; instead the assumption is made that the total charge density (from both aerosols and free ions) is zero.

4.4.3 Ion Concentration Calculation

From equation 4.23, we find the rate of change of the concentration of positive and negative ions are given by:

$$\frac{dn_+}{dt} = q - \alpha n_+ n_- - n_+\beta_+ N \tag{4.41}$$

and

$$\frac{dn_-}{dt} = q - \alpha n_+ n_- - n_-\beta_- N \tag{4.42}$$

respectively. In our equilibrium state, these rates of change are zero, so can write:

$$q - \alpha n_+ n_- = \sum(\beta_+ N)\, n_+ \tag{4.43}$$

and for negative ions,

$$q - \alpha n_+ n_- = \sum (\beta_- N)\, n_- \tag{4.44}$$

combining equations 4.43 and 4.44 gives:

$$n_- = \frac{\sum(\beta_+ N)}{\sum(\beta_- N)} n_+ = \xi n_+ \tag{4.45}$$

where ξ is the ratio of the total positive ion-aerosol attachment coefficient to the negative ion-aerosol attachment coefficient.

if we substitute equation 4.45 into equation 4.43, then we find:

$$0 = q - \alpha (n_+)^2 \xi - \sum(\beta_+ N) n_+ \tag{4.46}$$

We can solve to find the quadratic roots for this equation. Disregarding the unphysical root, we find a result for the number density of positive ions:

$$n_+ = \frac{\sqrt{\left(\sum(\beta_+ N)\right)^2 + 4q\xi\alpha} - \sum(\beta_+ N)}{2\alpha\xi}, \tag{4.47}$$

and for negative ions we find:

$$n_- = \frac{\sqrt{\left(\sum(\beta_- N)\right)^2 + \frac{4q\alpha}{\xi}} - \sum(\beta_- N)}{\frac{2\alpha}{\xi}} \tag{4.48}$$

4.4.4 Electrical Parameters

There are additional electrical parameters that can be determined for Venus' atmosphere once the ion number densities have been found. First is the conductivity of the atmosphere; the positive and negative ions in the atmosphere both contribute towards the atmospheric conductivity. Assuming that all ions of a given polarity have the same mobility, the contribution to the conductivity from each ion polarity is given by:

$$\sigma_\pm = e \mu_\pm n_\pm \tag{4.49}$$

where $\mu_\pm$ is the ion mobility for positive/negative ions, and e is the elementary charge. The total atmospheric conductivity is then given by:

$$\sigma_{Total} = \sigma_+ + \sigma_- \tag{4.50}$$

Next, we are able to determine the columnar resistance of the atmosphere. The columnar resistance at an altitude z is given by the integral of the resistivity of the atmosphere up to that altitude, where the resistivity is given by the inverse of the conductivity. That is, the resistivity is given by:

$$\rho_R = \frac{1}{\sigma_{Total}} \tag{4.51}$$

and the columnar resistance at an altitude z is given by:

$$R_C(z) = \int_0^z \rho_R \, dz' \tag{4.52}$$

4.4.5 Effect of Global Atmospheric Electric Circuit

As has been discussed in Chapter 2, it is unknown if a global atmospheric electric circuit is present in Venus' atmosphere. If such a circuit was present, then the fair weather conduction current would have important effects on the movement of ions in the atmosphere. For a given atmospheric conductivity, σ_{Total}, we can use Ohm's law to determine the atmospheric electric field when a constant current density $\mathbf{J}$ flows vertically in the atmosphere:

$$\mathbf{E} = \frac{\mathbf{J}}{\sigma_{Total}} \tag{4.53}$$

Additionally, we can determine the atmospheric potential at a given altitude using the definition of electric potential given by:

$$V = -\int \mathbf{E} \cdot d\mathbf{l} \tag{4.54}$$

If we set the atmospheric potential to be equal to zero at the planet's surface, we can write:

$$V_a(z) = -\int_0^z E dz' \tag{4.55}$$

Then, for an upwards flowing current density of magnitude J_C, we can write:

$$V_a(z) = -\int_0^z \frac{J_C}{\sigma_{Total}} dz' = -J_C \int_0^z \rho_R \, dz' \tag{4.56}$$

so,

$$V_a(z) = -J_C R_C(z) \tag{4.57}$$

These electrical parameters will be used to determine the charge collected by a spacecraft descending through the atmosphere. The calculations involved in this will be discussed in section 4.5.

In addition to requiring a changing atmospheric potential with height, the presence of a vertical conduction current will imply a drift of ions of both polarities in the atmosphere. This means that the ion number densities calculated via equations 4.47 and 4.48, as well as the atmospheric conductivities derived from these values, will be perturbed. The change to the ion number densities is governed by the continuity equation:

$$\frac{\partial \rho}{\partial t} = -\nabla \cdot \mathbf{J} \tag{4.58}$$

for charge density ρ and current density $\mathbf{J}$. We can consider the contributions to the conduction current density, J_C, from the positive and negative ions separately. Again, using ohms law, we find the current density for positive ions as:

$$J_+ = e n_+ \mu_+ E \tag{4.59}$$

and for negative ions, we find:

$$J_- = en_-\mu_-E \tag{4.60}$$

The current densities J_+, J_- are related to the total conduction current density via:

$$J_C = J_+ + J_- \tag{4.61}$$

So, using equation 4.59 along with equation 4.60, we find that the rate of change of the number density of positive ions, driven by the atmospheric electric field, is given by:

$$\left(\frac{dn_+}{dt}\right)_E = -\nabla \cdot J_+ = -\frac{d}{dz}(en_+\mu_+E) \tag{4.62}$$

and for negative ions,

$$\left(\frac{dn_-}{dt}\right)_E = -\frac{d}{dz}(en_-\mu_-E) \tag{4.63}$$

If we return to equation 4.22 and include the additional rate of change terms for the vertical movement of ions, given by equations 4.62 and 4.63, we find:

$$\frac{dn_\pm}{dt} = \left(\frac{dn_\pm}{dt}\right)_P + \left(\frac{dn_\pm}{dt}\right)_R + \left(\frac{dn_\pm}{dt}\right)_A + \left(\frac{dn_\pm}{dt}\right)_E \tag{4.64}$$

so, we obtain differential equations for the positive and negative ion number densities:

$$\frac{dn_+}{dt} = q - \alpha n_+n_- - n_\pm\beta_+N - \frac{d}{dz}(en_+\mu_+E) \tag{4.65}$$

$$\frac{dn_-}{dt} = q - \alpha n_+n_- - n_\pm\beta_-N - \frac{d}{dz}(en_+\mu_+E) \tag{4.66}$$

Given that E is a function of both the positive and negative ion number densities, it can be noted that the additional terms in these equations are dependent on the number densities of both positive and negative ions, and their gradient; i.e:

$$-\frac{d}{dz}(en_+\mu_+E) = \chi\big(n_+, n_-, \frac{dn_+}{dz}, \frac{dn_-}{dz}\big) \tag{4.67}$$

$$-\frac{d}{dz}(en_-\mu_-E) = \chi\big(n_-, n_+, \frac{dn_-}{dz}, \frac{dn_+}{dz}\big) \tag{4.68}$$

for some function χ. It can be seen that the ion-aerosol balance equations for a particular altitude now have a complicated dependence on the balance equations at other altitudes. It has been concluded that unlike for equations 4.41 & 4.42 there is not a simple analytical solution to these equations. In future it would be desirable to include these terms explicitly by determining the solution to the ion-aerosol balance equations numerically, however for our purposes we will evaluate the electrical parameters while assuming the vertical flux of ions is negligible compared to the recombination and attachment terms.

As such, when we consider a global circuit / conduction current to be present in the atmosphere, this will not perturb the ion concentrations in the atmosphere; the effects of this global circuit will be to imply the presence of a vertical electric field, and an atmospheric potential which varies with altitude.

4.4.6 Model Evaluation

Comparison Against Previous Model

In order to confirm that our model was performing as expected, we have compared some of the results against the values obtained by Borucki et al's numerical ionisation model [20]. In order to make this a reasonable comparison, the model inputs used by Borucki et al. were used, rather than the inputs described in section 4.3. This involved changing the temperature, pressure, ionisation rate, and aerosol size and concentration profiles.

The number density of positive and negative ions produced from Borucki et al's model are compared here, along with the total conductivity of the atmosphere.

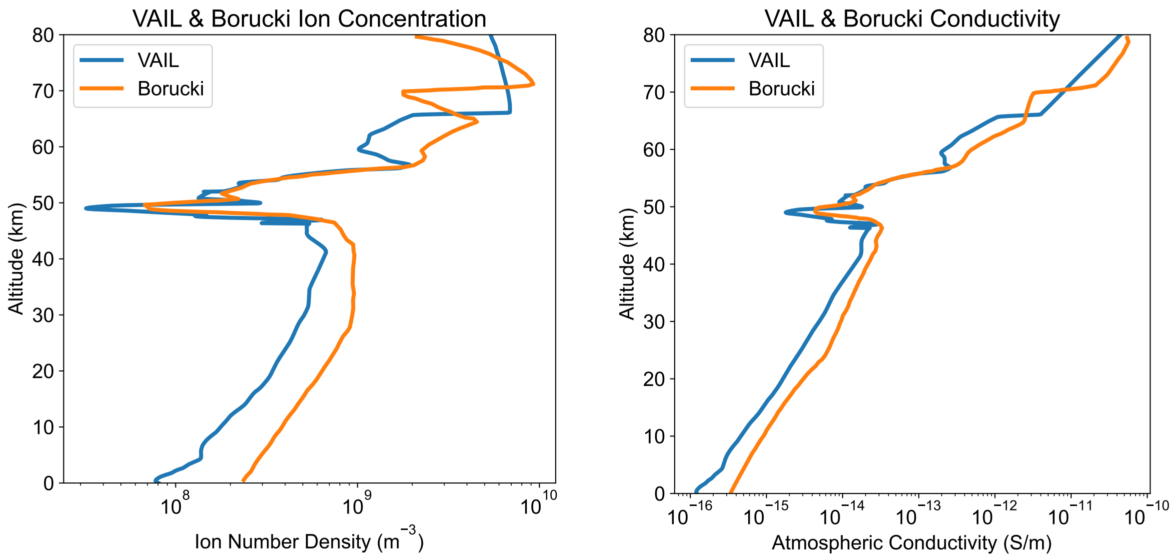

(a) Mean Ion Concentration

(b) Atmospheric Conductivity

Figure 4.13: Model results from the VAIL model developed here, compared against the previous ionisation model developed by Borucki et al. [20]. (a) shows the mean ion concentration profile from VAIL in blue compared against the ion concentration profile from Borucki et al. in orange. (b) shows the total atmospheric conductivity calculated by VAIL in blue, with this result from Borucki et al. in orange.

As can be seen, our VAIL model provides values at a similar order of magnitude to Borucki et al's model. We thus confirm that the results which are being output are reasonable.

Aerosol Distribution Assumptions

Next, we investigated the validity of the assumption made in section 4.3.3; i.e that the aerosol size distributions for each mode were well described by a single particle size. To test this assumption, a better approximation of the full particle distribution for each mode was used - with multiple particle sizes selected for each mode. The size and concentrations of these particles were found by reproducing the distributions described by Knollenberg and Hunten.

These were lognormal distributions for the mode 1 & 3 aerosols, and a Gaussian distribution for the mode 2 aerosol. These distributions found the aerosol concentration as a function of aerosol radius. The distributions of aerosol sizes are shown for an altitude of 55km in figure 4.14a, where the distribution for each mode was calculated for positive radius values in the range $[\mu - 2\sigma, \mu + 2\sigma]$, where μ and σ are the mean and standard deviations for each distribution, respectively. Additionally, profiles of the mean size and standard deviation for each aerosol mode are shown in figure 4.14b; For each mode, the mean size is shown as a solid line, with the region corresponding to $\pm$ 1 standard deviation indicated by a shaded area.

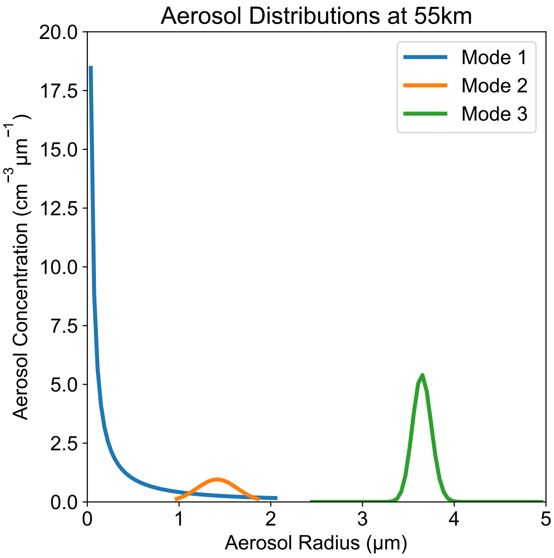

(a) Size Distributions at 55km.

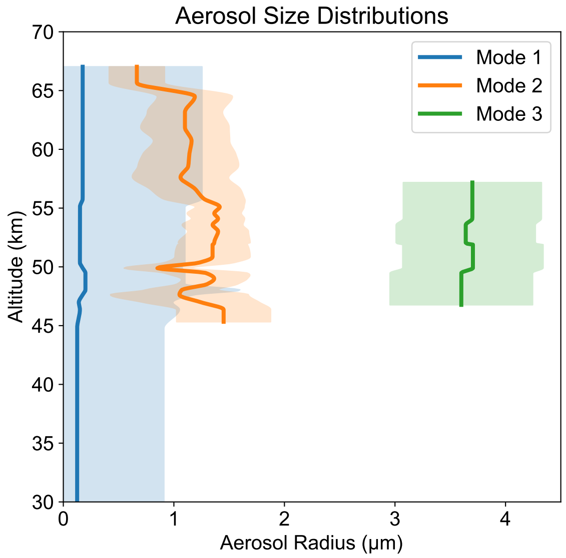

(b) Size of Aerosol Distributions

Figure 4.14: Shape of the aerosol size distributions used. (a) shows the shape of the size distributions for each of the three aerosol modes at 55km. The mode 1, 2, and 3 aerosols are shown using blue, orange, and green lines respectively. The distributions have been shown for positive radius values in the range of $\pm$ 2 standard deviations from the mean. (b) shows the profiles of the size of each of the 3 aerosol modes, with shaded areas corresponding to $\pm$ 1 standard deviation from this value. The mode 1, 2, 3 aerosols are shown using blue, orange, green lines/shaded areas respectively.

The positive ion number density calculated using these size distributions was then compared against the results found when monodisperse distributions were assumed. The comparison is shown in figure 4.15.

It was found from this comparison that there is a slight change to the ion number density when the full aerosol size distribution was included. The ion concentrations found when the full aerosol distribution was used were a similar order of magnitude, but slightly decreased from the concentrations found for the monodisperse distributions. For the remainder of this work, the monodisperse approximation will be used, however the limitations of this approximation should be noted. In section 4.7, the implications of this approximation are discussed further.

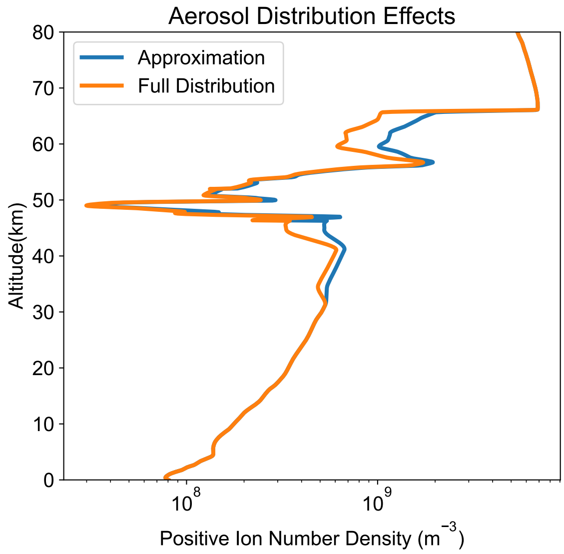

Figure 4.15: Comparison of the positive ion number densities calculated for two different aerosol size distribution regimes. The result found from assuming monodisperse distributions is shown in blue, and the result found from considering the size distributions fully is shown in orange.

Interpolators

In order to show that our results from the VAIL model are independent of the interpolation function used, we have determined the ion number density using a number of these interpolators. The positive ion concentration determined using a linear, cubic, and PCHIP interpolator are compared in figure 4.16.

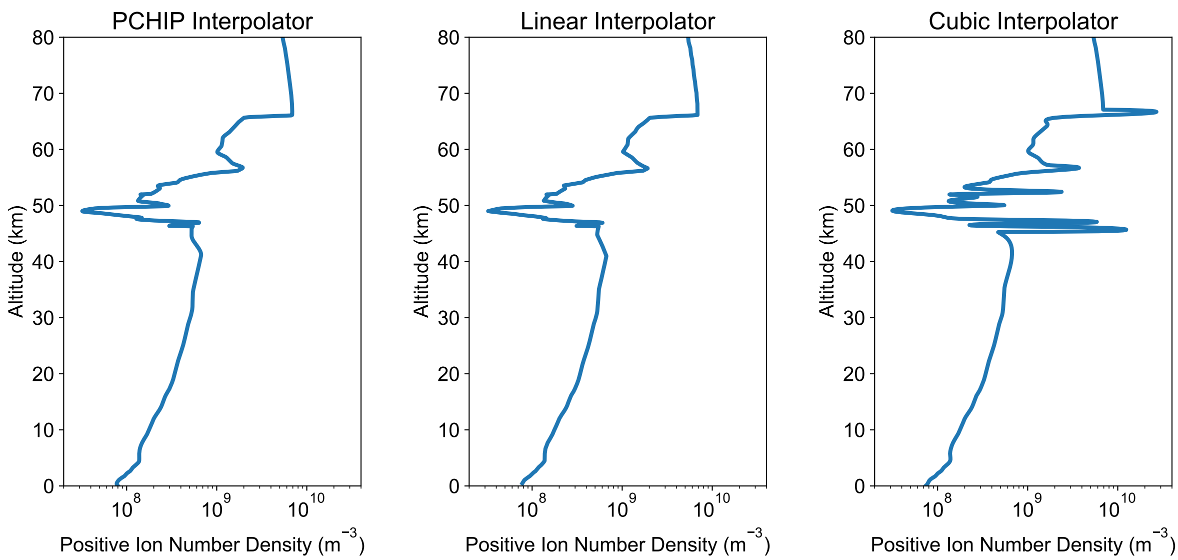

(a) PCHIP

(b) Linear

(c) Cubic

Figure 4.16: Positive ion number density profiles as calculated using different interpolators. (a) shows the result found using the PCHIP interpolator which is used in the remainder of this work. (b) shows the result found using a linear interpolator. (c) shows the result found using a cubic interpolator.

As can be seen in figure 4.16, the ion concentrations found using each of the three interpolators broadly agree, however there is some deviation between the cubic interpolator and the other two interpolators in the cloud layers; the ion concentration found for the cubic interpolator features several sharp peaks at certain altitudes. It is believed that the reason for these sharp peaks is the overshoots that were discussed in section 4.3. These overshoots are likely only present within the cloud layer since the cloud data was provided at a very coarse resolution. At other points in the atmosphere, the cubic interpolator is able to smoothly fit to the data, without large overshoot. For the remainder of the work, the PCHIP interpolator will be used, due to the advantages discussed in section 4.3.

4.4.7 Model Results

A number of results as calculated by the VAIL model are reported in this section. First, the number density of positive and negative ions were determined. Profiles of these quantities are shown in figure 4.17.

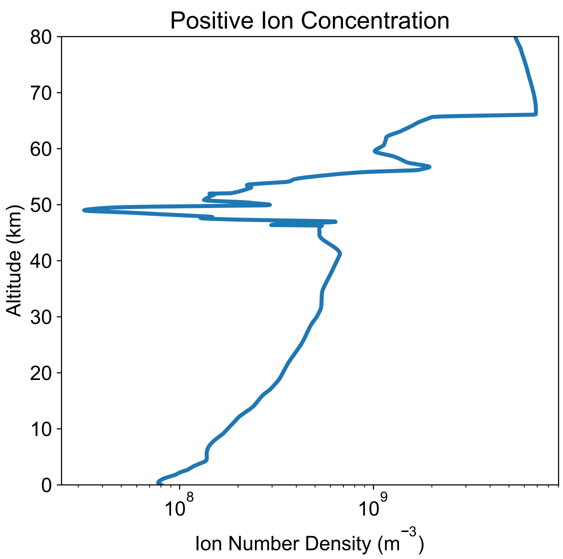

(a) Positive Ion Concentration

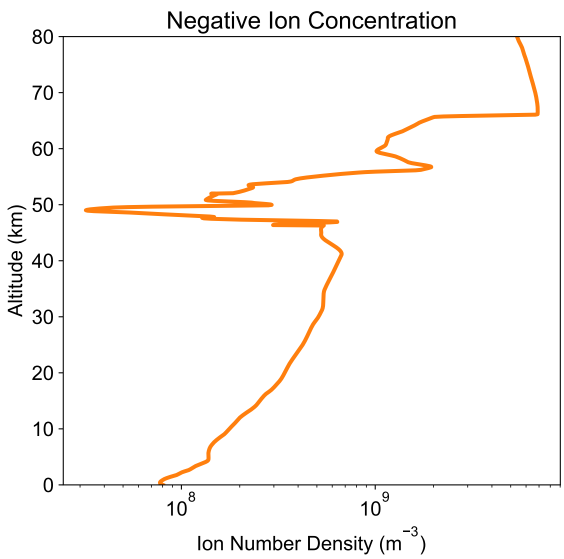

(b) Negative Ion Concentration

Figure 4.17: Ion concentration profiles as calculated by the VAIL model. (a) shows the profile for positive ions, and (b) the profile for negative ions.

From these quantities, the conductivity of the atmosphere was calculated. The profile of this conductivity is shown in figure 4.18a. This quantity allows the columnar resistance of the atmosphere to be calculated, as is shown in figure 4.18b.

If we assume that there is a global atmospheric electric circuit present, then we can find further electrical results. Given the magnitude and polarity of the conduction current, we are able to find profiles for the atmospheric electric field, and the atmospheric potential. These results are shown in figures 4.19a and 4.19b respectively for a conduction current comparable to that on Earth: a conventional current of 2pA/m^2 in a downwards direction.

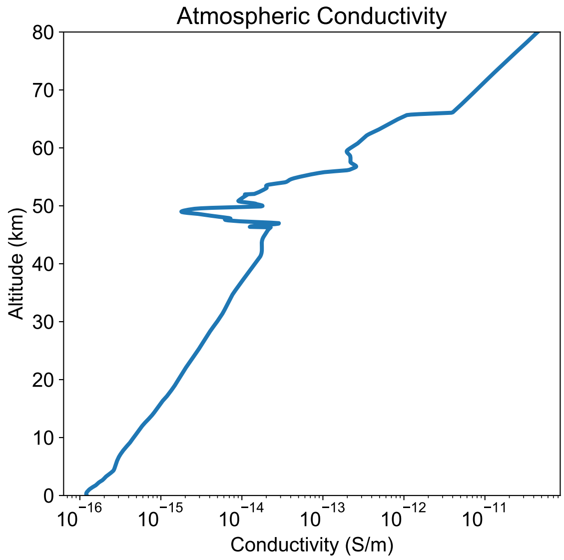

(a) Atmospheric Conductivity

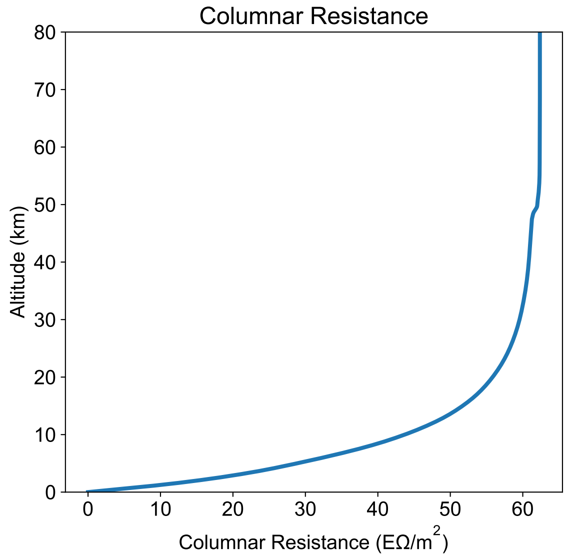

(b) Columnar Resistance

Figure 4.18: Results calculated by the VAIL model. (a) shows the profile for atmospheric conductivity. (b) shows the profile for columnar resistance.

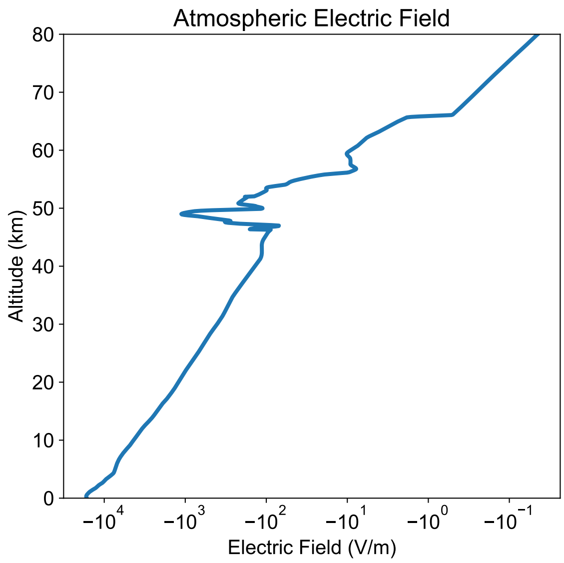

(a) Atmospheric Electric Field

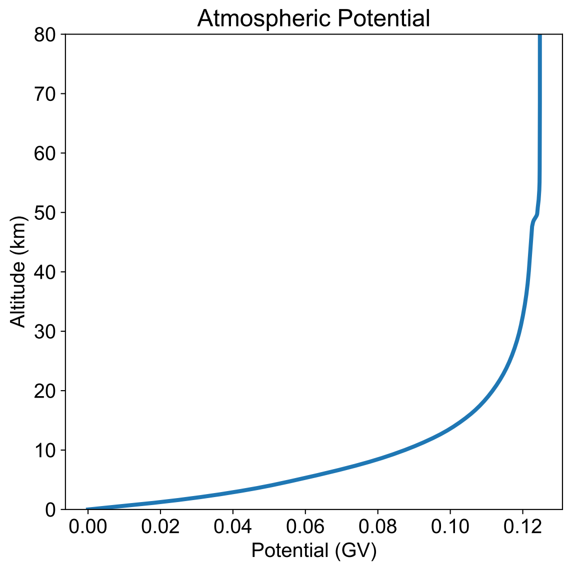

(b) Atmospheric Potential

Figure 4.19: Results calculated by the VAIL model, assuming an Earth-like global atmospheric electric circuit, with conduction current of 2pA/m^2 downwards. (a) shows the profile for atmospheric electric field. (b) shows the profile for atmospheric potential.

4.5 VAIL - Spacecraft Discharge Calculations

The electrical model of Venus' atmosphere was produced in order to compare the observed PDCs against the currents expected from a modeled spacecraft. The steps involved in determining the PDC for such a spacecraft are described in the following section.

We wish to find the Point Discharge Current (PDC) emitted by a spacecraft descending through Venus' atmosphere. As has been discussed in chapters 2 and 3, for a grounded point discharge needle the theoretical parameterisation derived by Chalmers [32] is:

$$I = -2\pi\epsilon_0(V - V_0)\bigg(W^2 + \mu^2F^2\bigg)^{\frac{1}{2}} \tag{4.69}$$

where I is the emitted PDC, ϵ_0 is the permittivity of free space, V is the potential difference between the needle and the atmosphere, V_0 is the minimum potential difference for PDC to occur, W is the wind speed, μ is the mobility of the charge carriers in the discharge current, and F is the potential gradient.

Note that the corona cut off, V_0, is given by:

$$V_0 = \begin{cases} |(V_0)_+|, & \text{if } V > 0 \\ -|(V_0)_-|, & \text{if } V < 0 \end{cases} \tag{4.70}$$

The final term in this equation, $(W^2 + \mu^2F^2)^{(1/2)}$, is given by the velocity of ions away from the needle tip, where the wind speed W is perpendicular to the potential gradient F.

If instead of wind speed, we consider the descent speed of the craft (v_W) - which is parallel to the electric field - then we would expect that our point discharge equation would take the form:

$$I = -2\pi\epsilon_0(V - V_0)\ |(v_W \pm E\mu_\pm)| \tag{4.71}$$

We find that the PDC emitted by a spacecraft is dependent on the potential difference between the spacecraft and the atmosphere. For a spacecraft moving vertically, both the potential of the spacecraft and the atmospheric potential surrounding it would be dependent on time, i.e:

$$V(t) = V_L(t) - V_a(t) \tag{4.72}$$

where V_L is the potential of the spacecraft, and V_a is the atmospheric potential.

Finally, the point discharge emitted by the spacecraft can be written as:

$$I = -2\pi\epsilon_0(V_L - V_a - V_0)\ |(v_w \pm E\mu_\pm)| \tag{4.73}$$

The atmospheric potential surrounding the spacecraft is determined from the results from the VAIL model. To determine the spacecraft potential, several different charging mechanisms need to be considered. The relevant charging mechanisms have been identified through comparison with aircraft on Earth.

It has been documented that aircraft can become charged via interactions with particles in the atmosphere. This can occur due to the collection of charges from these particles, and through the triboeletric effect - where collisions lead to a charge exchange [172, 110]. For our study here, this triboelectric effect will be neglected, with the charging of the spacecraft occurring through collisions with charged particles instead.

Additionally, several discharging mechanisms have been identified for aircraft. These craft will leak charge to the surrounding atmosphere, as a resistor-capacitor circuit [110]. Additionally, under large potential differences it is possible for point discharge currents to be initiated [172, 110]. These point discharges will also act to reduce the potential difference between the craft and atmosphere. For our investigation of the Venera 13 & 14 spacecraft, we assume that point discharge only occurs at the tip of the discharge electrode which has recorded the magnitude of these currents.

A final point to note is that for objects moving vertically in the atmosphere of Earth, the atmospheric electric field means that the ambient atmospheric potential will change as a function of altitude. As such, even if no charging processes are occurring, the vertical movement of a craft will lead to a non-zero potential difference between the craft and atmosphere, which will be removed by the discharging mechanisms.

The remainder of this section will discuss the charging mechanisms which have been considered in more detail. These charging mechanisms will be included in our modelling to determine the PDC emitted by a spacecraft desceinding through the atmosphere of Venus.

4.5.1 Charging - PDC

Here we develop an expression for the rate of change of charge of the spacecraft, due to the PDC process.

If we assume that the spacecraft is a charged sphere, then the electric potential of the spacecraft is given by:

$$V = \frac{Q_L}{4\pi\epsilon_0 r} \tag{4.74}$$

Now, given that electric current is the rate of change of charge, i.e. $I = dQ/dt$, we can write the rate of change of potential of the spacecraft, due to the PDC process as:

$$\left(\frac{dV_L}{dt}\right)_{PDC} = \frac{1}{4\pi\epsilon_0 r} I = -\frac{1}{2r}(V_L - V_a - V_0)\ |(v_w \pm E\mu_\pm)| \tag{4.75}$$

Note that this equation will only be valid in the case when the corona cut-off potential is exceeded, i.e. $|V_L - V_a| > |V_0|$. Otherwise, the rate of change of potential from PDC will be 0. This can be written:

$$\left(\frac{dV_L}{dt}\right)_{PDC} = \begin{cases} 0, & \text{if } |V_L - V_a| < |V_0| \\ -\frac{1}{2r}(V_L - V_a - V_0)\ |(v_w \pm E\mu_\pm)|, & \text{otherwise} \end{cases} \tag{4.76}$$

4.5.2 Charging - Capacitor discharge

We find that the potential on the spacecraft will decay due to the conductivity of the surrounding atmosphere. This mechanism is important, as it is able to reduce the spacecraft atmosphere potential difference even below the corona cut-off. The rate of change of spacecraft potential can be found by considering the system to be a discharging resistor-capacitor (RC) circuit. In this case, the rate of change of potential is given by:

$$\frac{dV}{dt} = \frac{-V(t)}{\tau_{RC}} \tag{4.77}$$

where τ_{RC} is the RC time constant given by:

$$\tau_{RC} = RC \tag{4.78}$$

for resistance R and capacitance C. For our discharging spacecraft, this time constant can be determined from the atmospheric conductivity via:

$$\tau_{RC} = \frac{\epsilon_0}{\sigma_{Total}} \tag{4.79}$$

The rate of change of spacecraft potential as a result of this discharging process is then given by:

$$\left(\frac{dV_L}{dt}\right)_C = -\frac{(V_L - V_a)}{\tau_{RC}} \tag{4.80}$$

4.5.3 Charging - Collection of Thermal Ions

As a spacecraft descends through the atmosphere, it will collect the charge of ions which are impacted onto the spacecraft. From our model assumptions, there is no space charge in the atmosphere - any net imbalance in ion number densities is matched with the opposite charge density of aerosols. As such, we would expect that the area of the atmosphere which the spacecraft passes through would contain a net neutral charge, so will not lead to a charge being accumulated.

However, as the spacecraft descends, ions not within this area may impact with the sides of the spacecraft. If there is a systematic difference in the speed of ions of one polarity compared to another, then it would be expected that more of the fast ions are collected than the slow ones, since the fast ions can be collected from a greater area. A schematic diagram indicating this is shown in figure 4.20. We will explore the change in potential brought about by this collection of ions.

We model the spacecraft as a cylinder with height h and radius r, travelling with velocity v_w parallel to its axis of symmetry. The time taken for the entire cylinder to pass a point at a given altitude is given by:

$$t = \frac{h}{v_w} \tag{4.81}$$

During this time, any ions which reach the outer edge of the cylinder will be collected. Ions which originate in the area swept out by the cylinder's descent will also be collected, but any charge collected will be neutralised by an opposite charge collected by aerosols swept out. As such, the effect of any particles which are swept out by the descent of the spacecraft will be neglected.

We calculate the number of ions collected at a specific altitude. This is a linear number density, with dimensions of 1/L. The infinitesimal linear number density of ions collected in a circular shell of area dA centered on the spacecraft is given by:

$$d\lambda_{collect} = f_{angle} f_{speed}\, n_{ion} dA = f_{angle} f_{speed}\, n_{ion} r' dr' d\theta \tag{4.82}$$

where f_{angle} and f_{speed} are the fractions of ions in this area with the correct speed and direc-

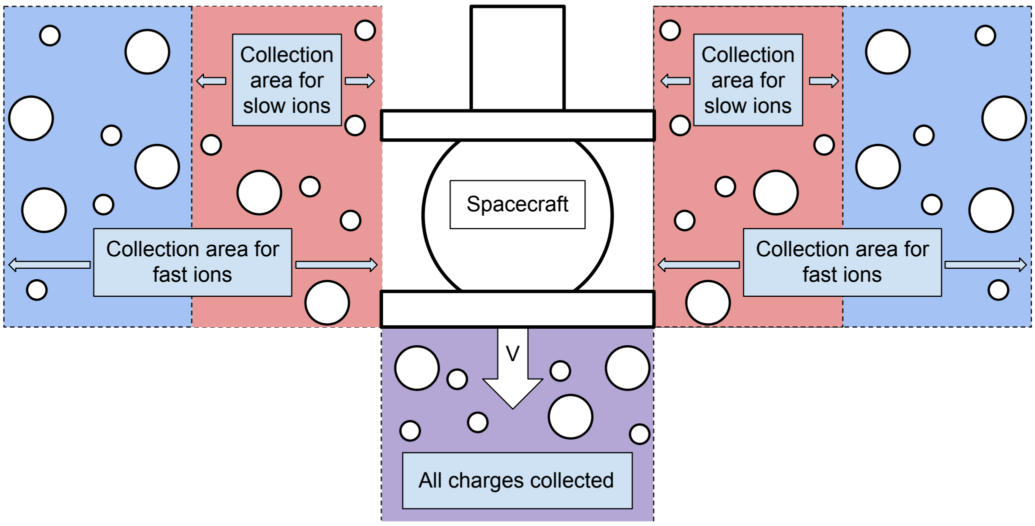

Figure 4.20: Schematic diagram showing the collection of ions by a falling spacecraft. In the area underneath the spacecraft, all charges will be collected. This results in zero net charge being collected. Horizontally, fast ions are collected by the spacecraft in a larger area than slower ions. The result of this is that more of the faster ions will be collected, and so a net charge will be accumulated.

tion to reach the spacecraft in the given time, and r', θ are the radial and angular coordinates of a polar coordinate system centred on the spacecraft.

The total linear number density of ions collected by the spacecraft, at altitude z is given by:

$$\lambda_{collect}(z) = \int_0^{2\pi} d\theta \int_r^{\infty} dr' f_{angle}\, f_{speed}\; n_{ion} r' = 2\pi\; n_{ion} \int_r^{\infty} dr' f_{angle}\, f_{speed}\; r' \tag{4.83}$$

In order to find f_{angle} we consider the angular size of the spacecraft in the sky as a fraction of all possible angles. Note that we consider that the motion of ions is purely horizontal, and so consider an angular size, rather than a solid angle.

From trigonometry, we find that the spacecraft has an angular radius of $\sin^{-1}(\frac{r}{r'})$. So, the fraction of ions moving in a direction which will lead to a collision is given by:

$$f_{angle}(r') = \frac{1}{\pi} \sin^{-1}(\frac{r}{r'}) \tag{4.84}$$

In order to find the number of particles with appropriate speed for a collision, we need to consider the distribution of particle speeds. For thermal particles, the velocity distribution is given by a Maxwell-Boltzmann distribution:

$$f(\mathbf{v})d^3\mathbf{v} = \left(\frac{m}{2\pi k_B T}\right)^{\frac{3}{2}} exp\left\{\frac{-m\mathbf{v}^2}{2k_B T}\right\} d^3\mathbf{v} \tag{4.85}$$

where $f(v)$ is the fraction of particles with velocity $\mathbf{v}$, m is the mass of the particles, T, is the temperature, and k_B is the Boltzmann constant. Assuming that all ion motions are horizontal, we can find the distribution of ion speeds as:

$$f(u)du = \left(\frac{mu}{k_B T}\right) exp\left\{\frac{-mu^2}{2k_B T}\right\} du \tag{4.86}$$

where u is the speed of the ions in this horizontal plane. We have made the assumption that positive ions and negative ions will have a different mass. This mass difference means that ions of one polarity will typically have greater speeds than the other.

The minimum speed required for an ion to be collected is given by the distance to the spacecraft, $d = r' - r$ divided by the time, t, that it takes for the entire spacecraft to pass the horizontal layer at altitude z. Note that in our estimations of f_{speed} we are assuming that the ions only need to travel the distance to the centre of the spacecraft, which is a slightly smaller distance than travelling to the outer edges. As such, the value of f_{speed} will be a very slight overestimate.

The fraction of ions with speed greater than this critical value is given by:

$$f_{speed} = \int_{d/t}^{\infty} f(u)du = \int_{d/t}^{\infty} \left(\frac{mu}{k_B T}\right) exp\left\{\frac{-mu^2}{2k_B T}\right\} du \tag{4.87}$$

Solving, we find:

$$f_{speed}(r') = exp\left\{\frac{-m}{2k_B T}\left(\frac{r'-r}{t}\right)^2\right\} \tag{4.88}$$

The Maxwell-Boltzmann distribution describes the velocity distribution of particles which exchange energy and momentum via collisions. For particles travelling distances $\gg$ their mean free path, these collisions will be important. The presence of collisions will act to "remove" some particles which would otherwise be collected by the descending spacecraft, by either changing the angle of their trajectory such that it misses the craft, or by decreasing their speed such that it is not sufficient to reach the craft in the required time. In addition, however, there will be particles which initially do not have the required trajectory or speed to be collected by the spacecraft, which then have their velocity changed following a collision, such that they now are able to be collected. As such, for our purposes we will assume that these collisions do not affect the net number of particles of a given species collected by the spacecraft.

In addition to the thermal velocity of the particles, the electric field of the spacecraft will cause a drift of ions towards/away from the craft, dependent on their polarity. This ion drift velocity would act to change the collection rate of ions such that the spacecraft potential is reduced. It was found, however, that for our purposes, this ion drift velocity was significantly smaller than the typical thermal velocities of ions, and was considered negligible.

Given the expressions for f_{angle} and f_{speed} in equations 4.84 and 4.88, we can write the linear number density of collected ions of one polarity at a particular altitude as:

$$\lambda_{collect}(z) = 2n_{ion} \int_{r}^{\infty} dr' \sin^{-1}(\frac{r}{r'})\, exp\left\{\frac{-m}{2k_B T}\left(\frac{r'-r}{t}\right)^2\right\} r' \tag{4.89}$$

The linear charge density collected at altitude z is given by the imbalance in the linear number densities found for positive and negative ions, ie:

$$\lambda(z) = q(\lambda_{collect}(z)_+ - \lambda_{collect}(z)_-) \tag{4.90}$$

where q is the charge of each ion - i.e. the elementary charge. Since the spacecraft is travelling in the negative z direction, this linear density of collected charges is equivalent to the negative rate of change of the electric charge of the lander, with respect to altitude. We can write this as:

$$\left(\frac{dQ_L}{dz}\right)_{ion} = -\lambda \tag{4.91}$$

In order to relate the charge collected by the spacecraft to its electric potential, we return to the assumption that the spacecraft is spherical. Using equation 4.74, we can then re-write equation 4.91 in terms of the spacecraft potential:

$$\left(\frac{dV_L}{dz}\right)_{ion} = \frac{1}{4\pi\epsilon_0 r}(-\lambda) \tag{4.92}$$

Instead, if we find the rate of change with respect to time, we can write:

$$\left(\frac{dV_L}{dt}\right)_{ion} = \frac{1}{4\pi\epsilon_0 r}(-\lambda)\frac{dz}{dt} \tag{4.93}$$

Given that the descent speed of the spacecraft, v_w, can be written as $(-dz/dt)$, we can finally write the rate of change of spacecraft potential with respect to time, as a result of the collection of ions, as:

$$\left(\frac{dV_L}{dt}\right)_{ion} = \frac{v_w\lambda}{4\pi\epsilon_0 r} \tag{4.94}$$

4.5.4 Resulting Spacecraft Charging

To find the potential of the spacecraft, we have to consider all the charging/discharging mechanisms together. The total rate of change of potential of the spacecraft is given by:

$$\frac{dV_L}{dt} = \left(\frac{dV_L}{dt}\right)_{PDC} + \left(\frac{dV_L}{dt}\right)_{C} + \left(\frac{dV_L}{dt}\right)_{ion} \tag{4.95}$$

In the case where a PDC is able to occur, i.e $|V_L - V_a| > |V_0|$, we can write:

$$\frac{dV_L}{dt} = -\frac{1}{2r}(V_L - V_a - V_0)\,|(v_w \pm E\mu_\pm)| - \frac{(V_L - V_a)}{\tau_{RC}} + \frac{v_w\lambda}{4\pi\epsilon_0 r} \tag{4.96}$$

For our purposes, we will assume that many of the parameters, such as v_w, E, $\mu_\pm$, V_0, λ are quasistatic. As such, they will be considered time independent, however when implemented into the model, their value will be reassigned at every altitude step.

Note that if we assume a non-zero, quasistatic electric field, and a non-zero vertical velocity, then the atmospheric potential must be time dependent. As such, we can find an expression for the rate of change of atmospheric potential using the chain rule:

$$\frac{dV_a}{dt} = \left(-\frac{dV_a}{dz}\right)\left(-\frac{dz}{dt}\right) = Ev_w \tag{4.97}$$

We wish to find an equation for V_L as a function of time. In order to find this, we will need to solve the differential equation in equation 4.96.

Using the substitutions

$$a = \frac{|(v_w \pm E\mu_\pm)|}{2r} + \frac{1}{\tau_{RC}} \tag{4.98}$$

and

$$b(t) = \frac{(V_a(t) + V_0)|(v_w \pm E\mu_\pm)|}{2r} + \frac{V_a(t)}{\tau_{RC}} + \frac{u\lambda}{4\pi\epsilon_0 r} \tag{4.99}$$

We can re-write equation 4.96 as:

$$\frac{dV_L}{dt} + aV_L = b(t) \tag{4.100}$$

Now, using the integrating factor of $\exp(at)$ We can write:

$$\exp(at)\frac{dV_L}{dt} + a\exp(at)V_L = \frac{d}{dt}\big(\exp(at)V_L\big) = b\exp(at) \tag{4.101}$$

Integrating with respect to time, we find:

$$\exp(at)V_L = \int b\exp(at)dt = \frac{b}{a}\exp(at) - \int \frac{db}{dt}\frac{1}{a}\exp(at)dt \tag{4.102}$$

We can find db/dt using the equation for b, equation 4.99. So,

$$\frac{db}{dt} = \frac{d}{dt}\bigg(\frac{|(v_w \pm E\mu_\pm)|}{2r} + \frac{V_a(t)}{\tau_{RC}} + \frac{u\lambda}{4\pi\epsilon_0 r}\bigg) = \bigg(\frac{|(v_w \pm E\mu_\pm)|}{2r} + \frac{1}{\tau_{RC}}\bigg)\frac{dV_a}{dt} \tag{4.103}$$

Substituting equation 4.97, this can be written as:

$$\frac{db}{dt} = \bigg(\frac{|(v_w \pm E\mu_\pm)|}{2r} + \frac{1}{\tau_{RC}}\bigg)Ev_w \tag{4.104}$$

From equation 4.104, we can see that the parameter db/dt is comprised only of variables we have assumed to be quasistatic, so it itself must be quasistatic also. As such, we can assume that db/dt is not dependent on time.

Now, substituting equation 4.104 into equation 4.102, we find:

$$\exp(at)V_L = \frac{b}{a}\exp(at) - \frac{1}{a}\bigg(\frac{|(v_w \pm E\mu_\pm)|}{2r} + \frac{1}{\tau_{RC}}\bigg)Ev_w \int \exp(at)dt \tag{4.105}$$

$$\exp(at)V_L = \frac{b}{a}\exp(at) - \bigg(\frac{|(v_w \pm E\mu_\pm)|}{2r} + \frac{1}{\tau_{RC}}\bigg)\frac{Ev_w}{a^2}\exp(at) + c \tag{4.106}$$

for integration constant c. The value of this integration constant can be found using the boundary condition that at time $t = 0$, $V_L = V_L(0)$, and $b = b(0)$. So, we find:

$$c = V_L(0) - \frac{b(0)}{a} + \bigg(\frac{|(v_w \pm E\mu_\pm)|}{2r} + \frac{1}{\tau_{RC}}\bigg)\frac{Ev_w}{a^2} \tag{4.107}$$

where $b(0)$ is found from equation 4.99, where $V_a = V_a(0)$.

Finally, we can re-arrange equation 4.106 to give a final equation for the lander potential as a function of time:

$$V_L(t) = \frac{b(t)}{a} - \left(\frac{|(v_w \pm E\mu_\pm)|}{2r} + \frac{1}{\tau_{RC}} \right) \frac{Ev_w}{a^2} + c\exp(-at) \tag{4.108}$$

where a, b, c, are given by equations 4.98, 4.99, 4.107 respectively.

In the case where PDC is unable to occur, i.e. $|V_L - V_a| > |V_0|$, we can follow a similar process to find:

$$V_L = \frac{b_2}{a_2} - \frac{Ev_w}{\tau_{RC} a_2^2} + c_2 \exp(-a_2 t) \tag{4.109}$$

where a_2, b_2, c_2 are given by:

$$a_2 = \frac{1}{\tau_{RC}} \tag{4.110}$$

$$b_2(t) = \frac{V_a(t)}{\tau_{RC}} + \frac{v_w \lambda}{4\pi\epsilon_0 r} \tag{4.111}$$

$$c_2 = V_L(0) - \frac{b_2(0)}{a} + \frac{Ev_w}{\tau_{RC} a_2^2} \tag{4.112}$$

Using equations 4.108 & 4.109 we are able to find the potential of the lander at each altitude step in the model, using information from the previous step. This method is able to be used if the PDC process is either active or inactive for the entire duration between the model steps. If this is not the case, then equations 4.108 & 4.109 will not be accurate, and will lead to the change in potential either under or overshooting the correct value. In these cases, in order to correctly calculate the spacecraft potential, the exact time of the switch between the PDC process being active/inactive needs to be assessed.

The following calculations only occur when the PDC process state changes state between two model steps. If the PDC changes from passive to active, the time of this change occurs when V_L as calculated by equation 4.109 is equal to $V_a(t) + V_0$. Here $V_a(t)$ is found by considering a linear interpolation between the two model steps. So,

$$V_a(t) = z(t) \frac{V_a|_i - V_a|_{i+1}}{z|_i - z|_{i+1}} \tag{4.113}$$

where the subscripts i,$i+1$ refer to the upper and lower model steps respectively.

The value of t in equations 4.109 & 4.113 is then fit for, such that

$$V_a(t) + V_0 = \frac{b_2}{a_2} - \frac{Ev_w}{\tau_{RC} a_2^2} + c_2 \exp(-a_2 t) \tag{4.114}$$

Following this, the spacecraft potential at the second model step is calculated, using the conditions determined at this value of t as starting boundary conditions.

A similar process is followed when the PDC process state changes from active to passive, with the time of this change being calculated from:

$$V_a(t) + V_0 = \frac{b(t)}{a} - \left(\frac{|(v_w \pm E\mu_\pm)|}{2r} + \frac{1}{\tau_{RC}} \right) \frac{Ev_w}{a^2} + c\exp(-at) \tag{4.115}$$

The selection of equation 4.108 or 4.109, and the use of this method of switching the PDC state between datapoints is illustrated in figure 4.21.

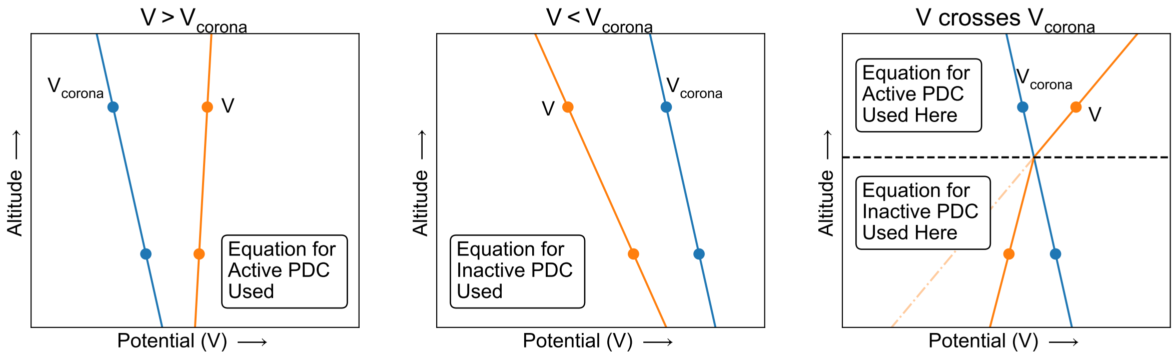

(a) Corona Active (b) Corona Inactive (c) Corona State Switched

Figure 4.21: Three figures illustrating the PDC activity states. The spacecraft-atmosphere potential difference, V, and the corona onset potential V_{corona} are shown for 2 datapoints indicated by blue and orange circles respectively. Note that time increases with decreasing altitude. (a) shows the case where the spacecraft-atmosphere potential difference, V, is greater than the corona onset potential for both datapoints. In this case, equation 4.108 would be used to determine V_L. (b) shows the case where the spacecraft-atmosphere potential is less than the corona onset for both datapoints. In this case, equation 4.109 would be used to determine V_L. Finally, (c) shows the case where the spacecraft-atmosphere potential is greater than the corona onset potential for only one of the datapoints. In this case, the time when the value of the spacecraft-atmosphere potential difference crosses the value of the corona onset potential would be identified from equation 4.115. The value for V_L at the second datapoint would then be determined by using equation 4.109 starting from this time.

Once the spacecraft potential has been determined, it is possible to calculate the point discharge current emitted by the lander. This is done by feeding the lander potential at each height step into equation 4.73.

4.6 Results

Using the electrical model of Venus' atmosphere, the Venera 13 & 14 PDC data was investigated. The PDC emitted by a descending spacecraft was determined from the VAIL model. This value was compared against the PDC data from the Venera landers.

Our criterion for a good fit to this PDC data was specified based on the reading error on the PDC data, estimated in section 4.2. So, the model result was considered to be a good fit to the Venera PDC data if it lay within $\pm$ 3.06nA of the data. This range of "good fit" values is illustrated in figure 4.22.

In this section, we will investigate the modelled PDC as it is affected by several perturbations to the model, with the intention of finding parameters which allow a good fit to the Venera PDC data. The corona onset value, the presence, magnitude, and polarity of a global atmospheric electric circuit, and the inclusion of haze layers will be investigated.

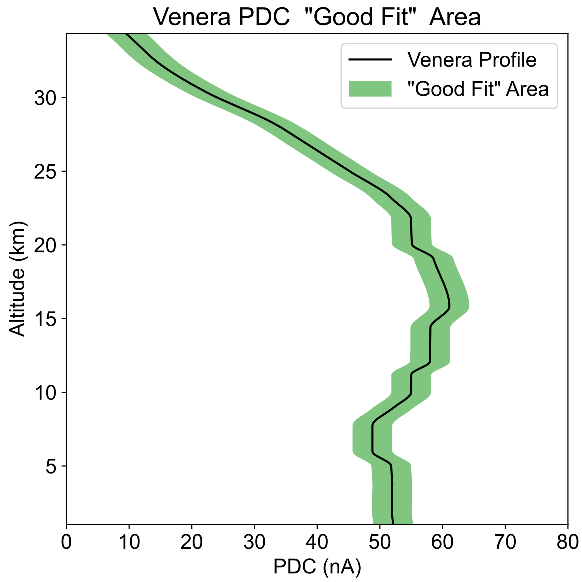

Figure 4.22: Profile of the Venera data, showing the region of reading error on the data. The area lying between the upper and lower error bounds are shown as a green shaded area.

4.6.1 Results from Initial Assumptions

Firstly, we consider the case where there is no global circuit. This is the simplest case, relying on the fewest assumptions. Using equations 4.108 & 4.109, the potential of a spacecraft was determined. Note that in this case, since there is no vertical electric field, the only charging mechanism for the spacecraft is the collection of thermal ions - there is no changing atmospheric potential which would affect the spacecraft-atmosphere potential difference. The spacecraft potential is shown in figure 4.23a along with the corona onset potential.

Next the amount of point discharge current which would be emitted was determined using equation 4.73. This emitted PDC is shown in figure 4.23b, and compared against the in-situ data recorded by the Venera 13 & 14 landers.

As can be seen, the modelled PDC in this case does not align with the in-situ data recorded by the Venera landers.

4.6.2 Variance of Corona Onset

From estimations of the corona onset voltage, we arrived at a value for the breakdown fraction of $\eta = 0.001$ in section 4.3. We have investigated the effects of varying the value of this fraction by an order of magnitude (increase or decrease). In figure 4.24a, the onset potentials investigated are shown for the lowest 40km of the atmosphere. In figure 4.24b, the resulting PDC calculated by the model for these corona onset potentials are shown. The PDC data recorded by the Venera 13 & 14 landers is also illustrated on these plots.

As can be seen from figure 4.24b, the act of decreasing the breakdown fraction from the $\eta = 0.001$ value has a notable effect on the resulting PDC. The change to the PDC in this way does not cause the model result to align better with the Venera PDC data, however. Increasing the breakdown fraction also had a notable effect, significantly changing the PDC emitted. In

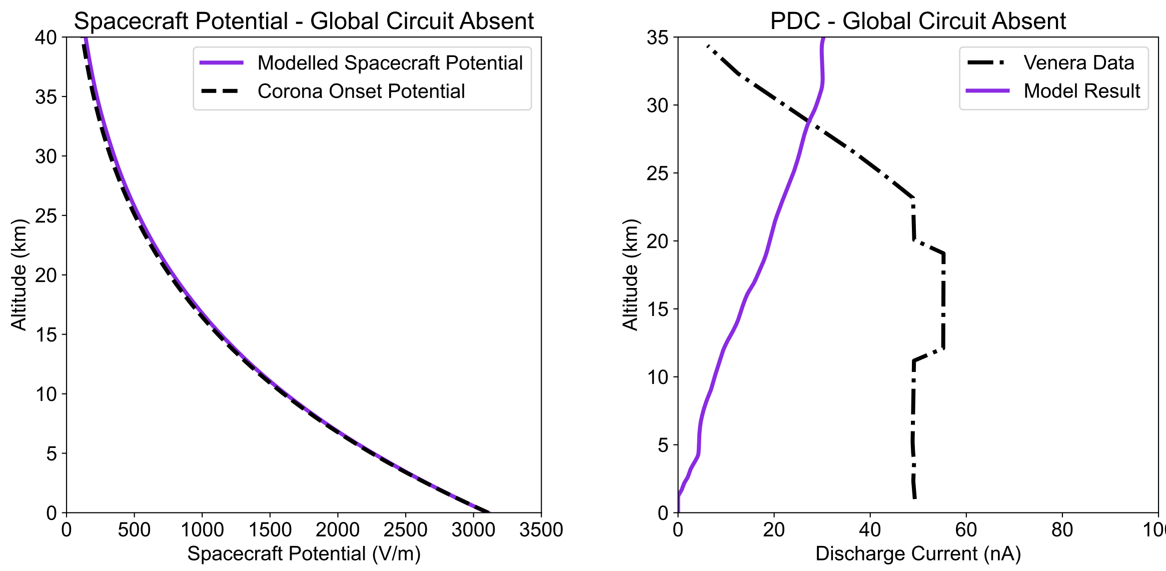

(a) Spacecraft Potential

(b) Emitted PDC

Figure 4.23: Electrical results for a spacecraft descending through Venus' atmosphere, with no global circuit present. (a) shows the electrical potential of the spacecraft (purple) compared against the corona onset potential (black dashed). (b) shows the modelled PDC (purple) compared against the in-situ Venera PDC data (black dot-dashed).

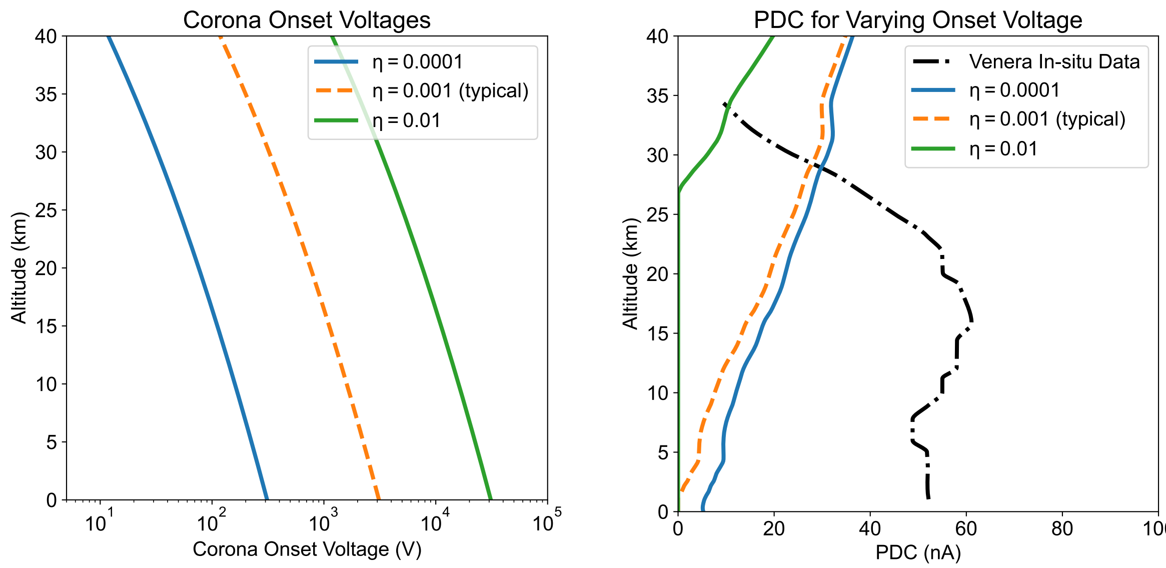

(a) Corona Onset Potentials

(b) Emitted PDCs

Figure 4.24: Effects of varying the breakdown fraction on the corona onset voltage, and the PDC emitted by a spacecraft. (a) shows the corona onset voltage determined for a range of breakdown fractions, η. The typical value used of $\eta = 0.001$ is shown as an orange dashed line, and values of $\eta = 0.0001$ and $\eta = 0.01$ are shown as blue and green lines respectively. In (b), the emitted PDC calculated for the onset voltages described in (a) are shown. The in-situ PDC data from the Venera 13 & 14 landers is shown as a black dot-dashed line.

addition to this, the increased corona potential in this case resulted in the PDC process being "quenched" as the spacecraft was unable to collect charge at a sufficient rate to enable the PDC process at low altitudes. The change to the PDC profile in this case again did not act to align the model data to the Venera 13 & 14 data. As such, we find that although the magnitude of the modeled point discharge current is sensitive to the corona onset voltage, variations in this voltage will not allow the in-situ PDC profile to be reproduced.

4.6.3 Addition & Variation of Global Circuit

Given the limited number of assumptions used so far, we have been unable to reproduce the Venera PDC data. We next consider if including a global atmospheric electric circuit into the model will allow the shape of the Venera PDC profile to be reproduced. By including the effects of a global circuit, we now have two charging mechanisms affecting the potential of a spacecraft travelling through the atmosphere. As before, the collection of thermal ions is still an important process - providing a positive charge to the lander. Now, however, the spacecraft will also acquire a charge with respect to the atmosphere as the atmospheric potential is changed. The polarity of this change in potential difference is dependent on the polarity of the vertical atmospheric electric field. When we have an “Earth-like” global atmospheric electric circuit, i.e. a negative conventional current flowing upwards, a spacecraft descending through the atmosphere will acquire a positive charge with respect to the surrounding atmosphere. In this case, the two charging mechanisms will work together to increase the potential difference between the spacecraft and the atmosphere, and as such will increase the magnitude of the PDC. In the other case, where we have an “Inverted” global atmospheric electric circuit, i.e a positive conventional current flowing upwards, a descending spacecraft will acquire a negative charge with respect to the atmosphere from the additional charging mechanism. This means that the two charging mechanisms will be competing.

We will investigate the shape of the PDC profiles found when different magnitudes of fair weather conduction currents are present. Firstly, an Earth-like circuit was considered. The magnitude of the electric field in the lowest 40km of the atmosphere is shown for several magnitudes of conduction current in figure 4.25a. Note that for this Earth-like circuit, these electric fields would be negative. The PDC emitted by a spacecraft was then calculated for the electrical environment in each of these cases. These PDC profiles are shown in figure 4.25b along with the in-situ Venera PDC.

As can be seen in all of these cases, the inclusion of a global electric circuit can have a large effect on the PDC emitted by a spacecraft. Further, by comparing the shapes of the profiles for each of the magnitudes of conduction current, it can be seen that the strength of the global electric circuit also is of large importance. Unfortunately, for all of these cases, we observe that the shape of the profiles was not representative of the in-situ data recorded by the Venera 13 & 14 landers.

We next considered the effects of a inverted global electric circuit. As for the earth-like case, a range of magnitudes of conduction current were considered, with the same magnitudes of current used in that case. From the assumptions used in our model, this results in the electric field having the same magnitude as in figure 4.25a, however in this case the electric field was positive. The PDC profiles found for these electric fields were shown in figure 4.25c. In all three cases considered, the PDC switched polarity during the altitude region of the Venera data. Since

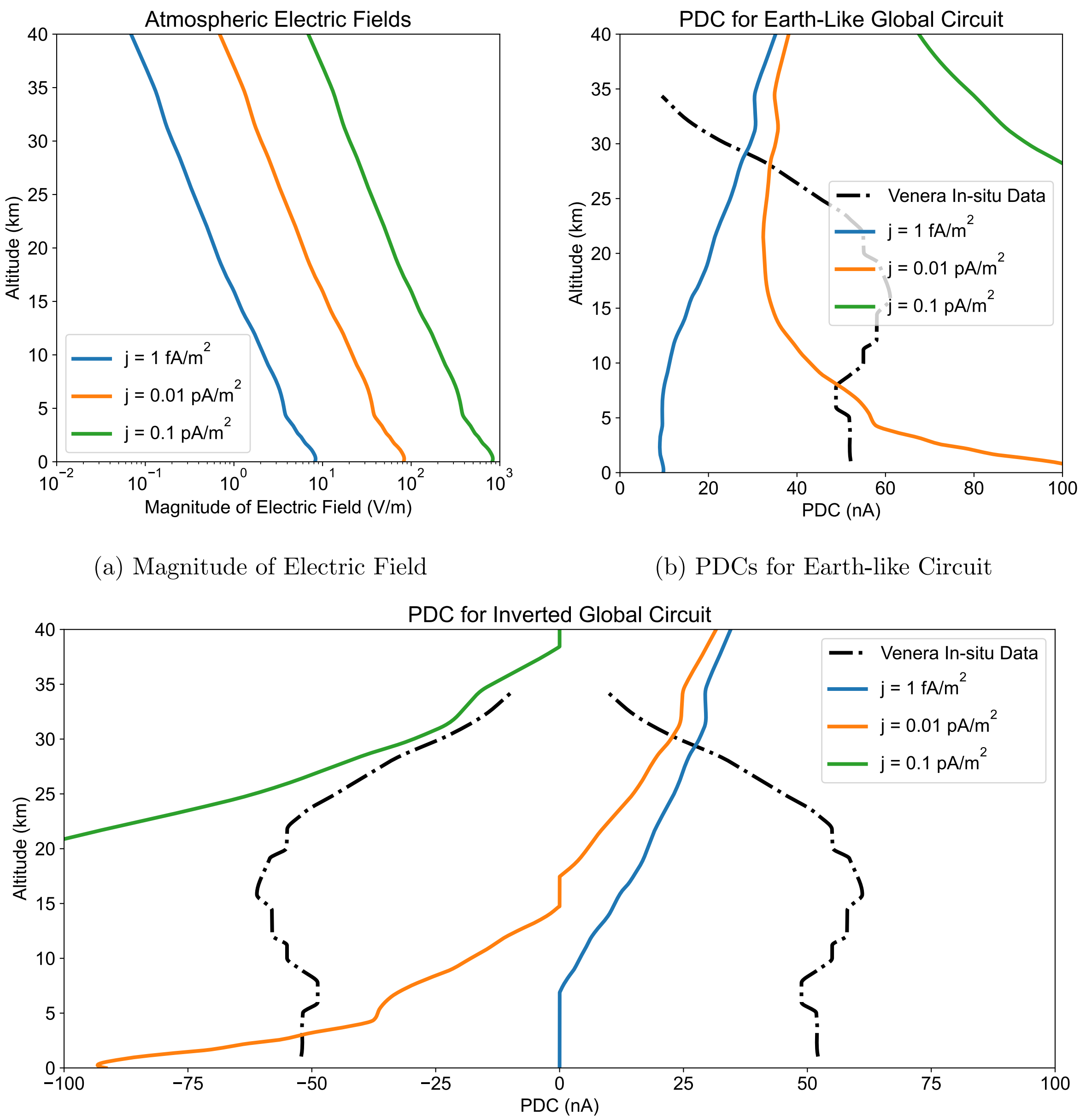

(a) Magnitude of Electric Field

(b) PDCs for Earth-like Circuit

(c) PDCs for Inverted Crcuit

Figure 4.25: Electric field and PDC profiles for varying conduction currents. The solid blue, orange, and green lines in each figure are for conduction current densities with magnitudes 1 fAm^{-2}, 0.01 pAm^{-2}, and 0.1 pAm^{-2} respectively. (a) shows the magnitude of the atmospheric electric field for each of these conduction currents magnitudes. (b) shows the PDC emitted by a spacecraft for negative conduction currents, with the specified magnitudes. The in-situ PDC data recorded by the Venera 13 & 14 landers is shown as a black dot-dashed line. (c) shows the PDC emitted by a spacecraft for positive conduction currents, across the same magnitudes. Again, the black dot-dashed line shows the in-situ data. Note that a symmetric log axis has been used to show currents of both polarities in this case. This axis has a linear section between +5 and -5 nA. Additionally, the Venera data has been shown for both polarities, since the true polarity of the data was unknown.

the polarity of the Venera PDC data was unknown, the shape of the profile has been reproduced for both polarities, for comparison.

As for the Earth-like case, we find that the inclusion of a global electric circuit has a large impact on the PDC profile. In this case, a notable feature is the switch between positive and negative PDCs. As discussed in section 4.2, it is unknown what polarity of PDC was recorded by the Venera 13 & 14 spacecraft, hence the Venera data being presented for both polarities in figure 4.25c. We do expect, however that the polarity of the signal does not change within the altitude range of the dataset. We find that, as for the Earth-like case, the inclusion of a global electric circuit can vary the shape and magnitude of the PDC profiles to a large degree.

Looking at both polarities of global circuit, we can conclude then that the effects of a global electric circuit are clearly important. We however note that the effects of these global circuits alone cannot explain the shape of the Venera PDC profiles.

4.6.4 Addition of Low Atmosphere Haze

It has previously been suggested that the shape of the Venera PDC profiles could be explained by the presence of low atmosphere haze [116]. We will explore the impacts of including different haze profiles in our model.

To investigate the effects of haze on the PDC emitted by a spacecraft, we first return to the case where there is no global circuit. In this case, the spacecraft accumulates charge through the collection of mobile thermal ions. A haze layer present in the atmosphere will act to reduce the number of free ions in the atmosphere, through attachment to the haze particles. This reduction in the ion number density will reduce the charge accumulated by the spacecraft, and reduce the PDC emitted. This effect has been showcased in figure 4.26 by comparing the PDC found when additional haze layers have been included to the case where it is neglected. Here the concentration and size of haze particles are constant with height. The emitted PDC has been shown for particles with a radius of 0.1 µm, in concentrations of 100 and 1000 cm^{-3}. This size of haze particle was selected to be outwith the observational range of the Pioneer particle detectors, which did not observe haze layers extending through the lower atmosphere [147].

As can be seen in figure 4.23b, above ∼30km, the modelled PDC is larger than the in-situ data. As such, in order for the model to describe the PDC at these altitudes, then some reduction to the PDC is required; this reduction can be performed by the inclusion of a haze layer above 30 km. Conversely, however, below ∼30km, the modelled PDC is smaller than the in-situ data. Since the inclusion of a haze layer will only decrease the PDC, it is unable to bring the model result into alignment with the in-situ data at these altitudes.

To show this, a fitting process has been performed to determine the concentration of haze particles which would bring the model result into the best possible agreement with the Venera data. At each height step in the model, the concentration of haze which reduced the difference between the Venera PDC data and the modeled PDC at that height was determined through least squares fitting. This process was performed starting from the highest altitudes, working downwards.

For this fitting process, a constant particle size of 0.1 µm has been used. This particle size was based on the estimated size of particles from previous spectrophotometric measurements [86]. The choice of particle size is fairly arbitrary however, and this process could have been performed with a different size of particle, with a particle size which varied with altitude, or even

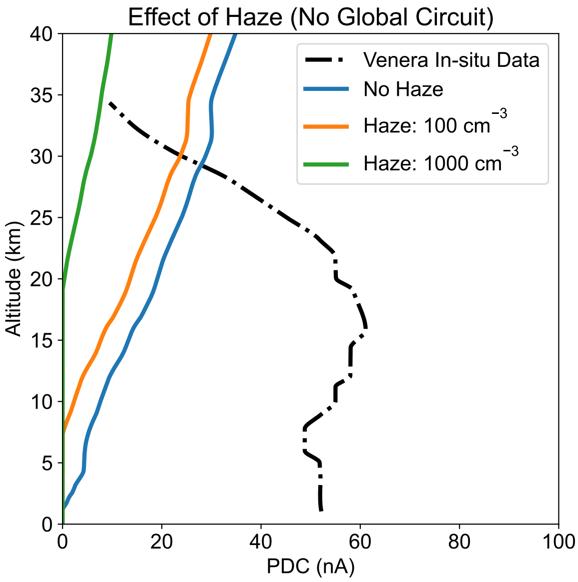

Figure 4.26: PDC profiles for different amounts of haze, where the effects of a global circuit are not present. In all cases, the haze particles have a radius of 0.1 microns, with constant concentration through the entire atmosphere. Three haze concentrations were considered, 0 cm^{-3} (blue), 100 cm^{-3} (orange), and 1000 cm^{-3} (green). The Venera PDC data has also been shown (black dot-dashed).

with multiple particle sizes. The impacts to the model from the presence of this haze arrives via the ion-aerosol attachment term, which is dependent on both the size and concentration of particles. As such, any particular value of ion-aerosol attachment term can be considered degenerate - with the concentration of particles being varied to give the desired result for any given particle size. For the remainder of this work, particles of size 0.1 µm will be used, and it should be noted that changing this particle size will only affect the concentration of these particles which is required to obtain the given result.

The best fit found from this process has been shown in figure 4.27a. The number density profile of the haze particles is shown in figure 4.27b.

In this case, it can be seen that above ~30km, it is possible to select a haze layer which will cause the model result to fit well to the Venera data. Below this altitude, however, the Venera data cannot be reproduced.

It has been seen that the inclusion of haze layers can have a significant effect on the PDC emitted by a spacecraft. However, the in-situ data was still unable to be reproduced in the case where there is no global circuit present. Next, we consider if the in-situ data can be reproduced if both a global circuit, and low atmosphere haze layer are included.

4.6.5 Haze & Global Circuit

Here we investigate if together the presence of a global atmospheric electric circuit and a low atmosphere haze layer can explain the shape of the Venera PDC data. The cases of Earth-like and inverted global circuits will be considered separately.

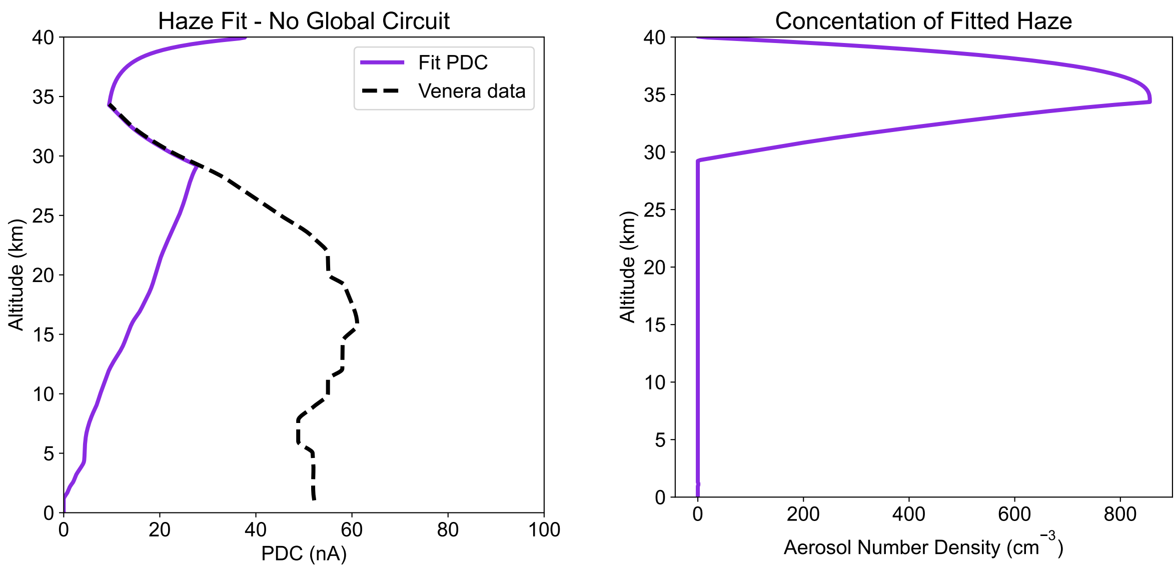

(a) Fit to In-Situ Data

(b) Haze Concentration Profile

Figure 4.27: Best fit of the model result to Venera data, in the case where a global circuit is not present. (a) shows the modelled PDC (purple) compared against the Venera data (black dashed). (b) shows the haze concentration which was used as a model input to produce (a). The haze particle radius was 0.1 µm.

Earth-Like Global Circuit

In the case where we have an Earth-like global circuit, the spacecraft accumulates charge with respect to the atmosphere both by the collection of thermal ions, and the changing atmospheric potential experienced by the spacecraft. Both of these mechanisms will cause the spacecraft to accumulate a positive charge with respect to the atmosphere. If we further include a haze layer into our model, this will act to reduce the concentration of ions in the atmosphere, which decreases the conductivity of the atmosphere, and therefore would increase the magnitude of the vertical electric field for a given conduction current. These changes will affect the two charging mechanisms in different ways. The reduction in the ion concentration leads to fewer thermal ions being collected by the spacecraft and therefore the spacecraft-atmosphere potential difference will be reduced. On the other hand, the increase in the magnitude of the electric field will mean that the atmospheric potential changes more rapidly from the reference frame of the spacecraft. This will lead to an increase in the spacecraft-atmosphere potential difference. These two competing mechanisms mean that the inclusion of haze will have variable effects on the PDC emitted by a spacecraft, under different conditions.

To illustrate this behaviour, the PDC emitted by a spacecraft has been modelled for an Earth-like global circuit for several different haze distributions. For this demonstration, in these cases the vertical conduction current has a magnitude 0.01pA/m^2, and haze particles have a radius 0.1µm. We have compared the emitted PDC profiles in the cases where there is no low-atmosphere haze, a constant haze number density of 100 particles per cubic cm, and a constant haze number density of 1000 particles per cubic cm. The PDC profiles for these three cases are shown in figure 4.28a, along with the Venera PDC data. Additionally, a plot has been produced showing the PDC found in the two haze cases, with the PDC found for no additional haze subtracted. This plot allows the effect of the haze on the PDC to be visualised clearly.

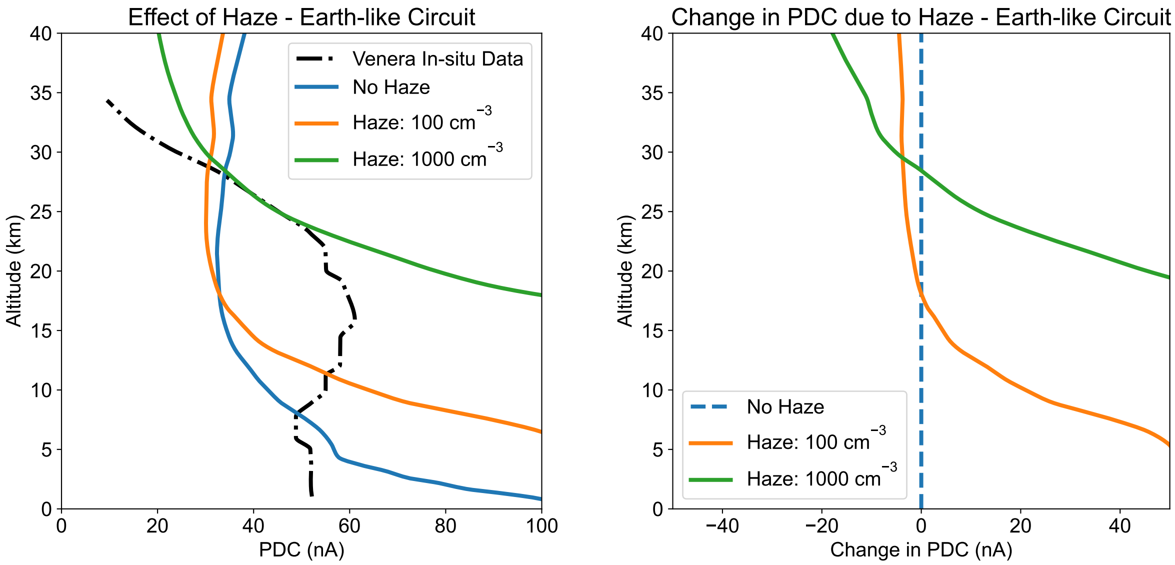

(a) PDC with varying Haze

(b) Change in PDC with Haze

Figure 4.28: PDC profiles for different amounts of haze, where an Earth-like global circuit is present, with conduction current of 0.01 pA/m^2. In all cases, the haze particles have a radius of 0.1 microns, with constant concentration through the entire atmosphere. Three haze concentrations were considered, 0 cm^{-3} (blue), 100 cm^{-3} (orange), and 1000 cm^{-3} (green). (a) shows the total value of these PDC profiles, while (b) shows the difference between the 100 and 1000 cm^{-3} profiles and the 0 cm^{-3} profile. In (a), the Venera PDC data has been shown (black dot-dashed).

From figures 4.28a and 4.28b we can see two regimes where the changes to the different charging mechanisms become dominant. For the 100 (1000) cm^{-3} concentration haze, we see that the inclusion of haze causes a decrease in the PDC above $\sim$20 ($\sim$ 30) km. Below this height, the inclusion of haze causes an increase in the PDC. It is also important to note that at a given altitude, the inclusion of haze will not always affect the PDC in the same way. This can be clearly illustrated by comparing the two haze profiles at an altitude of 25km. At this altitude, the inclusion of a 100 cm^{-3} haze leads to a decrease in the PDC. If the haze concentration is increased further, to 1000 cm^{-3}, then this will instead lead to an increase in the PDC.

Similar to the "absent global circuit" case, we want to try to find a haze distribution which when inputted into our model will best replicate the Venera data. As was done previously, this was investigated by adjusting the haze concentration at a given altitude such that the model PDC matched the Venera data. There is an additional complication to this method when used for this global circuit case, however. When the target Venera PDC is smaller than the PDC obtained by the model assuming no haze, then the competing changes to the two charging mechanisms will mean that it is possible for more than one solution which gives the target PDC to exist. This is illustrated in figure 4.29 by considering the change in PDC with increasing haze concentrations at an altitude of 29 km. In this figure, it can be seen that there are two haze concentrations which will give the required change in PDC at that altitude (i.e. $\sim$160 and

~850 cm^{-3}). As such, we need to be careful about which value to accept.

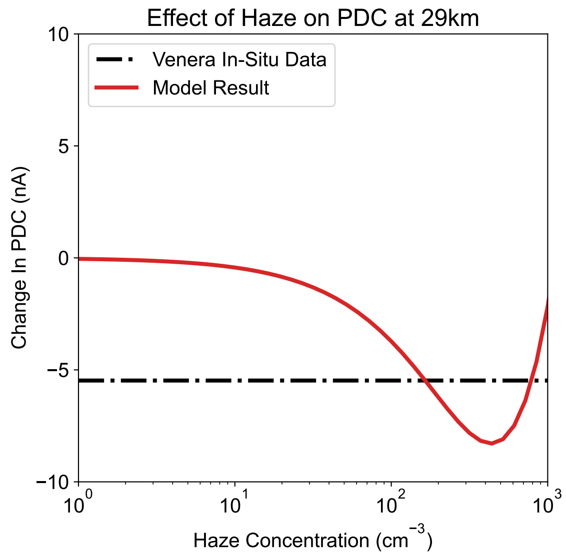

Figure 4.29: Change to the modelled PDC with increasing haze, at an altitude of 20km. The effects of an Earth-like global circuit, with conduction current of 0.01 pA/m^2, have been included in the determination of the PDC. The change to the modelled PDC with respect to the case where no haze is present has been shown as a red line. The difference required to reach the value of the Venera PDC at this altitude has been shown as a horizontal black dot-dashed line. Note that the two solutions which cause the model result to reproduce the Venera PDC occur at haze concentrations of ~150 and ~850 cm^{-3}.

For some datapoints, i.e. when the model result for no haze < the Venera PDC, only one solution will be present. We can then extrapolate from these datapoints to select the most plausible haze concentration at the altitudes which have two possible results; at these altitudes, we select the value which is closest to the result for a neighbouring altitude.

Finally, performing the same "haze fitting" method as for the absent global circuit case, we find that it is indeed possible for the model result to match the Venera data, as long as both a global circuit and haze layer are present. The model result found from this process is shown along with the Venera data in figure 4.30a. Note that in this case a conduction current of 0.5f A/m^2 has been used. The haze concentration required for the shape of the profile in figure 4.30a is shown in figure 4.30b, where a constant haze particle radius of 0.1 μm has been assumed.

Note that although this result has been shown for one magnitude of conduction current, it is possible to obtain similar results for a range of conduction currents. As a demonstration, the resulting PDC, along with the required haze concentrations for these profiles, have been shown for several magnitudes of conduction current in figure 4.31. As can be seen in figure 4.31b, the required concentration of haze particles increases as the magnitude of the conduction current decreases.

Although these fits are able to be obtained for a range of conduction currents, they cannot be created for all magnitudes of conduction current. From our investigation, we have found that above currents of 3 fA/m^2, some of the resulting best-fit PDC values lay outwith the "good fit" area specified earlier. As such, it is concluded that the model is unable to reproduce the

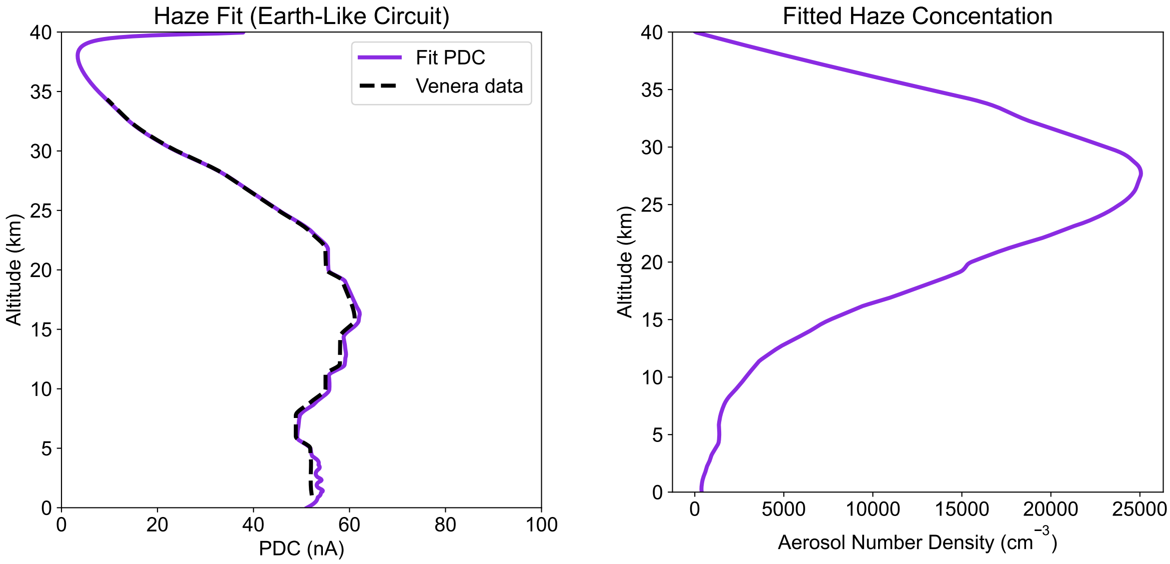

(a) Fit to In-Situ Data

(b) Haze Concentration Profile

Figure 4.30: Best fit of the model result to Venera data, in the case where an Earth-like global circuit is present, with conduction current of 0.5 fA/m^{-2}. (a) shows the modelled PDC (purple) compared against the Venera data (black dashed). (b) shows the haze concentration which was used as a model input to produce (a). The haze particle radius was 0.1 µm.

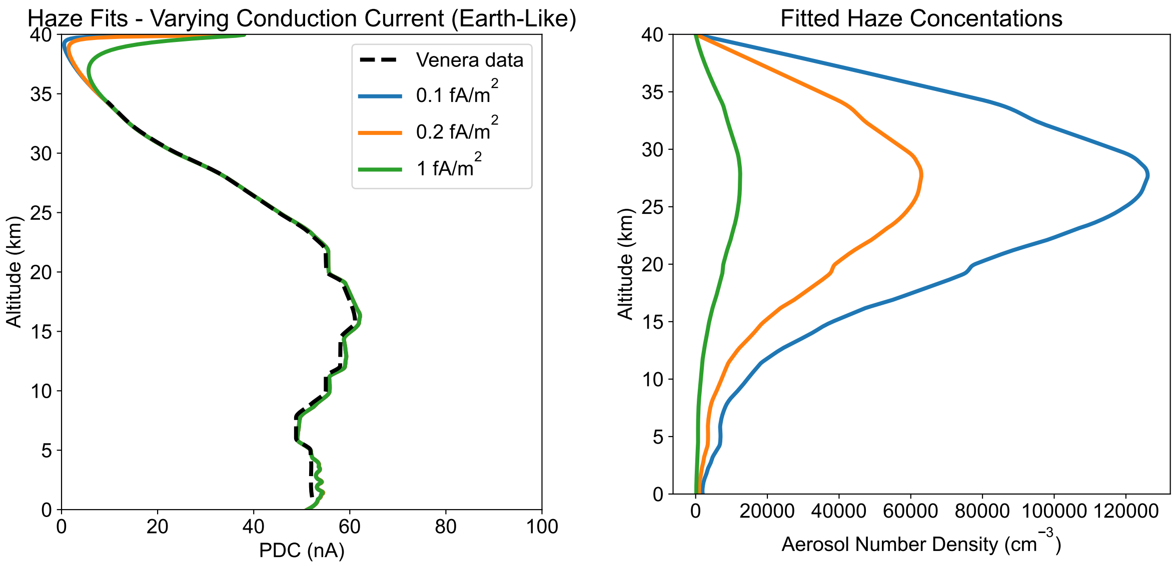

(a) Fit to In-Situ Data

(b) Haze Concentration Profile

Figure 4.31: Best fits of the model result to Venera data, for a range of different conduction currents. Three conduction currents have been considered, with magnitudes of 0.1, 0.2 and 1 fA/m^2. In all three of these cases, we have considered the global circuit to be Earth-like in its polarity. (a) shows the modelled PDC from each of these cases, shown as blue, orange, and green lines for 0.1, 0.2 and 1 fA/m^2 respectively. These are compared against the Venera data (black dashed line). (b) shows the three haze concentrations which were used as a model inputs to produce the profiles in (a). Again, blue, orange, and green lines were used for the conduction currents of 0.1, 0.2 and 1 fA/m^2. In all cases, the haze particle radius was 0.1 µm.

Venera data for these conduction currents. We are thus able to state that the upper limit for the magnitude of the Venusian conduction current in an Earth-like global circuit is 3 fA/m^2, under the assumptions we have made. Note that this is significantly lesser than the typical magnitude of the fair weather conduction current on Earth (i.e. ~ 1 pA/m^2) [158].

Inverted Global Circuit

As discussed previously, for an inverted global atmospheric electric circuit, the two charging mechanisms for a descending spacecraft are competing. When we introduce haze, however, the nature of the change to the emitted PDC is simpler than in the Earth-like case. As in this previous case, the presence of haze will reduce the concentration of free ions in the atmosphere, meaning that the spacecraft accumulates less charge through the ion collection mechanism. Also, as before, the magnitude of the electric field will be increased compared to the case where there is no haze present, meaning that the "changing atmospheric potential" charging mechanism is enhanced. In contrast to the Earth-like case, since this charging mechanism provides the spacecraft with the opposing charge to the net charge collected by thermal ions, the overall effect of the presence of haze will be to decrease the value of the PDC emitted; i.e. decreasing the magnitude of positive PDC and increasing the magnitude of negative PDC. In order to showcase this effect, modelled PDC profiles have been determined for different haze concentrations for a vertical conduction current of 0.01 pA/m^2. These profiles are shown in figure 4.32. For each of these cases a single haze particle size of 0.1μm has been assumed, and the haze concentration for each example is constant across the entire model range.

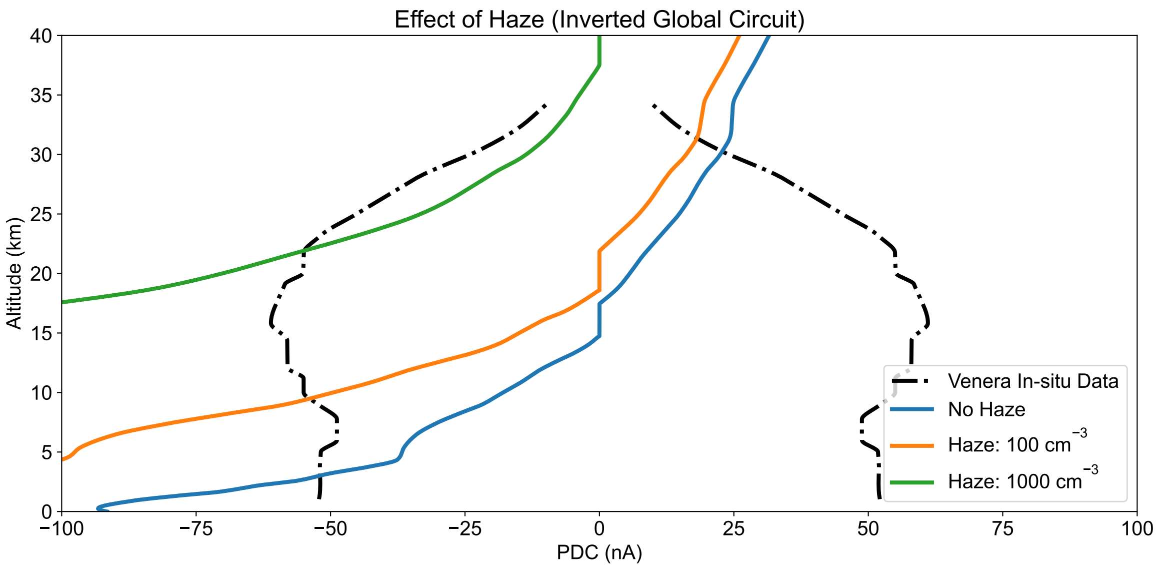

Figure 4.32: PDC profiles for different amounts of haze, where an inverted global circuit is present, with conduction current of 0.01 pA/m^2. In all cases, the haze particles have a radius of 0.1 microns, with constant concentration through the entire atmosphere. Three haze concentrations were considered, 0 cm^{-3} (blue), 100 cm^{-3} (orange), and 1000 cm^{-3} (green). A symmetric log axis has been used, with linear range between -5 and 5 nA. The Venera PDC data has been shown for both polarities of discharge current as a black dot-dashed line.

In figure 4.25c, it was observed that when no haze was present, the PDC profile often switched polarity during the range of the Venera PDC data. Since we expect the PDC profile to be changing smoothly with altitude, we will require for our investigation that only one polarity of PDC is present in a fit to the Venera data. Additionally, as is shown in figure 4.32, the presence of haze can only act to decrease the value of the emitted PDC. In order for the model to be able to produce a result which matches the positive Venera PDC, we require an increase in the PDC at some altitudes. We can thus conclude that we are unable to reproduce the positive Venera PDC profile, so will instead focus on fitting to the negative PDC profile.

We again perform the same haze fitting procedure as in the previous two cases. As for the Earth-like circuit, we find that it is possible to fit the model result to the Venera data, as long as both a global circuit and a low atmospheric haze are present. The fit performed for a conduction current of 0.5fA/m^2 is shown in figure 4.33a, with the concentration of 0.1 µm haze particles which is required for this PDC profile shown in figure 4.33b.

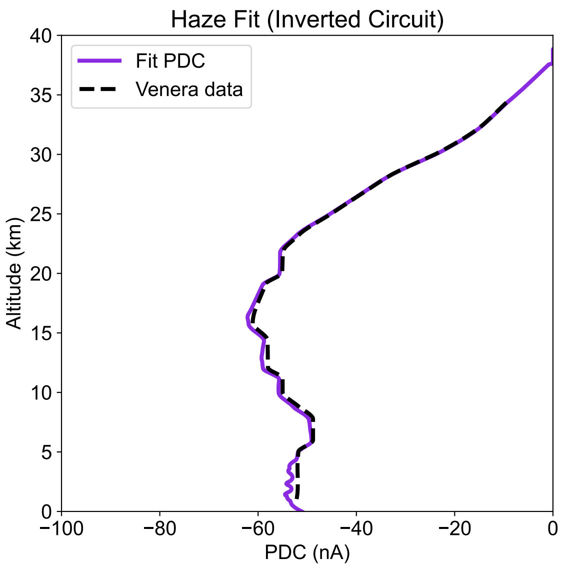

(a) Fit to In-Situ Data

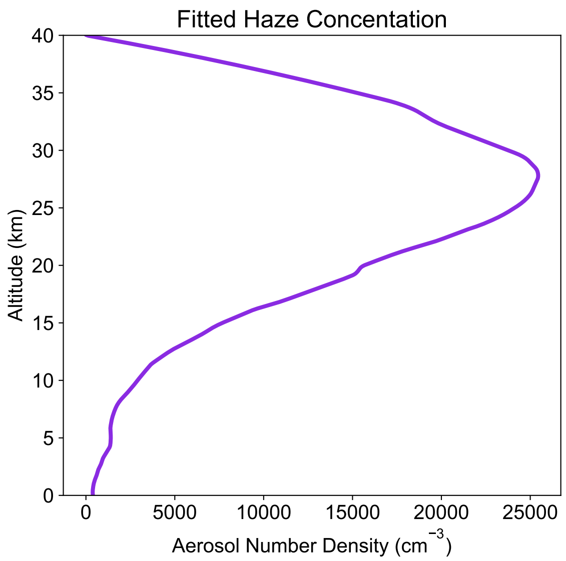

(b) Haze Concentration Profile

Figure 4.33: Best fit of the model result to Venera data, in the case where an inverted global circuit is present, with conduction current of 0.5 fA/m^{-2}. (a) shows the modelled PDC (purple) compared against the Venera data (black dashed). (b) shows the haze concentration which was used as a model input to produce (a). The haze particle radius was 0.1 µm.

As for the Earth-like case, we find that it is possible to determine these fits across a range of conduction currents. Several examples of the fitted PDC as well as the haze profiles required to produce them are shown in figure 4.34. From figure 4.34b it can be seen that the required haze profile increases as the conduction current decreases, as in the Earth-like case

Again, as for the Earth-like case, we are not able to fit the model PDC to the Venera data well for all magnitudes of conduction current. Above 6 fA/m^2 the PDC will have a larger magnitude than the Venera data at some altitudes. Since the presence of haze will only act to increase the magnitude of this PDC, we are thus unable to fit the model result to the in-situ data above this value of conduction current. Again, it should be noted that this value is significantly lower than the typical conduction currents in Earth's global electric circuit.

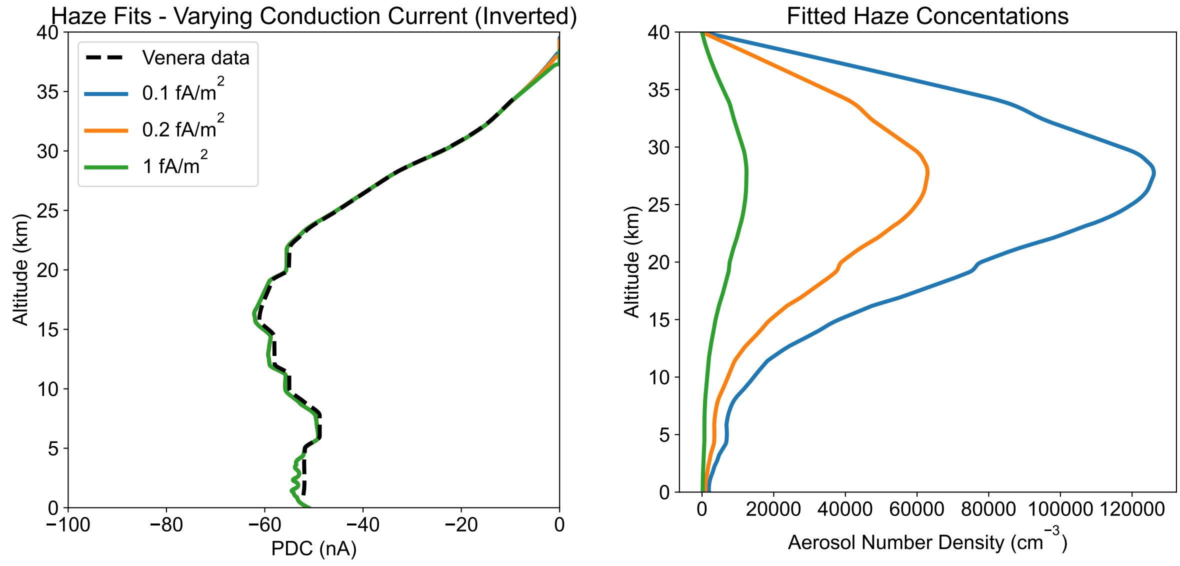

(a) Fit to In-Situ Data

(b) Haze Concentration Profile

Figure 4.34: Best fits of the model result to Venera data, for a range of different conduction currents. Three conduction currents have been considered, with magnitudes of 0.1, 0.2 and 1 fA/m^2. In all three of these cases, we have considered the global circuit to be inverted in its polarity. (a) shows the modelled PDC from each of these cases, shown as blue, orange, and green lines for 0.1, 0.2 and 1 fA/m^2 respectively. These are compared against the Venera data (black dashed line). (b) shows the three haze concentrations which were used as a model inputs to produce the profiles in (a). Again, blue, orange, and green lines were used for the conduction currents of 0.1, 0.2 and 1 fA/m^2. In all cases, the haze particle radius was 0.1 µm.

4.7 Discussion

An ionisation model, VAIL, has been produced to analytically calculate the number density of positive and negative ions in Venus' atmosphere. This model has been shown to provide similar results to the numerical model produced previously by Borucki et al. [20]. Further electrical parameters, such as the atmospheric conductivity and columnar resistance were calculated. Additionally, if we assume a global electric circuit is present, and the magnitude and polarity of the vertical conduction current is specified, then the atmospheric electric field and atmospheric potential are also able to be calculated by the model. These electrical results were used to determine the PDC which would be emitted by a spacecraft descending through Venus' atmosphere, as the Venera 13 & 14 landers did.

These modelled PDCs were compared against the data collected by the Venera 13 & 14 landers, in an attempt to determine the conditions which were required in order for the PDC profiles to be reproduced by an electrical model. A number of parameters, such as the corona onset potential, the presence and amount of haze, and the presence, polarity and magnitude of global atmospheric electric circuit were investigated, in order to determine the required parameters. From our investigation, we have found that the VAIL electrical model is only able to replicate the Venera 13 & 14 PDC data if there is both a global atmospheric electric circuit, and a low atmosphere haze layer present. The properties of the haze profile, the magnitude of the conduction current, and the polarity of this current are all unknown parameters, however.

The presence of such a global circuit in Venus' atmosphere has important implications for the electrical environment of Venus. In order to produce such a circuit, there must be some charge generation regions in Venus' atmosphere - akin to the disturbed weather regions in Earth's atmosphere. The processes responsible for this charge separation are uncertain, however it should be noted that the investigation performed here supports the presence of a global electric circuit regardless of its polarity. As such, there is no constraint made for the polarity of the charge separation process which would be required. In addition to necessitating some generator region, the presence of a global electric circuit in Venus' atmosphere will act to distribute the effects of charge throughout the atmosphere. This may lead to charge effects being more important to other aspects of Venus' atmosphere, than if such a circuit was not present. These charge effects will be discussed in more detail in the overall considerations of chapter 6.

Through our modelling approach, not all magnitudes of fair weather conduction current were able to reproduce the Venera PDC data. It was found that the conduction current density was limited between -3 and 6 fA/m^2. The magnitudes of these currents are significantly smaller than that of the typical currents in Earth's global atmospheric electric circuit, which are of the order of -1 pA/m^2. A possible explanation for this difference in magnitude is the very high columnar resistance of Venus' atmosphere compared to Earth's; for a fixed ionospheric potential, Ohm's law informs that the conduction current will be inversely proportional to the columnar resistance at the ionosphere. On Earth, measurements of the columnar resistance have shown it to be of the order of 100 PΩ[77]. From our modelling, we have found the columnar resistance of Venus' atmosphere at an altitude of 80km to be $\sim$60 EΩ. Assuming that the columnar resistance at Venus' ionosphere is similar to this value, we find that the columnar resistance of Venus' ionosphere is $\approx$ 600 times the columnar resistance of Earth's. This large columnar resistance may partially explain the difference between the magnitude of the conduction currents observed at Earth and the maximum magnitudes predicted at Venus, however, comparing the ratio of these currents, we find that the large columnar resistance cannot fully explain the difference in magnitude. Instead, we conclude that the ionospheric potential of the global circuit identified on Venus must be less than ionospheric potential of Earth's global electric circuit.

From in-situ spectrophotometric measurements, some estimates have been made for the optical depth of the haze layers in the lower atmosphere. From these estimates, it is expected that there is a relatively low concentration of particles at these altitudes. As such, the model results investigated in this chapter will likely be in better agreement with these previous spectrophotometric investigations if the particle concentrations are able to be minimised. From our modelling, it was found that the required concentration of particles increases with decreasing conduction current. As such, to satisfy the low particle concentration criterion, we would expect the conduction current to have a magnitude towards the larger end of the allowed range. In addition, by varying the haze particle size and the corona onset potential, the required concentration of particles may be reduced further.

It has additionally been proposed that the low atmosphere haze is variable in it's extent. Given this fact, and the shape of the haze concentration profiles which are required for the Venera data to be replicated - i.e an increased concentration of haze at elevated altitudes - it is possible that volcanic ash is a possible source of the haze. It is known that Venus has some volcanic activity, however a lot more has yet to be learned on the nature of any volcanic eruptions [86]. Additionally, it should be noted that the PDC profiles detected by the Venera 13 & 14 landers were broadly similar to each other, despite landing a significant distance apart. As such, a "transient haze" explanation would need to account for the spread of haze across significant horizontal distances.

A number of assumptions have been made, both within the VAIL model, and in the application of the VAIL model to reproducing the Venera PDC data. The importance of several of these assumptions have been investigated explicitly. It was found that our choice of interpolator had minimal impact on the model results. The main impacts on this choice occurred within the cloud layers, as the resolution of the input cloud data was relatively coarse. As such, we do not expect this to have an impact in the region of the atmosphere where the PDC was investigated in detail.

The assumption that our aerosol size distributions were well modelled as monodisperse distributions was shown to have had a minor effect on the model results. This is of particular interest here, as it was shown that considering the full aerosol size distribution - rather than assuming a monodisperse distribution - led to a greater decrease in the ion number density. As such, we can conclude that the haze profiles which were required for a particular perturbation to the PDC profiles were actually overestimates, as if the size distributions had been considered fully, then the same decrease in ion concentration could be achieved by a lower concentration of haze. This effect may result in our modelling approach predicting a more tenuous haze in the lower atmosphere.

Finally, the value of the corona onset potential was shown to have a notable effect on the magnitude of PDC emitted. Despite this impact, varying the onset potential was unable to allow the Venera PDC data to be reproduced, without both haze layers and a global electric circuit also present. Varying this value would have an effect on the required haze profile, however.

There are additional assumptions which have been made in this investigation, which will be summarised here. Firstly, since little information was available on the spacecraft descent speed above 50km, the assumption was made that the nature of the descent speed was the same as below 50km. This is likely a relatively bad approximation, however since this only affects the descent speed of the spacecraft above the region of the Venera PDC data, this assumption should have minimal effect on the investigation of the Venera data.

Several assumptions have been made on the nature of the electrical breakdown field, which informed the values of the corona onset potential. These assumptions may have an impact on the precise shape of haze profile which is required to reproduce the Venera PDC data.

For the calculations of the ion-aerosol attachment coefficients, we have considered the aerosols to have a neutral charge distribution. This assumption would likely have an impact on the ratio of positive and negative ion concentrations that were determined by the model. Additionally, in these calculations, the effects of image charges on the aerosol droplets has been neglected. This is likely an important effect, since it would mean that ions would still be able to attach to like-charged highly charged aerosols. Since we have concluded that the presence of a global circuit is most consistent with the Venera PDC data, this would suggest that highly charged aerosols are more likely than if such a circuit was not present.

Similarly, in our determination of the ion number densities we have not included the movement of ions due to the conduction current of a global electric circuit, or the space charge densities required to produce the electric fields of such a system. By neglecting these effects we have shown that some solutions are likely to be possible with a global atmospheric electric circuit, however, in order to model the effects of a global circuit properly these would need to be considered in our model.

For some of these assumptions, we are limited by the analytical model used. A future investigation utilising a numerical model of Venus' atmosphere may be able to avoid these limitations, at the cost of computational power. For other assumptions, we are limited by the data available for Venus' atmosphere. It is hoped that future spacecraft missions to Venus will be able to expand the amount of in-situ data which is available, reinforcing any assumptions which need to be made. In chapter 7, several future investigations which would be advantageous have been discussed.

4.8 Conclusions

In conclusion, we have found that the point discharge currents recorded by the Venera 13 & 14 landers are consistent with both a global atmospheric electric circuit and a low atmosphere haze layer being present in Venus' atmosphere. The presence of such a global circuit would have important implications for the electrical environment of Venus; in order to produce such a circuit, there must be some charge generation process present in Venus' atmosphere. Additionally, the presence of a global circuit would allow electrical charges to be distributed throughout the atmosphere, meaning that electrical processes could be important distant from any charge generation regions.

It was found that either polarity of global electric circuit was able to reproduce the Venera data. Based on the assumptions made in this investigation, however, the magnitude of the fair weather conduction current was able to be constrained. It was found that the Venera data could be reproduced for vertical currents between -3 and 6 $\mathrm{fA/m^2}$. This suggests that the ionospheric potential on Venus is significantly lesser than the ionospheric potential on Earth.

Chapter 5

Space Weather Effects in the Atmosphere of Venus

The presence of electrical effects in Venus' atmosphere has been investigated in Chapter 4. Here, we consider further whether such effects are present, by investigating the impacts that space weather events and cosmic ray variations have on Venus' atmosphere.

Our search for space weather/cosmic ray effects in Venus' atmosphere is motivated by previous investigations of such effects on other planets in our solar system. In particular, we wish to draw comparison between the ice giants - Uranus and Neptune - and Venus. On these planets, cosmic rays can affect the atmosphere through the process of ion-induced nucleation. This process is believed to be able to occur in Venus' atmosphere also, however cosmic rays can affect planetary atmospheres through other mechanisms - as is the case for Earth, where ion induced nucleation does not occur.

On earth, the effects of Forbush decreases and SEP events on the atmosphere have previously been investigated. The effects of these events have been identified by considering how some atmospheric parameter changes following the event. To investigate this, the response across several such events is compared - allowing the general trend following the event to be identified. This allows the polarity of changes in the atmosphere to be investigated, as well as investigations of the timescales of such changes.

Additionally, the effects of periodic variations in cosmic ray count rates on planetary atmospheres have previously been investigated. For Earth, variations with periods of 27 days and 1.68 years have been studied, with the 1.68 year periodicity also investigated for the ice giants. One of the methods performed in these analyses was to compare the periodic signals present in a cosmic ray dataset to periodic variations in some atmospheric dataset (i.e. the cloud base height, diffuse fraction, or apparent magnitude). If similar features were present in the two datasets at the same time, then this was interpreted to be some evidence for a cosmic ray effect on the atmosphere.

The investigation described in this chapter builds upon the methods utilised for other planets. This investigation is composed of two parts: First, the short term response of Venus' atmosphere to several space weather events is considered. Following the methods developed for Earth, the atmospheric responses to these space weather events were identified by compositing data across a number of events. Second, periodic variations in Venus' atmosphere, and their link to periodic variations in cosmic rays, are investigated. Similar to previous investigations, this was performed by identifying periodic signals present in both a cosmic ray dataset and an atmospheric dataset, however in this investigation, the coherence between these two datasets was used to identify a common signal between them.

In section 5.1, the data used in this analysis is described. In section 5.2, several of the analytical methods used throughout this investigation are described. In section, 5.3, the short term effects on Venus' atmosphere from space weather events are considered. First, the effects of Forbush events detected at Venus are considered, before considering Solar Energetic Particle (SEP) events detected at Venus, and finally considering Heliospheric Current Sheet (HCS) crossings also detected at Venus. Section 5.4 investigates the periodic signals present in both the albedo of Venus and several cosmic ray datasets, through calculations of the coherence between these signals. Finally, the results from both aspects of this investigation - covering space weather perturbations, and cosmic ray periodicities - are discussed in section 5.5.

5.1 Data

This section summarises the data used for the analysis in this chapter, along with the preliminary processing of this data. To explore energetic particle effects on Venus atmosphere, it was desired to have data describing the both the atmosphere and the cosmic ray environment.

To monitor atmospheric effects on Venus, a dataset on the albedo was used. This is described in section 5.1.1. To monitor the cosmic ray environment over the same time period as these albedo observations, several datasets were used. These are described in sections 5.1.2, 5.1.3, and 5.1.4. Key details on the cosmic ray (CR) datasets have been summarised in table 5.1:

Dataset Name	**Observation Location**	**Energies Observed**
Oulu Neutron Monitor	Earth	$\gtrapprox$ 500 MeV (GCRs)
ACE SIS	Earth-Sun L1 Point	30-100 MeV (SEPs, low-E GCRs)
Venus Express IMA	Venus Polar Orbit	$\gtrsim$1 MeV electrons, $\gtrsim$ 20 MeV protons (SEPs)

Table 5.1: Summary of cosmic ray data used.

5.1.1 Albedo Data

A dataset describing Venus' albedo was produced by Lee et al. [109]. This dataset was produced from data recorded by the Venus Monitoring Camera (VMC) instrument onboard Venus Express (VEX). The albedo dataset was produced from the data recorded at a wavelength of 365nm. At this wavelength, there is a large amount of absorption in the upper-cloud region of Venus' atmosphere [109]. As such, we interpret this albedo data as recording variations in clouds of Venus. In the investigation performed by Lee et al., several statistically significant periodic variations were identified in the data for latitudes between 30 and 35° South. The source of these variations was uncertain, however.

For our analysis, we will investigate this albedo data further to determine if cosmic ray effects are responsible for any variations in the data. The dataset produced by Lee et al. provided the albedo of Venus at local solar times between 0700 and 1700, in bins of size 0030. For our purposes, we have considered the albedo in one of these bins; this was arbitrarily selected to be the range 1200-1230. A time series of this albedo data is shown in figure 5.1.

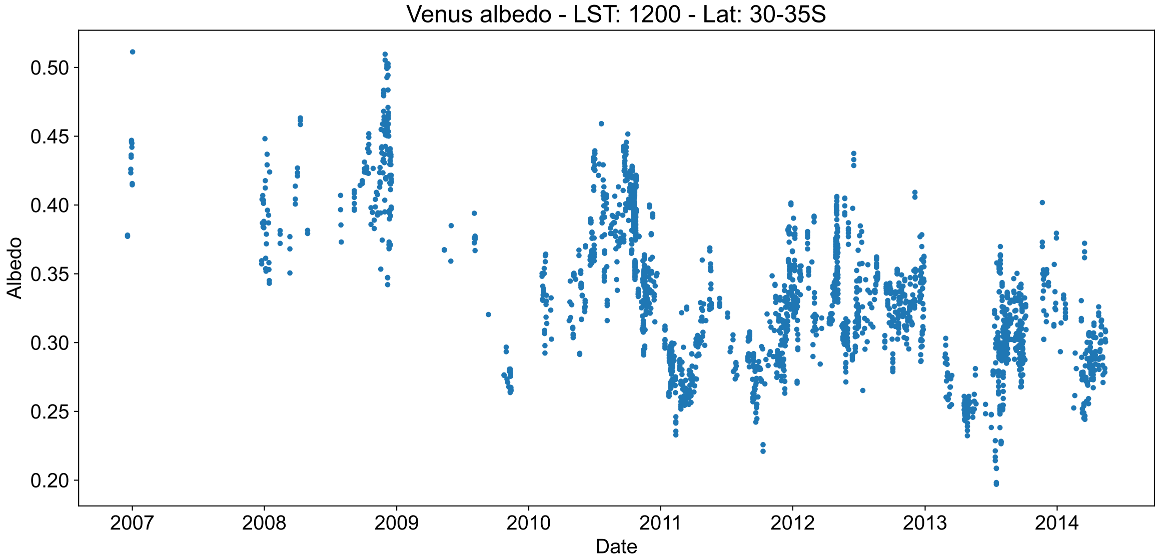

Figure 5.1: Time series of Venus' albedo determined from the Venus Express 365 nm data. The albedo at a latitude of 30-35° S and local solar time of 1200 has been shown. This albedo dataset was produced by [109].

5.1.2 Oulu Neutron Monitor Data

In order to measure the effects of GCR, data from a neutron monitor on Earth was used. As described in chapter 2, these devices are able to monitor the flux of GCR, via detection of the secondary neutrons produced in a cosmic ray cascade.

For our investigation, data from the Oulu neutron monitor was selected, as this monitor had easily accessible data from its long operational duration - data is available since 1964. The Oulu neutron monitor is located at a latitude of 65.05°N and a longitude of 25.47°E. For our analysis we have used the daily average neutron count data, provided by Oulu. A time series in the same time range as the VEX albedo data is shown in figure 5.2.

5.1.3 ACE Solar Isotope Spectrometer Data

To allow differences between the cosmic ray count rates at different energies to be considered, cosmic ray data from other sources has additionally been considered. Given that the Earth's magnetic field screens low energy particles from interactions with the atmosphere, in order to observe these particles we require a detector outside the Earth's magnetic field. Several spacecraft have charged particle detectors for this purpose. For our investigation, we have used the data from such a spacecraft; the data collected by the Solar Isotope Spectrometer (SIS) instrument on the ACE spacecraft was used. The ACE spacecraft is located at the L1 Lagrange point between the Earth and the Sun - so the charged particles detected will not be affected by Earth's magnetic field. Data was selected in the high energy (> 30 MeV) bin, and was provided

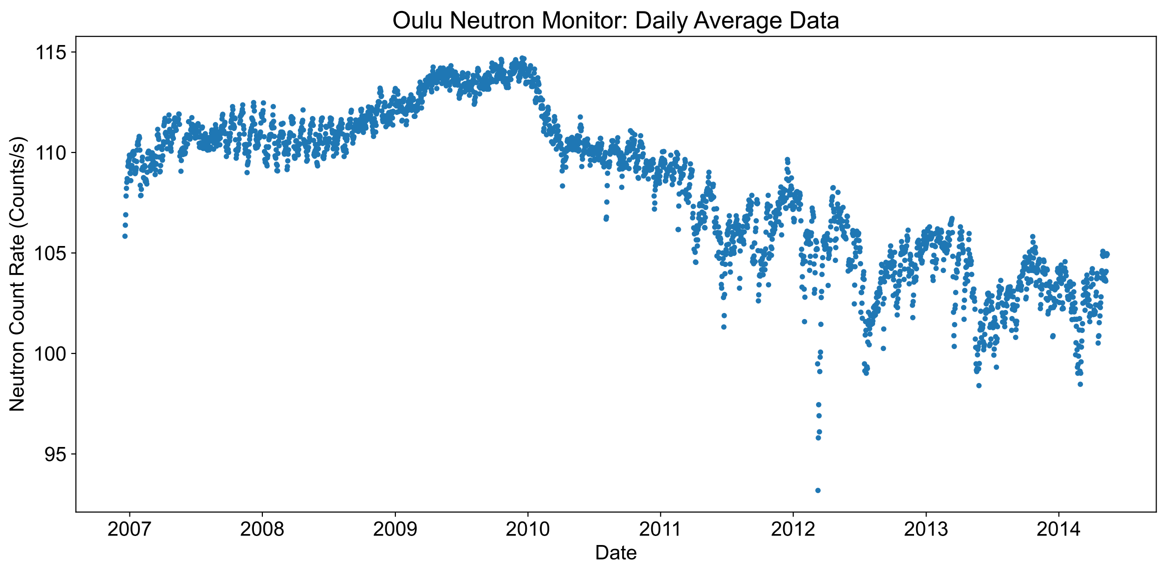

Figure 5.2: Oulu neutron monitor daily average count rate for the same time period as the albedo data, shown in figure 5.1. Data accessed from [192].

at 1h intervals. This data was resampled, taking the mean value in a 24h period, to provide daily data for the proton flux. A time series of this resampled data is shown in figure 5.3.

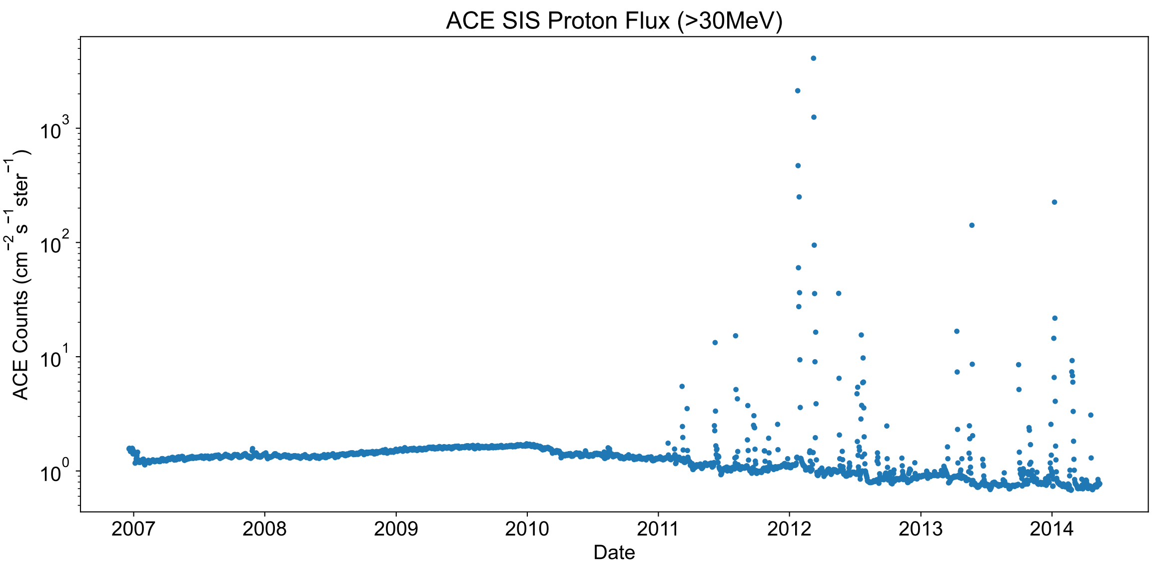

Figure 5.3: ACE Solar Isotope Spectrometer data for the same time period as the albedo data, shown in figure 5.1. Data for the high energy (>30MeV) bin has been shown. Data accessed from [1].

5.1.4 VEX Ion Mass Analyser Data

The two previous cosmic ray detectors were located at or near Earth. Since we are investigating the effects that charged particles have on Venus' atmosphere, it would be preferable to be able to measure cosmic ray count rates at Venus itself. Given that we require this data for the time period of the VEX albedo data, we are limited in the instrumentation which could be used.

One of the instruments onboard Venus Express was the Ion Mass Analyser (IMA). This instrument was designed to observe the mass, energy, and angle of incidence of solar wind particles. The IMA instrument operated by allowing only particles with aziumuthal and elevation angles within a certain range to enter the sensor. These particles were then passed through an electrostatic analyser and a velocity analyser which selected only particles with the correct energy and mass per charge.

The particles which passed the criteria for incident angle, energy, and mass were detected by a microchannel plate (MCP). During an observation period of the IMA instrument, the selection ranges for azimuthal angle, elevation angle, particle energy, and particle mass were all varied, with the number of particles collected in a given time counted for each set of criteria. As such, for each observation period, which took 192s to perform, a 4-D histogram of particle counts was produced. The particle counts recorded across two of the dimensions of this histogram (the particle energy and mass) have been shown in figure 5.4, averaged across several observations. The 4-D histogram was compressed to 2-D by summing across these other two dimensions.

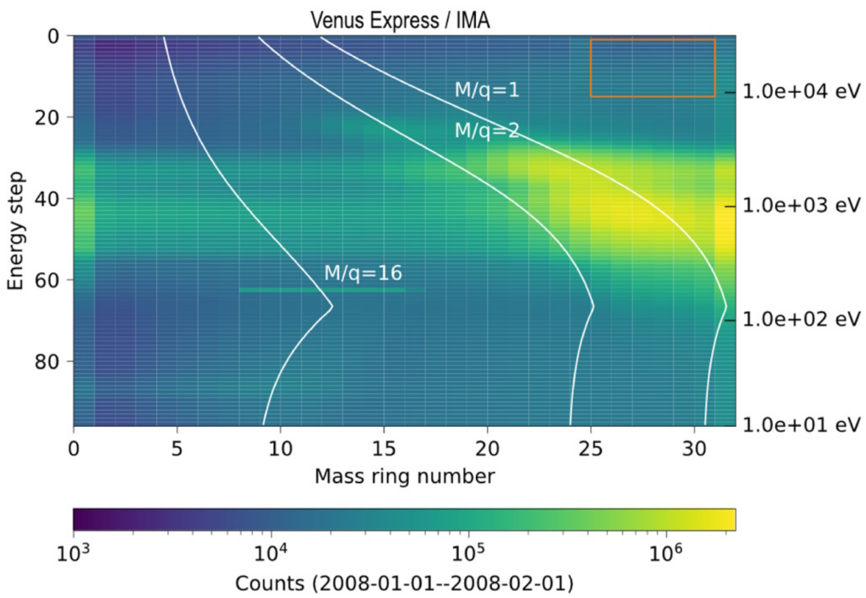

Figure 5.4: Venus Express IMA counts over a 1 month period, for the energy and mass bins, produced by [51]. The bins corresponding to particles with mass/charge ratios of 1,2, and 15 amu/e have been shown as white lines. The background channels of the instrument have been indicated by the orange box in the upper right.

Note that the mass bins in the histogram do not correspond trivially to the particle mass per charge, and instead are dependent on the particle energy per charge. The location of the bins with certain values of mass/charge ratio have been indicated on the figure.

The IMA instrument was designed to observe solar wind plasma, and as such was tailored towards relatively low energy protons; the sensor was able to select for particles in the energy range from 10 eV - 30 keV. This energy range is significantly lower than the energies typically considered for GCR and SEPs. It has been observed, however, that high energy cosmic rays are often a source of background counts observed by MCP instruments. A previous investigation by

Futaana et al. [51] found that the background counts of the IMA instrument could be estimated by considering certain bins in the 4-D histogram which do not correspond to correctly processed particles. These bins have been highlighted as an orange box in the upper right corner of figure 5.4. These background counts are not able to be translated accurately into a value for the cosmic ray flux, however can be used as a qualitative measure of this, and can be used comparatively - to compare how the flux changes with time. The particle energies responsible for these counts have additionally been considered [51]. It was estimated that the main contributions would be from electrons with energy > 1 MeV and protons with energy > 20 MeV.

In order to produce a time series of the cosmic ray flux as estimated by the IMA sensor, the background counts in each instrument observation were determined. The changes in these background counts were then interpreted as changes in the cosmic ray environment. The IMA instrument did not take measurements at a constant rate. Often, a number of observations were taken by the instrument in rapid succession, before a period of time without any measurements. The background data collected over a several day period has been shown in figure 5.5 to illustrate this.

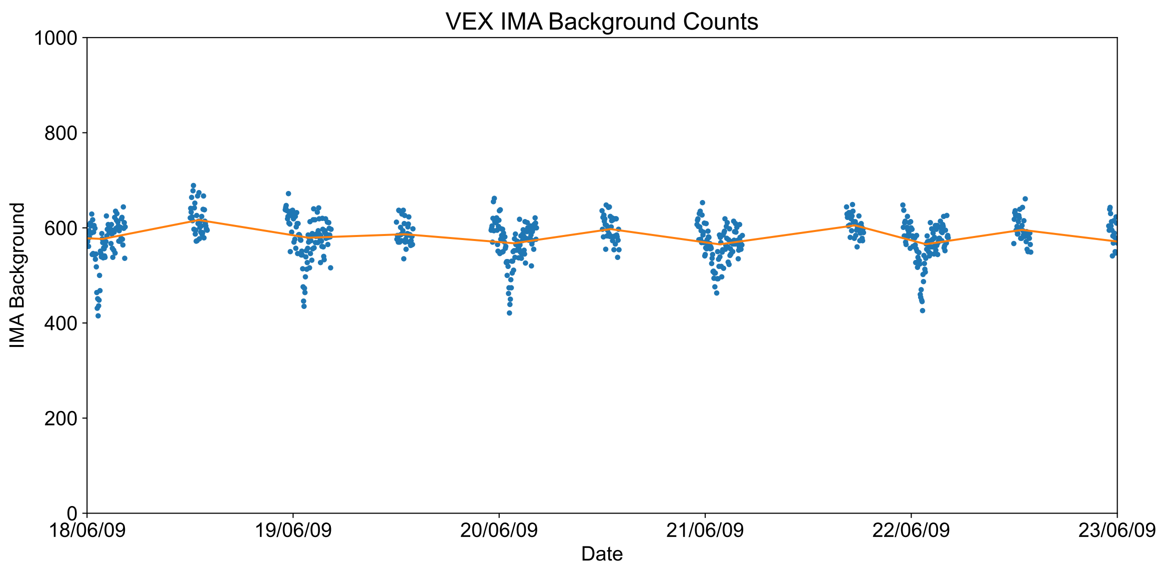

Figure 5.5: Venus Express IMA background data over a several day period. The data appears to form "clusters" in time. The average value of each of these clusters has been shown as a solid orange line.

It was observed that there were typically several of these clusters of observations in a given 24h period. These observations showed high frequency variations, occurring on time scales of several minutes. In order to look at variations occurring on the time scales of several hours, the average value of the counts in each cluster of observations was determined. The time series of these average values is shown in figure 5.5. The time series of this dataset across the same time period as the albedo data is shown in figure 5.6. It should be noted that in 2010 the data processing of the IMA instrument was changed to include the removal of some of the background - hence the change in magnitude of the background counts.

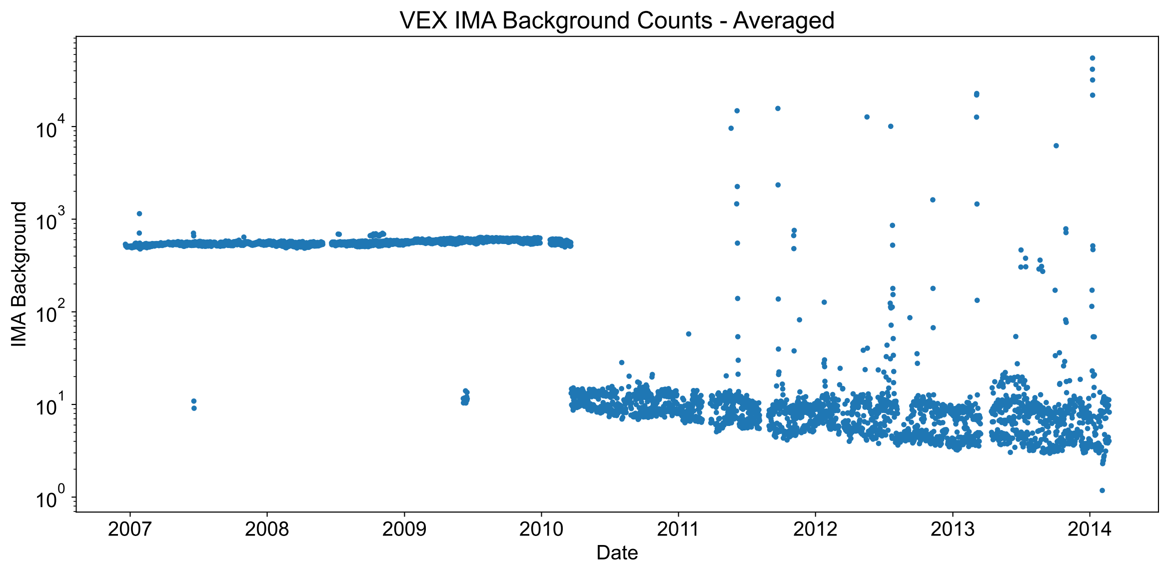

Figure 5.6: Venus Express IMA background data for the same time period as the albedo data, shown in figure 5.1. The original data was accessed from [198].

5.1.5 Magnetometer Data

To identify heliospheric current sheet crossings at Venus, data from the magnetometer (MAG) instrument onboard Venus Express was used. This dataset provided the x, y, and z components of the IMF as detected at Venus Express, at 1s intervals. These were provided in the Venus solar orbit (VSO) coordinate system. In this coordinate system, the xy plane is the orbital plane of Venus, with the x-axis pointing Sunward, and the y-axis perpendicular to this, with the positive direction opposite to Venus' orbital velocity. The z-axis completes the right handed coordinate system, pointing in the direction of Venus' orbital angular momentum. This coordinate system is shown in figure 5.7.

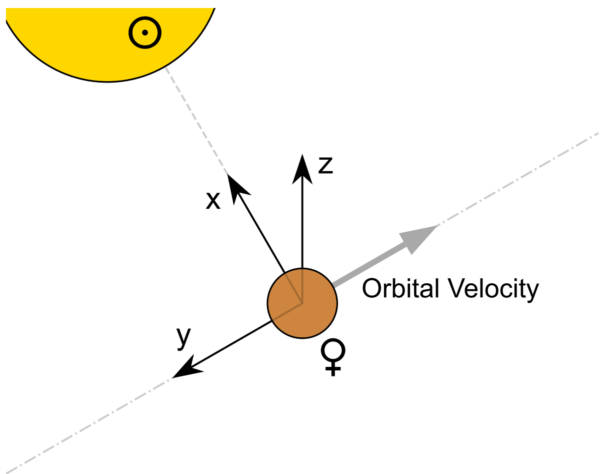

Figure 5.7: Venus Solar Orbit (VSO) coordinate system. The Sun and Venus have been shown via the symbols ⊙ and ♀ respectively. The (x,y,z) directions of the VSO system have been indicated.

For our analysis, both this Cartesian coordinate system, and a spherical polar coordinate system was used. In this spherical polar system the azimuthal angle, ϕ, was in the range $[0, 2\pi)$, with polar angle θ in the range $[-\pi/2, \pi/2]$. These spherical polar co-ordinates (r,ϕ,θ) are related to the Cartesian coordinates (x,y,z), via:

$$x = r\cos(\phi)\sin(\theta) \tag{5.1}$$

$$y = r\sin(\phi)\sin(\theta) \tag{5.2}$$

$$z = r\cos(\theta) \tag{5.3}$$

Short time series of the data from the MAG instrument have been shown in figure 5.8. Time series of both the Cartesian and spherical polar components have been included.

The further processing performed on the magnetic field data, allowing for the detection of HCS crossings is described in section 5.3.4.

5.1.6 Additional Datasets

Several additional datasets were used in our analysis; a list of CME events as detected by the Venus Express spacecraft was provided by HELCATS in their WP4 Catalogue [81]. For the events detected by Venus Express, we were provided with a start and end time for the CME event, as well as the size of the magnetic disturbance. The timing of these events was used.

The positions of the Earth, Venus, and the Sun at specific times were determined using the ephemerides provided by JPL Horizons [84]. This allowed the relative positions of the planets to be found at these times - in particular the angular separation between the Earth and Venus.

Finally, the daily sunspot numbers provided by NOAA [174] were used as a metric for solar activity. This data is shown in figure 5.9. The variation in sunspot number caused by the 11 year solar cycle can be observed across this $\sim$7 year time series.

5.2 Methods

5.2.1 Data Binning and Detrending

Some of the analysis performed in this section involved comparing data at different times. Since we were interested in investigating short term variations in the data, it was necessary to remove any long term variations. This was performed via a local detrending procedure. As a first step in this local detrending, the data was binned according to time.

The binning process was performed to ensure that the data in a given time range was spread across the range, rather than allowing a number of datapoints at similar times to affect the overall properties of the data. To perform this binning, a number of equal width bins were identified spanning the time range of interest. Next, a value for the data was selected for each of these bins. In the case where there was more than one datapoint, this value was given by the median of the data. In the case where there is only one datapoint, that value was selected.

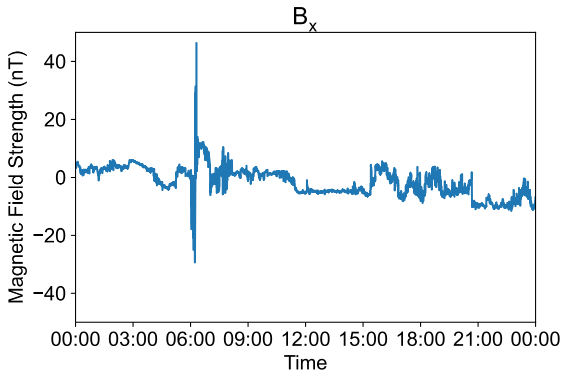

(a) x-component of B

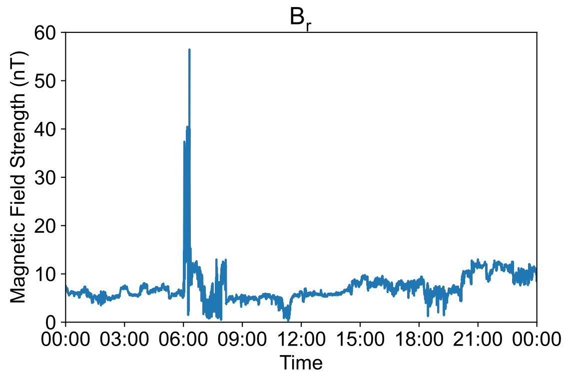

(b) r-component of B

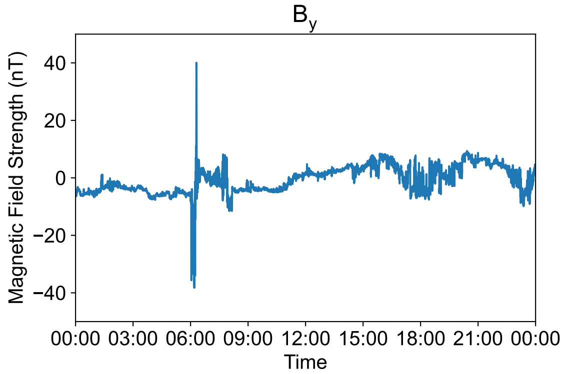

(c) y-component of B

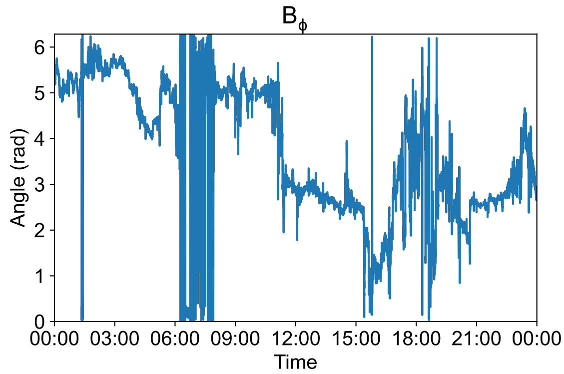

(d) ϕ-component of B

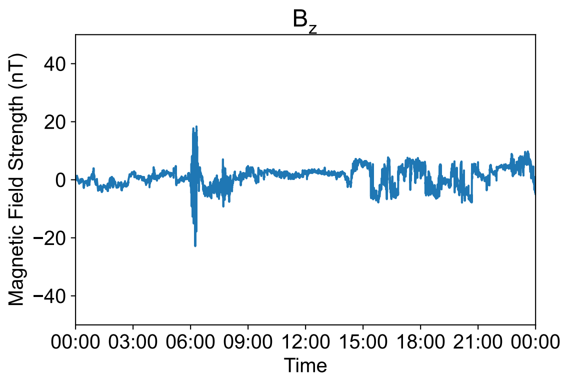

(e) z-component of B

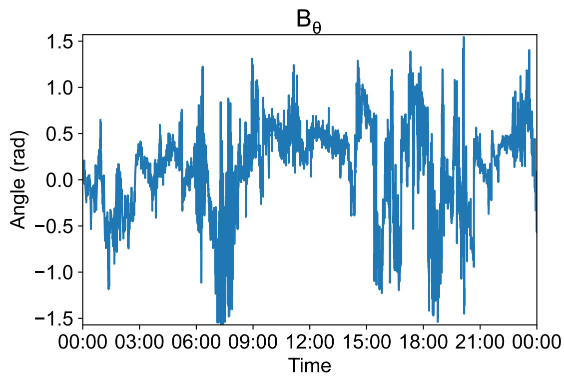

(f) θ-component of B

Figure 5.8: Components of the magnetic field vector detected by Venus express for a given day (2010-02-01). The cartesian components of the magnetic field are given in (a), (c), (e). The spherical-polar components of the magnetic field are given in (b), (d), (f).

Finally, if there are no datapoints in a given time bin, then the value will be set as NaN (not-a-number).

Following this binning, the data was locally detrended. This was performed by first determining the mean value of the data in a given time range. Next, the value of each datapoint in this range was calculated as a percentage of the mean. This local detrending was only performed in the case where there was a suitable number of datapoints involved in the calculation of the

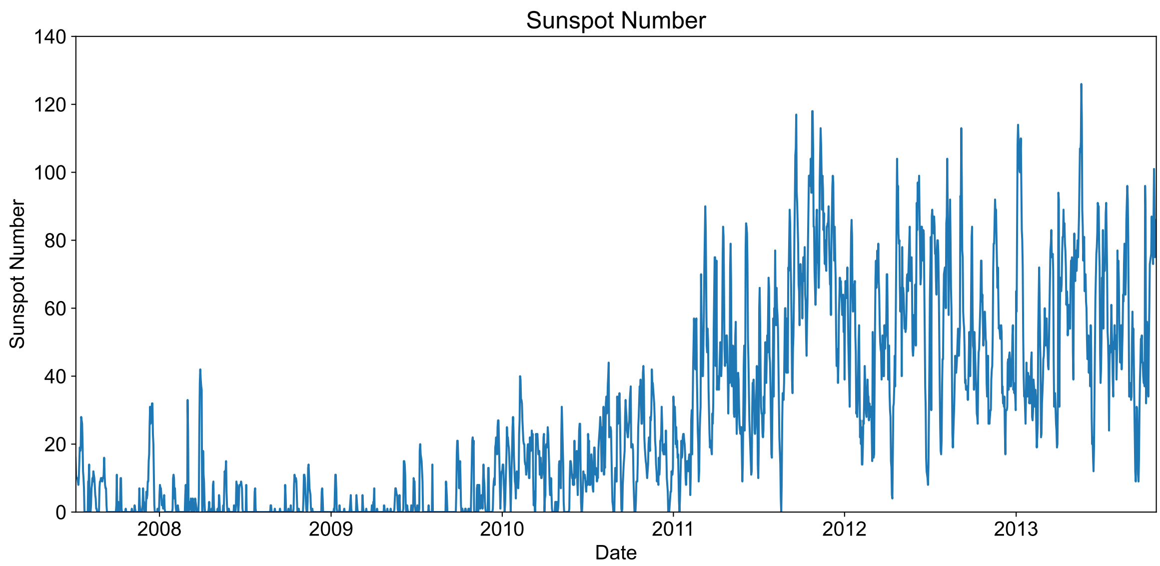

Figure 5.9: Time series of the sunspot number. The sunspot data was obtained from NOAA [174].

local mean. This cut-off value will be indicated when discussing the analysis in this chapter.

The binning and detrending process is illustrated in figure 5.10.

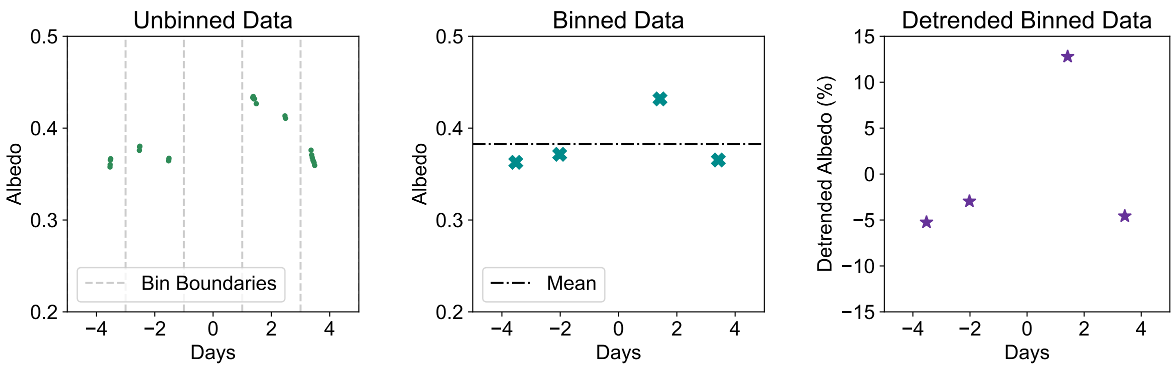

(a) Unbinned Data (b) Binned Data (c) Detrended and Binned Data

Figure 5.10: Figures explaining the binning and detrending process (a) shows the unbinned data. The boundaries of each bin have been overlaid as dashed lines. (b) shows the data from (a), after binning. A single value for the albedo was selected for each bin. The mean of these binned values has been indicated as a dot-dashed line. (c) shows this binned data after detrending. Each datapoint from (b) has been found as a percentage of the mean.

5.2.2 Statistical Independence of Binned Data

To perform statistical analysis on a given dataset, it is important that datapoints are statistically independent from one another. As part of the binning and detrending procedure described in 5.2.1, the size of the time bins were selected such that the datapoints from different bins were statistically independent.

This statistical independence was tested by applying the binning and detrending to a randomly sampled subset of the data, and then calculating the autocorrelation of the data. The parameters used in this test of statistical independence (such as the number and size of the bins, and the required number of datapoints for a calculation of the mean) were matched to the parameters which were to be used in the analysis. A number, n_{auto}, of random times were selected to form the subset of data. Following the binning and detrending process, the autocorrelation between adjacent bins was calculated. The 95% confidence level of the autocorrelation for this data was calculated via:

$$\delta_{95} = \frac{\sqrt{2}\,\mathrm{erf}^{-1}(0.95)}{\sqrt{n_{auto}}} \tag{5.4}$$

where $\mathrm{erf}^{-1}(x)$ is the inverse error function. For data with an autocorrelation lying below this confidence limit, it can be interpreted that the datapoints are statistically independent.

The random sampling of the data was performed a number, n_{MC}, of times. These repeated investigations allowed a mean value and standard error on the mean to be calculated for the autocorrelation. For the investigations performed here, it was necessitated that the mean value + 1 standard error on the mean be below the 95% confidence limit for it to be considered that the the binning and detrending process yielded statistically independent data.

This investigation of statistical independence is illustrated for both the albedo dataset and the IMA dataset in figure 5.11. In these cases, the autocorrelations are calculated for different sizes of bins, in a 15 day range, with a minimum cutoff of 4 points used to calculate each local mean. The 95% confidence cutoff has been indicated on this plot, allowing the minimum size of the bins which yields statistically independent data to be identified. In these cases, 1000 data samples were used in each calculation of autocorrelation, with the errorbars found from 100 Monte Carlo iterations.

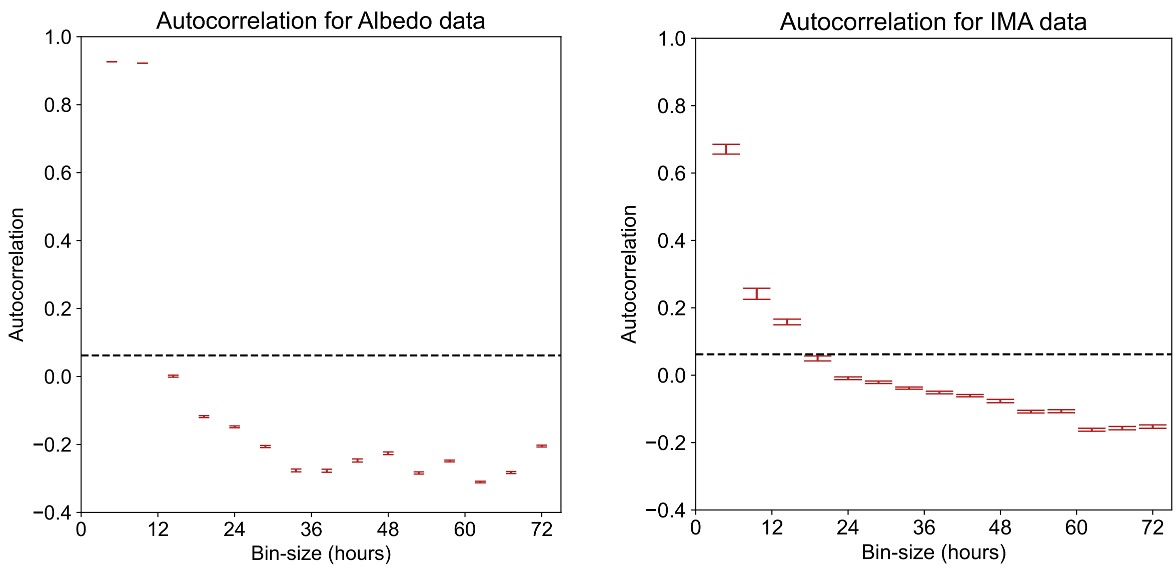

(a) Autocorrelations for Albedo data.

(b) Autocorrelations for IMA data.

Figure 5.11: Autocorrelations for the albedo data (a) and IMA data (b) at different lead/lag times. The 95% confidence limits have been plotted as dashed lines. For autocorrelation values below this dashed line, the datapoints are considered to be statistically independent.

From figures 5.11a and 5.11b, the bin sizes which will yield statistically independent datapoints in adjacent bins can be identified by considering the datapoints which lie below the 95% confidence limits. In much of the analysis performed, bins of size 24h will be used. It can be seen that for both datasets, this size of bin yields statistically independent data.

5.2.3 Power Spectral Density

Auto Spectral Density

For some of the analysis performed in this chapter, we are interested in investigating the periodic variations present in a dataset. One method to identify the periodic signals present in a time series is by considering the discrete Fourier transform (DFT) of the data. By taking the squared amplitude of this Fourier transform, the power spectral density (PSD) of the input signal can be determined; this gives the contribution of different frequencies of variation to the overall signal [196]. This power spectral density is often described as an autospectrum, to avoid confusion with other spectral densities which can be calculated when multiple datasets are considered.

A technique, sometimes employed when calculating the autospectrum for a dataset, is to divide the input data into several overlapping segments, and calculate the autospectrum for these individual segments, before finding the average across these. This technique is described as Welch's method, and is used to reduce the amount of noise present in the autospectrum. The amount of overlap between segments is varied across the implementations of this technique.

In addition to the DFT, there are other transforms which can be performed on an input signal to identify the periodicities present. The discrete wavelet transform allows the important frequencies of an input to be identified similarly to the DFT, while also providing information on the timing of these frequency contributions. For both of these transforms, however, it is typically required that the input data is regularly sampled in time. Irregularly sampled data is a particular concern in the field of astronomy, as many factors can prevent regular observations. To deal with this limitation, often a Lomb-Scargle Periodogram will be used to perform such analysis [196]. The Lomb-Scargle Periodogram is a method which allows the power spectral density of a time series to be determined at a range of prescribed frequencies, with an added benefit of being able to be used for data which is irregularly sampled, or features "gaps" in time. As such, we will use this method in our analysis.

The frequencies at which a DFT is calculated are determined solely from the input data. This is not the case for the Lomb-Scargle Periodogram, which is able to be calculated at any desired frequency. The frequency range used should be tailored to any individual investigation, however Vanderplas [196] discusses several sensible limitations which can be made. These suggested limitations, and how we will utilise them, have been summarised here:

For regularly sampled data, the Nyquist frequency is the highest frequency of variation which can be identified. This frequency is given by:

$$f_{nyq} = 0.5 \times \frac{1}{\Delta t} \tag{5.5}$$

where Δt is the time interval between data samples. For irregularly sampled data, such a frequency limit is not easily determined. Values for this limit are often approximated in different ways. For the work here, we will naively consider the nyquist limit to be given by:

$$f_x = \frac{1}{2\langle\Delta t\rangle} \tag{5.6}$$

This thus will provide the maximum frequency which should be considered when calculating the autospectrum for a dataset. The minimum frequency to be considered can be found by considering the period of the dataset. The periodic variation with period equal to the length of the dataset provides a good minimum frequency for the calculation of an autospectrum.

In our investigations, we will ensure that the frequencies considered lie within these upper and lower limits.

Cross Spectral Density & Coherence

In addition to considering the periodic variations in a single dataset, it is also possible to investigate the variations which are present across several datasets. This allows the cross spectral density or cross-spectrum to be determined.

In addition to this cross-spectrum, the coherence of two input signals can be found. The coherence spectrum is given by the ratio of the magnitude squared of the cross spectrum to the product of the auto spectra of the two signals. The coherence between two signals is a dimensionless number between 0 and 1. This quantity can be interpreted as the fraction of the variation in one of the datasets which is driven by a variation in the other, at a given frequency of variation. We will use this coherence quantity to investigate any periodic variations which are present across different datasets.

5.2.4 Lomb-Scargle Calculations

The calculations involved in determining auto-specta, cross-spectra, and coherence-spectra using Lomb-Scargle methods have previously been documented [161]. Schultz and Statteger [161] describe a program, SPECTRUM, designed to perform such spectral analysis. For the investigation here, the methodology described by Schultz and Statteger was implemented in Python-3 code, and has been described here.

As a first step in calculating the coherence, first Lomb-Scargle transforms were performed for each input time series. For a time series given by $x_n \equiv x(t_n)$, where $n = 0, 1, ..., N-1$, we subtract the mean value of the time series, $\langle x\rangle = \sum x_n/N$. Next, we separate this into a number, n_{50}, of segments, overlapping each other by 50%. These segments each contain N_{seg} points, such that:

$$N_{seg} = \frac{2N}{n_{50}+1} \tag{5.7}$$

Each of these segments is then multiplied by a time dependent window function, resulting in each segment having a series given by $x'_j \equiv x'(t_j)$ where $j = 0, 1, ..., N_{seg} - 1$. The window weights, w_j were chosen such that $\sum w_j^2 = N_{seg}$. Various shapes of window are able to be used in this analysis.

Next, the Lomb-Scargle transform is performed on each of these segments, according to:

$$X(\omega)_k = \frac{1}{\sqrt{2}}\left(\frac{\sum_j x'_j cos(w_k(t_j - \tau))}{\sqrt{\sum_j cos^2(w_k(t_j - \tau))}} + i\frac{\sum_j x'_j sin(w_k(t_j - \tau))}{\sqrt{\sum_j sin^2(w_k(t_j - \tau))}}\right) \tag{5.8}$$

where $k = 0, 1, ..., n_{50} - 1$, i is the imaginary unit, and,

$$\tau(\omega) = \frac{1}{2\omega}\, tan^{-1}\left(\frac{\sum_j sin(2\omega t_j)}{\sum_j cos(2\omega t_j)}\right) \tag{5.9}$$

Note, this is slightly simplified version of the equation in [161] since time displacements between different input signals are not considered in this analysis.

The auto-spectrum is calculated from the Lomb-Scargle transforms from each segment, using equation 5.10:

$$G_{xx}(\omega) = \frac{2\langle\Delta t\rangle}{n_{50}} \sum_k |X(\omega)_k|^2 \tag{5.10}$$

where $\langle\Delta t\rangle$ is the mean time separation between points in the time series segment, i.e.:

$$\langle\Delta t\rangle = \frac{1}{N_{seg} - 1} \sum_{j=0}^{N_{seg}-2} (t_{j+1} - t_j) \tag{5.11}$$

To find the cross spectrum between two signals, containing N_x & N_y points, the Lomb-Scargle transforms are performed as in equation 5.8 for both time series, providing $X(\omega)_i$, $Y(\omega)_i$ as outputs. The cross spectrum is then found from equation 5.12:

$$G_{xy}(\omega) = \frac{2\Delta t_{xy}}{n_{50}} \sum_k |X(\omega)_k\, Y^*(\omega)_k| \tag{5.12}$$

where * represents the complex conjugate, and Δt_{xy} is the geometric mean of the average time separations of the relevant segments of the two time series, given by:

$$\Delta t_{xy} = \sqrt{\langle\Delta t_x\rangle \cdot \langle\Delta t_y\rangle} \tag{5.13}$$

Note, this definition of Δt_{xy} is slightly different to the one used in [161], as it was chosen such that the coefficients in equations 5.10 and 5.12 will cancel in equation 5.14. This cancellation was also performed in [161], however a different coefficient was used in equation 5.10 when calculating the coherence. Using equation 5.13 allows us to keep the coefficients the same in all cases.

Finally, the coherence can be determined from the auto-spectra from the two inputs, and the cross spectrum of these signals.

$$Cxy(\omega) = \frac{|G_{xy}(\omega)|^2}{G_{xx}(\omega)\, G_{yy}(\omega)} \tag{5.14}$$

Note that in order to perform this coherence calculation, it is necessary that $n_{seg} > 1$.

5.2.5 Verification of Lomb-Scargle Code

In order to verify the python implementation of the auto-spectra, cross-spectra, and coherence spectra calculations, the results obtained from these methods were compared against the results obtained from the SPECTRUM program. To perform this validation, the test data included in the SPECTRUM program was used.

Firstly, the calculations were verified for a single segment of data. The results shown here are for a rectangular window. The auto-spectra found from both the SPECTRUM program and the python implementation are compared in figures 5.12a and 5.12b for the two datasets, respectively. Additionally, the magnitude of the cross-spectra from the two programs are compared in figure 5.12c.

As can be seen here, there is a very strong agreement between the two methods. Any slight variations between the results from the different methods are interpreted to be rounding errors. Similar results are obtained for varying window shapes.

Additionally, the results for a varying number of segments were investigated. To demonstrate this, the calculations were performed for 4 segments, again with rectangular windows. The auto spectra found from each program are compared in figures 5.13a and 5.13b for the two datasets. The cross-spectra found from the two programs are compared in figure 5.13c. Finally, the coherence spectra found from the two programs are compared in figure 5.13d.

It can be seen that although there is still good agreement between the spectra obtained for either method, there is now a slight variance between the two. This variation is most notable in the Coherence spectra, in figure 5.13d. It should be noted that in this figure, there is still a broad agreement between the two spectra, with peaks in the coherence appearing at the same frequencies in both. Given that the difference between the two methods only appears when the datasets are separated into segments as part of the calculation, it was interpreted that the source of this error was from some difference in the separation into segments. As such, it was considered that the python methodology was validated against the previous methodology as long as the division into segments was consistent across the analysis. The python implementation will be used for the spectral analysis in this chapter.

5.3 Space Weather Perturbations

In this section, we consider the response of Venus' albedo to space weather events. The space weather events we will consider affect the cosmic ray environment with timescales on the order of hours to days. We will then look for variations to Venus' atmosphere with similar timescales. First, we consider Forbush events and SEP events, both of which are caused by Interplanetary Coronal Mass Ejections (ICMEs). Next, heliospheric current sheet (HCS) crossings are investigated, with the desire of removing any non-electrical effects of the ICME from our observations.

5.3.1 Forbush Events

The first space weather event that we considered were Forbush events. The Oulu data was used to identify a number of these events at Earth. This was performed by finding the day to day percentage change in neutron count rate, via:

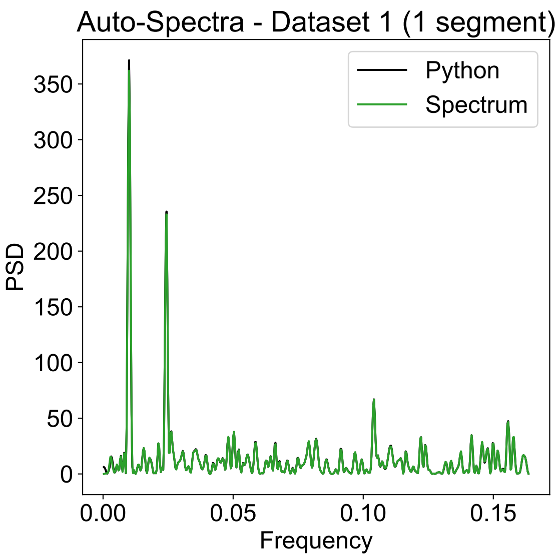

(a) Auto-spectra for Dataset 1

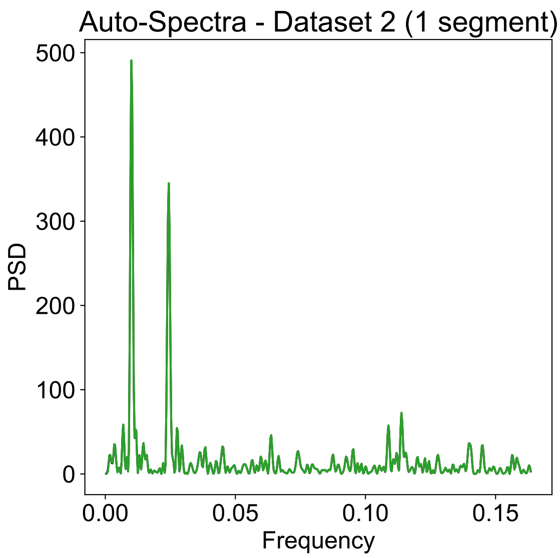

(b) Auto-spectra for Dataset 2

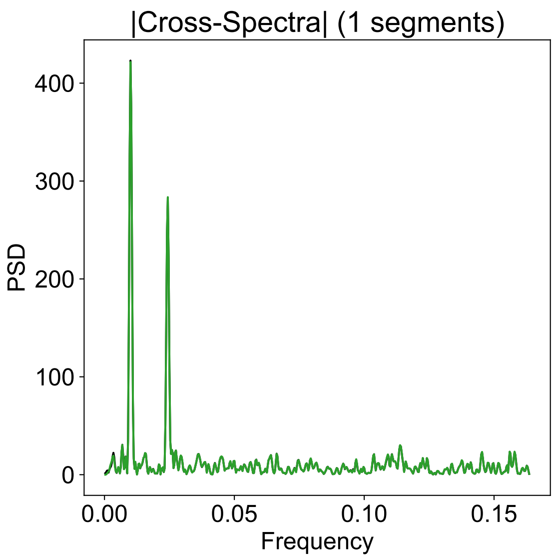

(c) Absolute Value of Cross-spectra

Figure 5.12: Spectra calculated using the SPECTRUM program (green), compared against those calculated from the python-3 code (black). 1 segment of data was used in the calculations of these spectra. (a) shows the auto-spectra calculated for the first dataset. (b) shows the auto-spectra calculated for the second dataset. (c) shows the cross-spectra calculated for the two datasets.

$$P_i = 100 \times \frac{N_{i+1} - N_{i-1}}{N_i} \tag{5.15}$$

where P_i is the percentage change on day i, and N_i is the count rate on day i. Forbush events were identified for times when this percentage change was less than -3%. For some previous investigations into Forbush events, a more strict cut-off has been used, however since there is a limited amount of albedo data provided, this cut-off was considered to be a good balance between the amount of datapoints provided and the magnitude of the Forbush decreases. This

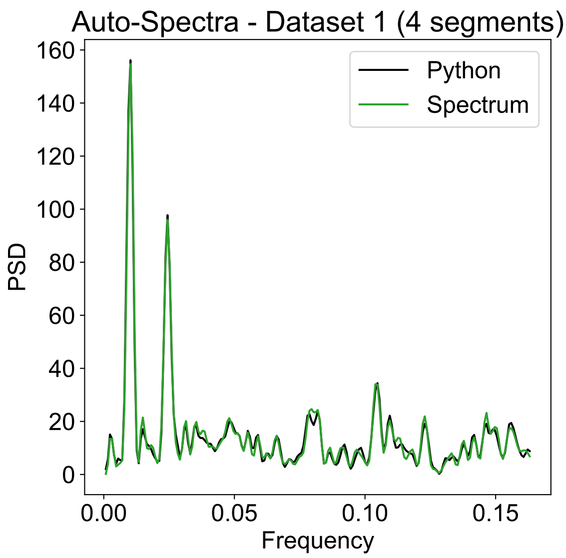

(a) Auto-spectra for Dataset 1

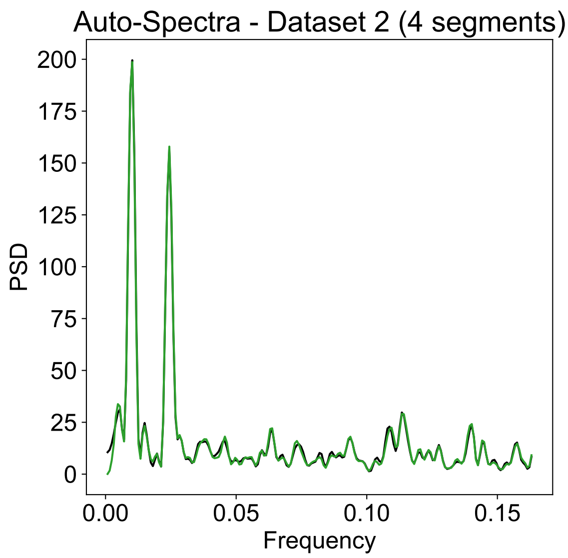

(b) Auto-spectra for Dataset 2

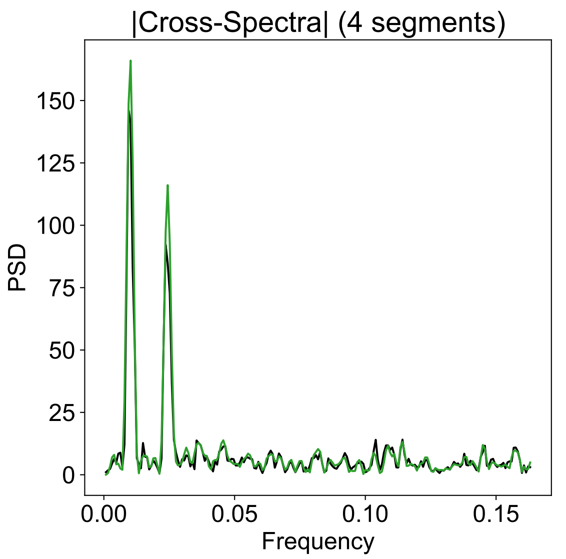

(c) Absolute Value of Cross-spectra

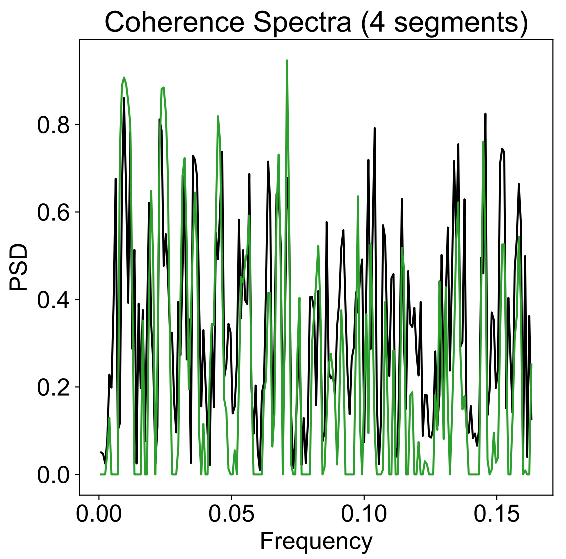

(d) Coherence Spectra

Figure 5.13: Spectra calculated using the SPECTRUM program (green), compared against those calculated from the python-3 code (black). 4 segments of data were used in the calculations of these spectra. (a) shows the auto-spectra calculated for the first dataset. (b) shows the auto-spectra calculated for the second dataset. (c) shows the cross-spectra calculated for the two datasets. (d) shows the coherence calculated for the two datasets.

day to day change in counts is shown in figure 5.14 along with the timing of all the Forbush decreases which were detected.

The time of each Forbush event was considered to be the day of minimum counts near to the large percentage decrease, rather than the day of largest decrease itself. This difference is indicated in figure 5.15.

For each of these events, the Oulu & albedo data was studied in a window spanning several days before to several days after the event. In order to compare the data from different events,

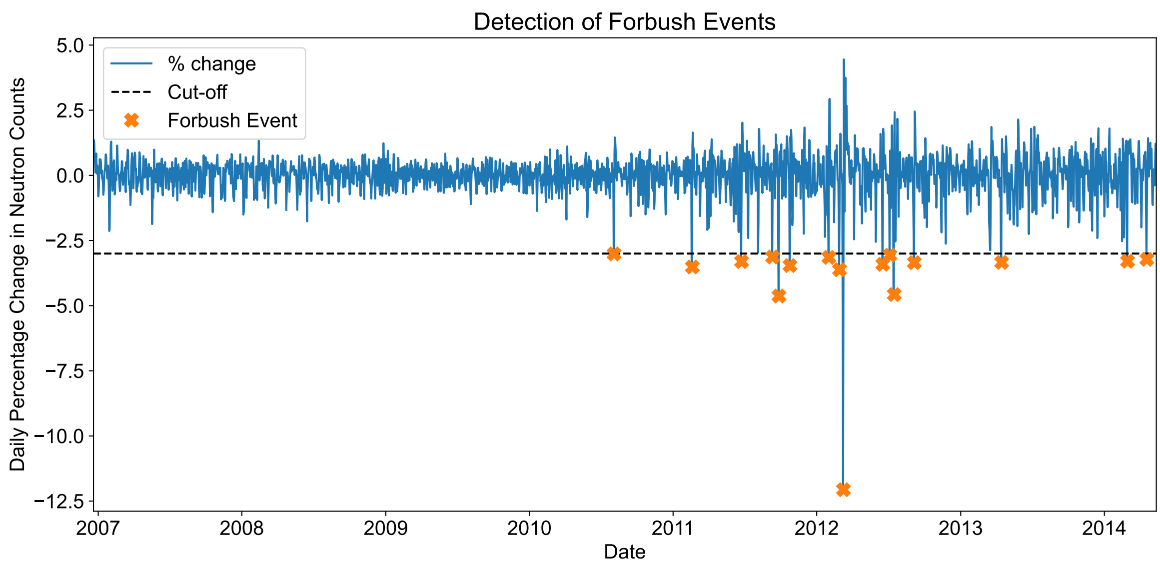

Figure 5.14: Day to day percentage change in Oulu counts. The -3% cut-off for identifying Forbush events used in this analysis has been shown using a dashed line. Additionally, the time of the Forbush decreases identified from this cut-off have been shown via crosses.

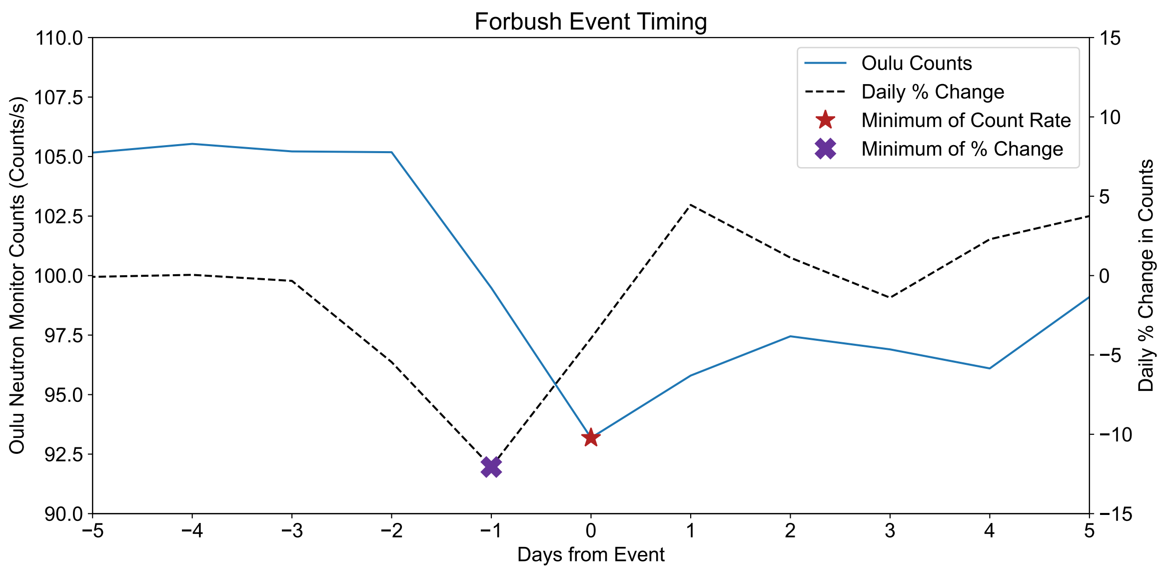

Figure 5.15: Figure showing the timing of a Forbush event. The solid line shows the daily counts from the Oulu neutron monitor. The dashed line shows the daily percentage change in these counts. The minimum of the Oulu counts (shown as a red star) is defined here to be the start time of the Forbush event. The minimum in the daily percentage change (purple cross) was used to identify the Forbush event, however does not occur at the same time as the start of the event.

it was locally detrended as described in section 5.1, using 24h bins. These bins spanned from 7.5 Earth days before the event to 7.5 Earth days after. For the detrending, a minimum cutoff of 3 datapoints from each event was required. In addition, it was required that for each event considered there was at least 1 of these datapoints in a bin before the event, and at least 1 in a bin after.

The albedo and Oulu data at times surrounding each Forbush event is shown in figure 5.16. In order to identify the general trends in the data, the median values of both the detrended albedo and the detrended Oulu counts were found across all events. The median values found for both datasets are shown as dashed lines in figure 5.16.

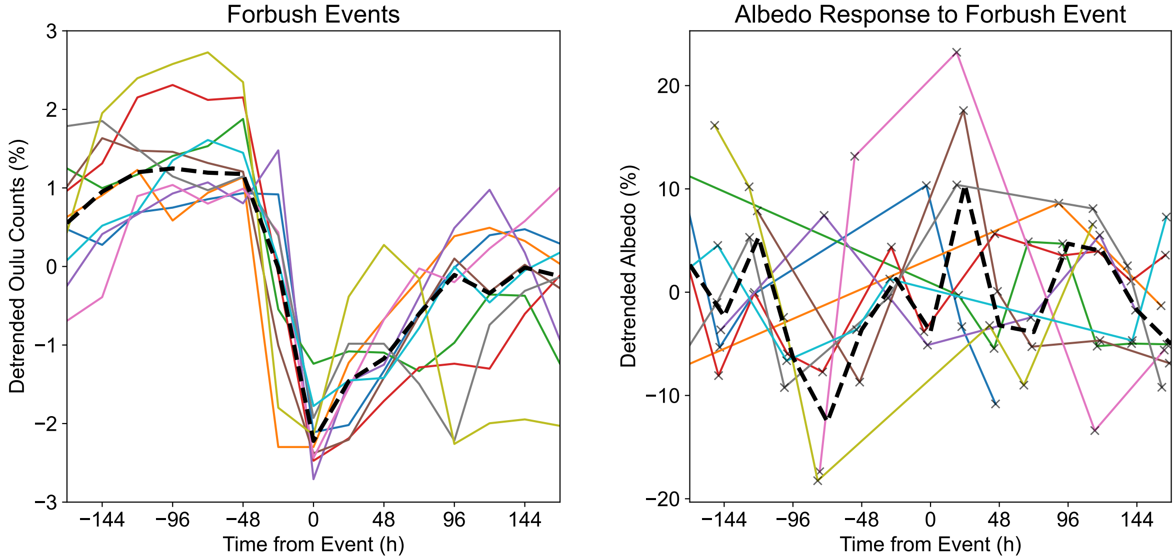

(a) Forbush decreases as detected in the Oulu data.

(b) The albedo response to Forbush events

Figure 5.16: GCR data from Oulu (a) and Venus' Albedo data (b) across several Forbush events. The data has been binned into 24h bins, and locally detrended. The median value for each bin, across all events has been indicated on each plot via a dashed line.

From inspection of figure 5.16b, there appears to be an increase in albedo 24h after the Forbush event. To explore the statistical significance of this increase, Monte Carlo methods were used to identify how large the typical changes in albedo were. For each Monte Carlo iteration, albedo data was selected at several random times, with no overlap with Forbush events. The data for each of these random times was detrended as in the previous analysis. The median value was then found across several of these times, with the same number of datapoints being used for each bin as was used for figure 5.16b. This entire process was then repeated a number of times, providing our Monte Carlo results. In this case, 1000 iterations were performed.

From this Monte Carlo dataset, confidence intervals on any perturbations to the albedo data were identified. This was performed by identifying a range including 95% of the albedo data, and any values lying outside this range were considered to be significantly deviated from the majority of the data. A range spanning from the percentiles of 2.5 and 97.5 was selected, allowing the 95% confidence interval to be identified.

The median line from figure 5.16b was plotted again in figure 5.17 with the 95% confidence interval on these values being indicated as a shaded area.

As can be seen in figure 5.17, the increase in albedo 24h after the event rises out of this confidence interval. This can be interpreted as the increase in albedo in response to Forbush events being statistically significant. It should additionally be noted that there is a decrease in albedo 36h before the event which also extends outwith the 95% confidence range. The source

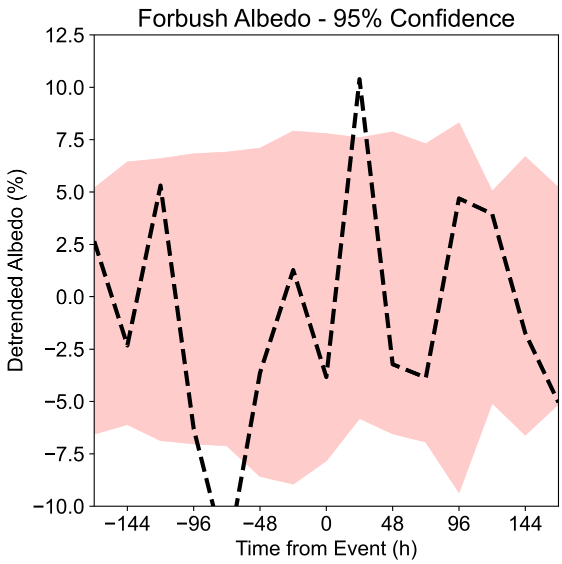

Figure 5.17: The median of Venus' albedo across a number of Forbush events (dashed line) is compared to the 95% confidence interval for this median (shaded area), as found via Monte Carlo methods.

of this decrease in albedo is unknown.

Events with Venus and Earth Co-located

The Forbush events studied here were detected solely at Earth. It is possible that not all of these events would have had a similar effect at Venus. In particular, since these events are caused by a CME originating at the Sun and propagating outwards, events detected when Earth and Venus are on opposite sides of the Sun are less likely to have been experienced at Venus.

To investigate the relative positions of Earth, Venus, and the Sun, data from JPL's ephemerides was used. This provided the positions of many celestial objects in the Solar system, at a range of times. From the ephemerides, the angular separation of Venus and Earth around the Sun was determined at the time of each of the Forbush events. The position of Venus, relative to the Earth and Sun, has been shown for each of the events from figure 5.16 in figure 5.18.

As can be seen in figure 5.18, for several of the Forbush events Venus and the Earth are on opposing sides of the Sun. It is assumed that these Forbush events are less likely to also affect Venus. We have repeated the analysis performed for the Forbush events, only considering events which occur with the Earth and Venus on the same side of the Sun. Reducing the dataset in this way means that there will be fewer datapoints involved in the calculation of the median of the albedo. To compensate for this, the bins used to calculate the median were adjusted - to ensure that each bin collected datapoints across a suitable number of the events.

For this analysis on a reduced dataset, the bin size was increased to 48h. These bins spanned from 8 Earth days before the event to 8 Earth days after, and a minimum cutoff of 3 datapoints from each event was required for the detrending, as before. Again, for each event considered it was required that there was at least 1 datapoint in a bin before the event and 1 datapoint in a bin afer the event. The Oulu and albedo data for these events is shown in figure 5.19.

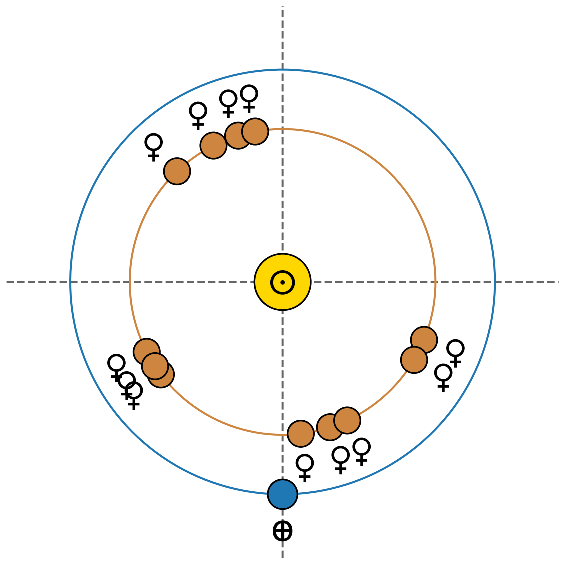

Figure 5.18: The position of Venus (♀) relative to the Sun (☉) and the Earth (⊕), at the time of each Forbush event in figure 5.14. Circular orbits were assumed for this illustration, and the positions of the celestial bodies were found from JPL's ephemerides data.

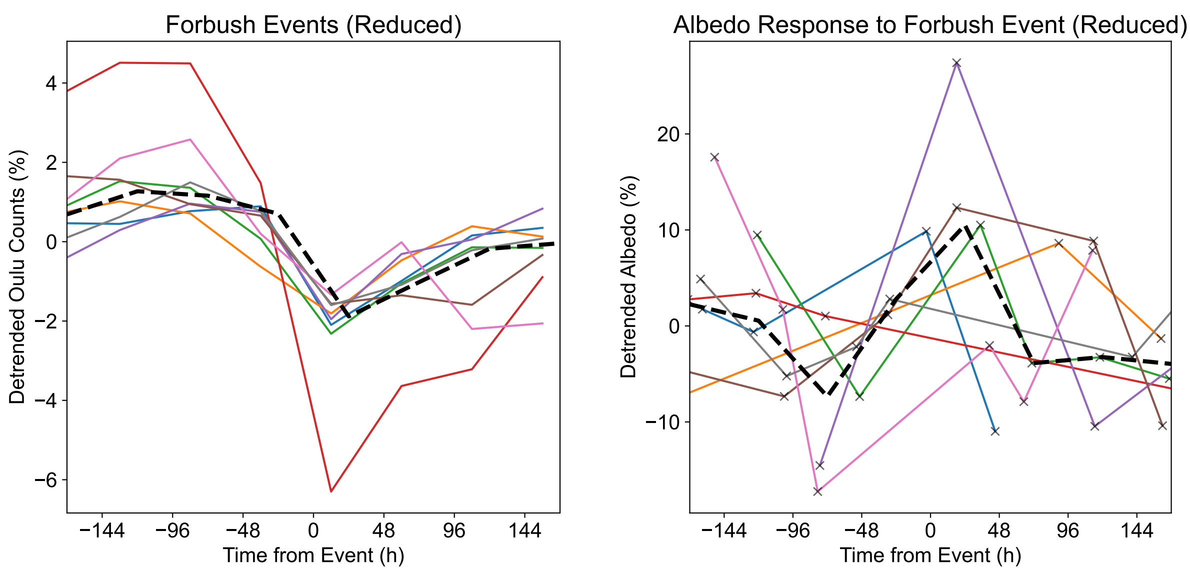

(a) Forbush decreases as detected in the Oulu data.

(b) The albedo response to Forbush events

Figure 5.19: GCR data from Oulu (a) and Venus' Albedo data (b) across a subset of the Forbush events, where the angular seperation between the Earth and Venus is less than 90°. The data has been binned into 24h bins, and locally detrended. The median value for each bin, across all events has been indicated on each plot via a dashed line.

As before, there appeared to be an increase in the albedo following the Forbush event. This statistical significance of this increase was investigated in the same method as for the previous dataset, utilising Monte Carlo methods. The median of the albedo, along with the 95% confidence interval found from 1000 iterations are shown in figure 5.20. As before, it can be seen that the increase in albedo rises above the 95% confidence interval, making it statistically significant. Again, however, there was a decrease in albedo before the event which also extended outwith the 95% confidence limit.

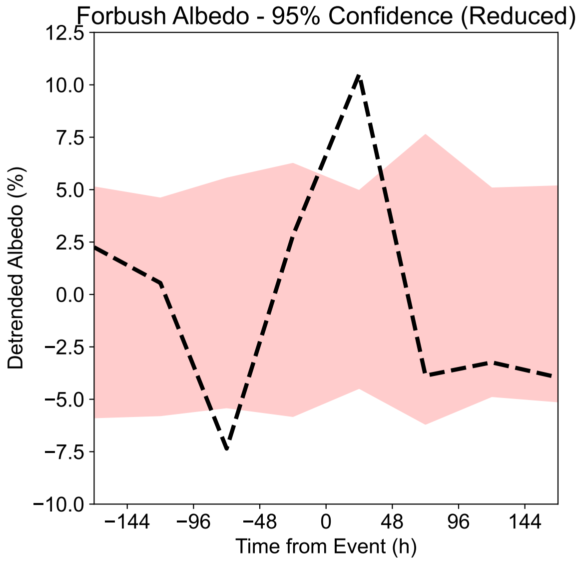

Figure 5.20: The median of Venus' albedo across a subset of Forbush events (dashed line) is compared to the 95% confidence interval for this median (shaded area), as found via Monte Carlo methods.

5.3.2 SEP Events

To confirm that the space weather events we are detecting have an influence on the cosmic ray environment at Venus, we ideally want to detect these events directly at Venus. It is difficult to detect Forbush events near to Venus, due to the limited cosmic ray data available, however it may be possible to detect other types of space weather event.

Identification of SEP Events at Venus

Firstly, we will attempt to observe SEP Events at Venus. In order to search for these SEP events, we will investigate perturbations in the cosmic ray counts at times near to the detection of an ICME at Venus. It should be noted that not all SEP events are caused by ICMEs [146], however, by only considering times near to these ICMEs, we can have an increased confidence that the perturbation we are able to observe is characteristic of an SEP event.

First, it was important to identify when ICMEs were detected at Venus. This was performed by considering the HELCATS catalogue of CME events. This provided a list of the start and end times of several CME events. Following this, any perturbations to the cosmic ray counts near to these events were identified via inspection of the background counts in the VEX IMA instrument. This allowed any changes to the cosmic ray counts asssociated with the ICME to be found, and allowed the time of these changes to be identified (as it is expected that an SEP event will occur before the arrival of the ICME). This provided a list of the times of a number of SEP events, detected at Venus.

In order to demonstrate this selection process, time series of the IMA background counts at the times of two ICMEs have been shown in figure 5.21. An SEP event was identified near to one of these ICMEs, with no such event identified for the other ICME.

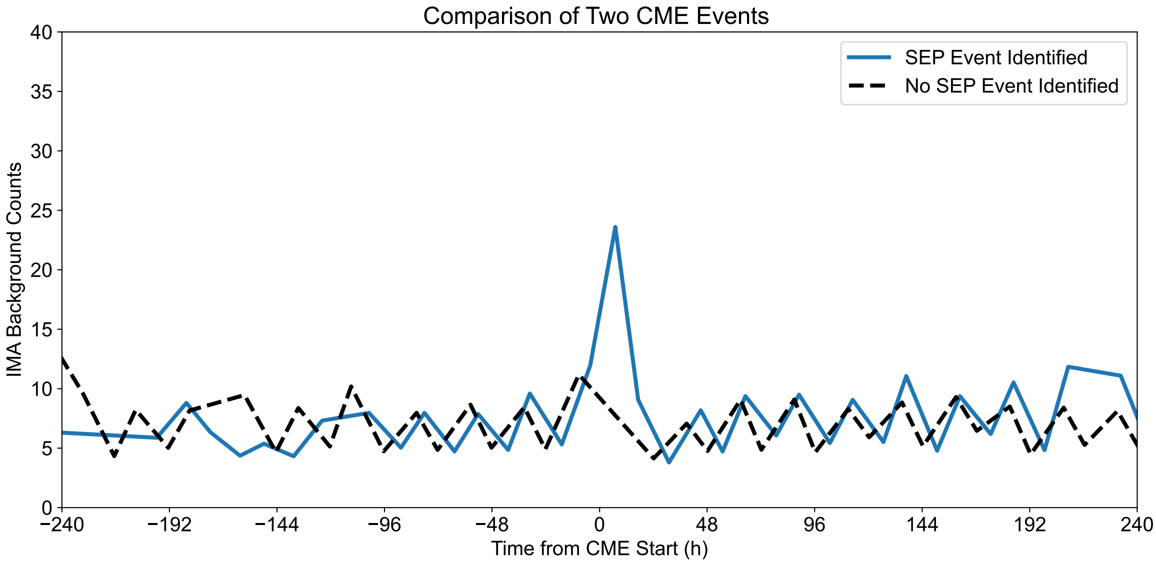

Figure 5.21: Background counts before and after the start time of two ICME events, as detected by the VEX IMA instrument. For one event (solid line), there is a clear perturbation to the background counts, which is interpreted as an SEP Event. For the other event (dashed line), there is no clear perturbation to the background counts.

Perturbations Caused by SEP Events

As for the Forbush events, the cosmic ray and albedo data was locally detrended in a time range surrounding each of the SEP events, with the detrended data compared across all of these events. Bins of size 24h were selected, from 7 days before to 7 days after each event, with the minimum cutoff for required datapoints set at 3. As for the Forbush events, it was necessitated that for each event there was at least one datapoint in a bin before the event, and at least one in a bin after the event. The composited cosmic ray and albedo data is shown in figure 5.22, along with the medians found across all of these events.

From figure 5.22b it can be seen that the albedo is increasing in response to the SEP events, however this increase occurs slightly later than for the Forbush events. As for these Forbush events, in order to explore the statistical significance of this increase in albedo, Monte Carlo methods were again used. This time, care was taken to ensure that the data selected from the Monte Carlo method did not include any data within several days of a CME detection at Venus.

For this Monte Carlo processing, 1000 iterations were performed. As for the Forbush events, the 95% confidence interval was identified and compared against the median albedo found following SEP events. This comparison is shown in figure 5.23.

As can be in figure 5.23, the albedo rises out of the 95% confidence interval. As such, the increase in albedo following these SEP events was interpreted to be statistically significant, at the 95% confidence level.

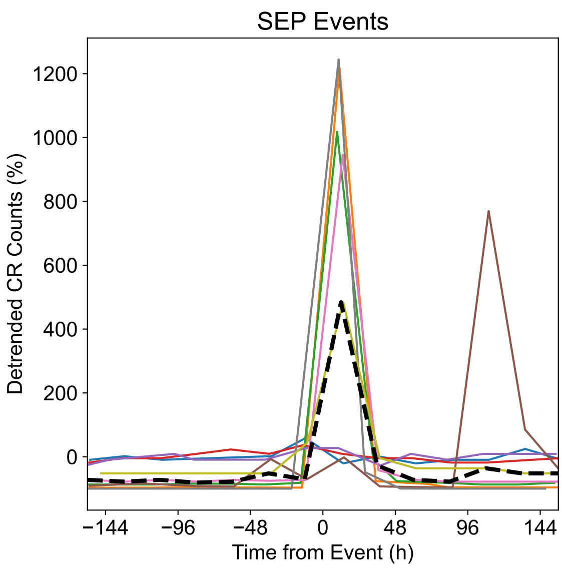

(a) SEP Events as detected in the IMA data.

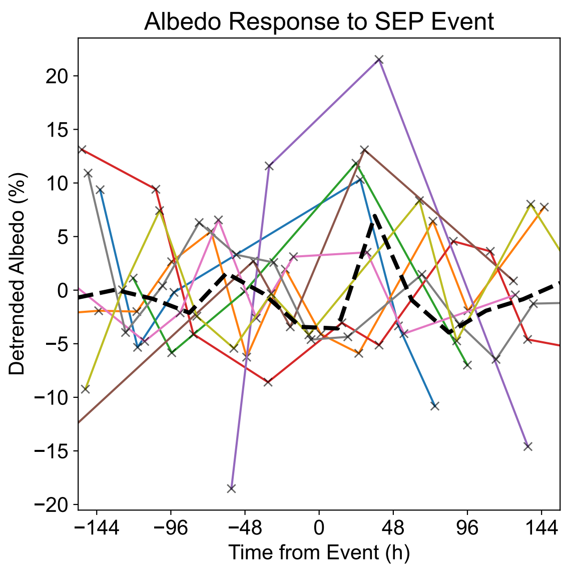

(b) The albedo response to SEP Events

Figure 5.22: CR data from the VEX IMA instrument (a) and Venus' Albedo data (b) across several SEP events. The data has been binned into 24h bins, and locally detrended. The median value for each bin, across all events has been indicated on each plot via a dashed line.

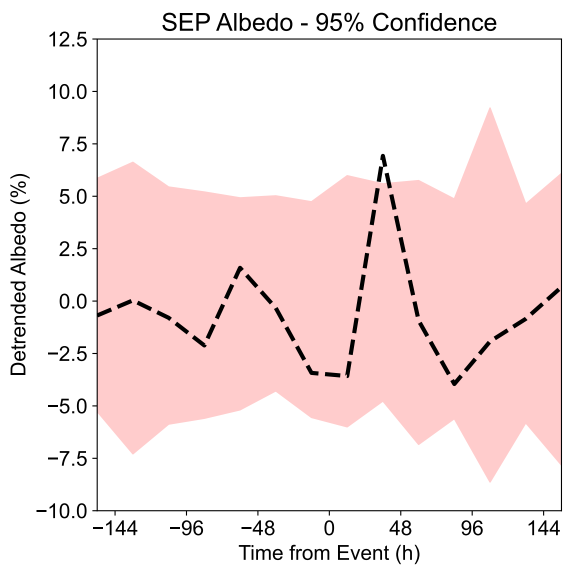

Figure 5.23: The median of Venus' albedo across a number of SEP events (dashed line) is compared to the 95% confidence interval for this median (shaded area), as found via Monte Carlo methods.

An initial discussion of the results found from the investigations of the effects of Forbush and SEP events on Venus' atmosphere will be considered now. These results will also be discussed in more detail in section 5.5.

5.3.3 CME Perturbations Summary

From our analysis of the two types of ICME based space weather events (Forbush decreases and SEP events) we have found that in both cases there was a statistically significant increase in albedo associated with the event. This is interesting, as when we consider the charged particle counts used to identify these events (i.e. the Oulu data for Forbushes, and the IMA data for SEP events), they are perturbed in different directions; the Oulu counts decrease during a Forbush event, while the IMA counts increase during an SEP event. The increase in albedo from both of these cases could be explained in several ways. Since the Oulu neutron monitor and the IMA instrument are observing different particle energies, it could be possible that the particle counts at a particular energy are perturbed in the same way for both types of event, which we are unable to observe due to the different energy ranges of the instruments. Additionally, this increase in albedo may be arising from some other effect than the change in charged particle counts. A potential non-electrical effect that could be causing this behaviour is the dynamical pressure of a CME impacting on Venus.

For both Forbush and SEP events, there is a variance in the strength of the perturbation to the cosmic ray count rate, with some events having a greater impact on the cosmic rays than others. By investigating if the magnitude of the changes in albedo are dependent on the magnitude of the change in cosmic rays, it may be possible to understand the source of the albedo changes. For the datasets described here, only a small number of events were able to be detected, so such analysis was not able to be performed.

To investigate if the albedo changes were in fact being caused by changes to the incident cosmic ray rate, rather than some other CME effect, the effects of other space weather events, not associated with ICMEs, will be considered next.

5.3.4 HCS Perturbations

Heliospheric current sheet crossings are a space weather event which is not associated with the passage of an ICME. These events have previously been shown to have an effect on the cosmic ray environment [185]. We will investigate if these HCS crossings have an impact on the albedo of Venus.

Detection of HCS Crossings

To determine the locations of HCS crossings, the azimuthal angle component of the magnetic field as detected by the magnetometer instrument on Venus Express was used.

To do this, the angle of the Towards (T) and Away (A) directions of the IMF at Venus needed to be determined. These were found by considering a histogram of the azimuthal angles for all the data in our set. This histogram is shown in figure 5.24. From the figure we can identify two peaks, roughly 180° apart; we thus find the A direction is at an angle of 140° and the T is at an angle of 322°. Since these angles are not quite 180° apart, we instead made the assumption that the TA axis lay halfway between the result for the two directions - i.e. at an angle of 141 °for A and 321 °for T.

For some of our analysis, we will need to find the average azimuthal angle of the magnetic

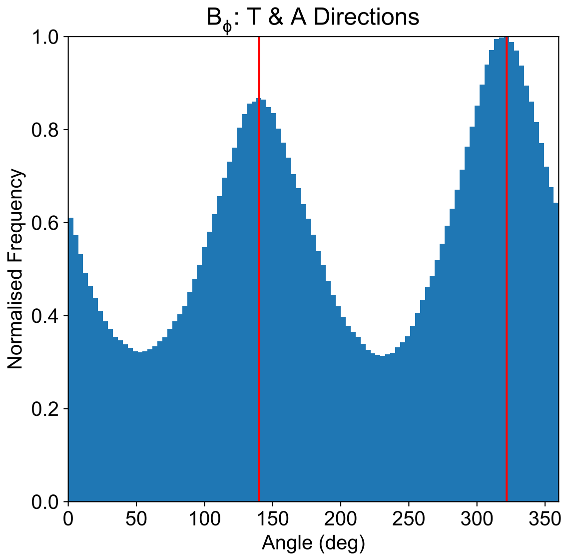

Figure 5.24: Histogram of mangetic field azimuthal angles. The global maximum at 322°, and the local maximum at 140° have been indicated by red vertical lines.

field in some time window. This is a non-trivial task, since the magnitude of the magnetic field is able to vary greatly. As such, if we find the average value of the magnetic field in cartesian co-ordinates, and then find the azimuthal direction from this, then the datapoints with large magnitudes of magnetic field will dominate the magnetic field direction. If we instead attempt to find the average coordinate values in spherical polar co-ordinates, then we are met with a different problem, since there is a co-ordinate singularity in the azimuthal angle. In order to avoid these issues, the average magnetic field direction was found by first finding the unit vector with the same direction as the magnetic field, and then averaging the cartesian components of this vector. The average azimuthal angle was then able to be calculated from these cartesian values.

When plotting the azimuthal magnetic field angle, it was often useful to make sure that both the T and A directions were centered on the plot. This was performed by transforming the angle into a new co-ordinate axis which was rotated slightly such that the A direction is at 90° and the T direction is at 270°. As such, these angles were centred in the [0°, 360°] range. This change to the co-ordinate system has been illustrated in figure 5.25. The direction of the azimuthal unit vector is the same as for VSO Coordinates, however the origin in the adjusted system is at an angle of 51° in VSO. The "adjusted" co-ordinate system will be used for the remainder of the HCS analysis.

In order to find the locations of current sheet crossings, we first determined the IMF direction for the times of the albedo datapoints. This allowed us to identify times when the direction flipped between datapoints: i.e. HCS crossings where we can compare albedo data before the crossing to after it. For investigations of the HMF polarity at Earth, often many spacecraft observations are considered together [139]. This helps to eliminate noise from the observations of the HMF direction. For Venus, we only have one observation of the HMF, so will need to employ other methods in order to mitigate noise.

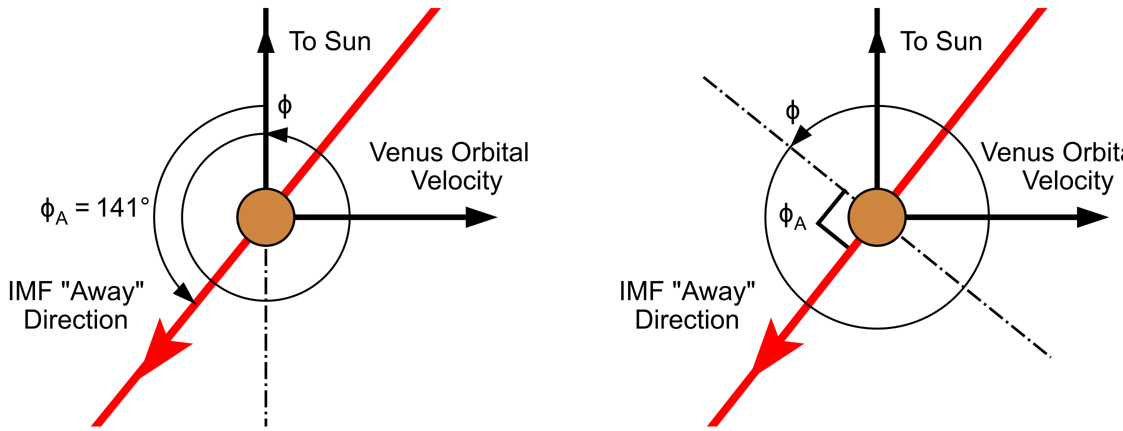

(a) Venus Solar Orbit Coordinates

(b) Adjusted coordinates for plotting

Figure 5.25: Diagrams illustrating the two coordinate systems used for the magnetic field direction. (a) shows the venus solar orbit coordinates, with azimuthal angle ϕ meassured from the Sun-Venus line. (b) shows the adjusted coordinate system used for plotting the magnetic field direction in this work. The origin in this system is such that the "Away" direction is at an azimuthal angle of 90 °.

Instead of considering the magnetic field direction at a single point in time, the spread of data in a wider time window was instead considered. For these time windows, the mean, and first and third quartiles of the azimuthal angle of the magnetic field were determined. Then, if all three of these values were within a certain range of either the T or A directions, then it was considered that that time window described a period where the HMF polarity at Venus was in the corresponding direction. This process is illustrated for a sample time in figure 5.26, illustrating cut-off areas for the towards and away directions with a width of 30°. For this analysis, a 4h rectangular window centred on the time of the datapoint being evaluated was used.

This process was used, using both a 24h window and a 4h window, to identify which albedo datapoints corresponded to the T and A directions. The 24h window determined the direction of HMF direction over a longer period of time - allowing the identification of the HMF direction in the time surrounding the albedo measurement. The additional 4h window ensured that the HMF direction did not vary on a shorter time scale, near to the albedo measurement.

Next, the HMF at the times of different albedo datapoints were investigated. The datapoints where the HMF polarity changed compared to previous points were identified. This was used to compile a list of times where the magnetic field direction changed from A to T, and vice versa. Through visual inspection of the magnetic field data, the timing of the crossings for the events in this list were identified. The timing of these events was then used for our analysis. The magnetic field for a typical event is shown in figure 5.27.

Effects of HCS Crossings

Our analysis thus far has yielded two types of HCS crossing events; crossings from the T to the A direction (TA crossings) and crossings from the A to the T direction (AT crossings). These two cases were analysed individually. The analysis will be explained first using just the AT

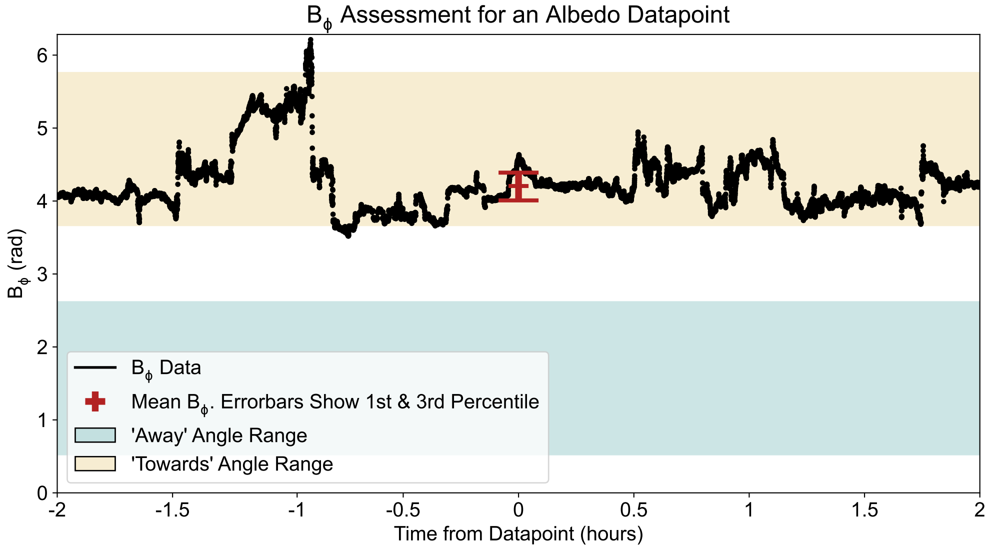

Figure 5.26: Diagram showing how the HCS side was determined for a particular datapoint. The magnetic field angle in a specific time window around the datapoint is shown as black points. The mean of this data is shown as a red cross, with errorbars corresponding to the first and third percentiles of the data. Finally, a blue shaded area spanning from $(\frac{\pi}{2} - \frac{\pi}{3})$ to $(\frac{\pi}{2} + \frac{\pi}{3})$, and a yellow shaded area spanning from $(\frac{3\pi}{2} - \frac{\pi}{3})$ to $(\frac{3\pi}{2} + \frac{\pi}{3})$ have been included to illustrate the areas corresponding to the "towards" and "away" directions.

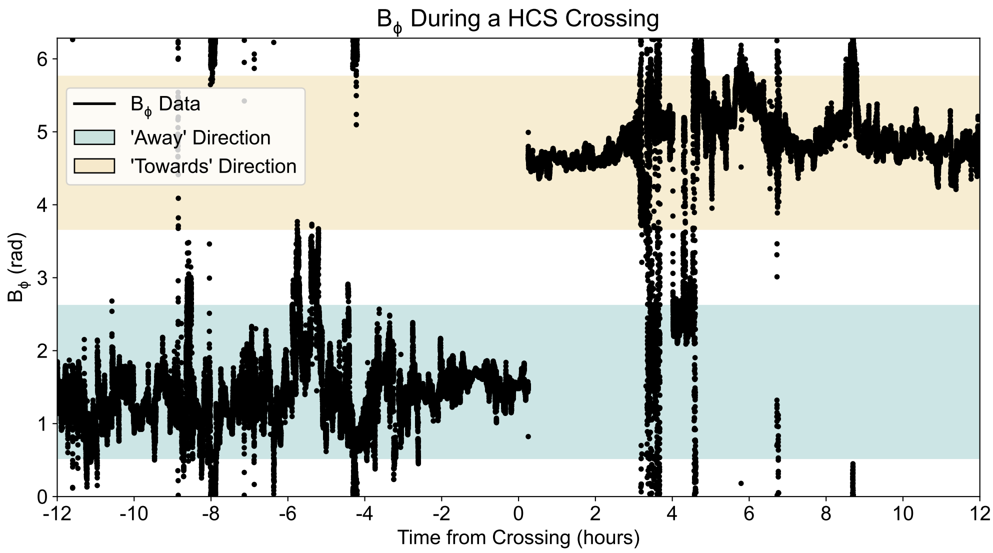

Figure 5.27: Magnetic field data during a HCS crossing. The azimuthal angle of the magnetic field is shown as black points. A blue shaded area spanning from $(\frac{\pi}{2} - \frac{\pi}{3})$ to $(\frac{\pi}{2} + \frac{\pi}{3})$, and a yellow shaded area spanning from $(\frac{3\pi}{2} - \frac{\pi}{3})$ to $(\frac{3\pi}{2} + \frac{\pi}{3})$ have been included to illustrate the areas corresponding to the "towards" and "awa" directions.

crossings.

First, for each event identified, the azimuthal component of the magnetic field was resampled into 24h bins. The resulting data was then plotted for each event on the same axes in figure 5.28a. These magnetic field angles were compared from 144h before the crossing event to 144h after. In some cases, the magnetic field direction changed again in this time; i.e there was a T-A event (A-T event) following or preceding the T-A event (A-T event). In these cases, the data was truncated before this 144h limit, such that only one crossing event was visible in the data from each identified event. In figure 5.28a it can be interpreted that the left hand side of the figure shows the "away" data, while right hand side shows the "towards" data.

Next, as for the events in the ICME analyses, the charged particle data was binned and locally detrended. Bins of size 24h were used, with the cutoff for mean calculations set at 3. These bins covered the same range as the magnetic field angles described before; i.e. in the event that an additional current sheet crossing occurred, the data was truncated. The data across these events has been compared in figure 5.28c.

Finally, the albedo at times surrounding each event was compared. As for the charged particle data, this data was binned and locally detrended, with a bin size of 24h and the cutoff for the mean calculation set at 3. Again, these bins spanned the same truncated range as the magnetic field angle data. The albedo data across each event is compared in figure 5.28e.

Different behaviour is observed from these three figures (in the left hand side of figure 5.28). In figure 5.28a, it can be seen that the magnetic field angle follows a similar trend across all the events. This is not the case for the charged particle or albedo datasets, however. In the previous terrestrial investigations of changes in the cosmic ray count rate at times surrounding HCS crossings, it was found that the neutron monitor count rate was decreased at times following the crossing, compared with before. To investigate if such a trend was present in the IMA cosmic ray data, the cosmic ray dataset following the events was compared against the dataset from before the events. Additionally, this analysis was performed for the albedo data. For both the cosmic ray data and the albedo data, histograms of the data before the event were compared with histograms of the data after the event. The histograms for the charged particle data are shown in figure 5.29a, and the histograms for the albedo data are shown in 5.29c.

The histograms in figure 5.29a (comparing the charged particle data before and after the event) appeared to have a broadly similar shape. For the histograms in figure 5.29c (comparing the albedo data before and after the event) there appeared to be some difference in the shape; in particular, the variance of the data before and after appeared to be slightly different.

Several statistical tests were performed to investigate the differences in data before and after the event. Firstly, since a difference in variance appeared to be present, Levene's test was used to investigate the null hypothesis that that the data before the event was drawn from a sample with the same variance as the data after the event. Levene's test was selected for this analysis since it does not require that the data is normally distributed. This test was first performed for the IMA data, where a p value >0.05 was found. As such, the null hypothesis was unable to be rejected in this case. The test was then performed for the albedo data, which again yielded a p value >0.05, preventing the null hypothesis from being rejected.

Next, a statistical test was used to investigate if there was any difference between the distributions of the two datasets (from before and after the events), rather than just a change in the variance. To perform this, a Kolmogorov-Smirnov (KS) test was used, investigating the null hypothesis that the data before the event was drawn from the same distribution as the data after the event. For the IMA data, the p value found from this test was >0.05, preventing this

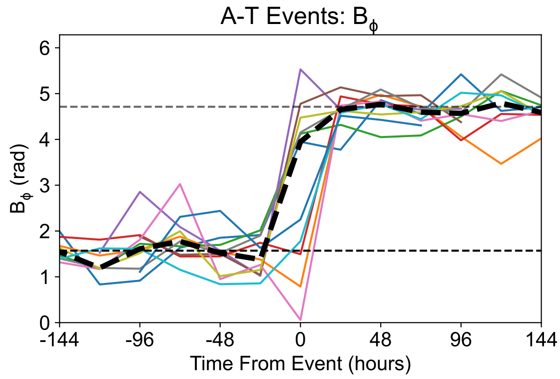

(a) B_ϕ across several AT crossings.

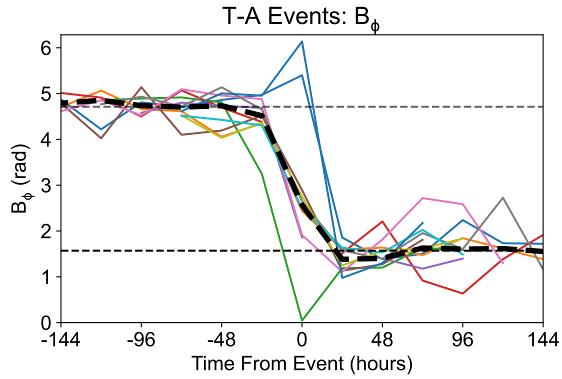

(b) B_ϕ across several TA crossings.

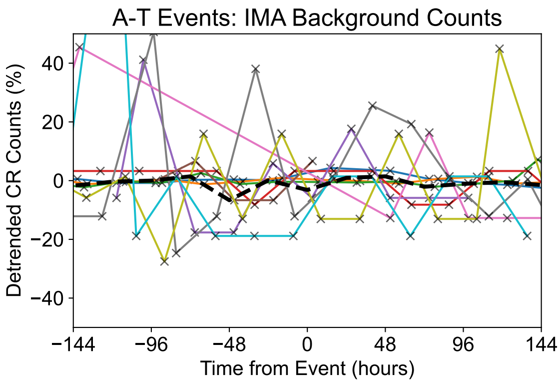

(c) IMA response to AT Events.

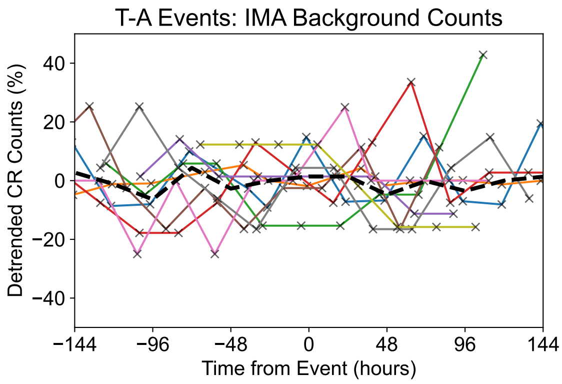

(d) IMA response to TA Events.

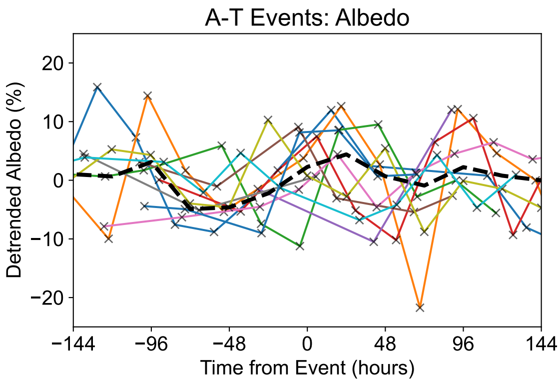

(e) Albedo response to AT Events.

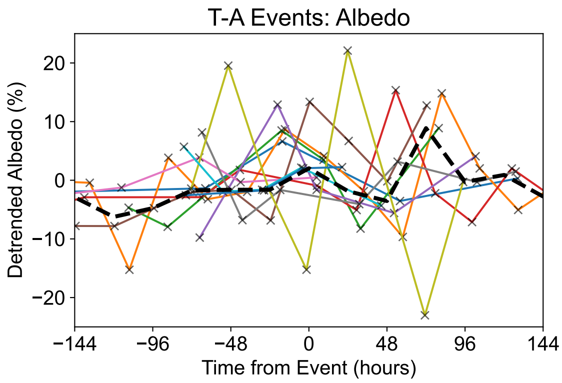

(f) Albedo response to TA Events.

Figure 5.28: Figures produced from the AT analysis (a,c,e), and the TA analysis (b,d,f). (a) & (b) show the azimuthal component of the magnetic field direction throughout the HCS crossings. The T and A directions have been indicated using dash-dotted lines. (c) & (d) show the cosmic ray data measured by the VEX IMA instrument. (e) & (f) show the albedo throughout the HCS crossings. For each plot, the data has been binned into 24h bins, and locally detrended. The median value for each bin, across all events has been indicated on each plot via a dashed line.

null hypothesis from being rejected. A similar KS test was performed for the albedo data, which also resulted in a p value >0.05. Based upon these statistical tests, we have been unable to find any statistically significant difference between the distributions of the albedo/cosmic ray data

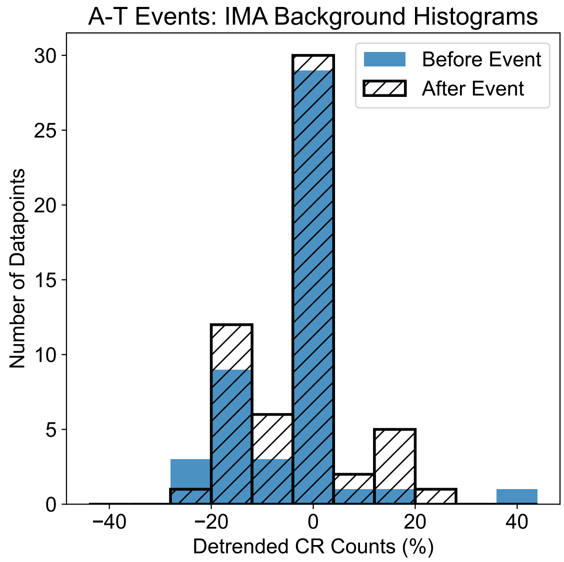

(a) Histograms for IMA data before/after AT crossing.

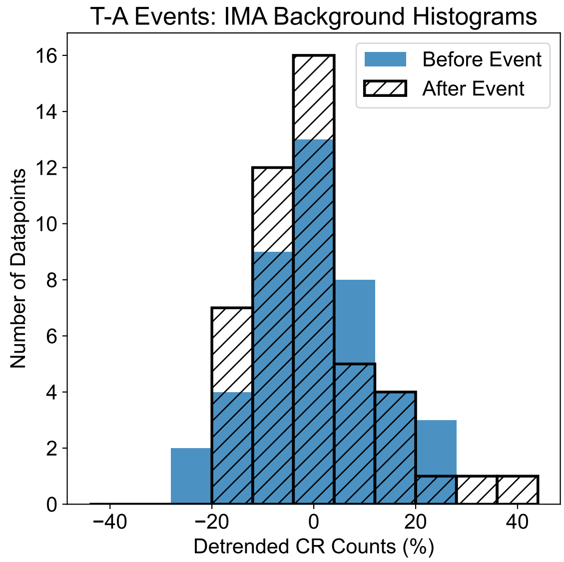

(b) Histograms for IMA data before/after TA crossing.

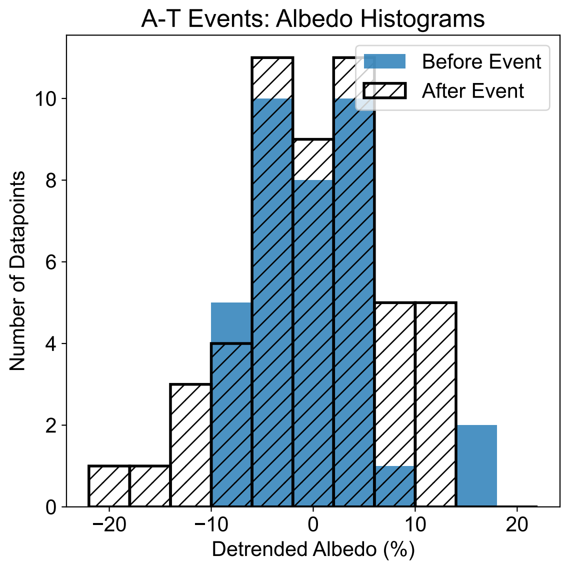

(c) Histograms for Albedo data before/after AT crossing.

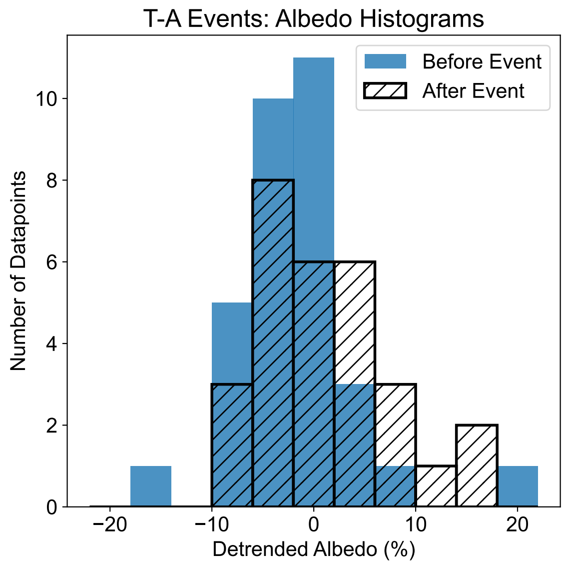

(d) Hisograms for Albedo data before/after TA crossing.

Figure 5.29: Histograms comparing the data before and after a HCS event. (a,c) describe AT crossings, and (b,d) describe TA crossings. The histograms in (a,b) compare the IMA cosmic ray data, and the histograms in (c,d) compare the albedo data.

from before and after the HCS crossings.

The analysis described here was then performed for the T-A events. The azimuthal magnetic field, IMA data, and albedo data at times surrounding these events are shown in figures 5.28b, 5.28d, and 5.28f respectively. As for the A-T events, it was difficult to observe a general trend in these datasets following the HCS event.

Next, histograms of the IMA and albedo data before and after the events were produced, as was done for the A-T events. These histograms are shown in figures 5.29b and 5.29d. As for the A-T events, it appeared that the shape of the histograms for the albedo before and after the event differed slightly.

Following the procedure outlined for the A-T events, statistical tests were performed on the IMA and Albedo datasets before and after the T-A crossings. Again, the statistical significance of any changes in the variances were investigated using Levene's test. For both the IMA and Albedo data, Levene's test yielded p values >0.05, preventing the null hypotheses from being rejected. Finally, the distributions were investigated using KS tests. The KS test performed for the IMA data yielded a p value >0.05, as before. For the KS test performed on the Albedo data, however, the p value found was <0.05. As such, this allowed the null hypothesis - that the albedo data before the T-A event was drawn from the same distribution as the albedo data after the T-A event - to be rejected. This result provided some statistical significance to the observation that the data shown in the histograms in figure 5.29d were drawn from different distributions.

HCS Summary

Several HCS crossings were detected using data recorded from near-Venus space. For the HCS crossings that we identified, it was found that there was no significant trend affecting the cosmic ray counts detected by the background channels of the IMA instrument. It was found, however, that there was a statistically significant difference in the albedo data recorded before some of the HCS crossings compared to the data recorded after. This effect was only able to be observed for crossings from the towards direction to the away direction.

5.3.5 Space Weather Perturbation Summary

The results found from our investigation into the effects of space weather events on the albedo of Venus are summarised in table 5.2.

Event Type	Cosmic Ray Perturbation	Albedo Change Observed?
Forbush Decreases	GCR Decrease	
All events		Yes
Only when Earth & Venus are close		Yes
SEP Events	SEP Increase	Yes
HCS Crossings	Change in CR	
AT Events	environment	No
TA Events	predicted	Yes

Table 5.2: Overview of the investigations performed in section 5.3. The perturbation to the cosmic ray environment associated with each space weather event, and whether these events caused an observable change in the albedo of Venus have been listed.

It was found that for Forbush events, SEP events, and TA HCS crossings, a statistically significant change in the albedo of Venus was observed. These results show that space weather events can impact on the atmosphere of Venus. To explore the effects that space weather and cosmic rays can have on Venus' atmosphere further, a different form of investigation, considering effects over long time scales was next considered.

5.4 Charged Particle Periodicities

Instead of considering the short term albedo response to perturbations in the charged particle environment, We now consider periodic variations in the cosmic ray data, and if these lead to variations in the albedo. The nature of the cosmic ray periodicities will be discussed first, before considering if these signals are present in the albedo also. To investigate if there are periodicities which are common to both the cosmic ray and albedo datasets, the coherence between these two datasets will be calculated. The calculations involved in this process have been discussed in section 5.2.4.

5.4.1 Solar Periods

The rotation rate of the Sun is dependent on solar latitude, with areas near the pole rotating slower than at the equator. This rotation period varies between ∼25 and ∼35 Earth days. If we consider the equator of the sun, rotating with a period of ∼25 days, then when viewed from Earth, this period will appear to be slightly longer at ∼27 days. This is because the Earth has moved forward in its orbit slightly in the time it took for the Sun to rotate, so the Sun needs to rotate slightly further than 360° for the same point on the Sun's surface to be visible from Earth again. Since Venus orbits closer to the Sun than Earth, and therefore has a greater orbital velocity (according to Kepler's third law), the angular distance travelled by the planet during each solar rotation will be larger for Venus than for the Earth. This means that the rotation period will appear even longer for Venus, at ∼28 days. This effect is described by equation 5.16 and illustrated in figure 5.30:

$$T_{planet} = \left(\frac{1}{T_{Sun}} - \frac{1}{Y_{planet}} \right)^{-1} \tag{5.16}$$

where T_{Sun} is the relevant rotation period of the Sun, and T_{planet} is the apparent period as observed from a planet which orbits the Sun with a period given by Y_{planet}.

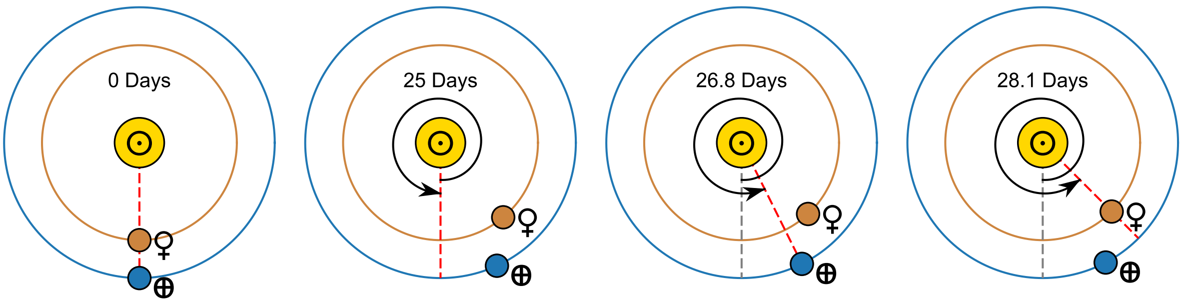

Figure 5.30: Diagram showing how the movement of planets around the Sun causes its "day" to appear to be larger. The positions of the Sun (⊙), the Earth (⊕), and Venus (♀) are shown after several time steps. After a complete rotation of the Sun (∼25 days) the planets have moved around the sun slightly, so to an observer on the planet, a full rotation has not been completed. The time taken for an observer on Earth to apparently observe a full rotation (∼27 days) is slightly shorter than for an observer on Venus (∼28 days).

To distinguish between these periods, we refer to the "true" rotation period as the "sidereal rotation period", and the period which is observed as the "synodic rotation period".

If we are wishing to compare periodic variations observed at Earth and Venus, then it is important that the correct periods are being compared. If the source of the variations is not due to the rotation of the Sun, then the coherency calculations as outlined in section 5.2.4 are valid. However, if we want to compare periodicities caused by this rotation, as observed at different planets, then we need to adjust the periods used for this analysis.

In order to do this, the Lomb-Scargle transforms were performed for both time series, as in equation 5.8. The frequency associated with this was however adjusted to be the frequency of the associated solar variation before further steps were carried out. For instance, for Earth (Venus) data, the Lomb-Scargle transform was performed for a period of 27 (28) days. These values were associated with a sidereal period of 25 days, so using this data the cross spectrum and coherence can be calculated for this period. Similar analysis is performed across all periods in the range of interest.

5.4.2 Moving Window Coherograms

To investigate the periodicities which are common between the cosmic ray and albedo datasets, moving window coherograms were produced. To produce such a plot, first, the coherence spectrum was determined for a subset of the data - selected in a particular time window. This provided the coherence as a function of the period of variation in that time window. This process was then repeated for other time windows, allowing the coherence to be found as both a function of time and period of variation. The coherence data found in this way was plotted on a 2D color-plot, with x axis as the center of each time window, and the y axis as the period of the variation. Pixels with high coherence on these plots indicate a periodic variation that is common between the two input datasets, at the given time. This is a necessary requirement for the two signals to be influencing each other, i.e. for the albedo to have a cosmic ray dependence.

5.4.3 Results

The Coherence between the Albedo and VEX IMA data was found for a range of periods between 24 and 35 days, for a large number of time windows. The periods were selected to coincide with variations to the charged particle count rates caused by solar rotation. The moving window coherogram created from this is shown in figure 5.31a.

There are a number of "bright" pixels in this figure, with coherence values greater than the apparent background. Further, there appears to be some level of spatial structure in these bright pixels; at several times, the bright pixels seem to form vertical "stripes", where a high coherence is present across several periods, at a given time. From investigation of test data, it is believed that these vertical stripes are caused by the coherence calculations causing the coherence peaks to be spread out in this "period" dimension. As such, it is difficult to interpret the specific periods of variation which lead to high coherence. For several of the vertical stripes, the high coherence values persist across several horizontal pixels. In these cases, it is interpreted that the coherence signal is present for a notable amount of time.

A pixel with high coherence is intended to indicate a time where a periodicitiy of a given period is present in both the cosmic ray and albedo datasets. If there is a particularly strong periodicity present in the cosmic ray dataset, however, it may be possible that a given pixel

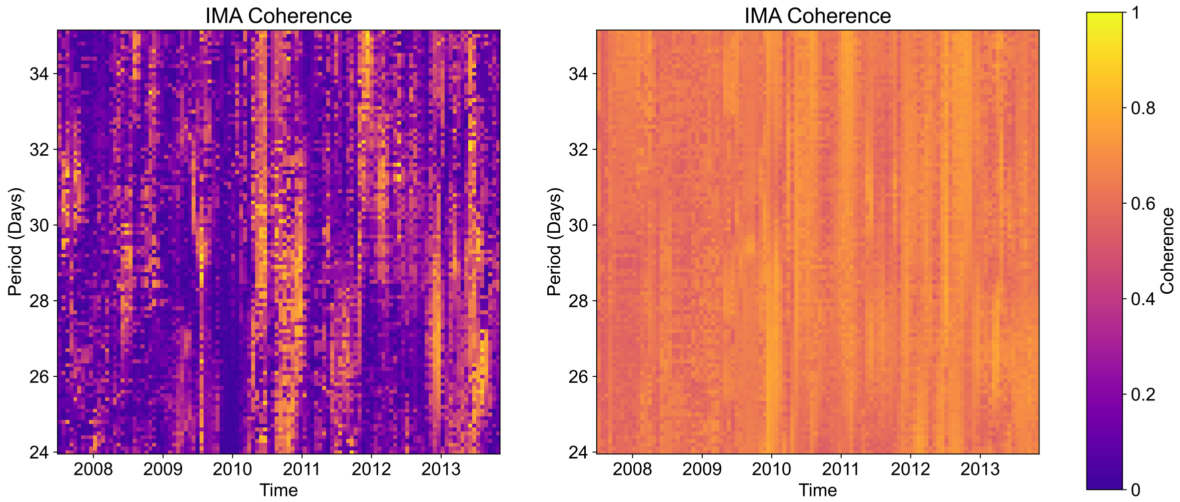

(a) Coherence for IMA and Albedo data

(b) 95% Confidence for IMA and Albedo Coherence

Figure 5.31: Moving window coherograms for the IMA and Albedo data. (a) shows the coherence between the two datasets, and (b) shows the 95% confidence limit for the coherence, as found from Monte Carlo methods.

will have a coherence greater than the background, irrespective of whether such a signal is present in the albedo. To ensure that this is not the case, a Monte Carlo bootstrapping method has been utilised in order to identify pixels corresponding to a significant coherence. For this method, a similar moving window coherogram was found between the albedo data and a randomised version of the IMA data. This randomised data was produced using a bootstrapping method, where the IMA data was randomly sampled, causing the data to be re-arranged in time. Following Monte Carlo methods, such coherograms were produced a number of times, with different randomisations performed for each iteration. Finally, for each pixel in the moving window coherogram, the 95th percentile value for the coherence across all these iterations was identified. This provided the 95% confidence limit for each pixel in the original, unrandomised, coherogram. The 95% confidence values found from this method, using 10,000 iterations, are shown in figure 5.31b.

The statistically significant pixels in figure 5.31a are those with a greater coherence than the 95% confidence level for that pixel (as shown in figure 5.31b). To allow the statistically significant pixels to be clearly identified, the coherogram from figure 5.31a was masked, such that any pixels which were not statistically significant were set to a black background colour. This masked coherogram is shown in figure 5.32a.

From figure 5.32a, it can be seen that there is still a large amount of structure present; the vertical stripes identified earlier still appear present at certain times, and in some cases (particularly between 2012 and 2013), these stripes persist across a number of horizontal pixels. This result is not inconsistent with a common periodicity existing between the albedo of Venus and the cosmic ray count rate, at these times.

The results from this coherogram have been compared against the sunspot number over the same period. For this comparison, the sunspot number has been resampled, finding the average

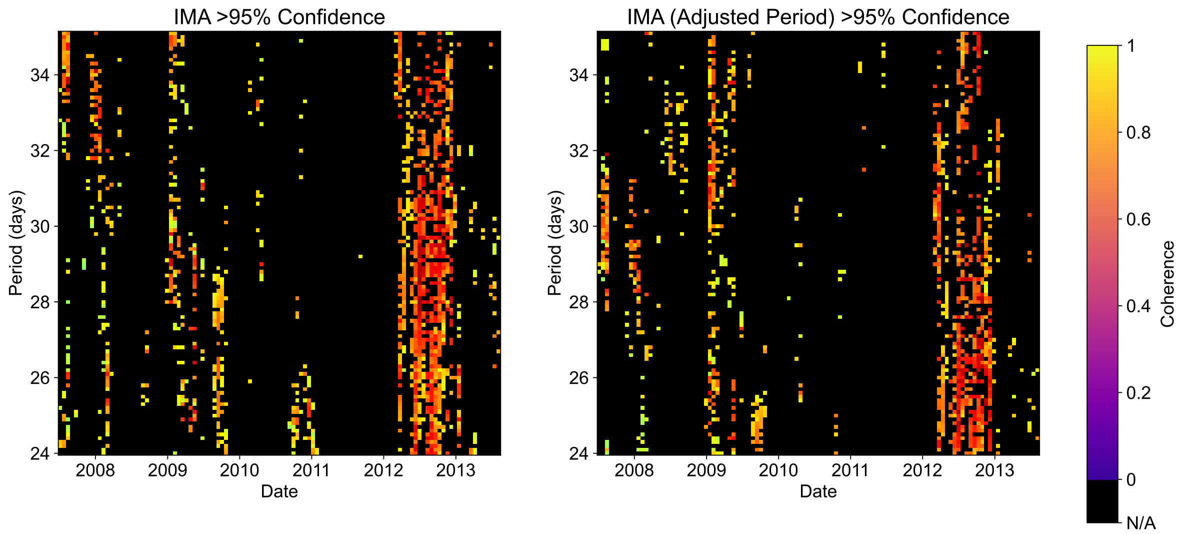

(a) Masked Coherogram for IMA & albedo data

(b) Masked Coherogram for IMA & albedo data (Period adjusted to corresponding solar period)

Figure 5.32: Coherograms for the IMA & albedo datasets, showing the coherence values which are greater than the 95% confidence limit. (a) is produced without any alteration to the periods in the input datasets. (b) is produced by adjusting the periods of the input datasets, such that they correspond to the rotation period of the Sun which would cause that periodicity at the observer.

value in the same time windows as was used for each pixel in the coherogram. The time series of resampled sunspot number is shown in figure 5.33.

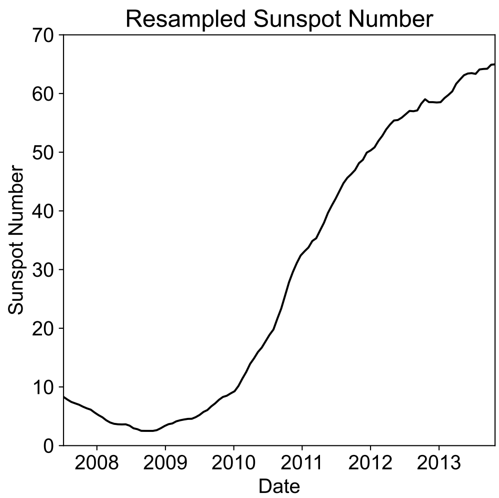

Figure 5.33: Sunspot number, resampled for the time windows in the coherograms in figure 5.32.

Comparing the time series of sunspot numbers in figure 5.33 to the times of the vertical stripes of significant coherence values in figure 5.32a, it can be seen that the large cluster of points in 2012 is coincident with a relatively high sunspot number as this time is close to solar maximum. Assuming that the albedo and cosmic ray count rates do share a common periodicity at these times, then the timing close to solar maximum makes sense - at these times, the increased solar activity is likely to cause more variations in the cosmic ray counts, which would further cause variations in the albedo, leading to a stronger coherence between the time series.

As discussed before, when considering periodic variations caused by the rotation of the Sun, we need to adjust the periods used in the coherence calculations such that they correspond to the desired sidereal period of the solar rotation. For the IMA dataset, both the cosmic ray and albedo data is recorded from Venus orbit. As such, the adjustment to the periods in the Lomb-Scargle transforms used to calculate the coherence between these datasets is the same for both datasets. This results in the coherogram having a similar form for this "adjusted" case as in the previous case, but the period axis is scaled differently. As in the previous case, Monte Carlo bootstrapping was performed to identify the 95% confidence interval, and the masked coherogram showing statistically significant datapoints is shown in figure 5.32b. As for the coherogram in figure 5.32a, there appears to be some spatial structure in the locations of the statistically significant pixels, with vertical stripes again present, preventing a particular periodicitiy from being identified. In this case, little additional information is provided by considering the coherence between sidereal periodicities.

Similar coherograms were further produced for the other cosmic ray datasets. The coherence between the Oulu neutron monitor data and albedo is shown in figure 5.34a and the coherence between the ACE SEP data and albedo is shown in figure 5.34c, where the statistically significant pixels have again been identified via Monte Carlo bootstrapping. As for the IMA dataset, the coherence for variations driven by the Sun was also determined in these cases by adjusting the periods of variation to the appropriate sidereal period. In these cases, since the albedo measurements were taking place at Venus, while the cosmic ray measurements were taking place at Earth, the adjustments for each dataset were slightly different. As such, the differences between the coherograms were more complex than a simple scaling of the period axis. The statistically significant points, as determined from Monte Carlo bootstrapping, are shown in figures 5.34b and 5.34d for the Oulu and ACE data respectively.

For the Oulu coherograms in figures 5.34a and 5.34b, as for the IMA coherograms, some spatial structure can be observed, with vertical stripes of unmasked pixels persisting across several horizontal pixels. These clusters of unmasked pixels are less widespread than for the IMA data, however again the result is not inconsistent with a common periodicity existing between the albedo of Venus and the cosmic ray count rate at some times. Given that the Oulu data is not co-located with the cosmic ray data in this case, there is additional implication to a common periodicity being present in both the ajusted and non-adjusted coherograms. If there was common periodicities present between the albedo and cosmic ray data for both synodic and sidereal periods, then it would suggest that the cosmic ray variations driving the albedo periodicities were caused both by the rotation of the Sun, and by some other factor.

Finally, for the ACE coherograms in figures 5.34c and 5.34d, there is even less visible structure than for the Oulu or IMA coherograms. Vertical stripes are still apparent in the unmasked pixels, however these do not appear to have the same horizontal extent as in the other coherograms. As such, no suggestion has been found for a common periodicity between the albedo of

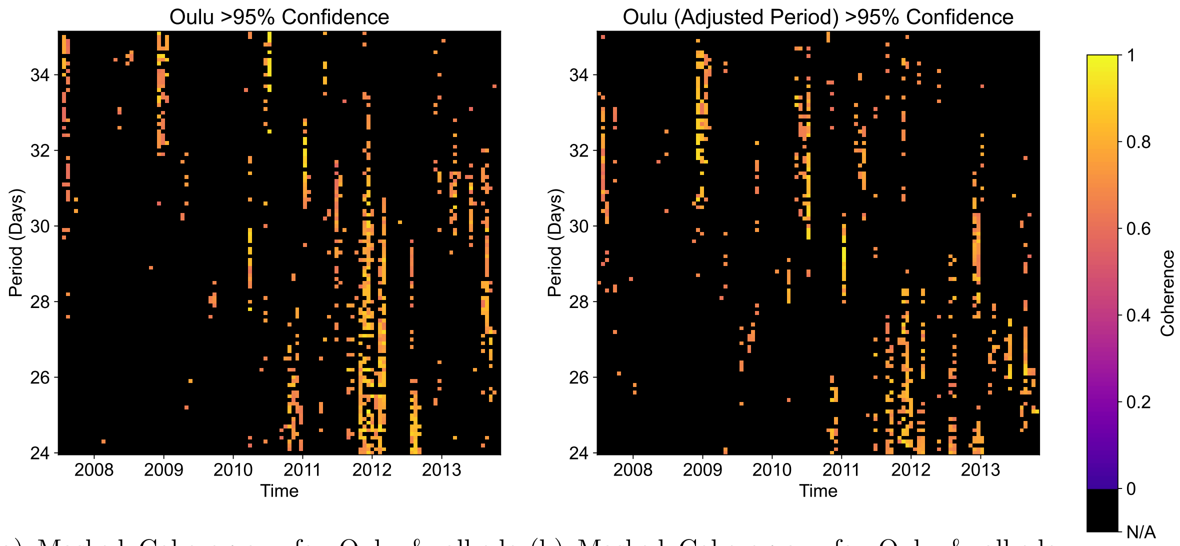

(a) Masked Coherogram for Oulu & albedo data

(b) Masked Coherogram for Oulu & albedo data (Period adjusted to corresponding solar period)

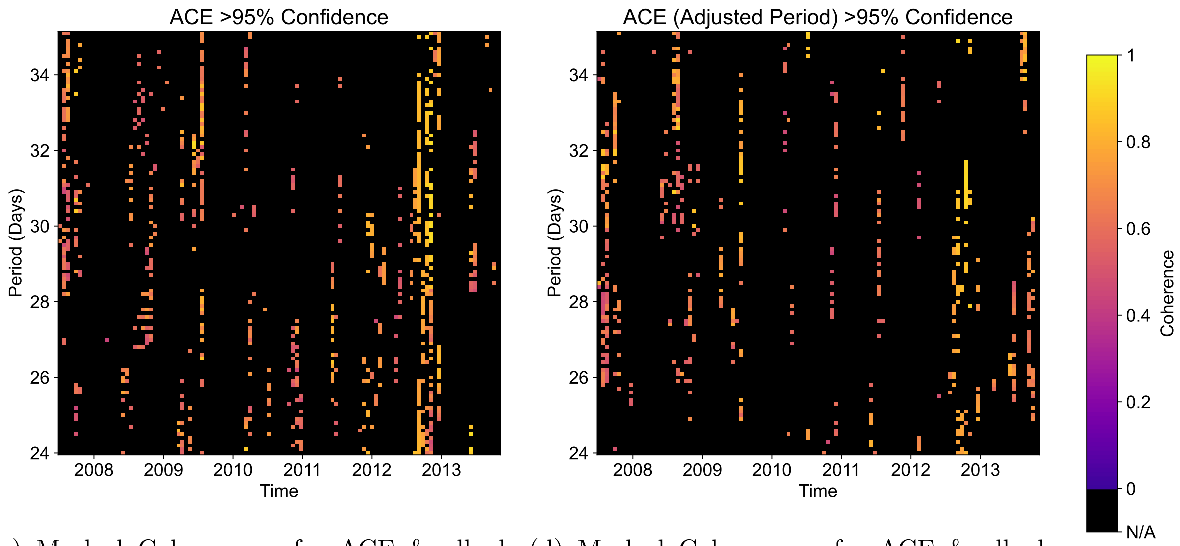

(c) Masked Coherogram for ACE & albedo data

(d) Masked Coherogram for ACE & albedo data (Period adjusted to corresponding solar period)

Figure 5.34: Coherograms for the Oulu & albedo datasets (a,b), and the ACE & albedo datasets (c,d) showing the coherence values which are greater than the 95% confidince limit. (a,c) are produced without any alteration to the periods in the input datasets. (b,d) is produced by adjusting the periods of the input datasets, such that they correspond to the rotation period of the Sun which would cause that periodicity at the observer.

Venus and the cosmic ray count rate at these energies.

5.5 Discussion

Several investigations were performed, with observers at different locations and at different cosmic ray energy levels, to investigate the effects which space weather events can have on the albedo of Venus. Firstly, the albedo response of Venus' atmosphere to Forbush events was investigated. These Forbush events were identified using neutron monitors at Earth. As such, we are investigating how the albedo is affected by a decrease in the GCR count rate at energies $\gtrapprox$ 500 MeV. From this investigation, it was found that there was an increase in the albedo following the Forbush events, which was significant above the 95% confidence level.

For this investigation, the Forbush events were detected using Earth-based sensors. As the Forbush events will be caused by ICMEs, it is expected that a Forbush event detected at Earth will only also be present at Venus if the two planets are located nearby one another. As such, further analysis has been performed, considering only the Forbush events which occurred when the angular separation between the Earth and Venus was less than 90°. Again, it was found that there was an increase in the albedo following the Forbush events, which was significant above the 95% confidence level.

In the previous investigations of the effects of Forbush decreases on the Earth's atmosphere, it was found that there was a decrease in the diffuse fraction following the events (suggesting a reduction in cloud cover). It is difficult to directly compare our results from Venus against these results, since we have been observing the changes in the albedo of the upper clouds, rather than the diffuse fraction. We note, however, that it is expected that changes to the concentration and size distribution of cloud particles will have impacts on the albedo - principally, an increase in the number of small cloud particles will lead to an increase in the albedo. The process of ion-induced nucleation has been considered as a mechanism for cosmic rays to have direct impact on the clouds of Venus. If this mechanism was important, it could be expected that a decrease in ionisation rate would lead to fewer cloud particles being produced, and therefore a lower albedo. This is counter to what was observed. There are several explanations for this difference between the expected and observed trends. Firstly, the impacts of the change in cosmic ray count rate may be more complicated than considered here - i.e. a decrease in ionisation rate may not directly lead to a decrease in the concentration of small particles. Secondly, it may be that variations in the cosmic rays at other energies are more important than at the energies considered for these Forbush decreases. This second point has been investigated further, by considering variations to cosmic rays at lower energies.

Several SEP events associated with ICMEs were detected at Venus. In lieu of a dedicated cosmic ray detector, variations in the cosmic ray count rate were identified by considering the background counts of the MCP in the IMA instrument of Venus Express. This background count rate was investigated at times surrounding the passage of ICMEs, to identify the presence of SEP events. As for the Forbush events, the response of Venus' albedo to these events was studied. It was found that these SEP events caused an increase in albedo which was significant above the 95% confidence level.

In the case of the SEP events, it was found that an increase in the cosmic ray count rate lead to an increase in the albedo of Venus. This is counter to what was observed for the Forbush decreases, where a decrease in the cosmic ray rate lead to an increase in albedo. As has been mentioned before, it may be that the different dependencies found here are related to the different cosmic ray energies which are present. However, another possible explanation is that the variations could be caused by some other mechanism than the changes to cosmic ray count rates. Both the Forbush and SEP events considered here are driven by ICMEs. It may be that the observed changes to the albedo were being driven by some other aspect of the ICME, such as the dynamical pressure.

The effects of space weather events on Venus' atmosphere were explored further, by considering HCS crossings. An investigation into these events was performed, since the events are not driven by ICMEs. For both A-T crossings and T-A crossings, data for cosmic ray count rate (again inferred from the IMA background counts) and albedo of Venus was compared for times before and after the events. From this comparison, it was noted that the datasets for before the event appeared visually different from the datasets for after the events. In the majority of cases, however, it was found that these differences were not statistically significant. It was found, however, that there was a statistically significant difference in the distributions of albedo data before T-A events compared to after these events.

From this investigation, we were unable to identify a trend in the cosmic ray data driven by the HCS crossings, despite this being found in previous terrestrial investigations. It is possible that this is due to the relatively few number of HCS crossings used in our investigation. Alternatively, it may be again related to the particle energies considered. The trends found for the previous studies used neutron monitor data at Earth. For our investigation, we considered the background counts of the IMA instrument, which is sensitive to lower energies than these neutron monitors.

It is surprising that a statistically significant change in the albedo was only observed for HCS crossings of one polarity - i.e. the T-A crossings. For the previous terrestrial investigations, it was found that there was a change to the cosmic ray environment for both polarities of crossing. It was noted, however, that a greater change was present for A-T crossings. It is interesting to note that this is the opposite polarity of crossing to those which we observed leading to the significant variation in albedo. It is possible that albedo variations do occur for both polarities of HCS crossing, however these variations were not severe enough to be significant in our dataset, which considered only a small number of events. The fact that we were able to observe a statistically significant change in the albedo data, related to these HCS crossings, is suggestive that the variations in albedo driven by other space weather events may have been driven by some cosmic ray effects, rather than other ICME effects.

Finally, the periodicities present in both the albedo of Venus and several cosmic ray datasets were investigated. For each of the cosmic ray datasets, the coherence between the CR data and the albedo of Venus was determined. Two such coherograms were produced for each dataset; the first considered the same periods of variation for the two inputs (i.e. albedo and cosmic ray data), while the second adjusted the periods such that they corresponded to the same period of solar rotation. In several of these coherograms, some spatial structure was identified in the statistically significant coherence datapoints. These signals were interpreted to be not inconsistent with a common periodicity being present between the albedo and the cosmic ray data, at some cosmic ray energies. Further, these signals were present both when considering the same period of variation between the CR and albedo datasets and when adjusting the periods to the same sidereal solar rotation period. Assuming that there was a common periodicity between the albedo and CR data, then this would suggest that the cosmic ray variations responsible for the periodicity were being driven by both the rotation of the Sun and by some other factor.

The investigation performed here has suggested that there may be a relationship between the cosmic ray count rate and the albedo of Venus, however future investigations will be required in order to confirm is such a relationship does exist.

5.5.1 Conclusions

From analysis of the albedo of Venus at times surrounding the detections of Forbush events at Earth, it was found that there was a statistically significant increase in the albedo associated with these events. SEP events were detected at Venus, and it was found that these events also caused statistically significant increases in the albedo. A number of HCS crossings were identified at Venus, in both the TA and AT directions. No perturbations to the cosmic ray environment associated with these events were able to be detected from the available data, however it was observed that TA crossings had a statistically significant effect on the albedo of Venus. Finally, via spectral analysis some features not inconsistent with a common periodicity between cosmic ray data and the albedo of Venus, were identified.

Currently, the mechanisms driving the relationship between cosmic rays and the albedo of Venus are unknown. Future investigations may be able to yield additional information which would allow the nature of the mechanisms to be determined. In particular, dedicated cosmic ray instrumentation at Venus would allow the variations to cosmic rays of different energies to be studied, which would aid in these investigations.

This link found between cosmic ray count rates and the albedo of Venus suggests that there are some electrical effects present in the atmosphere of Venus. The exact nature of these effects is unknown, however given the conclusions found in chapter 4 - that there is evidence suggesting a global atmospheric electric circuit exists in Venus' atmosphere - this is of importance. The presence of such a global electric circuit will act to distribute the effects of electric charge throughout the atmosphere. As such, if there is a global circuit present, then variations in the cosmic ray count rate will be able to cause variations throughout the entire atmosphere.

Chapter 6

Discussion

The investigations described in this thesis covered a range of topics. First, atmospheric electricity measurements on Earth were investigated, through analysis of the data from point discharge sensors (Chapter 3). Next, the electrical structure of Venus' atmosphere was investigated, which again utilised point discharge data (Chapter 4). Finally, the effects of cosmic rays and space weather events on Venus' atmosphere were investigated (Chapter 5).

Although these topics appear varied, there is a shared connection between them. Cosmic ray processes are responsible for ionisation in planetary atmospheres. This ionisation is important to the electrical structure of the atmosphere, which in turn affects electrical observations in the atmosphere. These links are illustrated in figure 6.1, where the topics covered in each of the three work chapters have been indicated.

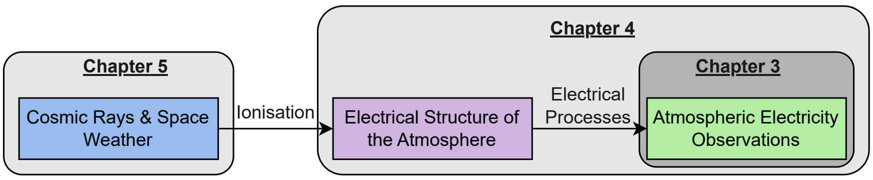

Figure 6.1: Overview of the links between the work in the 3 work chapters of this thesis.

The results from chapters 3, 4, and 5 will be discussed in the following three sections, followed by an overall discussion of how these results are related, and their implications, in section 6.4.

6.1 Point Discharge

The operation of several point discharge sensors at the Reading University Atmospheric Observatory were investigated. This investigation was performed in two parts. First, time series of point discharge data were investigated, and compared against time series of potential gradient data. It was found that several features in the point discharge time series occurred before similar features in the PG time series. Time series of the rate of change of PG were then considered, where it was found that features from the point discharge time series occurred after the features in the rate of change of PG. It was then shown that by considering a sum of electrostatic (dependent on the PG) and electrodynamic (dependent on the rate of change of PG) terms, the features in the point discharge time series could be described best. The conclusion of this investigation was that both electrostatic and electrodynamic terms appeared to be important to the description of the behaviour of point discharge sensors. Of note is that previous investigations into the operation of similar sensors have not reported the importance of these electrodynamic terms.

Following this, several parameterisations of a point discharge sensor were investigated. Based on previous investigations, two forms of parameterisation were considered. Additionally, following the previous results, the impact of including additional electrodynamic terms was evaluated. The quality of fit for each parameterisation was evaluated by finding the adjusted R squared value for the 1:1 line between the modelled PDC and the measured PDC. From this investigation it was found that the inclusion of electrodynamic terms improved the quality of fit for both forms of parameterisation. This result is in agreement with that found in the previous section of this investigation. It was additionally found that, for the dataset investigated, the parameterisation considering the effects of wind speed was a poorer fit than the one neglecting these effects. It is believed that the reason for this is that the dataset described only low wind speeds, and the parameterisation neglecting the effects of wind speed describes the point discharge process better than the low wind speed limit of the more complex parameterisation.

The source of the electrodynamic term affecting the PDC measurements was interpreted to be a Maxwell current. This suggests that the PDC sensor is sensitive to both free currents caused by the movement of charge, and displacement currents caused by changing electric fields.

6.2 Venera Reanalysis

The electrical environment of Venus was investigated via re-analysis of point discharge data from the Venera 13 & 14 spacecraft. First, an electrical model of Venus' atmosphere was produced. This model allowed the concentrations of positive and negative ions to be calculated as a function of altitude in Venus' atmosphere. From these concentrations, additional parameters such as the conductivity and columnar resistance were calculated. Additionally, the atmospheric electric field and atmospheric potential were determined under the assumption that a global electric circuit exists on Venus, with assumptions made on the magnitude and direction of the fair weather conduction current. Finally, the modelling approach considered the charge acquired by a spacecraft descending through this atmosphere, and therefore the discharge currents emitted by such a spacecraft.

The electrical model was then used to investigate what conditions are necessary for the Venera 13 & 14 point discharge data to be reproduced. From this investigation, it was discovered that the observed data could not be reproduced in the case where a global atmospheric electric circuit is not present. In addition to requiring a global circuit, it was found that it was also necessary to have particular lower-atmosphere haze layers present to reproduce the data.

6.3 Space Weather Effects

For the first time, several space weather events have been detected at Venus. Further, the effects of such space weather events on Venus' atmosphere were investigated. The impacts to the atmosphere were identified by monitoring the albedo of the atmosphere as a function of time. This investigation was formed of two parts, considering the short term impacts of space weather events, and long term trends in the cosmic ray count rates.

To observe the effect that space weather events have on the atmosphere of Venus, the albedo responses to each event were compared. A new approach for this was developed, based on previous compositing approaches. This approach involved comparing the albedo at times surrounding several events. This method allowed the general trends caused by the space weather events to be identified. Several types of event were considered, with the analysis initially focusing on Forbush events detected at Earth, and later considering SEP events detected by spacecraft at Venus.

For the Forbush events detected at Earth, it was acknowledged that not all events were likely to also affect Venus. To resolve this concern, a subset of events was identified where the angular separation between Venus and Earth was minimised. The analysis was repeated for this dataset. It was found that for both datasets the Forbush events had a significant impact on the albedo of Venus. A similar analysis was performed for the SEP events detected at Venus, where again it was found that the space weather events had a significant impact on Venus' albedo. In both of these cases, the driving factor behind the space weather event was an ICME. As such, it was uncertain if the change in albedo was driven by some electrical effect, caused by the perturbation to the cosmic ray flux, or by some other effect, such as the dynamic pressure of the ICME.

Additionally, HCS crossings were identified at Venus from spacecraft magnetometer data. The method of identifying these events did not allow precise timing of the event. As such, analysis was not performed as for the Forbush and SEP events. Instead, data from before and after the event was compared, to investigate the differences on either side of the HCS. First, the differences in cosmic ray environment were investigated. It was found that there was a significant difference in cosmic ray count rates for one polarity of HMF compared to the other. Next, it was investigated if this difference in cosmic ray count rate impacted the albedo of Venus. In this case, no significant difference in albedo was observed before vs after the HCS crossing.

Periodic variations in the cosmic ray count rate were compared against variations in the albedo of Venus. For this investigation the periodic variations caused by the differential rotation of the Sun were considered. To search for signals occurring in both the cosmic ray data and the albedo data, coherence analysis was used. Moving window coherograms were produced to search for signals with a particular period, at a particular time. Several cosmic ray datasets were compared against the albedo, covering different energy ranges and locations of detection. Additionally, the differences between cosmic ray variations driven by the rotation of the sun, and variations driven by other sources were considered. It was found that in many cases there was statistically significant coherence between the cosmic ray data and the albedo of Venus, for both of these sources. Consequently, this work was suggestive that variations in cosmic rays affect Venus' atmosphere.

6.4 Overall Considerations

The investigations performed in this thesis pertained to electrical effects in planetary atmospheres, particularly that of Venus. The investigation of point discharge sensors on Earth allowed knowledge of the point discharge process to be obtained. This knowledge was applied to the point discharge measurements taken by the Venera 13 & 14 spacecraft. The investigation of this point discharge data identified electrical effects as being important in Venus' atmosphere, through the presence of a global atmospheric electric circuit. Finally, further electric effects were identified in Venus' atmosphere through investigations of the effects of space weather effects and cosmic ray variations on the atmosphere.

The links between the processes relevant to these investigations are shown in figure 6.2.

The implications of the electrical effects observed in Venus' atmosphere will be discussed here. The findings from this investigation act as evidence for a global atmospheric electric circuit in Venus' atmosphere. It should be noted, however that this does not provide direct evidence for lightning in the atmosphere. On Earth, although lightning is a very dramatic process, it is not believed to be the dominant mechanism by which charge is brought to the surface of the planet, and so it is not necessary for a global electric circuit to exist. Instead, processes such as point discharge currents from the surface, or some process akin to the charged rains on Earth may be responsible for bringing a net charge to the surface of the planet.

The existence of a global electric circuit on Venus does offer some indirect evidence that lightning is possible in Venus' atmosphere, however. For such a circuit to be established, it is necessary for charge separation processes to occur in the atmosphere. Such processes would also be a prerequisite for lightning, so suggestions that these processes exist is encouraging for lightning searches.

It was observed that several space weather events, both those associated and not associated with coronal mass ejections, had significant impacts on the albedo of Venus. The mechanism driving these impacts is unclear. Previous investigations have discussed the possibility that the process of ion induced nucleation is important in Venus' atmosphere [5]. This process allows a link between the cosmic ray flux, which is expected to be perturbed by these space weather events, and the clouds of Venus. As such, the link between these events and the albedo of Venus could be due to variations in such a process.

The investigations described in this thesis have identified several electrical effects present in the atmosphere of Venus. It is currently unclear how widespread these effects are, however further investigation of the effects may allow electrical effects on atmospheres - both on Venus and through comparative studies, on Earth - to be understood more fully.

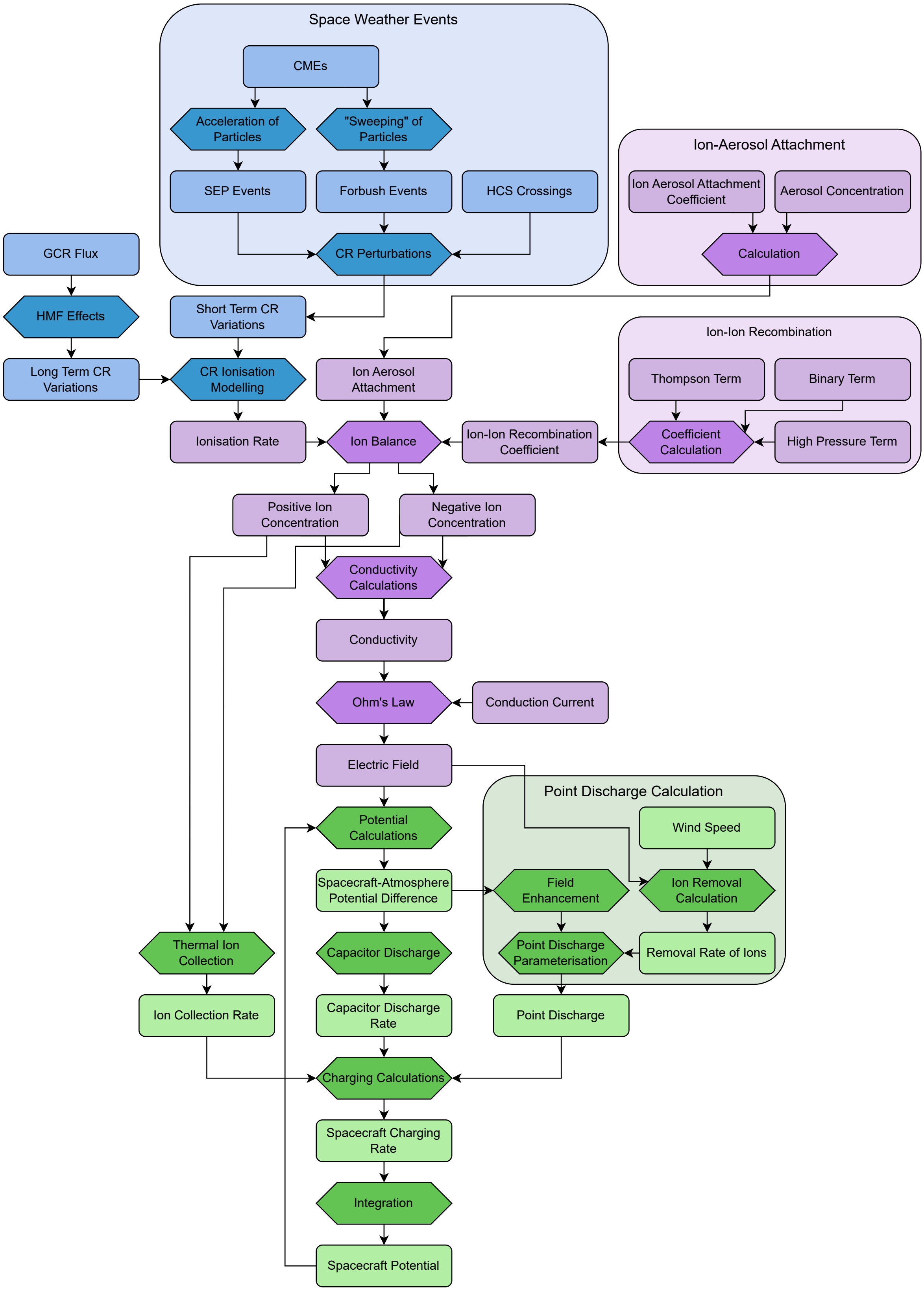

Figure 6.2: Flowchart showing how the atmospheric electricity and space weather systems discussed in this thesis are connected. The same shading as in figure 6.1 has been used, where blue shading shows cosmic ray & space weather effects, purple shading describes the electrical structure of the atmosphere, and green shading describes observations of atmospheric electricity. Rectangular boxes show quantities/parameters, hexagons show processes, and large rounded rectangles describe collections of these processes/parameters.

Chapter 7

Conclusions & Future Work

In this chapter, the conclusions from this thesis along with several avenues for future work will be discussed.

7.1 Conclusions

The work in this thesis consisted of several related investigations. First, the operation of two point discharge sensors at the Reading University Atmospheric Observatory (RUAO) were investigated. Through an investigation of the time response of one of these sensors, it was identified that the sensor was dependent on both electrostatic and electrodynamic processes. This was interpreted as the sensor recording both free and displacement currents. A subsequent investigation considered the parametrisation of a different point discharge sensor, also deployed at the RUAO. This investigation reinforced the previous result, finding that the operation of the sensor was described better if electrodynamic terms were included in the parameterisation.

The knowledge of point discharge sensors gained from these terrestrial investigations was then applied to an investigation of the point discharge data recorded by the Venera 13 & 14 landers. In this investigation, an electrical model of Venus' atmosphere was produced. This model allowed the point discharge currents emitted by a spacecraft descending through Venus' atmosphere to be determined for varying atmospheric conditions. Through this investigation, it was found that the best agreement to the Venera data was found when a global atmospheric electric circuit was present in the atmosphere, along with haze layers being present in the lower atmosphere. The presence of such a global circuit has important implications, suggesting that electrical processes would be able to have influence throughout the atmosphere of Venus.

Finally, the presence of electrical effects in Venus' atmosphere was investigated further by considering space weather and cosmic ray impacts on the atmosphere. For this investigation, several space weather events were identified. Some of these events were detected at Earth, as has been done previously, however in this investigation we additionally were able to detect Solar Energetic Particle (SEP) events, and Heliospheric Current Sheet (HCS) crossings at Venus, for the first time. The albedo of Venus' atmosphere following these events was observed. It was found that there was a statistically significant increase in the albedo following both Forbush decreases and SEP events. Additionally, it was found that the albedo following HCS crossings from the towards to away magnetic field directions was significantly different to the albedo before the events. These results are some of the first demonstrating that a space weather effect is present in Venus' atmosphere. These observations provided additional evidence for the importance of electrical effects in Venus' atmosphere. The effects were further investigated by considering periodic variations present in both the cosmic ray flux and the albedo of Venus. It was found that there were several periodic signals, at certain times, with statistically significant coherence between the albedo and several cosmic ray datasets. This result was again suggestive that charged particles have important impacts on Venus' atmosphere.

The main findings of the work can be summarised as follows:

- Point discharge sensors are sensitive to both electrostatic and electrodynamic terms, with the latter interpreted as taking the form of Maxwell currents
- The point discharge data recorded by the Venera 13 & 14 landers is consistent with both a global atmospheric electric circuit and a low atmosphere haze layer existing in Venus' atmosphere
- Perturbations to cosmic rays, on both short ($\mathcal{O}$ 1 day) and longer ($\sim$25 day) timescales are able to impact the albedo of Venus

Additionally, several space weather events were detected at Venus for the first time.

7.2 Future Work

From the investigations performed in this thesis, several future investigations which would be benefitial were identified. These have been discussed in this section.

7.2.1 Point Discharge

There is much work still to do in order to fully understand the the operation of point discharge sensors. Based on the findings discussed in chapter 3, a number of future investigations into understanding the operation of these sensors are proposed.

It would be beneficial to investigate the relative importance of the Maxwell term in the point discharge parameterisations further. There are several ways in which this investigation could be performed. One method would be to perform a similar analysis as was performed here, but with an expanded dataset. This investigation would be relatively easy to perform, however it relies on a suitable number of days with a large range in electrical activity. This method would allow the two parameterisations to be investigated further. Given a suitable amount of data, it would be possible to evaluate the quality of both parameterisations at different wind speeds. Such an investigation could help to identify a form of parameterisation which describes both the low and high wind speed limits well. This approach does have drawbacks, however. The exposed nature of the field site means that there are many factors which can affect the point discharge process. This could make it difficult to identify which effects cause a given variation. To remedy this, there are other forms of investigation which could be performed.

It could be possible to investigate the nature of the electrodynamic Maxwell term on a corona sensor in a laboratory environment. In this case, variable electric fields could be produced, with the resulting corona discharge measured. Through this method, it would be possible to identify how the corona discharge is dependent on both the electric field and rate of change of this field, with all other parameters kept constant.

Finally, the relative importance of the Maxwell term could be identified via electrostatic modelling. The Maxwell current flowing into a point discharge sensor is given by:

$$I_D = A\epsilon \frac{dF}{dt} \tag{7.1}$$

where ϵ is the permittivity of air, dF/dt is the rate of change of PG with respect to time, and A is some constant. The constant A has the dimensions of area, and can be interpreted as the horizontal area in which the field lines of the vertical atmospheric electric field are curved such that they meet the point of the PDC sensor. As such, via modelling of the electric fields around a point discharge sensor, the size of this area can be found. This would allow the relative importance of the Maxwell term to be identified, and would allow comparisons between this theory and the empirical results.

Additionally, through a similar electrical modelling process, it could be possible to identify the electric field enhancement of a given sensor. This would allow the corona onset field to be identified for a given sensor. Again, comparisons could be made between this theoretical value and the empirical results.

7.2.2 Venera Point Discharge Reanalysis

From the investigation described in chapter 4, evidence has been provided for the existence of both low atmosphere haze layers and a global atmospheric electric circuit in Venus' atmosphere. Specific details on the nature of both of these have not been acquired, however, which could be addressed in future investigations.

To describe the presence of a global atmospheric electric circuit in the electrical model, the fair weather conduction current was specified. It was found that a range of magnitudes of current were able to reproduce the Venera point discharge data, for both polarities of current. It may be beneficial then to constrain the properties of this current via other methods. For Earth, the global atmospheric electric circuit has previously been modelled as a traditional electronic circuit [157]; several aspects of the atmosphere, such as thunderstorm areas, were regarded as individual electronic components. A similar modelling approach could be applied for Venus, allowing estimates to be made for the properties of the conduction current based on other observations of atmospheric electricity.

The exact properties of the haze predicted to be present in Venus' lower atmosphere are uncertain. If accurate information was available for details such as the vertical size and concentration profiles, or the shape of the size distribution at a given altitude, then assumptions could be made for the origin - potentially via comparison with hazes on Earth. These parameters were unable to be determined from our methodology, however. For our investigation, we considered a monomodal, monodisperse aerosol distribution of constant particle size. These assumptions may provide a poor description of the true haze layer. It may be possible to reproduce the

Venera discharge data while considering haze layers with multiple modes, having the size of these modes change with height, and having different distribution shapes at given height steps. By implementing these changes, we would not impact the main conclusion of this work - i.e that both a low-atmosphere haze layer and a global atmospheric electric circuit are required to reproduce the Venera discharge data - however, it could have other implications for the nature of the haze. Firstly, these changes would affect optical properties of the haze, which would be relevant for any attempts to observe it directly. Additionally, by investigating the range of possible solutions, it may be found that the haze layer properties suggest a particular origin for the haze, such as volcanic ash or advected dust.

As for the conduction current, the properties of the low atmosphere haze could also be constrained by other observations of Venus' atmosphere. Several spacecraft have attempted to measure particle distributions in-situ in Venus' atmosphere. These investigations have not yielded specific information on the particle sizes or concentrations of the haze, however, they still might allow us to constrain the haze properties. It is important to consider that the operational range of the instruments used to search for haze may have limited the detections which were possible. For example, the cloud particle size spectrometer onboard the Pioneer Venus sounder probe, which observed the presence of haze down to 30km, was only able to measure particles with size greater than 0.5 µm. As such, there may have been a large number of particles present which were unable to be detected due to their size being outwith the detector's range. It should also be noted that one conclusion drawn from the spectrophotometric investigations was that there is evidence that the sub-cloud hazes of Venus are variable. As such, it is to be expected that different spacecraft would experience a different haze environment. As such, it may be difficult to compare the haze properties obtained from one spacecraft's dataset, to that of another spacecraft.

The expected variability of the low atmosphere haze on Venus means that if we wish to compare the haze profiles found from our electrical modelling to haze properties found from other methods, then ideally the data for both methods would be taken from co-located (both spatially and temporally) observations. Given that we have used electrical data from the Venera 13 & 14 landers, we thus would ideally want to use haze observations also made by these spacecraft. This requirement makes the Venera 13 & 14 spectrophotometer data very interesting for a search for haze, as it would allow comparisons of the haze properties from two independent methods. Analysis of this dataset has previously found evidence for haze at an altitude of 2km, however further analysis, combined with the electrical observations, may yield further results [56].

A number of assumptions were made in the production of the electrical model used in this investigation. These included the assumption that the aerosols at a given altitude had a neutral charge distribution, the assumption that the vertical movement of ions was negligible, and the assumption that all free electrons readily formed negative ions. It should be noted that this final assumption is believed to be valid at low altitudes, i.e. in the range of the Venera PDC data, however in general these assumptions do not hold. In order to improve the accuracy of the electrical model, it would be beneficial to explicitly consider these effects, rather than assume them to be negligible. This is a non trivial task, however, due to the analytic nature of the electrical model. In order to consider these effects, it may be desirable to produce a numerical model of Venus' electrical environment. Such a model would have the benefit of allowing these effects to be included explicitly, and additionally could allow investigations into the time response of Venus' atmosphere. If such a model was produced, then the methodology developed in this work - comparing model results to the in-situ PDC data from Venera 13 & 14 - could be applied to that model also.

In order to validate some of the assumptions made in the production of this model, it would be beneficial to verify the electrical results found against observations. Such a verification could be performed for Earth's atmosphere, by considering the charge collected during the ascent of balloons or aircraft. It should be noted, however, that the differences between these examples and the descent of the Venera landers may lead to large variations in the modelled results.

This investigation of Venus' atmosphere was reliant upon some of the only in-situ atmospheric electricity data for Venus. Specific information on the operation and geometry of the sensor has been lost to time, requiring that assumptions be made about the design of the device. Given these limitations, it is believed that future investigations could greatly benefit from additional in-situ atmospheric electricity data - either from similar, point discharge instrumentation, or from other sensors. Such future investigations would be advantageous for many reasons; additional point discharge investigations would allow accurate information on the sensor to be recorded - aiding in its interpretation. This would allow for an increased confidence in the results obtained from modelling of the spacecraft, and as such would allow the electrical environment of Venus to be constrained more accurately. If modern instrumentation is used for such an investigation, it may be possible to resolve greater structure in Venus' atmosphere than the instrumentation from the Venera spacecraft allows. It may additionally prove useful to compare data recorded by future spacecraft to the data recorded by Venera 13 & 14. Both of the Venera 13 & 14 spacecraft recorded similar discharge current profiles, despite the spatial and temporal separations of their atmospheric descents. The similarity of the signals recorded by these spacecraft was interpreted to be indicative of some feature which was inherent to Venus' atmosphere, so it would be of interest to investigate if additional datasets also showed a similar signal.

In addition to point discharge data, there is a great number of other atmospheric electricity observations which may be of interest. In order to validate VAIL, the conductivity profile calculated from the model was compared against a profile found from a previous ionisation model of Venus' atmosphere. Future in-situ measurements of the conductivity of the atmosphere would be of great interest for a number of reasons; These measurements could be used to validate electrical models of Venus' atmosphere, or they could be used to investigate the presence of haze in the atmosphere by identifying regions of lower conductivity.

To investigate the presence of a global atmospheric electric circuit in Venus' atmosphere, we have considered the effects that a vertical electric field would have on the charging (and discharging) of a spacecraft. Instead of inferring the presence of such an electric field, it could be possible to detect it directly. Electric field mills which are typically used for observations of the terrestrial atmospheric electric field would likely be too delicate for such a harsh environment as Venus, however other methods of measuring the vertical electric field would be possible. In addition to attempting to observe the presence, magnitude, and polarity of the vertical electric field, the vertical flow of current could also be observed. The presence of a vertical electric field or flow of current would act as evidence for the presence of a global atmospheric electric circuit.

Finally, it may be of some benefit to carry a charge sensor to Venus' atmosphere. On Earth, such sensors have been used on radiosondes to measure the presence of cloud edge charging. One such sensor, developed by Nicoll et al. [134] determined the presence of charge from the displacement currents induced by a changing electric field, as the sensor approached or receded from an area of space charge. In principle, such a sensor design could be used for a spacecraft descending through the atmosphere, rather than for a balloon ascending. The data from such a charge sensor could be used to search for regions of space charge originating from cloud edge charging, or from some other charge separation process.

7.2.3 Space Weather Effects

The identification of space weather events at Venus was performed using a limited amount of in-situ data. To improve on this method, it could be possible to combine our observations with solar wind / ICME models. Through such a process it may be possible to detect more space weather events, to be more accurate with the assessment of which events will affect Venus, and to determine the exact timing of events with greater detail. Given a more refined dataset achieved via such methods, it may be possible to identify the impacts of space weather events on Venus' atmosphere with more detail.

To investigate the effects of cosmic rays on Venus further, additional periodicities in the cosmic ray data could be investigated. The 1.68 year periodicity in GCR count rates has previously been used to identify cosmic ray effects on the ice giants, so would appear to be a good candidate for investigation on Venus. During the period of the albedo data from Venus Express, this periodicity is not present in the GCR data, however. As such, this dataset cannot be used to investigate if the 1.68 year periodicity is present in the atmosphere of Venus. To circumvent this issue, other datasets could be considered, such as ground based observations of Venus' apparent magnitude.

Additionally, alternate datasets could be used to investigate the same periodicities as were considered in this investigation. The results from such an investigation could be used to reinforce the findings of the investigation described here, and to understand the nature of the link between cosmic rays and Venus' atmosphere further. The alternate datasets could also be used to aid in the investigations of the impact of space weather events, allowing even more events to be studied than occurred during the operation of Venus Express. Ideally, future spacecraft missions to Venus would carry dedicated cosmic ray instrumentation, which would allow variations to be observed for different particle energies. Investigating how the atmosphere of Venus is affected by particle variations at these different energies would hopefully allow any important mechanisms to be identified.

7.3 Closing Remarks

Through our understanding of the point discharge signals detected by the Venera 13 & 14 landers, and the observation that space weather variations have an impact on Venus' albedo, it is clear that electrical effects are important to the atmosphere of Venus.

To the author's knowledge, the work in this thesis presents the first evidence of a global atmospheric electric circuit in Venus' atmosphere. It is hoped that these results can help inform future investigations of Venus' atmosphere, and future spacecraft missions to Venus.

Data Availability

I am grateful for the data supplied by various sources which was used for the analysis in this PhD. These sources of data will be listed here.

- Various data from the Reading University Atmospheric Observatory was used, obtainable at: `https://research.reading.ac.uk/meteorology/atmospheric-observatory`
- The point discharge data recorded by Venera 13 & 14 was reported by Ksanfomaliti [103]
- Atmospheric profiles for Venus' atmosphere were obtained from the Venus International Reference Atmosphere (VIRA) [95].
- Cloud data for Venus' atmosphere was obtained from the analysis performed by Knollenberg and Hunten [98].
- Ionisation rate profiles for Venus' atmosphere were obtained from the modelling performed by Nordheim et al. [138].
- The albedo data produced by lee et al. [109] is obtainable at: `http://doi.org/10.5281/zenodo.3754455`
- Data from the Oulu neutron monitor was used, obtainable at: `https://cosmicrays.oulu.fi/`
- Data from the ACE SIS instrument was used, obtainable at: `https://www.swpc.noaa.gov/products/ace-real-time-solar-wind`
- Various data from Venus Express instruments were used. This data is obtainable at: `https://www.cosmos.esa.int/web/psa/venus-express`
- The CME data catalogued by HELCATS was obtained at `https://www.helcats-fp7.eu/`
- The JPL Horizons ephemerides were obtained at: `https://ssd.jpl.nasa.gov/horizons/`
- Sunspot data provided by NOAA was obtained at: `https://www.ngdc.noaa.gov/stp/solar/ssndata.html`

The code developed and data generated for the analysis in this thesis will be made available in the following location: https://doi.org/10.6084/m9.figshare.c.7770257.

Appendix A

Chalmers' Derivation

The derivation of the relationship between potential gradient, wind speed, and point discharge current, as outlined by Chalmers [32] has been reproduced here [32].

For this derivation, we consider a needle tip held at one potential, placed in an environment at a different potential. Two regions around the needle were considered: In region A, the dominant force on charges arises from the electric force from the needle tip. In region B, this force is no longer dominant. Two cases are considered for the force which becomes dominant in region B; in section A.1, this force arises from the wind speed, and in section A.2 this force arises from the Potential Gradient of the atmosphere.

For this derivation, spherical symmetry is assumed. Additionally, any changes in ion mobility, i.e. ions becoming "large ions" have been neglected. Finally, in regions A and B the "non-dominant" force is neglected, and it is assumed that once a charge reaches region B it is immediately removed - i.e. there is no space charge build up in this region.

We consider a radial distance from the point, a, within which the field strength needed for ionisation by collision, E_0, is met. As, such, we can assume that everywhere within the radius a has a sufficient population of free charges to be conductive, and thus is at the same potential as the point. We define this potential to be zero, $V_a = 0$.

Now let the distance to the boundary between regions A and B be b, and consider a sphere within region A with radius r such that $a < r < b$.

The current flowing through this sphere is given by:

$$I = 4\pi r^2 ne\mu E(r) \tag{A.1}$$

Where n is the number density of ions carrying charge e, μ is the mobility of these ions, and $E(r)$ is the electric field at a distance r from the needle tip.

We then use Gauss' law:

$$\nabla \cdot \mathbf{E} = \frac{\rho}{\epsilon_0} \tag{A.2}$$

$$\frac{1}{r^2}\frac{d}{dr}(r^2 E) = \frac{ne}{\epsilon_0} \tag{A.3}$$

substituting for I yields:

$$\frac{d}{dr}(r^2E) = \frac{1}{\epsilon_0}\frac{I}{4\pi\mu E} \tag{A.4}$$

If we make the substitution $y = r^2E$, then:

$$\frac{dy}{dr} = \frac{r^2}{y}\frac{I}{4\pi\mu\epsilon_0} \tag{A.5}$$

$$y\,dy = \frac{I}{4\pi\mu\epsilon_0}r^2\,dr \tag{A.6}$$

Integrating between a and some radius r, we find:

$$\int_{y_a}^{y_r} y\,dy = \frac{I}{4\pi\mu\epsilon_0}\int_a^r r'^2 dr' \tag{A.7}$$

$$\left[\frac{y^2}{2}\right]_{y_a}^{y_r} = \left[\frac{r'^4E(r')^2}{2}\right]_a^r = \left[\frac{Ir'^3}{12\pi\mu\epsilon_0}\right]_a^r \tag{A.8}$$

$$\frac{r^4E(r)^2}{2} - \frac{a^4E_0^2}{2} = \frac{Ir^3}{12\pi\mu\epsilon_0} - \frac{Ia^3}{12\pi\mu\epsilon_0} \tag{A.9}$$

if we assume that a is very small, and consider $r \gg a$, then we find that the terms that are dependant on a are also very small and can be neglected. So,

$$\frac{r^4E(r)^2}{2} = \frac{Ir^3}{12\pi\mu\epsilon_0} \tag{A.10}$$

$$E^2 = \frac{I}{6\pi\mu\epsilon_0 r} = K^2r^{-1} \tag{A.11}$$

where we have defined $K^2 = \frac{I}{6\pi\mu\epsilon}$

We can find the potential difference between the radii a and b:

$$V_b - V_a = \int_a^b -E\,dr = \int_a^b -Kr^{-\frac{1}{2}}dr \tag{A.12}$$

$$V_b = -2K(b^{\frac{1}{2}} - a^{\frac{1}{2}}), \tag{A.13}$$

since $V_a = 0$. As $a \ll b$ we can write:

$$V_b \approx -2Kb^{\frac{1}{2}} \tag{A.14}$$

or, using equation A.11 to write $b = \frac{K^2}{E(b)^2}$:

$$V_b = \frac{-2K^2}{E(b)} \tag{A.15}$$

If we now consider the case where $r > b$, we can find the electric field as a function of distance using Gauss' Law:

$$\oiint_S \mathbf{E}.d\mathbf{A} = \frac{Q}{\epsilon_0} \tag{A.16}$$

where Q is the charge enclosed in surface S, and A is the area vector of this surface. Since in region B there is no space charge, any region which encloses the entirety of region A will be enclosing the same charge. So, we can write:

$$E(r)\left(4\pi r^2\right) = E(b)\left(4\pi b^2\right) \tag{A.17}$$

$$E(r) = E(b)\frac{b^2}{r^2} \tag{A.18}$$

We can then find the potential difference between the radii b and r:

$$V_r - V_b = \int_b^r -E(r')dr' = -E(b)\,b^2 \int_b^r \frac{1}{r'^2}dr' \tag{A.19}$$

$$V_r - V_b = \left[\frac{-E(b)\,b^2}{r'}\right]_b^r \tag{A.20}$$

If we then consider the potential as r tends to infinity as V, we find:

$$V - V_b = -E(b)\,b \tag{A.21}$$

Using equation A.11 again:

$$V - V_b = -\frac{K^2}{E(b)} \tag{A.22}$$

We can then use equation A.15 along with equation A.22 to find the potential difference between the needle and infinity:

$$V = -\frac{K^2}{E(b)} - \frac{2K^2}{E(b)} = \frac{-3K^2}{E(b)} \tag{A.23}$$

substituting for K:

$$V = \frac{-I}{2\pi\mu\epsilon_0}\frac{1}{E(b)} \tag{A.24}$$

A.1 Conditions of high wind and small field

For large wind speeds, we can consider the boundary between regions A and B to occur at the point where the wind speed exceeds the drift velocity of charges, in the needle's electric field.

This boundary thus occurs at a distance b, such that:

$$W = \mu E(b) \tag{A.25}$$

where W is the wind speed. Using equations A.11 and A.23 we can find that the boundary between regions A and B will occur at a distance:

$$b = \frac{K^2\mu^2}{W^2} = -\frac{V\mu}{3W} \tag{A.26}$$

Using equation A.25 to substitute for E(b) in equation A.24 yields:

$$V = \frac{-I\mu}{3\pi\mu\epsilon_0 W} \tag{A.27}$$

$$I = -2\pi\epsilon_0 VW \tag{A.28}$$

In setting a very small compared to b, we have neglected the fact that there is a minimum magnitude of potential required for point discharge to occur. To accommodate for this, we replace V with $(V - V_0)$, where V_0 is this critical value:

$$I = -2\pi\epsilon_0 (V - V_0)W \tag{A.29}$$

From equations A.15 and A.23, we can see that at a distance b, the potential is $\frac{2}{3}V$. So, if we find that b is small, then the potential would change rapidly with distance from the needle point. This would confine the change of potential to a region close to the needle point, and our assumption of spherical symmetry would be valid. Conversely, for large values of b, our assumption of spherical symmetry breaks down.

As can be seen in equation A.26, for large values of W or small magnitudes of V, the distance b will be small. So, our assumption of spherical symmetry will hold as long as the wind speed is large. If we instead have a small values for W, or a large magnitude for V, b will become very large, and our assumptions are will no longer be valid. In this case an alternate description of the boundary between regions A and B needs to be used, as is discussed in section A.2.

A.2 Conditions of low wind

In cases where the wind speed is low, we can instead define the boundary between regions A and B as the point where the strength of the atmospheric Potential Gradient exceeds the electric field from the needle, as at this point the motion of particles is more strongly affected by the PG than the needle.

This boundary condition can be written as:

$$E(b) = F \tag{A.30}$$

Where F is the magnitude of the Potential Gradient of the atmosphere. Using equation A.11, we find that in this case, the boundary between the regions A and B occurs at a distance:

$$b = \frac{K^2}{F^2} \tag{A.31}$$

Beyond this distance, the potential is equal to that of the surroundings, and the needle has no further effect. We thus want to look at the potential at this distance, given by equation A.15. If we use equation A.31 to substitute for $E(b)$, then:

$$V = V_b = \frac{-2K^2}{F} \tag{A.32}$$

substituting for K,

$$V = \frac{-I}{3\pi\mu\epsilon_0 F} \tag{A.33}$$

$$I = -3\pi\epsilon_0\mu F V \tag{A.34}$$

Again, we have neglected the minimum potential required for point discharge, so we can replace V with $(V - V_0)$ as in equation A.29:

$$I = -2\pi\epsilon_0(V - V_0)\frac{3}{2}\mu F \tag{A.35}$$

A.3 General case

We now have two equations for the point discharge current, in different limiting cases: equations A.29 and A.35. Equation A.29 is proportional to the horizontal speed of particles in region B (given by W) and equation A.35 is proportional to the vertical speed of particles in region B (given by (μF). As such, it has been proposed that a general solution to this equation would be proportional to the vector addition of these two velocities, i.e:

$$(W^2 + \mu^2 F^2)^{\frac{1}{2}} \tag{A.36}$$

We note that, for a vertical needle of length h in the Earth's Potential Gradient, F, the potential V is given simply by:

$$V = F \cdot h \tag{A.37}$$

So a proposed general solution for the point discharge current is given by:

$$I = -2\pi\epsilon_0(V - V_0)\left(W^2 + \frac{\mu^2}{h^2}V^2\right)^{\frac{1}{2}} \tag{A.38}$$

Appendix B

Logarithmic Electrometer Circuit Diagram

The circuit diagram of the logarithmic electrometer used to produce the logarithmic point discharge sensor deployed at the Reading University Atmospheric Observatory is presented here.

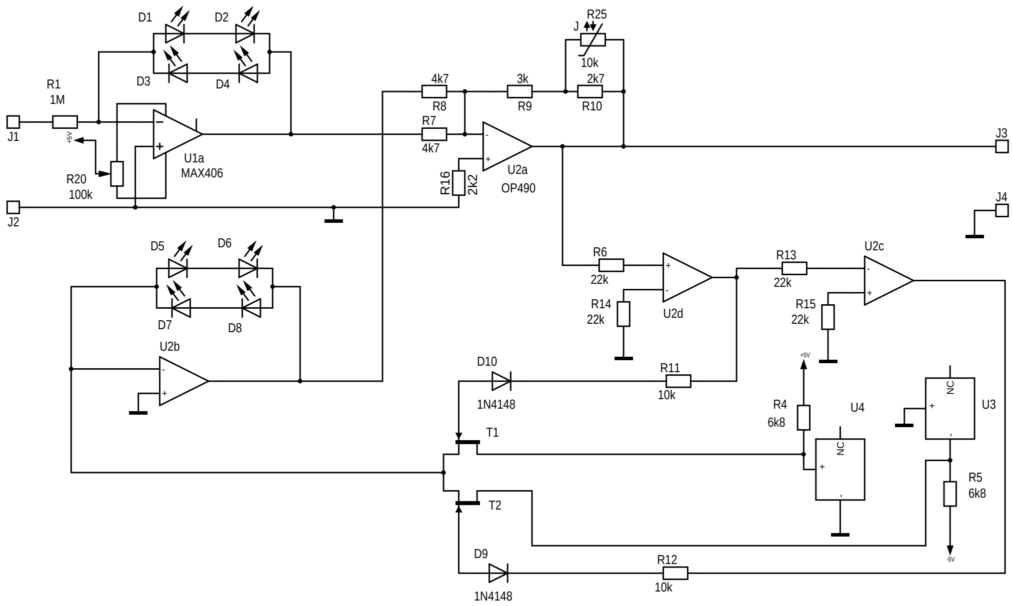

Figure B.1: Schematic of the logarithmic electrometer used. The current input is presented at J1, with final output of the circuit provided at J3. U1 is the electrometer amplifier, and U2a-U2b provides temperature compensation partly through a reference current. U2c and U2d select the polarity of reference current required. (Power supplies of ±5 V, are not shown for clarity).

Bibliography

[1] *ACE Real-Time Solar Wind*. https://www.swpc.noaa.gov/products/ace-real-time-solar-wind.

[2] T. Achtzehn et al. “The Coulomb instability of charged microdroplets: dynamics and scaling”. In: *The European Physical Journal D - Atomic, Molecular, Optical and Plasma Physics* 34 (2005), pp. 311–313. DOI: 10.1140/epjd/e2005-00102-1.

[3] M. W. Airey et al. “Electrical effects on droplet behaviour”. In: *Journal of Physics: Conference Series* 2702 (2024), p. 012015. DOI: 10.1088/1742-6596/2702/1/012015.

[4] M. H. P. Ambaum. “Cloud Drops”. In: *Thermal Physics of the Atmosphere*. John Wiley & Sons, Ltd, 2010, pp. 125–152. DOI: https://doi.org/10.1002/9780470710364.ch7.

[5] K. L. Aplin. “Atmospheric Electrification in the Solar System”. In: *Surveys in Geophysics* 27 (1 2006), pp. 63–108. DOI: https://doi.org/10.1007/s10712-005-0642-9.

[6] K. L. Aplin and G. Fischer. “Lightning detection in planetary atmospheres”. In: *Weather* 72.2 (2017), pp. 46–50. DOI: https://doi.org/10.1002/wea.2817.

[7] K. L. Aplin and R. G. Harrison. “Determining solar effects in Neptune’s atmosphere”. In: *Nature Communications* 7 (1 2016).

[8] K. L. Aplin and R. G. Harrison. “Solar-Driven Variation in the Atmosphere of Uranus”. In: *Geophysical Research Letters* 44.24 (2017), pp. 12, 083–12, 090.

[9] K. L. Aplin, R. G. Harrison, and M. J. Rycroft. “Investigating Earth’s Atmospheric Electricity: a Role Model for Planetary Studies”. In: *Space Science Reviews* 137 (2008), pp. 11–27. DOI: https://doi.org/10.1007/s11214-008-9372-x.

[10] C. H. Bachman, D. G. Hademenos, and L. S. Underwood. “Ozone and air ions accompanying biological applications of electric fields”. In: *Journal of Atmospheric and Terrestrial Physics* 33.3 (1971), pp. 497–505. DOI: https://doi.org/10.1016/0021-9169(71)90153-X.

[11] R. G. Barry and R. J. Chorley. *Atmosphere Weather and Climate - 9th Edition*. Routledge, 2010.

[12] G. Bazilevskaya. personal communication.

[13] G. A. Bazilevskaya. “Observations of Variability in Cosmic Rays”. In: *Space Science Reviews* 94 (2000), pp. 25–38.

[14] G. A. Bazilevskaya et al. “Cosmic Ray Induced Ion Production in the Atmosphere”. In: *Space Science Reviews* 137 (2008), pp. 149–173.

[15] K. V. Beard, H. T. Ochs, and C. H. Twohy. “Aircraft measurements of high average charges on cloud drops in layer clouds”. In: *Geophysical Research Letters* 31.14 (2004). DOI: `https://doi.org/10.1029/2004GL020465`.

[16] R. E. Belin. “A Radiosonde Method for Atmospheric Potential Gradient Measurements”. In: *Proceedings of the Physical Society* 60.4 (1948), pp. 381–287. DOI: `10.1088/0959-5309/60/4/307`.

[17] M. J. S. Belton et al. “Images from Galileo of the Venus Cloud Deck”. In: *Science* 253.5027 (1991), pp. 1531–1536. DOI: `10.1126/science.253.5027.1531`.

[18] A. J. Bennett and R. G. Harrison. “Evidence for global circuit current flow through water droplet layers”. In: *Journal of Atmospheric and Solar-Terrestrial Physics* 71.12 (2009), pp. 1219–1221. DOI: `https://doi.org/10.1016/j.jastp.2009.04.011`.

[19] A. Bologa et al. “Influence of gas composition, temperature and pressure on corona discharge characteristics”. In: *International Journal on Plasma Environmental Science & Technology* 5 (2011), pp. 110–116.

[20] W. J. Borucki et al. “Predicted electrical conductivity between 0 and 80 km in the Venusian atmosphere”. In: *Icarus* 51.2 (1982), pp. 302–321.

[21] W. J. Borucki et al. “Laboratory simulation of Venusian lightning”. In: *Geophysical Research Letters* 10.10 (1983), pp. 961–964. DOI: `https://doi.org/10.1029/GL010i010p00961`.

[22] W. J. Borucki et al. “Spectra of simulated lightning on Venus, Jupiter, and Titan”. In: *Icarus* 64.2 (1985), pp. 221–232. DOI: `https://doi.org/10.1016/0019-1035(85)90087-9`.

[23] W. J. Borucki et al. “Pioneer Venus Orbiter search for Venusian lightning”. In: *Journal of Geophysical Research: Space Physics* 96 (1991), pp. 11033–11043. DOI: `https://doi.org/10.1029/91JA01097`.

[24] S. W. Bougher et al. *Venus II: Geology, Geophysics, Atmosphere, and Solar Wind Environment*. University of Arizona Press, 1997.

[25] S. Burt. “The gust that never was: a meteorological instrumentation mystery”. In: *Weather* 77.4 (2020), pp. 123–126. DOI: `https://doi.org/10.1002/wea.3830`.

[26] G. J. Byrne, A. A. Few, and S. M. F. “The effects of atmospheric parameters on a corona probe used in measuring thunderstorm electric fields”. In: *Journal of Geophysical Research: Atmospheres* 91 (1986), pp. 9911–9920.

[27] G. J. Byrne, A. A. Few, and M. E. Weber. “Altitude, thickness and charge concentration of charged regions of four thunderstorms during trip 1981 based upon in situ balloon electric field measurements”. In: *Geophysical Research Letters* 10 (1983), pp. 39–42. DOI: `https://doi.org/10.1029/GL010i001p00039`.

[28] J. Caesar. *The African War*. Trans. by A. Way. Harvard University Press, 1955. (∼40 BCE).

[29] H. V. Cane. “Coronal Mass Ejections and Forbush Decreases”. In: *Space Science Reviews* 93 (2000), pp. 55–77.

[30] J. A. Chalmers. “The relation between point discharge current and field”. In: *Journal of Atmospheric and Terrestrial Physics* 2.5 (1952), pp. 292–300.

[31] J. A. Chalmers. “Point-discharge current, potentential gradient and wind-speed”. In: *Journal of Atmospheric and Terrestrial Physics* 11.3 (1957), pp. 301–302. DOI: `https://doi.org/10.1016/0021-9169(57)90081-8`.

[32] J. A. Chalmers. “The relation of point-discharge current to potential difference and wind-speed”. In: *Journal of Atmospheric and Terrestrial Physics* 24.5 (1962), pp. 339–344.

[33] J. A. Chalmers. *Atmospheric Electricity.* 2nd ed. Pergamon Press, 1967.

[34] J. A. Chalmers and W. W. Mapleson. “Point discharge currents from a captive balloon”. In: *Journal of Atmospheric and Terrestrial Physics* 6.1 (1955), pp. 149–159. DOI: `https://doi.org/10.1016/0021-9169(55)90022-2`.

[35] S. Chapman. “Electrostatic field measurements, corona discharge, and thunderclouds”. In: *Cornell Aeronautical Laboratory Reports* 68 (1956).

[36] S. Chapman. “Thundercloud Electrification in Relation to Rain and Snow Particles”. In: *Thunderstorm Electricity.* Ed. by H. R. Bryers. University of Chicago Press, 1953.

[37] T. von Clarmann et al. “Experimental evidence of perturbed odd hydrogen and chlorine chemistry after the October 2003 solar proton events”. In: *Journal of Geophysical Research: Space Physics* 110 (2005). DOI: `https://doi.org/10.1029/2005JA011053`.

[38] C. F. Clement and R. G. Harrison. “Charge-Distributions on aerosols”. In: *Electrostatics 1991.* Vol. 118. Institute of Physics Conference Series. IOP Publishing LTD, 1991, pp. 275–280.

[39] E. B. Curran, R. L. Holle, and R. E. López. “Lightning fatalities, injuries, and damage reports in the United States, 1959-1994”. In: (1997).

[40] E. J. Davis and M. A. Bridges. “The rayleigh limit of charge revisited: light scattering from exploding droplets”. In: *Journal of Aerosol Science* 25.6 (1994), pp. 1179–1199. DOI: `https://doi.org/10.1016/0021-8502(94)90208-9`.

[41] G. Delory, W. Farrell, and M. Desch. “A Global Electric Circuit on Mars”. In: *”Lunar and Planetary Science XXXII”* (2001).

[42] G. Elhalel et al. “Influence of short-term solar disturbances on the fair weather conduction current”. In: *J. Space Weather Space Clim.* 4 (2014). DOI: `https://doi.org/10.1051/swsc/2014022`.

[43] A. D. Erlykin, T. Sloan, and A. W. Wolfendale. “Correlations of clouds, cosmic rays and solar irradiation over the Earth”. In: *Journal of Atmospheric and Solar-Terrestrial Physics* 72.2 (2010), pp. 151–156. DOI: `https://doi.org/10.1016/j.jastp.2009.11.002`.

[44] A. A. Evtushenko, N. V. Ilin, and F. A. Kuterin. “On the existence of a global electric circuit in the atmosphere of Mars”. In: *Moscow University Physics Bulletin* 70 (2015), pp. 57–61. DOI: `https://doi.org/10.3103/S0027134915010063`.

[45] W. M. Farrell and M. D. Desch. “Is there a Martian atmospheric electric circuit?” In: *Journal of Geophysical Research: Planets* 106 (2001), pp. 7591–7595. DOI: https://doi.org/10.1029/2000JE001271.

[46] D. L. Finney et al. “A projected decrease in lightning under climate change”. In: *Nature Climate Change* 8 (3 2018), pp. 210–213. DOI: https://doi.org/10.1038/s41558-018-0072-6.

[47] G. Fischer et al. “Saturn lightning recorded by Cassini/RPWS in 2004”. In: *Icarus* 183 (2006), pp. 135–152. DOI: https://doi.org/10.1016/j.icarus.2006.02.010.

[48] S. E. Forbush. “On the Effects in Cosmic-Ray Intensity Observed During the Recent Magnetic Storm”. In: *Phys. Rev.* 51 (12 1937), pp. 1108–1109. DOI: 10.1103/PhysRev.51.1108.3.

[49] B. Franklin. “The Kite Experiment”. In: *The Pennsylvania Gazette* (1752).

[50] M. Füllekrug, E. A. Mareev, and M. J. Rycroft. *Sprites, Elves and Intense Lightning Discharges.* Springer Dordrecht, 2019. DOI: https://doi.org/10.1007/1-4020-4629-4.

[51] Y. Futaana et al. “Galactic Cosmic Rays at Mars and Venus: Temporal Variations from Hours to Decades Measured as the Background Signal of Onboard Microchannel Plates”. In: *The Astrophysical Journal* 940.2 (2022). DOI: https://dx.doi.org/10.3847/1538-4357/ac9a49.

[52] H. George et al. “Non-Lightning-Generated Whistler Waves in Near-Venus Space”. In: *Geophysical Research Letters* 50.19 (2023). DOI: https://doi.org/10.1029/2023GL105426.

[53] M. Gilmore et al. “Venus Surface Composition Constrained by Observation and Experiment”. In: *Space Science Reviews* 212 (3 2017), pp. 1511–1540. DOI: https://doi.org/10.1007/s11214-017-0370-8.

[54] A. Gomez and K. Tang. “Charge and fission of droplets in electrostatic sprays”. In: *Physics of Fluids* 6 (1994), pp. 404–414. DOI: 10.1063/1.868037.

[55] J. S. Greaves et al. “Phosphine gas in the cloud decks of Venus”. In: *Nature Astronomy* 5 (7 2021), pp. 655–664.

[56] B. Grieger et al. “Indication of a near surface cloud layer on Venus from reanalysis of Venera 13/14 spectrophotometer data”. In: *Proc. Int. Workshop ‘Planetary Probe Atmospheric Entry and Descent Trajectory Analysis and Science’, ESA Publ. Div., 63-70 (2004)* (Feb. 2004).

[57] S. N. Grover and K. V. Beard. “A Numerical Determination of the Efficiency with which Electrically Charged Cloud Drops and Small Raindrops Collide with Electrically Charged Spherical Particles of Various Densities”. In: *Journal of Atmospheric Sciences* 32.11 (1975), pp. 2156–2165. DOI: 10.1175/1520-0469(1975)032<2156:ANDOTE>2.0.CO;2.

[58] R. Gunn. “Diffusion Charging of Atmospheric Droplets by Ions, and the Resulting Combination Coefficients.” In: *Journal of Atmospheric Sciences* 11.5 (1954), pp. 339–347.

[59] J. Guo et al. "Measurements of Forbush decreases at Mars: both by MSL on ground and by MAVEN in orbit". In: *A&A* 611 (2018). DOI: 10.1051/0004-6361/201732087. URL: https://doi.org/10.1051/0004-6361/201732087.

[60] J. Guo et al. "Radiation environment for future human exploration on the surface of Mars: the current understanding based on MSL/RAD dose measurements". In: *The Astronomy and Astrophysics Review* 29 (2021). DOI: https://doi.org/10.1007/s00159-021-00136-5.

[61] D. A. Gurnett et al. "Non-detection at Venus of high-frequency radio signals characteristic of terrestrial lightning". In: *Nature* 409 (6818 2001), pp. 313–315. DOI: https://doi.org/10.1038/35053009.

[62] D. A. Gurnett et al. "Lightning and Plasma Wave Observations from the Galileo Flyby of Venus". In: *Science* 253.5027 (1991), pp. 1522–1525. DOI: 10.1126/science.253.5027.1522.

[63] M. Haidara, A. Denat, and P. Atten. "Corona discharges in high pressure air". In: *Journal of Electrostatics* 40-41 (1997). Proceedings of the 8th International Conference on Electrostatics, pp. 61–66. DOI: https://doi.org/10.1016/S0304-3886(97)00015-6.

[64] S. A. Hansell, W. K. Wells, and D. M. Hunten. "Optical Detection of Lightning on Venus". In: *Icarus* 117.2 (1995), pp. 345–351. DOI: https://doi.org/10.1006/icar.1995.1160.

[65] A. Hanslmeir. *The Sun and Space Weather*. Springer Dordrecht, 2007.

[66] R. G. Harrison. "The Global Atmospheric Electrical Circuit and Climate". In: *Surveys in Geophysics* 25.5-6 (2004), pp. 441–484.

[67] R. G. Harrison. "Discrimination between cosmic ray and solar irradiance effects on clouds, and evidence for geophysical modulation of cloud thickness". In: *Proceedings of the Royal Society A: Mathematical, Physical and Engineering Sciences* 464.2098 (2008), pp. 2575–2590. DOI: 10.1098/rspa.2008.0081.

[68] R. G. Harrison. "The Carnegie Curve". In: *Surveys in Geophysics* 34 (2 2013), pp. 209–232. DOI: 10.1007/s10712-012-9210-2.

[69] R. G. Harrison et al. "Applications of Electrified Dust and Dust Devil Electrodynamics to Martian Atmospheric Electricity". In: *Space Science Reviews* 203 (2016), pp. 299–345. DOI: https://doi.org/10.1007/s11214-016-0241-8.

[70] R. G. Harrison. "Behind the curve: a comparison of historical sources for the Carnegie curve of the global atmospheric electric circuit". In: *History of Geo- and Space Sciences* 11.2 (2020), pp. 207–213. DOI: 10.5194/hgss-11-207-2020.

[71] R. G. Harrison and M. H. P. Ambaum. "Enhancement of cloud formation by droplet charging". In: *Proceedings of the Royal Society A: Mathematical, Physical and Engineering Sciences* 464.2098 (2008), pp. 2561–2573. DOI: 10.1098/rspa.2008.0009.

[72] R. G. Harrison and M. H. P. Ambaum. "Observing Forbush decreases in cloud at Shetland". In: *Journal of Atmospheric and Solar-Terrestrial Physics* 72.18 (2010), pp. 1408–1414.

[73] R. G. Harrison, M. H. P. Ambaum, and M. Lockwood. “Cloud base height and cosmic rays”. In: *Proceedings of the Royal Society A: Mathematical, Physical and Engineering Sciences* 467.2134 (2011), pp. 2777–2791. DOI: 10.1098/rspa.2011.0040.

[74] R. G. Harrison, K. A. Nicoll, and M. H. P. Ambaum. “On the microphysical effects of observed cloud edge charging”. In: *Quarterly Journal of the Royal Meteorological Society* 141.692 (2015), pp. 2690–2699. DOI: https://doi.org/10.1002/qj.2554.

[75] R. G. Harrison and D. B. Stephenson. “Empirical evidence for a nonlinear effect of galactic cosmic rays on clouds”. In: *Proceedings of the Royal Society A: Mathematical, Physical and Engineering Sciences* 462.2068 (2006), pp. 1221–1233. DOI: 10.1098/rspa.2005.1628.

[76] R. G. Harrison and I. Usoskin. “Solar modulation in surface atmospheric electricity”. In: *Journal of Atmospheric and Solar-Terrestrial Physics* 72.2 (2010), pp. 176–182. DOI: https://doi.org/10.1016/j.jastp.2009.11.006.

[77] R. Harrison. “Columnar resistance changes in urban air”. In: *Journal of Atmospheric and Solar-Terrestrial Physics* 67.8 (2005), pp. 763–773. DOI: https://doi.org/10.1016/j.jastp.2005.01.006.

[78] R. Harrison et al. “Applications of Electrified Dust and Dust Devil Electrodynamics to Martian Atmospheric Electricity”. In: *Space Science Reviews* 203 (2016), pp. 299–345. DOI: 10.1007/s11214-016-0241-8.

[79] C. J. Hatton. “The Neutron Monitor”. In: *Progress in Elementary Particle and Cosmic Ray Physics*. North-Holland Publishing Co., 1971.

[80] D. F. Heath, A. J. Krueger, and P. J. Crutzen. “Solar Proton Event: Influence on Stratospheric Ozone”. In: *Science* 197.4306 (1977), pp. 886–889. DOI: 10.1126/science.197.4306.886.

[81] *HELCATS*. https://www.helcats-fp7.eu/.

[82] B. L. Hess, S. Piazolo, and J. Harvey. “Lightning strikes as a major facilitator of prebiotic phosphorus reduction on early Earth”. In: *Nature Communications* 12 (2021). DOI: https://doi.org/10.1038/s41467-021-21849-2.

[83] W. A. Hoppel. “Ion-aerosol attachment coefficients, ion depletion, and the charge distribution on aerosols”. In: *Journal of Geophysical Research: Atmospheres* 90 (1985), pp. 5917–5923. DOI: https://doi.org/10.1029/JD090iD04p05917.

[84] *Horizons System*. https://ssd.jpl.nasa.gov/horizons/.

[85] T. Howard. *Coronal Mass Ejections*. Springer New York, 2013.

[86] D. M. Hunten et al. *Venus*. University of Arizona Press, Tucson, 1983.

[87] W. T. Huntress and M. Y. Marovm. *Soviet Robots in the Solar System*. Springer New York, 2011. DOI: https://doi.org/10.1007/978-1-4419-7898-1.

[88] M. N. S. Immelman. “X. Point-discharge currents during thunderstorms”. In: *The London, Edinburgh, and Dublin Philosophical Magazine and Journal of Science* 25.166 (1938), pp. 159–163. DOI: https://doi.org/10.1080/14786443808561998.

[89] J. D. Jackson. *Classical Electrodynamics, 2nd Edition*. John Wiley & Sons, 1975.

[90] M. Z. Jacobson and D. G. Streets. "Influence of future anthropogenic emissions on climate, natural emissions, and air quality". In: *Journal of Geophysical Research: Atmospheres* 114 (2009). DOI: `https://doi.org/10.1029/2008JD011476`.

[91] C. de Jager and I. Usoskin. "On possible drivers of Sun-induced climate changes". In: *Journal of Atmospheric and Solar-Terrestrial Physics* 68.18 (2006), pp. 2053–2060. DOI: `https://doi.org/10.1016/j.jastp.2006.05.019`.

[92] S. Jiang, A. Ma, and S. Ramachandran. "Plant-based release system of negative air ions and its application on particulate matter removal". In: *Indoor Air* 31.2 (2021), pp. 574–586. DOI: `https://doi.org/10.1111/ina.12729`.

[93] A. Khain et al. "Rain Enhancement and Fog Elimination by Seeding with Charged Droplets. Part I: Theory and Numerical Simulations". In: *Journal of Applied Meteorology* 43.10 (2004), pp. 1513–1529. DOI: `10.1175/JAM2131.1`.

[94] J. R. Kirkman and J. A. Chalmers. "Point discharge from an isolated point". In: *Journal of Atmospheric and Terrestrial Physics* 10.5 (1957), pp. 258–265.

[95] A. J. Kliore, V. I. Moroz, and G. M. Keating. "The Venus International Reference Atmosphere." In: *Advances in Space Research* 5.11 (1985).

[96] M. G. Knivelson and C. T. Russell. *Introduction to Space Physics*. Cambridge University Press, 1995.

[97] D. R. Kniveton and B. A. Tinsley. "Daily changes in global cloud cover and Earth transits of the heliospheric current sheet". In: *Journal of Geophysical Research: Atmospheres* 109 (2004). DOI: `https://doi.org/10.1029/2003JD004232`.

[98] R. G. Knollenberg and D. M. Hunten. "The microphysics of the clouds of Venus: Results of the Pioneer Venus Particle Size Spectrometer Experiment". In: *Journal of Geophysical Research: Space Physics* 85.A13 (1980), pp. 8039–8058.

[99] V. A. Krasnopolsky. "Lightnings and nitric oxide on Venus". In: *Planetary and Space Science* 31.11 (1983), pp. 1363–1369. DOI: `https://doi.org/10.1016/0032-0633(83)90072-7`.

[100] V. A. Krasnopolsky. "A sensitive search for nitric oxide in the lower atmospheres of Venus and Mars: Detection on Venus and upper limit for Mars". In: *Icarus* 182 (2006), pp. 80–91. DOI: `https://doi.org/10.1016/j.icarus.2005.12.003`.

[101] L. V. Ksanfomaliti et al. "Electrical discharges in the atmosphere of Venus". In: *Soviet Astronomy Letters* 5 (1979).

[102] L. V. Ksanfomaliti. "Discovery of frequent lightning discharges in clouds on Venus". In: *Nature* 284 (1980), pp. 244–246. DOI: `https://doi.org/10.1038/284244a0`.

[103] L. V. Ksanfomality et al. "The low-frequency electromagnetic field in the Venus atmosphere-evidence from VENERA-13 and VENERA-14". In: *Astron. Lett.* 8 (1982), pp. 230–232.

[104] L. V. Ksanfomality. “Venus as a natural laboratory for search of life in high temperature conditions: Events on the planet on March 1, 1982”. In: *Solar System Research* 46 (2012), pp. 41–53. DOI: https://doi.org/10.1134/S0038094612010042.

[105] L. V. Ksanfomality et al. “Acoustic Measurements of the Wind Velocity at the VENERA-13 and VENERA-14 Landing Sites”. In: *Soviet Astronomy Letters* 8 (1982).

[106] L. V. Ksanfomality et al. “Hypothetical signs of life on Venus: revising results of 1975 – 1982 TV experiments”. In: 62.4 (2019), p. 378. DOI: 10.3367/UFNe.2018.12.038507.

[107] B. A. Laken and Č. Jasa. “Solar irradiance, cosmic rays and cloudiness over daily timescales”. In: *Geophysical Research Letters* 38.24 (2011). DOI: https://doi.org/10.1029/2011GL049764.

[108] M. I. Large and E. T. Pierce. “The dependence of point-discharge currents on wind as examined by a new experimental approach”. In: *Journal of Atmospheric and Terrestrial Physics* 10.5 (1957), pp. 251–257. DOI: https://doi.org/10.1016/0021-9169(57)90123-X.

[109] Y. J. Lee et al. “Spatial and Temporal Variability of the 365-nm Albedo of Venus Observed by the Camera on Board Venus Express”. In: *Journal of Geophysical Research: Planets* 125.6 (2020).

[110] T. I. Lekas. “Electrostatic charging of an aircraft due to airborne dust particles impacts”. In: *CEAS Aeronautical Journal* 10 (3 2019), pp. 903–908. DOI: https://doi.org/10.1007/s13272-018-00355-0.

[111] B. Little et al. “Galileo Images of Lightning on Jupiter”. In: *Icarus* 142.2 (1999), pp. 306–323. DOI: https://doi.org/10.1006/icar.1999.6195.

[112] J. A. Lockwood. “Forbush decreases in the cosmic radiation”. In: *Space Science Reviews* 12 (5 1971), pp. 658–715.

[113] M. Lockwood. “Solar Influence on Global and Regional Climates”. In: *Surveys in Geophysics* 33 (3 2012), pp. 503–534. DOI: 10.1007/s10712-012-9181-3.

[114] L. B. Loeb. “The Recombination of Ions”. In: *Electron-Emission Gas Discharges I / Elektronen-Emission Gasentladungen I.* 1956, pp. 471–503.

[115] L. B. Loeb. *Electrical Coronas, Their Basic Physical Mechanisms.* University of California Press, 1965.

[116] R. D. Lorenz. “Discharge current measurements on Venera 13 & 14 – Evidence for charged aerosols in the Venus lower atmosphere?” In: *Icarus* 307 (2018), pp. 146–149.

[117] R. D. Lorenz. “Lightning detection on Venus: a critical review”. In: *Progress in Earth and Planetary Science* 5.34 (2018).

[118] R. D. Lorenz et al. “Constraints on Venus Lightning From Akatsuki’s First 3 Years in Orbit”. In: *Geophysical Research Letters* 46.14 (2019), pp. 7955–7961. DOI: https://doi.org/10.1029/2019GL083311.

[119] R. D. Lorenz et al. "Point discharge current measurements beneath dust devils". In: *Journal of Atmospheric and Solar-Terrestrial Physics* 150-151 (2016), pp. 55–60. DOI: `https://doi.org/10.1016/j.jastp.2016.10.017`.

[120] D. R. MacGorman and W. D. Rust. *The Electrical Nature of Storms*. Oxford University Press, 1998.

[121] D. Malan. *Physics of Lightning*. English Universities Press LTD., 1963.

[122] J. Mao et al. "Global Impact of Lightning-Produced Oxidants". In: *Geophysical Research Letters* 48.21 (2021). DOI: `https://doi.org/10.1029/2021GL095740`.

[123] G. J. Marlton, R. G. Harrison, and K. A. Nicoll. "Note: Atmospheric point discharge current measurements using a temperature-compensated logarithmic current amplifier". In: *Review of Scientific Instruments* 84.6 (2013). DOI: `https://doi.org/10.1063/1.4810849`.

[124] N. D. Marsh and H. Svensmark. "Low Cloud Properties Influenced by Cosmic Rays". In: *Phys. Rev. Lett.* 85 (23 2000), pp. 5004–5007. DOI: `10.1103/PhysRevLett.85.5004`.

[125] T. A. Mather and R. G. Harrison. "Electrification of volcanic plumes". In: *Surveys in Geophysics* 27 (4 2006), pp. 387–432. DOI: `https://doi.org/10.1007/s10712-006-9007-2`.

[126] M. McAuley and R. Alanis. *JPL Photojournal*. `https://photojournal.jpl.nasa.gov/`. Accessed 2024-09-29.

[127] B. McGinness et al. "Evaluation of a modern point discharge sensor as an atmospheric electricity instrument". In: *Journal of Physics: Conference Series* 2702 (2024), p. 012004. DOI: `10.1088/1742-6596/2702/1/012004`.

[128] R. McIlveen. *Fundamentals of Weather and Climate*. Chapman and Hall, 1992.

[129] M. Michael et al. "Highly charged cloud particles in the atmosphere of Venus". In: *Journal of Geophysical Research: Planets* 114 (2009). DOI: `https://doi.org/10.1029/2008JE003258`.

[130] M. Michelarakis. "Electric field distribution of sphere-plane gaps: A SIMULATION APPROACH". PhD thesis. KTH Royal Institute of Technology, 2016.

[131] S. L. Miller. "A Production of Amino Acids Under Possible Primitive Earth Conditions". In: *Science* 117.3046 (1953), pp. 528–529. DOI: `10.1126/science.117.3046.528`.

[132] I. A. Mironova et al. "Energetic Particle Influence on the Earth's Atmosphere". In: *Space Science Reviews* 194 (2015), pp. 1–96. DOI: `https://doi.org/10.1007/s11214-015-0185-4`.

[133] D. P. Mitchell. "Anomalies in video transmissions from Venera-13 are probably not life forms". In: *Solar System Research* 46 (5 2012), pp. 382–384. DOI: `https://doi.org/10.1134/S0038094612050036`.

[134] K. A. Nicoll. "Note: A self-calibrating electrometer for atmospheric charge measurements from a balloon platform". In: *Review of Scientific Instruments* 84.9 (2013). DOI: `https://doi.org/10.1063/1.4821500`.

[135] K. A. Nicoll and R. G. Harrison. "Vertical current flow through extensive layer clouds". In: *Journal of Atmospheric and Solar-Terrestrial Physics* 71.17 (2009), pp. 2040–2046. DOI: https://doi.org/10.1016/j.jastp.2009.09.011.

[136] K. A. Nicoll and R. G. Harrison. "Detection of Lower Tropospheric Responses to Solar Energetic Particles at Midlatitudes". In: *Phys. Rev. Lett.* 112 (22 2014). DOI: 10.1103/PhysRevLett.112.225001.

[137] K. A. Nicoll and R. G. Harrison. "Stratiform cloud electrification: comparison of theory with multiple in-cloud measurements". In: *Quarterly Journal of the Royal Meteorological Society* 142.700 (2016), pp. 2679–2691. DOI: https://doi.org/10.1002/qj.2858.

[138] T. A. Nordheim et al. "Ionization of the venusian atmosphere from solar and galactic cosmic rays". In: *Icarus* 245 (2015), pp. 80–86.

[139] M. J. Owens et al. "Modulation of UK lightning by heliospheric magnetic field polarity". In: *Environmental Research Letters* 9.11 (2014), p. 115009.

[140] M. J. Owens et al. "Lightning as a space-weather hazard: UK thunderstorm activity modulated by the passage of the heliospheric current sheet". In: *Geophysical Research Letters* 42.22 (2015), pp. 9624–9632.

[141] M. J. Owens and R. J. Forsyth. "The Heliospheric Magnetic Field". In: *Living Reviews in Solar Physics* 10 (2013).

[142] C. Pei et al. "Three-Dimensional Wavy Heliospheric Current Sheet Drifts". In: *The Astrophysical Journal* 744.2 (2011), p. 170.

[143] Pliny the Elder. *The Natural History*. Trans. by J. Bostock and H. Riley. George Bell & Sons, 1855. (77 CE).

[144] C. Price. "Global surface temperatures and the atmospheric electrical circuit". In: *Geophysical Research Letters* 20.13 (1993), pp. 1363–1366.

[145] H. R. Pruppacher and J. D. Klett. *Microphysics of Clouds and Precipitation*. Springer Netherlands, 1996.

[146] G. Qin and Y. Wang. "Simulations of a Gradual Solar Energetic Particle Event Observed by Helios 1, Helios 2, and IMP 8". In: *The Astrophysical Journal* 809.2 (2015). DOI: https://dx.doi.org/10.1088/0004-637X/809/2/177.

[147] B. Ragent and J. Blamont. "The structure of the clouds of Venus: Results of the Pioneer Venus Nephelometer Experiment". In: *Journal of Geophysical Research: Space Physics* 85 (1980), pp. 8089–8105. DOI: https://doi.org/10.1029/JA085iA13p08089.

[148] B. Ragent et al. "Particulate matter in the Venus atmosphere". In: *Advances in Space Research* 5.11 (1985), pp. 85–115. DOI: https://doi.org/10.1016/0273-1177(85)90199-1.

[149] V. A. Rakov. "Electrical structure of thunderclouds". In: *Fundamentals of Lightning*. Cambridge University Press, 2016, pp. 31–51.

[150] L. Rayleigh. “On the equilibrium of liquid conducting masses charged with electricity”. In: *The London, Edinburgh, and Dublin Philosophical Magazine and Journal of Science* 14.87 (1882), pp. 184–186. DOI: 10.1080/14786448208628425.

[151] N. Rehbein and V. Cooray. “NOx production in spark and corona discharges”. In: *Journal of Electrostatics* 51-52 (2001). Electrostatics 2001: 9th International Conference on Electrostatics, pp. 333–339. DOI: https://doi.org/10.1016/S0304-3886(01)00115-2.

[152] A. Rouillard and M. Lockwood. “Oscillations in the open solar magnetic flux with a period of 1.68 years: imprint on galactic cosmic rays and implications for heliospheric shielding”. In: *Annales Geophysicae* 22.12 (2004), pp. 4381–4395.

[153] L. H. Ruhnke. “A rocket borne instrument to measure electric fields inside electrified clouds”. In: *NOAA Technical Report* (1971).

[154] C. T. Russell. “Planetary Lightning”. In: *Annual Review of Earth and Planetary Sciences* 21 (1993), pp. 43–87. DOI: https://doi.org/10.1146/annurev.ea.21.050193.000355.

[155] C. T. Russell et al. “Lightning on Venus inferred from whistler-mode waves in the ionosphere”. In: *Nature* 450 (7170 2007), pp. 661–662. DOI: https://doi.org/10.1038/nature05930.

[156] M. J. Rycroft, S. Israelsson, and C. Price. “The global atmospheric electric circuit, solar activity and climate change”. In: *Journal of Atmospheric and Solar-Terrestrial Physics* 62.17 (2000), pp. 1563–1576. DOI: https://doi.org/10.1016/S1364-6826(00)00112-7.

[157] M. J. Rycroft et al. “New model simulations of the global atmospheric electric circuit driven by thunderstorms and electrified shower clouds: The roles of lightning and sprites”. In: *Journal of Atmospheric and Solar-Terrestrial Physics* 69.17 (2007), pp. 2485–2509. DOI: https://doi.org/10.1016/j.jastp.2007.09.004.

[158] M. J. Rycroft et al. “An Overview of Earth’s Global Electric Circuit and Atmospheric Conductivity”. In: *Space Science Reviews* 137 (2008), pp. 83–105. DOI: https://doi.org/10.1007/s11214-008-9368-6.

[159] F. L. Scarf and C. T. Russell. “Lightning measurements from the Pioneer Venus Orbiter”. In: *Geophysical Research Letters* 10.12 (1983), pp. 1192–1195. DOI: https://doi.org/10.1029/GL010i012p01192.

[160] F. L. Scarf et al. “Lightning on Venus: Orbiter detection of whistler signals”. In: *Journal of Geophysical Research: Space Physics* 85 (1980), pp. 8158–8166. DOI: https://doi.org/10.1029/JA085iA13p08158.

[161] M. Schulz and K. Stattegger. “Spectrum: spectral analysis of unevenly spaced paleoclimatic time series”. In: *Computers & Geosciences* 23.9 (1997), pp. 929–945.

[162] R. G. Semonin and H. R. Plumlee. “Collision efficiency of charged cloud droplets in electric fields”. In: *Journal of Geophysical Research (1896-1977)* 71.18 (1966), pp. 4271–4278. DOI: https://doi.org/10.1029/JZ071i018p04271.

[163] A. Seppälä et al. “Solar proton events of October–November 2003: Ozone depletion in the Northern Hemisphere polar winter as seen by GOMOS/Envisat”. In: *Geophysical Research Letters* 31.19 (2004). DOI: `https://doi.org/10.1029/2004GL021042`.

[164] A. Simmons et al. “Low frequency variability and trends in surface air temperature and humidity from ERA5 and other datasets”. In: *ECMWF* (2021).

[165] G. C. Simpson. “XV. On the electricity of rain and its origin in thunderstroms”. In: *Philosophical Transactions of the Royal Society of London. Series A, Containing Papers of a Mathematical or Physical Character* 209.441-458 (1909), pp. 379–413. DOI: `10.1098/rsta.1909.0015`.

[166] G. C. Simpson and G. D. Robinson. “The distribution of electricity in thunderclouds, II”. In: *Proceedings of the Royal Society of London. Series A. Mathematical and Physical Sciences* 177.970 (1941), pp. 281–329. DOI: `10.1098/rspa.1941.0013`.

[167] G. C. Simpson and F. J. Scrase. “The distribution of electricity in thunderclouds”. In: *Proceedings of the Royal Society of London. Series A - Mathematical and Physical Sciences* 161.906 (1937), pp. 309–352. DOI: `10.1098/rspa.1937.0148`.

[168] J. A. Simpson. “The Latitude Dependence of Neutron Densities in the Atmosphere as a Function of Altitude”. In: *Phys. Rev.* 73 (11 1948), pp. 1389–1391. DOI: `10.1103/PhysRev.73.1389`.

[169] J. A. Simpson, W. Fonger, and S. B. Treiman. “Cosmic Radiation Intensity-Time Variations and Their Origin. I. Neutron Intensity Variation Method and Meteorological Factors”. In: *Physical Review* 90 (5 1953), pp. 934–950. DOI: `10.1103/PhysRev.90.934`.

[170] D. Singh. “Venus nightside surface temperature”. In: *Scientific Reports* 9 (2019). DOI: `https://doi.org/10.1038/s41598-018-38117-x`.

[171] N. N. Slyunyaev et al. “A new link between El Niño—Southern Oscillation and atmospheric electricity”. In: *Environmental Research Letters* 16.4 (2021), p. 044025.

[172] E. C. Starr. “Aircraft Precipitation-Static Radio Interference”. In: *Transactions of the American Institute of Electrical Engineers* 60.6 (1941), pp. 363–370. DOI: `https://doi.org/10.1109/T-AIEE.1941.50583477`.

[173] P. Sukanjanajtee and K. L. Aplin. “Electrostatic modelling of the Groza-2 discharge sensor on the Venera missions to Venus”. In: *Journal of Physics: Conference Series* 2702 (2024), p. 012021. DOI: `10.1088/1742-6596/2702/1/012021`.

[174] *Sunspot Number Data*. `https://www.ngdc.noaa.gov/stp/solar/ssndata.html`.

[175] H. Svensmark and E. Friis-Christensen. “Variation of cosmic ray flux and global cloud coverage—a missing link in solar-climate relationships”. In: *Journal of Atmospheric and Solar-Terrestrial Physics* 59.11 (1997), pp. 1225–1232. DOI: `https://doi.org/10.1016/S1364-6826(97)00001-1`.

[176] I. Szostakiewicz. personal communication. Apr. 17, 2024.

[177] Y. Takahashi et al. “An optical flash on Venus detected by the AKATSUKI spacecraft”. Preprint. DOI: `https://doi.org/10.21203/rs.3.rs-379882/v1`.

[178] F. Taylor and D. Grinspoon. "Climate evolution of Venus". In: *Journal of Geophysical Research: Planets* 114 (2009). DOI: https://doi.org/10.1029/2008JE003316.

[179] F. W. Taylor, H. Svedhem, and J. W. Head. "Venus: The Atmosphere, Climate, Surface, Interior and Near-Space Environment of an Earth-Like Planet". In: *Space Science Reviews* 214 (2018). DOI: https://doi.org/10.1007/s11214-018-0467-8.

[180] H. A. Taylor and P. A. Cloutier. "Venus: Dead or Alive?" In: *Science* 234.4780 (1986), pp. 1087–1093. DOI: 10.1126/science.234.4780.1087.

[181] H. A. Taylor and P. A. Cloutier. "Comment on "Further evidence for lightning at Venus"". In: *Geophysical Research Letters* 14.5 (1987), pp. 568–570. DOI: https://doi.org/10.1029/GL014i005p00568.

[182] H. A. Taylor, J. M. Grebowsky, and P. A. Cloutier. "Venus nightside ionospheric troughs: Implications for evidence of lightning and volcanism". In: *Journal of Geophysical Research: Space Physics* 90 (1985), pp. 7415–7426. DOI: https://doi.org/10.1029/JA090iA08p07415.

[183] W. W. L. Taylor et al. "Evidence for lightning on Venus". In: *Nature* 279 (5714 1979), pp. 614–616. DOI: https://doi.org/10.1038/279614a0.

[184] *The Steward Observatory 61" Kuiper Telescope*. https://james.as.arizona.edu/~psmith/61inch/. Accessed 2024-09-20.

[185] S. Thomas et al. "Galactic Cosmic Ray Modulation near the Heliospheric Current Sheet". In: *Solar Physics* 289 (2014).

[186] B. A. Tinsley. "Influence of Solar Wind on the Global Electric Circuit, and Inferred Effects on Cloud Microphysics, Temperature, and Dynamics in the Troposphere". In: *Space Science Reviews* 94 (2000), pp. 231–258. DOI: 10.1023/A:1026775408875.

[187] B. A. Tinsley et al. "Effects of Image Charges on the Scavenging of Aerosol Particles by Cloud Droplets and on Droplet Charging and Possible Ice Nucleation Processes". In: *Journal of the Atmospheric Sciences* 57.13 (2000), pp. 2118–2134. DOI: 10.1175/1520-0469(2000)057<2118:EOICOT>2.0.CO;2.

[188] D. V. Titov et al. "Clouds and Hazes of Venus". In: *Space Science Reviews* 214 (8 2018).

[189] S. N. Tripathi and R. G. Harrison. "Enhancement of contact nucleation by scavenging of charged aerosol particles". In: *Atmospheric Research* 62 (2002), pp. 57–70. DOI: https://doi.org/10.1016/S0169-8095(02)00020-0.

[190] S. N. Tripathi, M. Michael, and R. G. Harrison. "Profiles of Ion and Aerosol Interactions in Planetary Atmospheres". In: *Space Science Reviews* 137.1-4 (2008), pp. 193–211.

[191] I. G. Usoskin and G. A. Kovaltsov. "Cosmic rays and climate of the Earth: Possible connection". In: *Comptes Rendus Geoscience* 340.7 (2008), pp. 441–450. DOI: https://doi.org/10.1016/j.crte.2007.11.001.

[192] I. Usoskin. *Oulu Cosmic Ray Station*. https://cosmicrays.oulu.fi/.

[193] R. Vainio et al. "Dynamics of the Earth's Particle Radiation Environment". In: *Space Science Reviews* 147 (3 2009), pp. 187–231. DOI: 10.1007/s11214-009-9496-7.

[194] J. F. Valdés-Galicia, R. Pérez-Enríquez, and J. Otaola. "The cosmic-ray 1.68-year variation: A clue to understand the nature of the solar cycle?" In: *Solar Physics* 167 (1996), pp. 409–417. DOI: https://doi.org/10.1007/BF00146349.

[195] J. A. Van Allen and R. W. Fillius. "Propagation of a large Forbush decrease in cosmic-ray intensity past the Earth, Pioneer 11 at 34 AU, and Pioneer 10 at 53 AU". In: *Geophysical Research Letters* 19.14 (1992), pp. 1423–1426. DOI: https://doi.org/10.1029/92GL01445.

[196] J. T. VanderPlas. "Understanding the Lomb–Scargle Periodogram". In: *The Astrophysical Journal Supplement Series* 236 (2018). DOI: 10.3847/1538-4365/aab766.

[197] D. Venkatesan and Badruddin. "Cosmic-ray intensity variations in the 3-dimensional heliosphere". In: *Space Science Reviews* 52 (1990), pp. 121–194. DOI: https://doi.org/10.1007/BF00704241.

[198] *Venus Express - PSA*. https://www.cosmos.esa.int/web/psa/venus-express.

[199] M. E. Weber and A. A. Few. "A balloon borne instrument to induce corona currents as a measure of electric fields in thunderclouds". In: *Geophysical Research Letters* 5.4 (1978), pp. 253–256. DOI: https://doi.org/10.1029/GL005i004p00253.

[200] M. E. Weber, M. F. Stewart, and A. A. Few. "Corona point measurements in a thundercloud at Langmuir Laboratory". In: *Journal of Geophysical Research: Oceans* 88 (1983), pp. 3907–3910. DOI: https://doi.org/10.1029/JC088iC06p03907.

[201] F. J. W. Whipple and F. J. Scrase. *Point discharge in the electric field of the earth, an analysis of continuous records obtained at Kew observatory.* H.M. Stationery Off., 1936.

[202] D. R. Williams and E. Bell. *NASA Space Science Data Coordinated Archive.* https://nssdc.gsfc.nasa.gov/nmc/. Accessed 2024-09-30.

[203] E. R. Williams. "The tripole structure of thunderstorms". In: *Journal of Geophysical Research: Atmospheres* 94 (1989), pp. 13151–13167. DOI: https://doi.org/10.1029/JD094iD11p13151.

[204] E. R. Williams. "C.T.R. Wilson versus G.C. Simpson: Fifty years of controversy in atmospheric electricity". In: *Atmospheric Research* 91.2 (2009), pp. 259–271. DOI: https://doi.org/10.1016/j.atmosres.2008.03.024.

[205] C. T. R. Wilson. "III. Investigations on lighting discharges and on the electric field of thunderstorms". In: *Philosophical Transactions of the Royal Society of London. Series A, Containing Papers of a Mathematical or Physical Character* 221.582-593 (1921), pp. 73–115. DOI: 10.1098/rsta.1921.0003.

[206] R. M. Winslow et al. "Opening a Window on ICME-driven GCR Modulation in the Inner Solar System". In: *The Astrophysical Journal* 856.2 (2018), p. 139. DOI: 10.3847/1538-4357/aab098.

[207] O. Witasse et al. “Interplanetary coronal mass ejection observed at STEREO-A, Mars, comet 67P/Churyumov-Gerasimenko, Saturn, and New Horizons en route to Pluto: Comparison of its Forbush decreases at 1.4, 3.1, and 9.9 AU”. In: *Journal of Geophysical Research: Space Physics* 122.8 (2017), pp. 7865–7890. DOI: https://doi.org/10.1002/2017JA023884.

[208] H. Xie et al. “Long-lived geomagnetic storms and coronal mass ejections”. In: *Journal of Geophysical Research: Space Physics* 111 (2006). DOI: https://doi.org/10.1029/2005JA011287.

[209] B. R. S. Yadav and N. R. Vadav. “Intensity variation of cosmic rays near the heliospheric current sheet”. In: *Planetary and Space Science* 33.2 (1985), pp. 191–201. URL: https://doi.org/10.1016/0032-0633(85)90129-1.

[210] Y. Yair. “Lightning hazards to human societies in a changing climate”. In: *Environmental Research Letters* 13 (Dec. 2018). DOI: 10.1088/1748-9326/aaea86.

[211] A. M. Zadorozhny et al. “Nitric oxide and lower ionosphere quantities during solar particle events of October 1989 after rocket and ground-based measurements”. In: *Journal of Atmospheric and Terrestrial Physics* 54.2 (1992), pp. 183–192. DOI: https://doi.org/10.1016/0021-9169(92)90127-7.

[212] L. Zhou and B. A. Tinsley. “Production of space charge at the boundaries of layer clouds”. In: *Journal of Geophysical Research: Atmospheres* 112 (2007). DOI: https://doi.org/10.1029/2006JD007998.